ASME
SETTING THE STANDARD

Journal of Fluids Engineering

Published Monthly by ASME

VOLUME 129 • NUMBER 3 • MARCH 2007

TECHNICAL PAPERS

(Contents continued on inside back cover)

Transactions of the ASME, Journal of Fluids Engineering (ISSN 0098-2202) is published monthly by The American Society of Mechanical Engineers, Three Park Avenue, New York, NY 10016. Periodicals postage paid at New York, NY and additional mailing offices.
POSTMASTER: Send address changes to Transactions of the ASME, Journal of Fluids Engineering, c/o THE AMERICAN SOCIETY OF MECHANICAL ENGINEERS, 22 Law Drive, Box 2300, Fairfield, NJ 07007-2300.
CHANGES OF ADDRESS must be received at Society headquarters seven weeks before they are to be effective. Please send old label and new address.
STATEMENT from By-Laws. The Society shall not be responsible for statements or opinions advanced in papers or ... printed in its publications (B7.1, Par. 3).

This journal is printed on acid-free paper, which exceeds the ANSI Z39.48-1992 specification for permanence of paper and library materials. ♾™
♻ 85% recycled content, including 10% post-consumer fibers.

Journal of Fluids Engineering **Volume 129, Number 3** **MARCH 2007**

The ASME Journal of Fluids Engineering is abstracted and indexed in the following:

Applied Science & Technology Index, Chemical Abstracts, Chemical Engineering and Biotechnology Abstracts (Electronic equivalent of Process and Chemical Engineering), Civil Engineering Abstracts, Computer & Information Systems Abstracts, Corrosion Abstracts, Current Contents, Ei EncompassLit, Electronics & Communications Abstracts, Engineered Materials Abstracts, Engineering Index, Environmental Engineering Abstracts, Environmental Science and Pollution Management, Excerpta Medica, Fluidex, Index to Scientific Reviews, INSPEC, International Building Services Abstracts, Mechanical & Transportation Engineering Abstracts, Mechanical Engineering Abstracts, METADEX (The electronic equivalent of Metals Abstracts and Alloys Index), Petroleum Abstracts, Process and Chemical Engineering, Referativnyi Zhurnal, Science Citation Index, SciSearch (The electronic equivalent of Science Citation Index), Shock and Vibration Digest, Solid State and Superconductivity Abstracts, Theoretical Chemical Engineering

Experimental Investigation of Secondary Flow Structure in a Blade Passage With and Without Leading Edge Fillets

G. I. Mahmood
Research Associate

S. Acharya[1]
Professor
e-mail: acharya@me.lsu.edu

Turbine Innovation and Energy Research (TIER) Center,
Louisiana State University,
Baton Rouge, LA 70803

Velocity and pressure measurements are presented for a blade passage with and without leading edge contouring in a low speed linear cascade. The contouring is achieved through fillets placed at the junction of the leading edge and the endwall. Two fillet shapes, one with a linear streamwise cross-section (fillet 1) and the other with a parabolic cross-section (fillet 2), are examined. Measurements are taken at a constant Reynolds number of 233,000 based on the blade chord and the inlet velocity. Data presented at different axial planes include the pressure loss coefficient, axial vorticity, velocity vectors, and yaw and pitch angles. In the early stages of the development of the secondary flows, the fillets are seen to reduce the size and strength of the suction-side leg of the horseshoe vortex with associated reductions in the pressure loss coefficients and pitch angles. Further downstream, the total pressure loss coefficients and vorticity show that the fillets lift the passage vortex higher above the endwall and move it closer to the suction side in the passage. Near the trailing edge of the passage, the size and strength of the passage vortex is smaller with the fillets, and the corresponding reductions in pressure loss coefficients extend beyond the mid-span of the blade. While both fillets reduce pressure loss coefficients and vorticity, fillet 1 (linear fillet profile) appears to exhibit greater reductions in pressure loss coefficients and pitch angles.
[DOI: 10.1115/1.2427075]

Introduction

Secondary flows in turbine blade passages contribute to increased aerodynamic losses and reduction in efficiency. The dominant secondary flow is referred to as the passage vortex whose origin begins with the leading edge horseshoe vortex and is driven by the pressure gradient in the passage. It is well known that the horseshoe vortex is formed along the stagnation-line plane at the junction of the turbine blade leading edge and the blade passage endwall region. This horse-shoe vortex propagates into the passage as a pressure side vortex and a suction side vortex [1] on the pressure and suction sides of the blade, respectively. The two vortex legs eventually merge downstream in the blade passage to form the passage vortex, which is further driven by the cross flow from the passage pressure side to the suction side [2,3]. As the vortex moves through the passage, it grows in size and migrates toward the blade suction side. The passage secondary flows increase thermal loading on the passage end-wall and increase pressure losses across the passage. The passage vortex also lifts the film cooling flows from the endwall region and significantly reduces the effectiveness of the film coolant injected through the upstream endwall region.

Reduction of the passage vortex strength and size can be potentially beneficial by reducing the losses and endwall thermal loading. Leading edge fillets on the blade leading edge have been proposed as a possible strategy for reducing the secondary flows. However, in order to determine a suitable profile for the fillets and in order to optimize their geometrical parameters, a detailed understanding of the role of the fillets on the secondary flow structures is necessary. This is the primary motivation behind the proposed work.

Measurements of the secondary flow structures in stationary linear cascades have been reported by several investigators. The role of the pressure side vortex in the development of the passage vortex has been studied in detail by Langston et al. [4]. Goldstein et al. [5] have used the mass transfer (naphthalene sublimation) technique to track and identify the path of the secondary flow structures in the blade passage. Yamamoto [6], Gallus et al. [7], and Smith and Cleak [8] have reported measurements of the passage vortex and the effects of inlet conditions on the passage vortex in linear blade cascades. The unsteady nature of the passage vortex in a linear blade cascade at different flow incidence angles has been studied by Ma et al. [9]. The development of the streamwise vorticity downstream of an annular two-dimensional cascade has been measured and reported in [10]. The details of the leading edge horseshoe vortex and the development of the passage vortex in a linear vane passage has been studied experimentally by Kang and Thole [11] and Kang et al. [12]. Numerical predictions of the horseshoe vortex, passage vortex, and profile losses in two-dimensional turbine blade/vane passages have been presented in [13–15].

A number of studies have explored the role of leading edge fillets on the secondary flow development in vane or blade passages. Davenport et al. [16] and Simpson [17] report that the horseshoe vortex structure is altered when fillets or fairings are employed on the leading edge of a two-dimensional wing. By thickening the blade profile at the leading edge near the endwall, Sauer et al. [18] reduced the pressure loss and flow angles in the exit plane of a blade passage. Measurements of flow angle, velocity vector, vorticity, and turbulent kinetic energy in a turbine blade passage were reported by Eymann et al. [19] with a thickened blade profile near the blade-endwall junction. Total pressure losses were observed to be reduced near the endwall. However, in the measurements of Becz et al. [20,21], where bulbs and fillets on the blade leading edge are employed along one end wall, the pressure loss on the opposite end wall was observed to increase. An 8%

[1]Corresponding author.

Contributed by the Fluids Engineering Division of ASME for publication in the JOURNAL OF FLUIDS ENGINEERING. Manuscript received January 9, 2005; final manuscript received June 8, 2006. Assoc. Editor: Yoshinobu Tsujimoto.

reduction in the total pressure loss coefficient was observed with a small bulb and a fillet. However, in [19–21] measurements were reported only downstream of the blade passage, and no in-passage measurements are reported. Zess and Thole [22] studied an asymmetric elliptical leading edge fillet with height and length proportional to the incoming boundary layer thickness, and reported reduction in secondary flows, vorticity, and turbulent kinetic energy. Lethander et al. [23] reported a numerical study that optimizes the leading edge fillet profile with the objective of reducing the secondary flows in a vane passage. Shih and Lin [24] numerically predicted the secondary flows in a vane passage with two types of leading edge fillets and inlet swirl levels, and observed that the total pressure loss across the passage is reduced without any swirl. Recently, Mahmood et al. [25] reported endwall heat transfer measurements for four different fillet profiles and demonstrated that the endwall heat transfer is the lowest for a fillet with a parabolic fillet profile. However, detailed flow measurements are not reported.

The goal of the present study is to report detailed pressure and velocity measurements at different axial chord locations within the blade passage in order to understand the role of the fillets on the secondary flow structures in the passage of a two-dimensional linear blade cascade. As noted above, reported experimental studies have primarily focused on pressure loss and heat transfer data, and flow measurements have been rather limited. Further, the pressure measurements have been generally reported [19–21] downstream of the blade passage where they are more easily measured. In the present work, measurements are reported at four axial locations within the blade passage in order to track the development of the passage vortex.

Two profiles for the fillet cross-section are studied in the present paper: a linear profile and a parabolic profile that are shown in [25] to yield the lowest endwall heat transfer. A five-hole probe has been primarily used for the flow measurements. The data reported in the present study include pressure loss, velocity vectors, vorticity, and yaw/pitch flow angles at several axial-chord planes in the blade passage. These measurements are compared for the baseline unfilleted case and the two filleted cases in order to quantitatively assess the role of the fillets and the fillet profile on the secondary flow structures and the pressure loss.

Experimental Facility: Linear Cascade

The test facility is shown schematically in Fig. 1(*a*) and consists of a low speed wind tunnel housing a linear cascade test section. Three linear blades, scaled up ten times, form the two passages in the cascade test section. The two-dimensional blade profiles represent the hub side section of the first stage GE-E^3 high pressure turbine blade. The geometric parameters employed in the cascade are given in Table 1.

For the present experiment, the blades are solid and constructed out of wood. The blade tips are lined with foam weather strips to prevent tip leakage between the blade and endwalls. As shown in Fig. 1(*a*), the outer side of the suction side blade is removed to prevent any flow blockage between the blade and side wall. The two tailboards pivoted at the trailing edges of the side blades are moveable with lead screws from the side walls and enable pressure adjustments on the blade profiles to maintain periodic conditions in the two passages. The facility operates in an open circuit mode under suction of a 3.73 kW duct fan blower. Ambient air enters the rectangular cross-section inlet channel of aspect ratio 1.36:1 through a two-dimensional nozzle of contraction ratio 3.4:1, and then flows through the test section. Inclined slots machined in the channel walls serve as suction bleed of the boundary layer along the side walls. A passive turbulence grid made of cylindrical rods of diameter 12.20 mm is placed in the channel just downstream of the nozzle and 4.2 chord upstream of the center blade to increase the free stream turbulence of the inlet flow. The top endwall of the test section has machined slots and holes to enable insertion of flow measuring probes. The unused

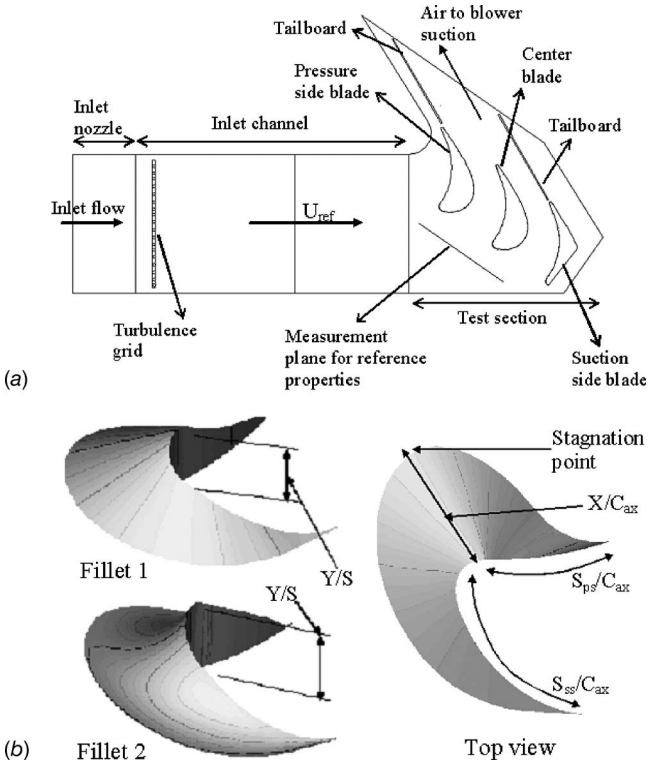

Fig. 1 (*a*) Schematic of the blade cascade test facility. (*b*) Profiles and geometric parameters of the two fillets.

holes and slots during measurements are filled in with foam weather strips or covered with tapes to prevent air leakage from outside into the test section. Also, the slot being used is covered with a pair of partially overlapping tape strips to minimize any flow leakage.

Machined grooves along the span of the blade are located all along the blade profiles and accommodate 1.65 mm diameter steel tubes. The steel tube has one or two drilled holes of diameter 0.30 mm that serve as static pressure taps. The tube can be traversed along the groove and static pressure can be measured at multiple spanwise locations. The second hole on the tube is masked with a tape while data are measured from the first hole. The open ends of the tubes come out of the test section though mating holes on the top wall, which are aligned with the grooves on the blade profile. During measurements, the tube surface is made flush with the blade profile by masking the grooves (except in the vicinity of the hole) with thin scotch tapes. This ensures a smooth blade profile and no interaction between the groove corners and passage flow.

Fillet Profile and Parameters

As noted earlier, in Mahmood et al. [25] four types of leading edge fillets are tested, and endwall heat transfer results are reported. For the present study, the two fillets that have yielded the

Table 1 Geometric parameters for the cascade test section

Radial location of the blade profile in the GE-E^3 turbine stage (cm)	32.337
Scale up factor for present test model	10
Actual chord length, C (cm)	35.86
Axial chord length, C_{ax} (cm)	30.36
Aspect ratio (true chord length to blade span), C/S	0.78
Solidity ratio (true chord length to blade pitch), C/P	1.23
Flow inlet angle (deg)	0

Table 2 Fillet geometric parameters

Fillet	Description	$(Y/S)_{max}$	$(X/C_{ax})_{max}$	s_{ss}/C_{ax}	s_{ps}/C_{ax}
1	Blends simultaneously into endwall and blade surface, linear profile from blade to endwall	0.10	0.299	0.566	0.322
2	Blends simultaneously into endwall and blade surface, concave circular (or parabolic) profile from blade to endwall	0.10	0.299	0.566	0.322

best results from the perspectives of the endwall heat transfer are selected for detailed flow measurements. The profiles of these two fillets, called fillet 1 and fillet 2 in this paper, are shown in Fig. 1(*b*). Note that in [25], fillet 2 is referred to as fillet 4 since four different fillets are tested in that study. Table 2 provides the geometric parameters of the fillet profiles. Both the fillets blend into the endwall and blade wall simultaneously. The height of fillet 1 varies linearly from the blade surface to the endwall, while for fillet 2, the height varies on a concave circular arc (parabolic profile) from the blade to endwall. The fillets are attached to the bottom endwall along the blade leading edges with double sided tape. No fillets are employed at the junction of the top wall and blade leading edge.

The highest point of each fillet is located on the blade stagnation location and at a height of one boundary layer thickness of the incoming flow. Fillet height along the blade surface then decreases to zero downstream from the stagnation point along both sides of the blade. The outer edge of the fillet section is described by two ellipses, one on the suction side and one on the pressure side. The curvature of the two ellipses matches at the stagnation location. As shown in Fig. 1(*b*) and Table 2, the circumferential length of the fillets on the suction side is larger than that on the pressure side. The fillets are fabricated using a three-dimensional stereo lithography system.

Measurement Techniques

Measurements are obtained at four pitchwise normal planes located in the passage between the center blade and the pressure side blade. Figure 2 shows the coordinate system employed for the measurements and the axial locations of the planes. Reference quantities of the flow field are measured in a plane parallel to the passage inlet and located 115 mm upstream of the leading edge of the center blade. The global coordinates (X_G, Z_G) in Fig. 2 originate at the farthest upstream point on the center blade profile. The spanwise coordinate Y or Y_G originates at the bottom endwall. The local coordinates (X, Y, Z) originate on the pressure side of the center blade and are parallel to the global coordinate system. The velocity components (U, V, W) are parallel to (X, Y, Z), respectively. The positive yaw angle is directed counter-clockwise from the $+X$ direction and the positive pitch angle is directed toward $+Y$ from the $+X$ direction.

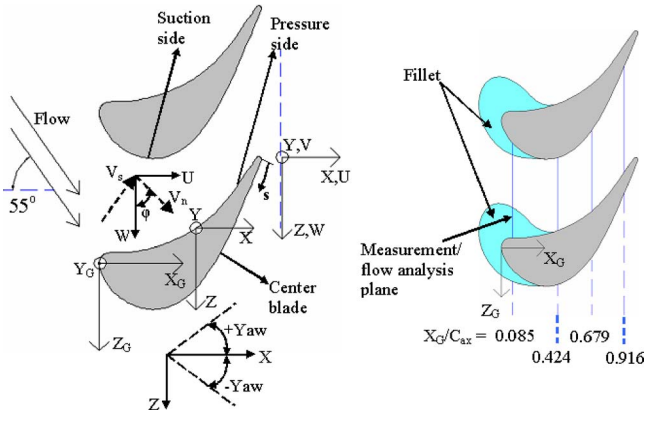

Fig. 2 Coordinate systems and measurement locations in the test section

Flow Structure Measurements. A miniature five-hole pressure probe of tip diameter 1.30 mm is employed for the flow field measurements. The probe is calibrated in the inlet channel of the test facility for yaw and pitch angles between +30 and −30 deg at a streamwise velocity of 10.26 m/s based on the procedures described in Ligrani et al. [26]. Pressure signals from the five tubes of the probe are fed into five Omega differential transducers from which the voltage signals then are obtained and recorded on a HP3497A data acquisition unit controlled by a Dell Dimension desktop PC. Data are acquired at a sampling rate of 20 Hz over a time period of 15 s from each tube. Thus, data from each tube are time-averaged over 300 samples. The probe is approximately oriented along the streamwise direction to obtain the measurements so that the yaw and pitch corrections are minimized. The time-averaged voltage signals are converted into pressure with the transducer calibrations. The calibration curves for the five-hole probe are then applied to the converted pressure signals to deduce the local total pressure, static pressure, and velocity components of the flow. These quantities are determined after applying the spatial resolutions and downwash corrections [27] on the raw data because of the finite tip diameter of the probe. The total pressure loss coefficients are determined from the equation,

$$C_{pt,loss} = \frac{P_{tot,0} - P_t}{0.5 * \rho_{air} * U_{ref}^2} \tag{1}$$

where the P_t is the measured total pressure in a location. The air density is obtained at the inlet temperature from property charts.

The probe is traversed in a plane through the slots in the top wall with a Unislide two-axis motorized traverse controlled by a Velmex Inc. stepper motor controller. The same Dell Dimension PC used for data acquisition is employed to control the motor controller. Thus, a single in-house programming code is used to coordinate data recording from the probe and positioning the probe at different locations. Data are measured from the bottom endwall to the mid-span height with the pitchwise- and spanwise-spatial increments that range from 3.0 mm near the endwall and suction side of the blade to 12.0 mm near the mid-span location. Thus, particular care is taken to adequately resolve the secondary flow structures near the endwall.

Wall Static Pressure Measurements. To measure the static pressure on the blade profile, the open end of the steel tubes in the grooves on the blade profile are connected via rubber tubes to a Validyne differential transducer, which transmits signals to the HP3497A data acquisition unit. Pressure signals from each tube are recorded and time-averaged at 20 Hz sampling rate for 60 s. The following equation is used to determine the surface static pressure coefficients.

$$C_p = \frac{P_{stat,0} - P_{stat}}{0.5 * \rho_{air} * U_{ref}^2} \tag{2}$$

Here, P_{stat} is the measured surface pressure.

Table 3 Upstream and reference flow parameters

Stagnation temperature, $T_{o,in}$ (K)	300
Stagnation pressure, $P_{o,in}$ (Pa)	1.013×10^5
Average freestream velocity, U_{ref} (m/s)	10.26
Inlet Reynolds number, Re_{in}	233,000
Freestream turbulence intensity	4.0%
Average reference static pressure (below atmospheric), $P_{stat,0}$ (Pa, gage)	121.9
Average reference total pressure (below atmospheric), $P_{tot,0}$ (Pa, gage)	60.5
Boundary layer thickness, δ (mm)	46.0

Uncertainty Estimates. Uncertainties in the measured data are estimated according to the procedures in Holman [28] and Moffat [29] and are presented here based on a 95% confidence level. The maximum uncertainties in the surface static pressure and static pressure coefficient C_p along the blade are 0.7% and 6.0%, respectively. For the five-hole pressure probe measurements, since the inner diameter of each tube is very small (0.20 mm) and these tubes are relatively long (56.0 cm), the time response of the probe is slow, which contributes the most in the uncertainty of the data. In the pitchwise middle locations of the passage, uncertainties in the total pressure are 2.0% near the endwall and 1.1% in the inviscid region. At the same locations, static pressure uncertainties are 1.1% and 0.8%, respectively. The total pressure loss coefficients and the static pressure loss coefficients have maximum uncertainty of 7.2% and 6.5%, respectively, in the mid-pitch locations. Uncertainties in the other flow quantities are determined from the pressure and pitch-yaw angle measurements of the local flow vector in the pitchwise mid-locations of the passage. Interpolations of the calibration curves to determine the correct pitch-yaw angles contribute to the velocity uncertainty. Thus, uncertainties in the flow angles are high in the secondary flow regions, and where flow angles are usually close to the maximum range of the calibration pitch-yaw angles. Pitch and yaw angle uncertainty is 2.5% in the inviscid region and 12.0% in the secondary flow region. The corresponding maximum values of the velocity and axial vorticity uncertainties are 3.0% and 7.0%, respectively.

Experimental Results and Discussions

The measured quantities are normalized by the reference flow properties measured in an upstream plane parallel to the passage inlet, as mentioned earlier. Table 3 presents the measured reference quantities. The Reynolds number in the table is determined based on the actual blade chord length and inlet freestream velocity.

Periodicity of Passage Flow. The flow conditions in the two passages are made periodic by adjusting the locations of the tailboards. Such conditions simulate the flow periodicity present in a blade row in an actual turbine stage. The static pressures on the suction sides of the center blade and the inner blade (the blade located near the pressure side of the center blade—see Fig. 1) are matched, while the static pressures on the pressure sides of the center blade and the outer blade (blade located near the suction side of the center blade) are matched to obtain the periodicity in the passages. The resulting pressure distributions on the blade profiles at a spanwise location of $Y/S=0.33$ in the form of static pressure coefficients C_p are shown in Fig. 3. The blade surface coordinate $s/C=0.0$ corresponds to the trailing edge of the suction side. The blade stagnation region then is located at $s/C=1.50$ where C_p is the highest. The C_p distributions on the suction sides downstream of the throat region ($s/C<1.20$) for the center blade and the inner blade (pressure-side blade) are slightly offset from each other. However, in general, the static pressure coefficients are in reasonable agreement on all sides in the two passages, and reflect periodicity in the two passages.

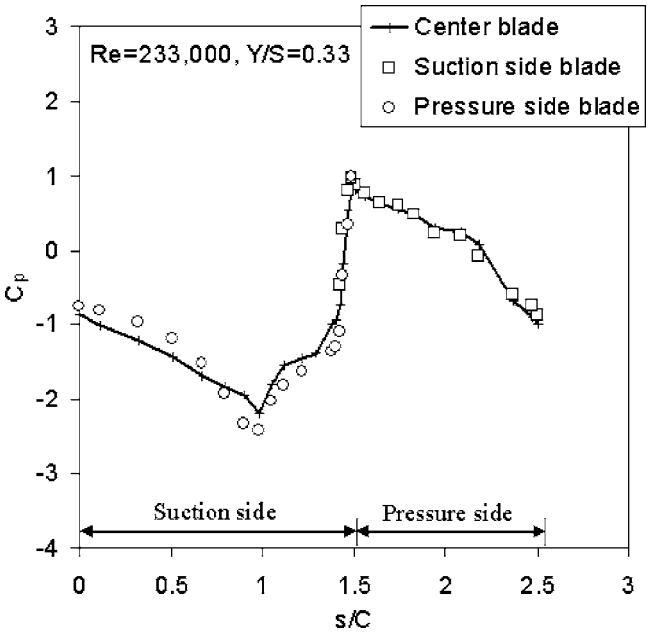

Fig. 3 Static pressure coefficients on the three blade surfaces in the two passages at spanwise location Y/S=0.33

Total Pressure Loss Coefficients $C_{pt,loss}$. The contour plots of the total pressure loss coefficients in the pitchwise normal planes at three axial locations ($X_G/C_{ax}=0.085$, 0.424, and 0.916) are presented in Figs. 4–6 for the baseline, fillet 1, and fillet 2. The axial plane at $X_G/C_{ax}=0.085$ is located slightly downstream of the center blade stagnation line (see Fig. 2). The plane at $X_G/C_{ax}=0.424$ is located downstream of the fillets while $X_G/C_{ax}=0.916$ is located slightly upstream of the passage exit plane. In Figs. 4–6, the pitchwise position $Z/P=0.0$ is always located on the pressure side. Data measured very close to the pressure and suction sides are not reported as they are influenced by the flow blockage between the probe body and the blade surface. Although measurements have been made up to the mid-span locations, plots are presented in the area where the differences between baseline and fillet data are significant.

In Fig. 4, $Z/P=-0.30$ represents the mid-pitch location at $X_G/C_{ax}=0.085$, and therefore the region shown corresponds to the location where the suction-side vortex appears. The direction of streamwise velocity varies significantly from the pressure side to suction side in this plane and the probe tip needs to be reoriented for any measurement for $Z/P>-0.30$ to be within the yaw calibration range. Such a probe reorientation places the probe tip in a slightly different axial location than $X_G/C_{ax}=0.085$. Thus, data are presented only for $Z/P<-0.30$ where only one probe orientation is maintained at all locations. When the fillets are present, these measurement locations correspond to the region between the fillet profiles on the pressure and suction side. No contour data are present in the bottom left corner for the fillets in Fig. 4 because of the presence of fillet volume. The high magnitude region of $C_{pt,loss}$ between $Z/P=-0.63$ and -0.43 just above the endwall corresponds to the suction side leg of the leading edge horseshoe vortex. Both the magnitude of the loss coefficient and the area representative of the vortex are smaller for fillet 1 and fillet 2 compared to those for the baseline. This indicates that the fillet reduces the size and weakens the leading edge horseshoe vortex, which, in turn, decreases the size and the strength of the vortex leg on the blade suction side (shown in Fig. 4), and also on the pressure side (not shown at $X_G/C_{ax}=0.085$). $C_{pt,loss}$ contours are nearly the same above the vortex region ($Y/S>0.06$) extending up to the mid-span for the baseline and the cases with fillets.

At $X_G/C_{ax}=0.424$, Fig. 5 shows the significantly larger contour

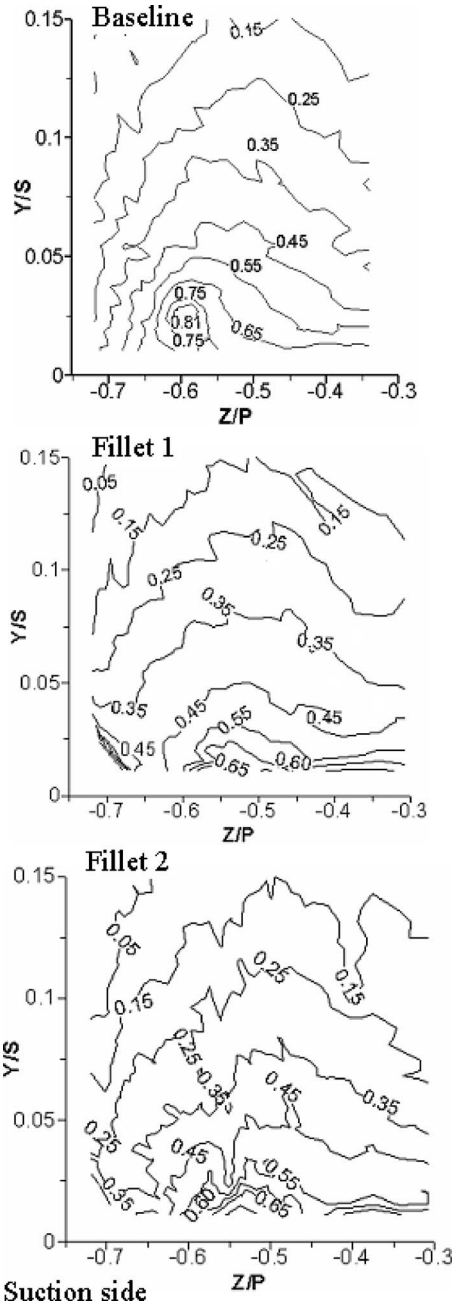

Fig. 4 Total pressure loss coefficient $C_{pt,loss}$ in pitchwise normal plane at $X_G/C_{ax}=0.085$ for baseline, fillet 1, and fillet 2

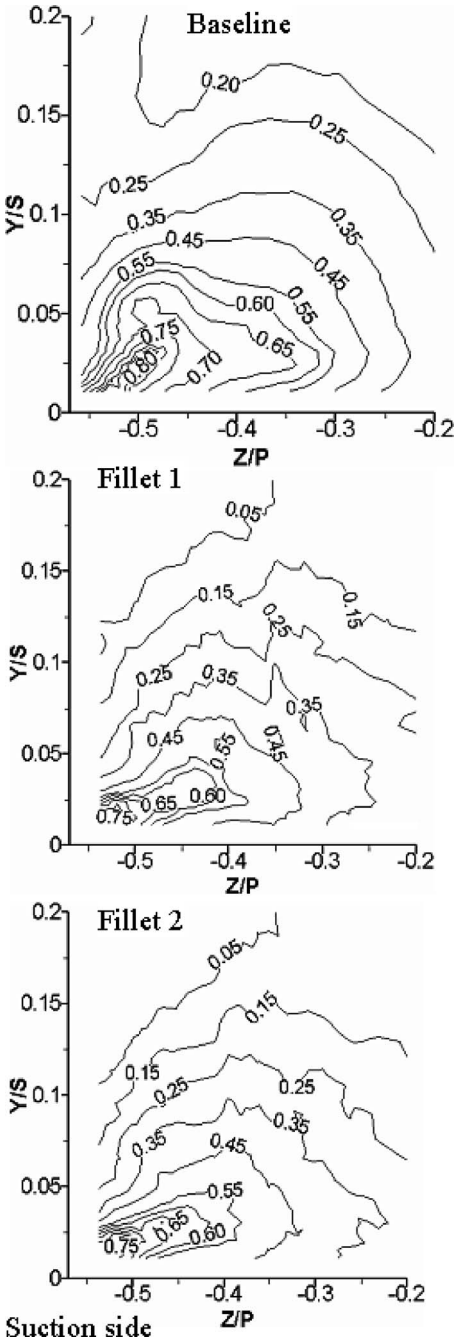

Fig. 5 Total pressure loss coefficient $C_{pt,loss}$ in pitchwise normal plane at $X_G/C_{ax}=0.424$ for baseline, fillet 1, and fillet 2

values of $C_{pt,loss}$ for the baseline case in the region between $Z/P=-0.54$ to -0.30 and $Y/S=0.01$ to 0.1 representative of the passage vortex. The passage vortex at this position has moved closer to the suction side, but is still located close to the endwall. When the size of the passage vortex is compared between the various cases in Fig. 5, it is clearly observed that the area of the high contour values (e.g., an arbitrary value of 0.6 may be chosen for comparison purposes) for fillet 1 and fillet 2 is less than half the area of that for the baseline. Further, the pressure loss magnitudes themselves in the passage vortex regions are lower (by greater than 10% in local regions) for the cases with fillets than for the baseline. This further confirms that the fillets reduce both the size and the strength of the passage vortex. However, in comparing the contour magnitudes and size of the passage vortex between fillet 1 and fillet 2, no appreciable differences are seen in Fig. 5.

Figure 6 compares the $C_{pt,loss}$ in a plane located downstream of the passage throat and close to the exit plane of the blade passage ($X_G/C_{ax}=0.916$). The region shown is primarily occupied by the passage vortex and represents about 62% of the pitchwise distance from the suction side to the pressure side at this axial location. The magnitude of the $C_{pt,loss}$ contours shown ranges from 0.25 to nearly 2. From a qualitative perspective, one may consider the inner core of the vortex to be represented by $C_{pt,loss}$ magnitudes greater than 0.85 (arbitrarily selected), while magnitudes in the range of 0.45–0.85 can be considered to represent the outer portions of the vortex. $C_{pt,loss}$ values of 0.25 may be considered to be outside the passage vortex region. If one examines the area en-

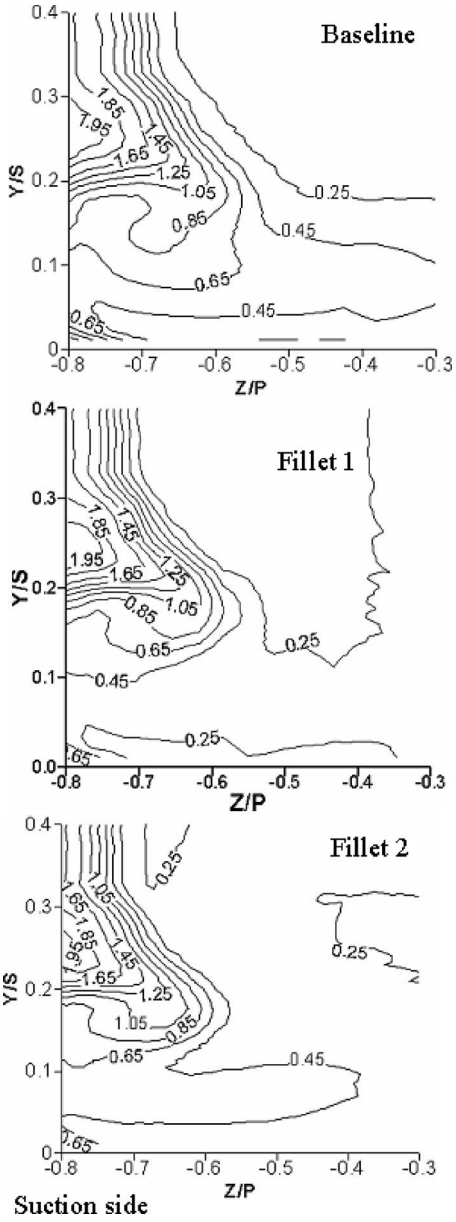

Fig. 6 Total pressure loss coefficient $C_{pt,loss}$ in pitchwise normal plane at X_G/C_{ax}=0.916 for baseline, fillet 1, and fillet 2

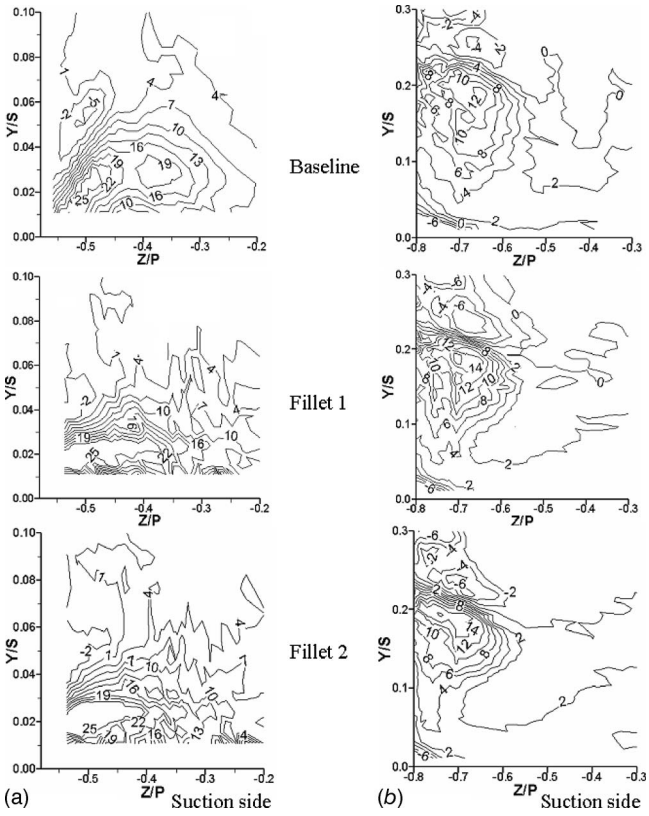

Fig. 7 Normalized axial vorticity $\omega_x{}^*C/U_{ref}$ contours at (*a*) X_G/C_{ax}=0.424 and (*b*) X_G/C_{ax}=0.916 for baseline, fillet 1, and fillet 2

closed by a contour level of 0.65, providing a qualitative measure of the vortex size, it is apparent that the passage vortex is the smallest for fillet 1 and largest for the baseline unfilleted case. The inner core of the passage vortex, denoted by the contour values higher than 0.85, is seen to be lifted considerably above the endwall for all the configurations. The center of the vortex appears to be in the Y/S range between 0.15 and 0.25 (see vorticity contours in Fig. 7(*b*)) and appears to be nearest to the endwall for the baseline case (compare the location of the 0.65 $C_{pt,loss}$ contour line for the three cases in Fig. 6). The higher $C_{pt,loss}$ magnitudes near the bottom left corner in the plots occur due to the presence of the suction side corner vortex.

The $C_{pt,loss}$ in Fig. 6 are computed based on the average velocity at the reference plane as given in Table 3. The average streamwise exit velocity is higher (14.5 m/s) and, based on this, the dynamic pressure in the denominator of Eq. (1) becomes nearly twice the present value. The $C_{pt,loss}$ magnitudes in the free-stream region will then be nearly half of the present values if the exit velocity is chosen to normalize the total pressure loss data.

Normalized Axial Vorticity $\omega_x{}^*C/U_{ref}$. Axial vorticity is computed by taking derivatives of the spline-curve fits of the measured velocity components V and W. The two-dimensional plot of the axial vorticity component provides a measure of the location and the strength of the vortex in the axial direction. Contours of the normalized vorticity components for the baseline, fillet 1, and fillet 2 are compared at X_G/C_{ax}=0.424 and 0.916 in Fig. 7. Because of the three-dimensional nature of the passage vortex, the magnitude of the axial vorticity is strongly dependent upon the orientation of the axis of rotation of the vortex flow. Therefore the magnitude of the axial vorticity and the location of its peak in a two-dimensional axial plane cannot be used as a direct measure of the three-dimensional passage vortex. However, it does enable a comparison of the vortex strength and size between the various cases. Positive $\omega_x{}^*C/U_{ref}$ magnitudes indicate vorticity vectors in the $+X$ direction and the sense of rotation is in the clockwise direction.

The high contour magnitudes of the normalized vorticity in Fig. 7, signifying the passage vortex system, are located just above the endwall at X_G/C_{ax}=0.424 (center at $Y/S\approx$0.02, Fig. 7(*a*)), and away from the endwall at X_G/C_{ax}=0.916 (center at $Y/S\approx$0.2, Fig. 7(*b*)). At X_G/C_{ax}=0.424 (Fig. 7(*a*)), the axial vorticity contours show two neighboring regions of vorticity of opposite signs; the larger positive region represents the pressure side vortex, which has migrated to the mid-passage region (and is typically referred to a the passage vortex), and the smaller negative vorticity region is the suction side vortex, which has moved upwards and is located in a small region adjacent to the suction side and above the pressure side vortex region. At the same plane, for the fillet cases, the vorticity magnitudes of the pressure side vortex are slightly higher as the vortex axis is oriented closer to the axial direction for the fillets than for the baseline. This will be further illustrated in Fig. 10 where pitch and yaw angles are presented.

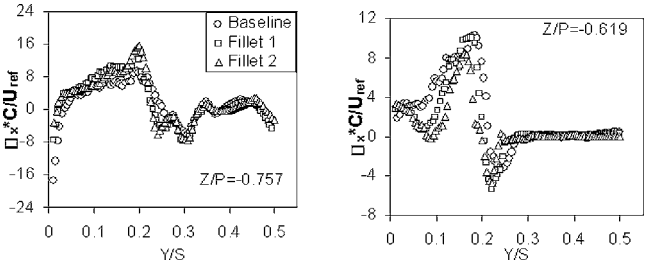

Fig. 8 Normalized axial vorticity $\omega_x^* C/U_{ref}$ in two pitchwise locations at $X_G/C_{ax}=0.916$ for baseline, fillet 1, and fillet 2

The vorticity magnitudes of the suction-leg vortex are smaller for the fillets (Fig. 7(*a*)) as this vortex structure is weakened by the fillets (also evidenced earlier in Fig. 4).

At $X_G/C_{ax}=0.916$, Fig. 7(*b*) shows that the passage pressure gradients have caused the passage vortex ($\omega_x^* C/U_{ref}=4.0$) to migrate to the suction side of the blade, and the vortex is lifted away from the endwall. This is consistent with the pressure loss contours in Fig. 6; however, as noted earlier, Fig. 7 only presents one component of the vorticity, and therefore does not fully depict the three-dimensional vortex structure. The negative vorticity magnitudes above the passage vortex indicate the suction side vortex. The $\omega_x^* C/U_{ref}$ magnitudes in the passage vortex region at $X_G/C_{ax}=0.916$ are slightly smaller compared to those at $X_G/C_{ax}=0.424$. This is partly because the cross flow and passage structure orient the axis of the passage vortex further away from the axial direction $+X$ at $X_G/C_{ax}=0.916$. Further, at $Z/P<-0.65$ the peak vorticity magnitudes (vortex core) of the passage vortex and suction side vortex for the filleted cases are higher than for the baseline, indicating the vortex-core axis with the fillets is directed more toward the $+X$ direction, which is further illustrated by the flow angles in Fig. 10.

In order to provide a more quantitative comparison, the axial vorticity data are presented in the form of line plots at two pitchwise locations ($Z/P=-0.757$ and $Z/P=-0.619$) at $X_G/C_{ax}=0.916$ in Fig. 8. At this axial location, the pitchwise location of the peak vorticity is near $Z/P=-0.7$ (see Fig. 7(*b*)). Therefore the $Z/P=-0.757$ and $Z/P=-0.619$ locations are chosen for quantitative comparison. As the passage vortex is lifted away from the endwall at this axial location, the positive vorticity values associated with the vortex are the highest in the spanwise region $0.15<Y/S<0.21$. At $Z/P=-0.757$ the highest vorticity in the passage vortex is associated with fillet 2 followed by fillet 1, while at $Z/P=-0.619$ the highest axial vorticity is associated with the baseline case with no fillets. This indicates that the vorticity peaks closer to the suction surface in the presence of fillets, and therefore the center of the vortex inner core (region with higher vorticity values) is located closer to the suction surface with the fillets. Fillet 2 moves the vortex closer to the suction surface compared to fillet 1. Note that at $Z/P=-0.619$, the axial vorticity values for the baseline are higher over the spanwise extent from $Y/S=0$ to 0.23, while the baseline values at $Z/P=-0.757$ are comparable to both the fillet values near the endwall ($Y/S<0.1$). This is clearly indicative of the smaller size (in the pitchwise direction) of the passage vortex for the filleted cases.

Normalized Secondary Velocity Vectors. The normalized secondary velocity vectors at $X_G/C_{ax}=0.085$ and $X_G/C_{ax}=0.916$ are presented in Fig. 9. As in [11,22] the vectors are determined from velocity components (V and V_n in Fig. 2) that are normal to the local streamwise direction at the mid-span. The velocity component V is obtained from the direct measurements of the five-hole pressure probe, while V_n is computed from the following equation:

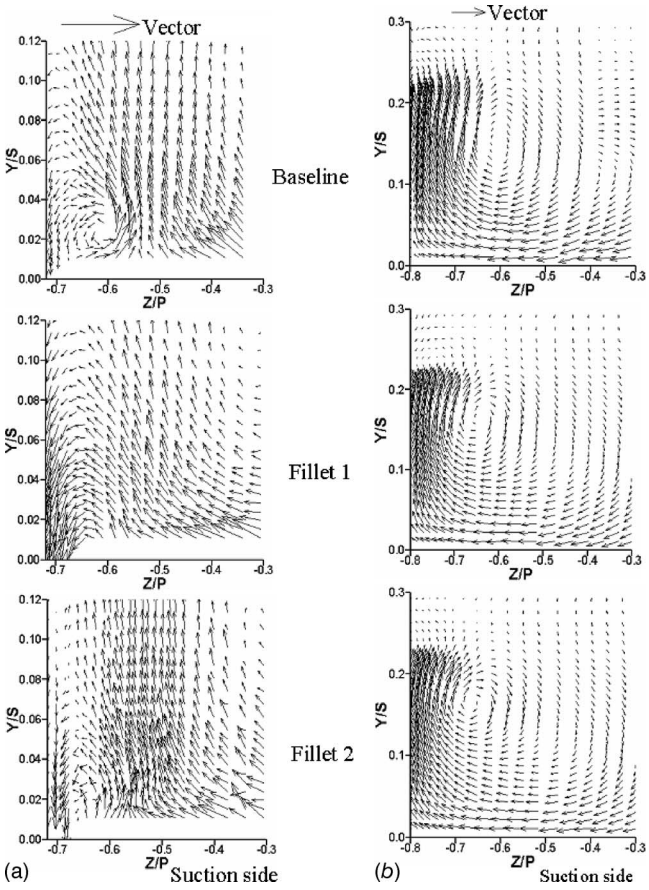

Fig. 9 Normalized velocity vectors from velocity components normal to streamwise direction at (*a*) $X_G/C_{ax}=0.085$ and (*b*) $X_G/C_{ax}=0.916$ for baseline, fillet 1, and fillet 2

$$V_n = U\sin(\varphi_{ms}) + W\cos(\varphi_{ms}) \tag{3}$$

where φ_{ms} is the local yaw angle at the mid-span at a pitchwise location, and U and W are measured velocity components along the axial and pitchwise direction, respectively. The velocity components are then normalized by U_{ref} in Table 3 to obtain the plots in Fig. 9. The length of a unit vector is also shown at the top of each figure for comparison.

The baseline velocity vectors in Fig. 9(*a*) show clear indication of the counter-clockwise rotating suction side vortex between $Z/P<-0.54$ and $Y/S<0.04$ near the suction side. For fillet 1, a clear vortex structure is not apparent at the same location near the suction side although there is a general counter-clockwise orientation of the velocity vectors. For fillet 2, a weakened vortex structure can, however, be seen. This indicates that the suction side vortex is weakened more by fillet 1 than by fillet 2.

Figure 9(*b*) shows the secondary velocity vectors in the passage vortex region at $X_G/C_{ax}=0.916$ for the baseline and fillets. The clockwise rotating passage vortex is clearly apparent between $Y/S=0.05$ and 0.24 for all the configurations. However, two differences are discernible in the passage vortex structure between the baseline and fillets: (1) *Vortex center:* the center of vortical flow is located at $(Z/P, Y/S)=(-0.60, 0.17)$ for baseline, $(Z/P, Y/S)=(-0.65, 0.17)$ for fillet 1, and $(Z/P, Y/S)=(-0.68, 0.17)$ for fillet 2. This indicates that the fillets move the passage vortex slightly closer to the suction surface. (2) *Vortex size:* the vortex size indicated qualitatively by the turning vectors is somewhat smaller for the fillets than for the baseline. These differences are more apparent in the secondary flow vector plots in Fig. 9(*b*) than in Fig. 7, which presents the axial vorticity, since the secondary flows are normal to the local streamwise direction.

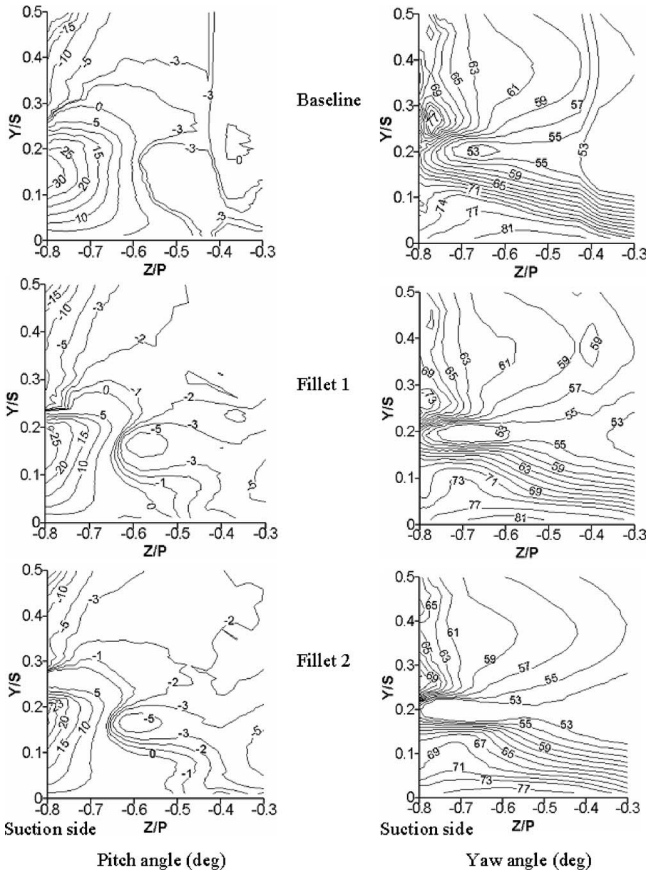

Fig. 10 Flow angles at $X_G/C_{ax}=0.916$ for baseline, fillet 1, and fillet 2

Flow Angles. The yaw and pitch angles provide a measure of the direction of the secondary flows and the orientation of the axis of vortex rotation in a plane. Figure 10 shows the local pitch and yaw angles in the $X_G/C_{ax}=0.916$ plane. These angles are measured relative to the axial direction $+X$ as mentioned earlier. As will be seen, these flow angles provide more direct quantitative comparisons between the baseline and filleted cases, and bring out differences that were harder to discern in the earlier plots of axial vorticity or secondary flow vectors.

The high magnitudes of positive pitch angles for $Z/P<-0.67$ and $Y/S<0.23$ signify the passage vortex location near the suction side. These large pitch angles are a consequence of the vertical velocity component associated with the passage vortex, which, in turn, skews the streamwise velocity. The peak pitch angles are clearly higher for the baseline case, and these higher values are associated with the stronger passage vortex. Further the region associated with the positive pitch angles is larger for the baseline case indicative of the vortex size. No significant difference is seen between the filleted cases, with fillet 2 showing only slightly lower values than fillet 1.

Significant differences in the yaw angle contours are seen between the baseline and fillet cases, as seen in Fig. 10. These differences are perhaps most evident in the vicinity of the vortex core corresponding to the locations of contours of magnitude 53 deg and lower. Yaw angles are smaller for the fillets in this region corresponding to the vortex core, as well as in the region $Z/P<-0.60$ and $Y/S<0.10$ (below the vortex core). These lower yaw angle values imply that the passage vortex is more oriented in the axial direction with the fillets.

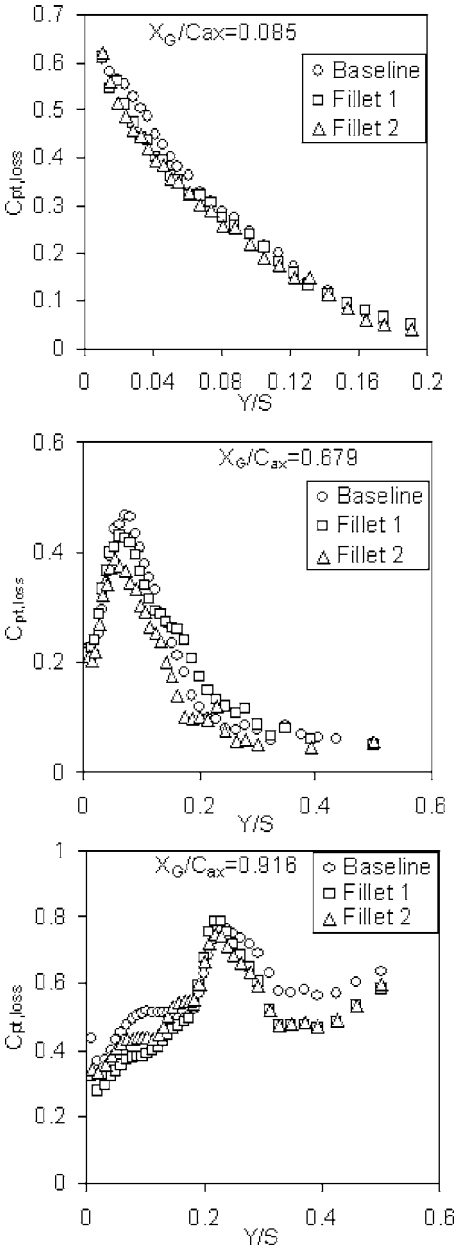

Fig. 11 Pitchwise-averaged total pressure loss coefficient for baseline, fillet 1, and fillet 2 in different axial locations

Pitchwise-Averaged Total Pressure Loss Coefficients and Flow Angles. Figures 11 and 12 present the pitchwise-averaged total pressure loss coefficients and flow angles, respectively, in three pitchwise normal planes. To determine the pitchwise-averaged quantity at a Y/S location, the local data is arithmetically averaged over a constant pitchline at that particular Y/S location. These two plots provide a summary assessment of the effect of fillets.

Figure 11 shows that the pitchwise-averaged $C_{pt,loss}$ distributions at $X_G/C_{ax}=0.085$ decreases as Y/S increases. High values near the endwall occur because of the strong secondary motions in the suction side leg vortex. The average $C_{pt,loss}$ at $X_G/C_{ax}=0.085$ is about 9.0% to 13.0% smaller between $Y/S=0.02$ and 0.04 with the fillets than for the baseline. This occurs because of the stronger suction leg vortex structure in the baseline configuration. At $X_G/C_{ax}=0.679$, the pitchwise-averaged $C_{pt,loss}$ increases from $Y/S=0.01$ to 0.10 because the passage vortex has moved away from the endwall, and the vortex core is located close to

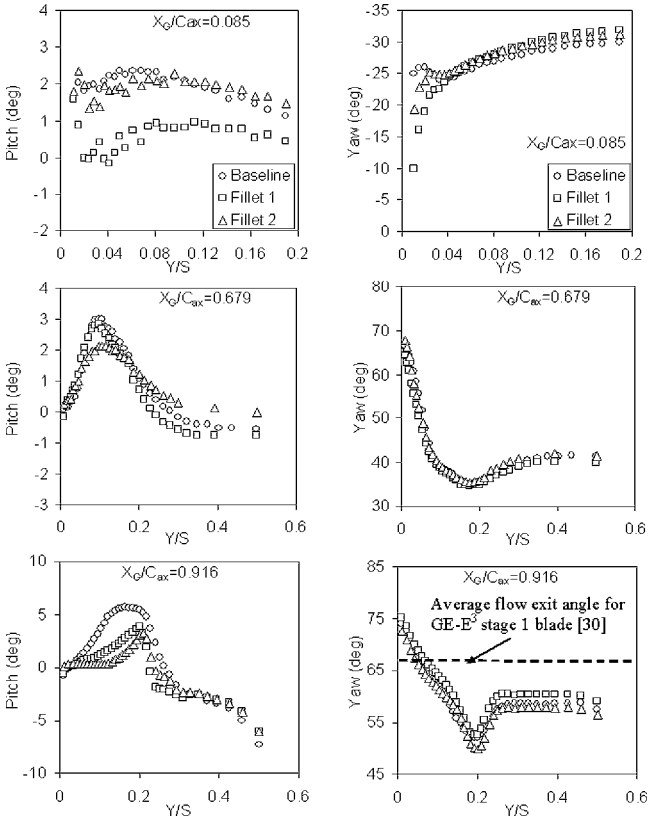

Fig. 12 Pitchwise-averaged flow angles for baseline and fillets

$Y/S=0.1$. At this X_G/C_{ax} location, the peak pressure loss coefficient is 9.0% and 17.0% lower for fillet 1 and fillet 2, respectively, compared to the baseline. At $X_G/C_{ax}=0.916$, the pitchwise-averaged $C_{pt,loss}$ distribution is the lowest for fillet 1 in the region $Y/S<0.20$ in Fig. 11. The average $C_{pt,loss}$ for both the fillets is much lower for $Y/S>0.27$ compared to the baseline data. Clearly, at this X_G/C_{ax} location, the effect of the passage vortex extends to mid-span locations (and beyond, although no measurements were taken beyond $Y/S=0.5$), and the fillets favorably affect the pressure loss coefficients over most of the vertical span of the blade. This was seen earlier in the pressure loss contours in Fig. 6.

Pitchwise-averaged flow angles in Fig. 12 are plotted at the same axial locations as the average pressure loss coefficients in Fig. 11. At $X_G/C_{ax}=0.085$ the average pitch angles are significantly higher for the baseline and fillet 2 than for fillet 1 as the suction side leg vortex is the weakest for fillet 1 in this plane (see Fig. 9). Since the passage vortex migrates upwards and grows in size, the average pitch angles at $X_G/C_{ax}=0.679$ and 0.916 peak at higher Y/S locations. At $X_G/C_{ax}=0.679$, the average pitch values near the peak of the distribution at $Y/S=0.08$ are considerably smaller (nearly 30%) for fillet 2 than for fillet 1 and baseline. At $X_G/C_{ax}=0.916$, the average pitch angles are the highest for the baseline for $Y/S<0.20$ and are again smallest for fillet 2. These observations are consistent with the pressure loss and velocity vector plots presented earlier, with fillet 1 being the most effective in reducing the suction side leg of the horseshoe vortex and fillet 2 being the most effective further downstream in reorienting the passage vortex toward the axial (+X) direction.

For the pitchwise-averaged yaw angles the most notable difference is observed at $X_G/C_{ax}=0.085$, where the negative yaw angles are reduced considerably in magnitude (in the range of 10–15 deg) by fillet 1 in the suction-leg vortex region. At other X_G/C_{ax} locations, no substantial differences in the averaged yaw angle are seen between the three cases, although local differences

Table 4 Overall mass-averaged $C_{pt,loss}$

Axial distance	$X_G/C_{ax}=0.679$	$X_G/C_{ax}=0.916$
Baseline	$C_{pt,loss}=0.18$	$C_{pt,loss}=0.37$
Fillet 1	$C_{pt,loss}=0.17$	$C_{pt,loss}=0.32$
Fillet 2	$C_{pt,loss}=0.14$	$C_{pt,loss}=0.35$

were observed earlier in Fig. 10. This reflects the effect of pitchwise-averaging that smoothens out the differences. At $X_G/C_{ax}=0.916$, the average exit angle for the three-dimensional GE-E^3 blade [30] in an actual turbine stage is reported to be 66.0 deg. The measurements in [30] are reported for high speed compressible flows, 3D airfoil geometry, and pressure ratio of 1.7. In the present low-Mach number study, at $X_G/C_{ax}=0.916$, the measured average yaw angle in the two-dimensional cascade is about 60.0 deg with and without the fillets.

Table 4 provides the overall mass-averaged pressure-loss coefficient data in the axial planes at $X_G/C_{ax}=0.679$ and 0.916. The overall pressure loss coefficients $C_{pt,loss}$ increase with the axial distance, which is consistent with the local distributions presented earlier. In the throat region, at $X_G/C_{ax}=0.679$, the mass-averaged $C_{pt,loss}$ is the lowest for fillet 2, while near the exit (at $X_G/C_{ax}=0.916$), the mass-averaged $C_{pt,loss}$ is the lowest for fillet 1 (about 14% smaller compared to the baseline case) as seen earlier in Figs. 6 and 11.

Concluding Remarks

Detailed measurements of the secondary flow structures in a linear blade cascade passage are presented with and without leading edge fillets. Two types of leading edge fillets are employed at the blade leading edge, one with a linear profile (fillet 1) and the second with a parabolic profile (fillet 2). Measurements are presented for both the baseline and the filleted cases, and include total pressure loss coefficient, nondimensional axial vorticity, normalized secondary velocity vectors, and yaw and pitch flow angles at different axial planes.

The following are the key observations made in this study.

- Immediately downstream of the leading edge, the fillets weaken the suction-side leg of the horseshoe vortex, in size and strength, and the associated pressure loss coefficients and pitch angles are lower. Fillet 1 is the most effective in reducing the vortex at this early stage in the vortex development. Fillet 1 is also the most effective in reducing the pitch and yaw angles at this location.
- The passage vortex, as it develops downstream in the passage, is lifted away from the end wall and migrates toward the suction side of the blade. At $X_G/C_{ax}=0.424$, upstream of the throat, and at $X_G/C_{ax}=0.679$ (throat) the passage vortex is still weaker (represented by lower pressure loss coefficient) and smaller in size for the filleted cases.
- Near the trailing edge of the passage, the passage vortex is smaller in size with the fillets, and is shifted closer to the suction surface. This leads to lower pitchwise-averaged pressure loss coefficients for the filleted cases. At the trailing edge of the passage, fillet 1 has the lowest pitch-averaged loss coefficients, with the peak pitchwise-averaged values for fillet 1 being 14% lower than for the baseline, and the impact of the fillets in reducing pressure losses extends beyond the mid-span.
- The passage vortex impacts the pitch and yaw angles considerably. The pitch and yaw angles are both reduced by the fillets. On the suction side and slightly downstream of the inlet, flow pitch angles are strongly negative above the fillet profile, which in turn contribute to the significantly reduced average pitch angles near the endwall for fillet 1. Near the trailing edge, the passage vortex for the filleted cases is

oriented more in the axial direction (lower yaw angles) compared to the baseline case, and exhibits lower pitch angles.
- While both fillets reduce pressure loss coefficients across the passage, fillet 1 appears to exhibit greater reductions in pressure loss coefficients.

Acknowledgment

This work was supported by a grant from DOE (DE-FC26-02NT41431) through the SCIES-UTSR program (Grant No. 02-01-SR098). Ross Gustafson aided in setting up the experiments and in obtaining some of the measurements. His help is sincerely appreciated.

Nomenclature

C = actual chord length of scaled up blade profile
C_{ax} = axial chord length of the scaled up blade profile
C_p = static pressure coefficient on blade surface
$C_{pt,loss}$ = total pressure loss coefficient
P = blade pitch
P_{stat} = static gage pressure on blade surface
$P_{stat,0}$, $P_{tot,0}$ = average static and total gage pressure in reference plane, respectively
P_{tot} = measured total gage pressure
$P_{o,in}$ = stagnation pressure on blade leading edge
Re_{in} = Reynolds number, defined as $\mathrm{Re}_{in}=\rho U_{ref} C/\mu_{air}$
S = span of the scaled up two-dimensional blade
s = blade coordinate referring to distance on blade surface
$T_{o,in}$ = stagnation temperature in reference plane
U,V,W = velocity components in (X,Y,Z) coordinate system
U_{ref} = average streamwise velocity in reference plane
V_s, V_n = velocity components in streamwise coordinates
X,Y,Z = Cartesian coordinate system

Greek Symbols

δ = boundary layer thickness
μ = dynamic viscosity
ρ = air density
ω = vorticity
φ = flow yaw angle

Subscripts

air = properties related to air
ax = quantity related along X or axial direction of blade
G = global coordinate
max = maximum quantity
ms = mid-span
o,ref = reference quantity
$stat,tot$ = static and total quantity, respectively
ss,ps = blade suction side and pressure side, respectively

References

[1] Wang, H. P., Olson, S. J., Goldstein, R. J., and Eckert, E. R. G., 1997, "Flow Visualization in a Linear Turbine Cascade of High Performance Turbine Blades," ASME J. Turbomach., **119**, pp. 1–8.
[2] Goldstein, R. J., and Spores, R. A., 1988, "Turbulent Transport on the Endwall in the Region Between Adjacent Turbine Blades," ASME J. Heat Transfer, **110**, pp. 862–869.
[3] Sieverding, C. H., and Bosche, V. P., 1983, "The Use of Colored Smoke to Visualize Secondary Flows in a Turbine-Blade Cascade," J. Fluid Mech., **134**, pp. 85–91.
[4] Langston, L. S., Nice, M. L., and Hooper, R. M., 1977, "Three-Dimensional Flow Within a Turbine Cascade Passage," ASME J. Eng. Power, **99**, pp. 21–28.
[5] Goldstein, R. J., Wang, H. P., and Jabbari, M. Y., 1995, "The Influence of Secondary Flows Near the Endwall and Boundary Layer Disturbance on Convective Transport from a Turbine Blade," ASME J. Turbomach., **117**(4), pp. 657–665.
[6] Yamamoto, A., 1987, "Production and Development of Secondary Flows and Losses in Two Types of Straight Turbine Cascades: Part 2- A Rotor Case," ASME J. Turbomach., **109**(2), pp. 194–200.
[7] Gallus, H. E., Zeschky, J., and Hah, C., 1995, "Endwall and Unsteady Flow Phenomena in an Axial Turbine Stage," ASME J. Turbomach., **117**, pp. 562–570.
[8] Gregory-Smith, D. G., and Cleak, J. G. E., 1992, "Secondary Flow Measurements in a Turbine Cascade with High Inlet Turbulence," ASME J. Turbomach., **114**(1), pp. 173–183.
[9] Ma, H., Jiang, H., and Qiu, Y., 2002, "Visualizations of the Unsteady Flow Field Near the Endwall of a Turbine Cascade," *Proc. ASME Turbo Expo*, Paper No. GT-2002-30350.
[10] Treiber, M., Abhari, R. S., and Sell, M., 2002, "Flow Physics and Vortex Evolution in Annular Turbine Cascades," *Proc. ASME Turbo Expo*, Paper No. GT-2002-30540.
[11] Kang, M. B., and Thole, K. A., 2000, "Flowfield Measurements in the Endwall Region of a Stator Vane," ASME J. Turbomach., **122**, pp. 458–466.
[12] Kang, M. B., Kohli, A., and Thole, K. A., 1999, "Heat Transfer and Flowfield Measurements in the Leading Edge Region of a Stator Vane Endwall," ASME J. Turbomach., **121**, pp. 558–569.
[13] Hermanson, K., Kern, S., Picker, G., and Parneix, S., 2002, "Predictions of External Heat Transfer For Turbine Vanes and Blades With Secondary Flowfields," *Proc. ASME Turbo Expo*, Paper No. GT-2002-30206.
[14] Hah, C., 1984, "A Navier-Stokes Analysis of Three-Dimensional Turbulent Flows Inside Turbine Blade Rows at Design and Off-Design Conditions," ASME J. Eng. Gas Turbines Power, **106**, pp. 421–429.
[15] Granovski, A. V., and Kostege, M. K., 2002, "Investigations of Flow Structure and Losses at the Endwall Sections of the Last Stage Blade," *Proc. ASME Turbo Expo*, Paper No. GT-2002-30349.
[16] Davenport, W. J., Agarwal, N. K., Dewitz, M. B., Simpson, R. L., and Poddar, K., 1990, "Effects of a Fillet on the Flow Past a Wing-Body Junction," AIAA J., **28**(12), pp. 2017–2024.
[17] Simpson, R. L., 2001, "Junction Flows," Annu. Rev. Fluid Mech., **33**, pp. 415–443.
[18] Sauer, H., Müller, R., and Vogeler, K., 2001, "Reduction of Secondary Flow Losses in Turbine Cascades by Leading Edge Modifications at the Endwall," ASME J. Turbomach., **123**, pp. 207–213.
[19] Eymann, S., Förster, W., Beversdorff, M., Reinmöllar, U., Niehuis, R., and Gier, J., 2002, "Improving 3D Flow Characteristics in a Multistage LP Turbine by Means of Endwall Contouring and Airfoil Design Modification- Part 1: Design and Experimental Investigation," *Proc. ASME Turbo Expo*, Paper No. GT-2002-30352.
[20] Becz, S., Majewski, M. S., and Langston, L. S., 2003, "Leading Edge Modification Effects on Turbine Cascade Endwall Loss," *Proc. ASME Turbo Expo*, Paper No. GT-2003-38898.
[21] Becz, S., Majewski, M. S., and Langston, L. S., 2004, "An Experimental Investigation of Contoured Leading Edges for Secondary Flow Loss Reduction," *Proc. ASMR Turbo Expo*, Paper No. GT-2004-53964.
[22] Zess, G. A., and Thole, K. A., 2001, "Computational Design and Experimental Evaluation of Using a Leading Edge Fillet on a Gas Turbine Vane," *Proc. ASME Turbo Expo*, Paper No. GT-2001-0404.
[23] Lethander, A. T., Thole, K. A., Zess, G., and Wagner, J., 2003, "Ortimizing the Vane-Endwall Junction to Reduce Adiabatic Wall Temperatures in a Turbine Vane Passage," *Proc. ASME Turbo Expo*, Paper No. GT-2003-38939.
[24] Shih, T.I-P., and Lin, Y.-L., 2002, "Controlling Secondary-Flow Structure by Leading-Edge Airfoil Fillet and Inlet Swirl to Reduce Aerodynamic Loss and Surface Heat Transfer," *Proc. ASME Turbo Expo*, Paper No. GT-2002-30529.
[25] Mahmood, G. I., Gustafson, R., and Acharya, S., 2005, "Experimental Investigation of Flow Structure and Nusselt Number in a Low Speed Linear Blade Passage With and Without Leading Edge Fillets," ASME J. Heat Transfer, **127**, pp. 499–512.
[26] Ligrani, P. M., Singer, B. A., and Baun, L. R., 1989, "Miniature Five-hole Pressure Probe for Measurement of Three Mean Velocity Components in Low-Speed Flows," J. Phys. E, **22**, pp. 868–876.
[27] Ligrani, P. M., Singer, B. A., and Baun, L. R., 1989, "Spatial Resolution and Downwash Velocity Corrections for Multiple-Hole Pressure Probes in Complex Flows," Exp. Fluids, **7**, pp. 424–426.
[28] Holman, J. P., 2001, *Experimental Methods for Engineers*, 7th ed., McGraw Hill, New York, pp. 51–77.
[29] Moffat, R. J., 1988, "Describing the Uncertainties in Experimental Results," Exp. Therm. Fluid Sci., **1**(1), pp. 3–17.
[30] Timko, L. P., "Energy Efficient Engine High Pressure Turbine Component Test Performance Report," Contract Report for NASA, Report No. NASA CR-168289.

Large Eddy Simulation of Acoustical Sources in a Low Pressure Axial-Flow Fan Encountering Highly Turbulent Inflow

Hauke Reese
Ph.D. student
Institute of Fluid- and Thermodynamics,
University of Siegen,
D-57068 Siegen, Germany
e-mail: hauke.reese@uni-siegen.de

Chisachi Kato
Professor
Institute of Industrial Science,
The University of Tokyo,
4-6-1 Kamaba, Meguro-ku,
Tokyo, 153-8505, Japan
e-mail: ckato@iis.u-tokyo.ac.jp

Thomas H. Carolus
Professor
Institute of Fluid- and Thermodynamics,
University of Siegen,
D-57068 Siegen, Germany
e-mail: thomas.carolus@uni-siegen.de

A large eddy simulation (LES) was applied to predict the unsteady flow in a low-speed axial-flow fan assembly subjected to a highly "turbulent" inflow that is generated by a turbulence grid placed upstream of the impeller. The dynamic Smagorinsky model (DSM) was used as the subgrid scale (SGS) model. A streamwise-upwind finite element method (FEM) with second-order accuracy in both time and space was applied as the discretization method together with a multi-frame of reference dynamic overset grid in order to take into account the effects of the blade-wake interactions. Based on a simple algebraic acoustical model for axial flow fans, the radiated sound power was also predicted by using the computed fluctuations in the blade force. The predicted turbulence intensity and its length scale downstream of the turbulence grid quantitatively agree with the experimental data measured by a hot-wire anemometry. The response of the blade to the inflow turbulence is also well predicted by the present LES in terms of the surface pressure fluctuations near the leading edge of the blade and the resulting sound power level. However, as soon as the effects of the turbulent boundary layer on the blades become important, the prediction tends to become inaccurate. [DOI: 10.1115/1.2427077]

1 Introduction

The aero-acoustic noise of a low-Mach-number axial flow fan results from the encounter of the blades with inflow disturbances (gust noise), interaction of the rotating blades with stationary parts such as stator vanes and motor struts (interaction noise), and the flow over the blades themselves (self noise). The first noise source may sometimes dominate the overall noise level from a fan because it drastically increases the noise level when exists. For example, axial flow fans used in air conditioning systems often suffer from poor inflow conditions. They range from steady but spatially asymmetric velocity profiles of the inflow due to non-ideal intake geometry, to ingested vortices or turbulence that fluctuate with respect to time. The resulting periodic and/or random forces acting on the blades cause tonal and/or broadband gust noise.

Previous studies that used advanced numerical methods have helped to advance the understanding of the generation of fluctuating pressures and resulting forces on axial flow fan blades. For example, Algermissen et al. [1] employed the unsteady-Reynolds-average-Navier-Stokes (URANS) method to predict the noise radiation from axial flow fans for use in automotive cooling. Struts were placed directly upstream of the fan impeller. Kouidri et al. [2] investigated the effects of swept blades on the aerodynamic and acoustic behavior of low-pressure fans. Their numerical simulations yield steady and unsteady loading on the blades, which they subsequently fed into the Ffowcs Williams and Hawkings formulation [3] to obtain acoustic spectra. Despite the relatively small size of the computational grids, their computations show a satisfactory agreement with the measured performance of the fan [1,2]. Algermissen et al. [1] also compared the predicted sound pressure spectrum with measured quantities and obtained a reasonable agreement for the tonal noise components that result from the periodic interactions between the rotating blades and the stationary struts placed just upstream of the blades. Their computation, however, failed to predict noise spectra in the case where upstream struts are removed. For this case, the broadband components dominate the overall noise level. Computations based on URANS may be able to predict some parts of the broadband noise if the turbulence model is properly selected or tuned. Large eddy simulation (LES) is, however, much more suitable for predicting broadband noise because it directly computes inviscid interactions of vortices larger than the numerical grid, from which "turbulence" essentially originates.

You et al. [4] employed LES to investigate the tip clearance flow. Based on LES Kato et al. [5] developed a numerical code and applied it, for instance, to the prediction of the internal flow of the complete stage of a mixed-flow pump. The predicted unsteady flow field agreed reasonably well with the measured quantities.

This paper is concerned with the LES prediction of the dipole sound sources of an axial flow fan. Basically, the dipole sources are the fluctuating forces set up on the fan blades due to the unsteady flow. Primarily we investigate a fan assembly where the blades are subjected to highly turbulent ingestion. The turbulent velocity fluctuations are generated by a coarse grid installed upstream of the impeller. The complex wake/vortex flow behind the turbulence grid is thought to produce both "random" (i.e., broadband) and periodic velocity fluctuations. The former dominates the overall fluctuations. In addition, we consider those cases where the turbulence generator is removed. We present and compare LES predictions and measurements, concentrating on velocity fluctuations downstream of the turbulence generator and the unsteady pressure fluctuations on the fan blades. Furthermore, a simple algebraic acoustic model is employed to predict a first order approximation of the resulting aeroacoustic dipole sound. Given limited (but still large) computer capacity we try to give further insight into the predictability of broadband noise by a high level numerical method such as LES.

Contributed by the Fluids Engineering Division of ASME for publication in the JOURNAL OF FLUIDS ENGINEERING. Manuscript received October 25, 2005; final manuscript received October 5, 2006. Assoc. Editor: Akira Goto.

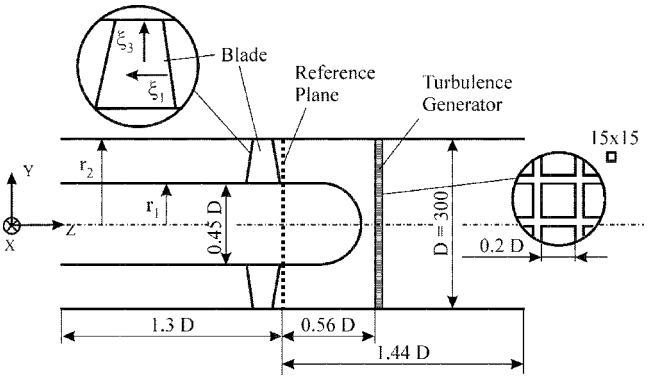

Fig. 1 Fan assembly with main flow from right to left. Clean inflow (CI) condition is achieved by removing the turbulence generator.

2 Fan Assembly

The fan assembly investigated in the present study is depicted in Fig. 1. The axial-flow impeller has a diameter of $D=300$ mm and a hub/tip ratio $r_1/r_2=0.45$. It is installed in a circular duct without guide vanes and rotates at 3000 rpm, resulting in a tip speed $U=47.1$ m/s and a circumferential Mach number Ma $=0.14$. The six cambered blades have a NACA 4509 profile. The Reynolds number, based on the chord length C of the blade and the mean relative flow velocity, varies from 118,000 at the hub to 178,000 at the tip. The radial tip clearance is 0.5 mm, which corresponds to 0.18% of the rotor diameter D or 0.9% of the blade chord C at the tip. The operating point of the maximum efficiency (designed operating point) corresponds to a volume flow rate of $\dot{V}=0.59$ m^3/s. This operating point was selected for all the investigations in this study. A turbulence generator is installed $0.56D$ upstream of the impeller's leading edge plane (hereafter, referred to as the "reference plane"). The turbulence grid is made up of nine struts with a square cross section of 15×15 mm^2 and a separation distance of 60 mm. This case is hereafter referred to as the "highly turbulent inflow conditions" (HT). The impeller may also run without this turbulence generator, which is hereafter referred to as the "clean inflow condition (CI)."

3 Simulation Method

The numerical flow code employed throughout this study is named FrontFlow/blue; it was developed by C. Kato and has been successfully used for various applications (see, e.g., [6,7]). The code is based on a finite element discretization of the governing equations.

3.1 Governing Equations. The governing equations are the spatially filtered continuity equation (1) and the Navier-Stokes equations (2) in Cartesian coordinates:

$$\frac{\partial \bar{u}_i}{\partial x_i}=0 \tag{1}$$

$$\frac{\partial}{\partial t}\bar{u}_i+\frac{\partial}{\partial x_j}\bar{u}_i\bar{u}_j=-\frac{1}{\rho}\frac{\partial \bar{p}}{x_i}+\frac{\partial}{\partial x_j}\left\{\nu\left(\frac{\partial \bar{u}_i}{\partial x_j}+\frac{\partial \bar{u}_j}{\partial x_i}\right)-\overline{u_i'u_j'}\right\}+f_i \tag{2}$$

where the overbar denotes the grid scale (i.e., resolved scale) components while the apostrophe indicates the subgrid scale (unresolved scale) components that have to be modeled. In Eq. (2) f_i represents the inertial force associated with the motion of the frame of reference. In particular, for a rotational frame of reference the centrifugal forces and the Coriolis forces must be taken into account while in the stationary frame of reference f_i is set to zero:

$$f_1=\Omega^2x_1+2\Omega\bar{u}_2;\quad f_2=\Omega^2x_2-2\Omega\bar{u}_1;\quad f_3=0 \tag{3}$$

The subgrid scale stresses are modeled according to Smagorinsky [8]:

$$\overline{u_i'u_j'}-\frac{1}{3}\delta_{ij}\overline{u_k'u_k'}=-\nu_{SGS}\left(\frac{\partial \bar{u}_i}{\partial x_j}+\frac{\partial \bar{u}_j}{\partial x_i}\right) \tag{4}$$

$$\nu_{SGS}=(C_S\Delta)^2\sqrt{2\bar{S}_{ij}\bar{S}_{ij}};\quad \bar{S}_{ij}=\frac{1}{2}\left(\frac{\partial \bar{u}_i}{\partial x_j}+\frac{\partial \bar{u}_j}{\partial x_i}\right) \tag{5}$$

In the present study, the model coefficient C_S is determined as a function of flow state as proposed by Germano [9,10] since a preliminary investigation showed that it gives better predictions of the overall performance of the fan than the standard Smagorinsky model does. In Eq. (5), Δ is the size of the grid filter that is equal to the minimum length of each element [10].

3.2 Numerical Scheme. In an LES the motion of large eddies is resolved directly by the numerical grid. This requires a high accuracy and stability of the discretizing method. Numerical schemes with a high numerical dissipation are not appropriate because they would damp out the motion of large eddies. In this study, a streamline-upwind finite element formulation previously reported by Kato and Ikegawa [11] is used to discretize the governing equations. This scheme combines the streamline upwind-Petrov-Galerkin (SU-PG) method [12] with the Taylor-Galerkin-method [13] and has second order accuracy in terms of both space and time. For solving the filtered continuity equation, the fractional step method is used with the BiCGStab method [14] as the matrix solver. Details of the numerical scheme have been described by Kato and Ikegawa [11] and Kato et al. [6].

The flow field in the investigated fan assembly is rather complex and the characteristic Reynolds number is comparably high. This requires a large number of grid elements, which results in an unacceptably long computational time if a single CPU is used for the computation. Therefore, the numerical formulations are implemented as a parallel code by using the domain decomposition programming model.

The interactions between the rotating impeller and the stationary parts are taken into account by a dynamic oversetting of the grids for multiple frames of reference [6]. Each grid domain includes appropriate overlapped regions with its neighboring grid domains downstream and upstream. At each time step in an overset region, the values of the static pressure and the velocity components are interpolated to the corresponding neighbor element by a tri-linear interpolation. Due to the different frame of reference, the overset velocity components require an appropriate coordinate transformation between the rotational and stationary domains. In order to achieve a higher flexibility of grid generation, the oversetting method can also be used without a change of the reference system. With this *static* oversetting grid, blocks of different grid topology and density can be connected. The interpolation method has been discussed in detail by Kaiho et al. [15].

3.3 Numerical Grid and Boundary Conditions. The numerical grid is divided into four sections as shown in Fig. 2. The most upstream grid covers the inlet section, i.e., a cylindrical duct. A uniform axial velocity profile is set at the inlet. Because of the complex geometry associated with the turbulence generator, a static oversetting is used between the turbulence generator and inlet sections. The impeller grid downstream of the turbulence generator is divided into several blocks with each blade passage occupying five blocks. An O-grid is used near the blade region. Each blade passage has approximately 450,000 grid elements. In order to reduce the computational cost, the leakage flow through the tip clearance is not simulated.

The hub of the impeller is extended down to the outlet as in the experiments mentioned later. At the outlet boundary surface the static pressure is set to zero. The "outlet" boundary condition implemented in the code is not able to handle reverse flows. In

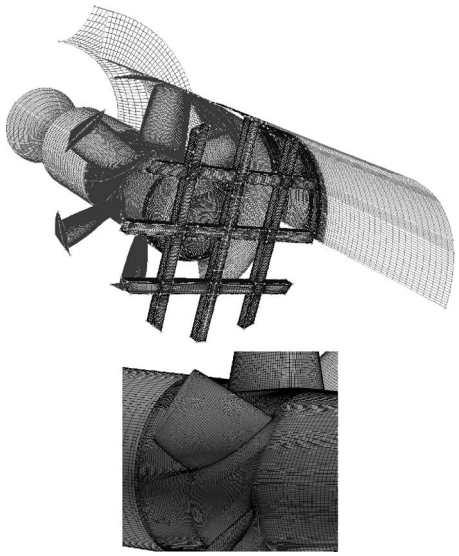

Fig. 2 Numerical grid of the complete flow domain (top) and details in the vicinity of the fan blades (bottom)

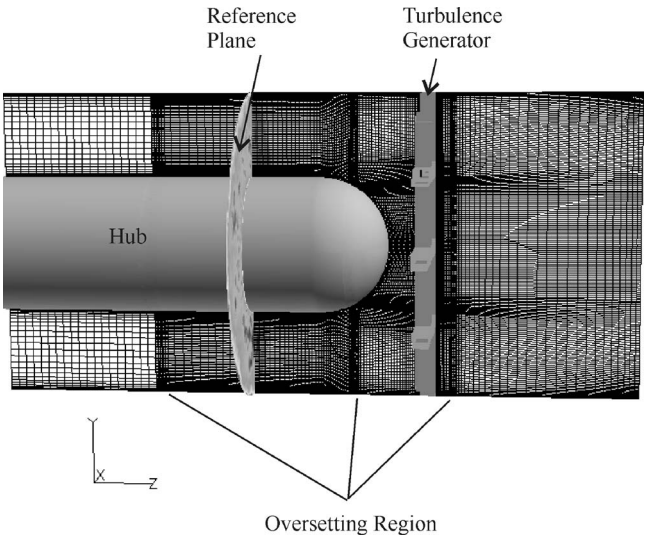

Fig. 3 Overview of the numerical grid for the case without fan blades

order to prevent reverse flow from taking place at the outlet during iteration, the circulation generated by the impeller must be damped before the flow reaches the outlet boundary. This is achieved by using an artificial duct section upstream of the outlet boundary with a sudden expansion and a subsequent gradual contraction of the cross-sectional area (diffusor/nozzle). A no-slip wall condition is applied to all wall boundaries of the flow domain.

In order to ensure an acceptable simulation time, the overall number of the hexahedral elements for the entire flow domain is limited to approximately 5 million. Keeping this number of elements constant, the numerical grid was optimized iteratively during this study in order to achieve the best possible prediction of the flow field of interest. Note, however, that due to this limitation the turbulent boundary layer that develops on the suction surface of the blades as well as on the casing wall is not resolved by the present LES.

Initially the velocity and the pressure are set to zero in the whole flow field. In order to stabilize the simulation at the initial stage of the calculation, an exponential start-up function is used and the velocity is gradually increased at the inlet boundary. The time increment Δt_{Solv}, which is primarily determined by the stability limit of the simulation, is set such that 10,000 time steps corresponded to one revolution of the impeller, i.e., $\Delta t_{Solv}=2\times10^{-6}$ s.

4 Validation and Verification

Because of the complexity of the flow field in the fan assembly, the numerical results are validated in the following two different conditions: first by considering flow through the turbulence generator with the fan blades removed and second by analyzing the flow through the impeller with clean inflow (CI). For the former case, the calculations are done only with the hub. For both cases some measurement data are available from [16,17].

4.1 Flow Downstream of the Turbulence Generator. In order to validate and verify the accuracy of the predicted steady and unsteady flow in the vicinity of the turbulence generator, the fan blades are removed from the hub as in the experiments reported by Schneider and Carolus [17]. The numerical grid is subdivided into four sections in the stationary frame of reference as shown in Fig. 3. Turbulent statistics are compared with measured quantities at three monitoring points on the reference plane shown in Fig. 4: P1 just behind a strut of the turbulence generator, P2 behind a joint of two struts, and P3 behind an open area between two struts. At these points the local streamwise turbulence intensity defined by Eq. (6)

$$\mathrm{Tu}_{\mathrm{loc}}=\frac{\sqrt{\widetilde{\overline{w}'^2_{loc}}}}{\widetilde{\overline{w}}_{loc}} \tag{6}$$

the integral length scale of the axial velocity

$$\Lambda_{loc}=\widetilde{\overline{w}}_x\int_0^\infty \frac{\widetilde{\overline{w}'_{loc}(t)\overline{w}'_{loc}(t-\tau)}}{\widetilde{\overline{w}'^2_{loc}}}\,d\tau \tag{7}$$

and the temporally averaged axial velocity $\widetilde{\overline{w}}_{loc}$ are calculated.

In order to investigate the grid dependency of the computed results, two different grids with approximately 1.5 million (G1)

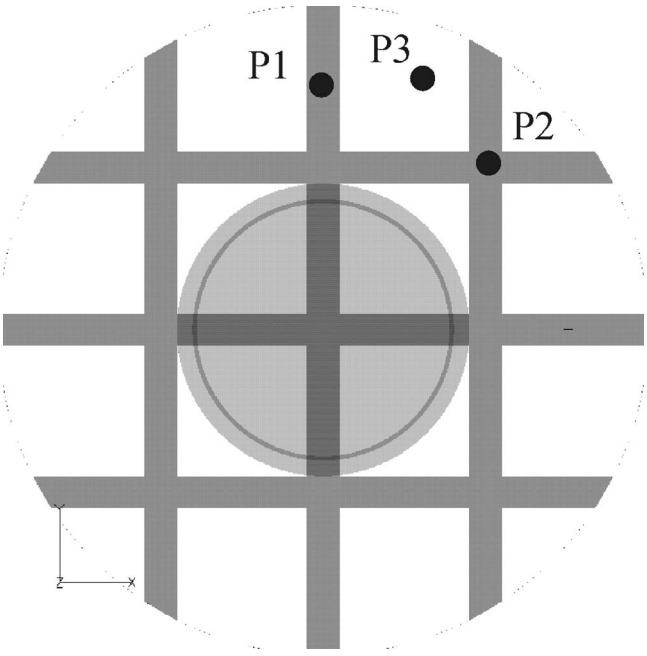

Fig. 4 Monitoring points in the reference plane 0.56 D downstream of the turbulence generator

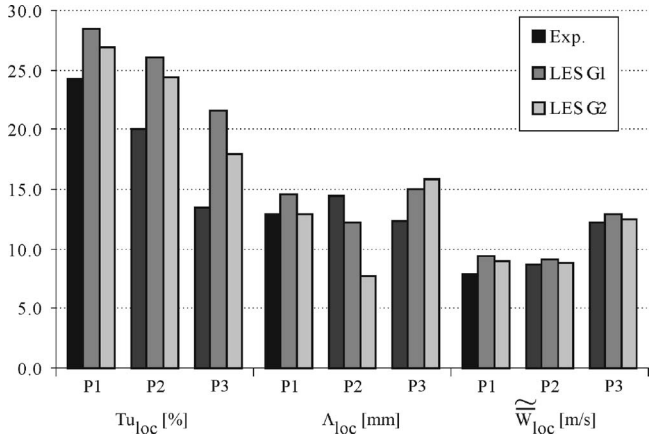

Fig. 5 Local turbulence intensity, integral length scale, and mean streamwise velocity behind the turbulence generator at three monitoring points: comparison of predictions (G1=1.5 million, G2=3 million grid elements) with measurements

and 3 million (G2) grid elements were investigated.

Figure 5 compares the predicted and measured (by hot-wire anemometry [17]) turbulence intensity, integral length scale, and mean streamwise velocity at the three monitoring points. Considering the uncertainties in the measurements, the agreement between prediction and measurement is satisfactory. The finer numerical grid G2 tends to yield a better agreement.

Figure 6 depicts fringe plots of the predicted distribution of the temporally averaged axial velocity in the reference plane, normalized by the inflow velocity $w_{\text{vol}}=\dot{V}/(0.25\pi D^2)$. The wake/vortex structure of the flow is well predicted both quantitatively and qualitatively. In addition, the predicted turbulence intensity and the length scale are in the same order of magnitude as found experimentally by Roach [18].

Figure 7 compares power spectral density of the axial velocity fluctuations $\text{PSD}_w=d(\overline{w}'^2_{loc}/w^2_{\text{vol}})/df$ at the three monitoring points. Here the influence of the computational grid becomes evident. The cutoff frequency, where the predicted spectrum starts to deviate from the theoretical slope $f^{-5/3}$ of the inertia subrange, is approximately 200 Hz for the coarser grid (G1) and 300 Hz for the finer grid (G2). Note that the finer grid improves the agreement with the measurements also in the low frequency range from 10 to 100 Hz. These facts clearly indicate that the energy cascade from the mean shear to the resolved smallest scale is more accurately reproduced with the finer grid. Thus, all the results mentioned later are obtained utilizing the finer grid G2.

4.2 Characteristics of the Fan With Clean Inflow (CI). The accuracy of the predicted flow field in the impeller is validated in terms of the fan characteristics for the clean inflow case. The LES is performed for two different sizes of the numerical grid around the impeller: 2.9 million (G3) and 3.3 million (G4) grid elements. G4 not only differs in the number of elements but also in their distribution. Compared to G3, the cell density around the blade is increased by approximately 80%, which results in 18,000 elements per blade surface.

Figure 8 compares the predicted total-to-static pressure rise and total-to-static efficiency with the measured equivalents, where the volume flow rate coefficient, pressure-rise coefficient, and total-to-static efficiency are defined as:

$$\phi=\frac{\dot{V}}{\frac{\pi^2}{4}D^3n};\quad \psi_{ts}=\frac{\Delta p_{ts}}{\frac{\pi^2\rho}{2}D^2n^2};\quad \eta_{ts}=\frac{\dot{V}\Delta p_{ts}}{P} \tag{8}$$

The power P in the total-to-static efficiency η_{ts} is obtained via integration of the time averaged surface pressure over all blade surfaces. Taking into account that the tip clearance is not included in the LES, the agreement is rather satisfactory. In terms of the predicted fan characteristics the influence of the numerical grid size is marginal. Nevertheless, all subsequent calculations are carried out with the finer grid G4.

5 Results and Discussion

5.1 Unsteady Data Processing. In order to avoid effects of the unphysical flow field during the startup of the calculation on the statistical averages, the evolution of the impeller forces is monitored for the case of the highly turbulent (HT) and clean inflow (CI). Figure 9 shows fluctuations of the predicted impeller forces during the data-sampling period that corresponded to ten revolutions of the impeller. F_{rx}, the lateral component of the force perceived from the stationary frame of reference, fluctuates around zero as expected whereas the magnitude of the force F, dominated by the axial component, is nearly steady. Apparently both quantities are in a statistically equilibrium state and no effects of the initial condition can be detected.

The power spectral density is estimated by dividing the discrete time signals into seven sections with 50% overlapping, applying a Hanning window, and averaging the spectrum from all sections.

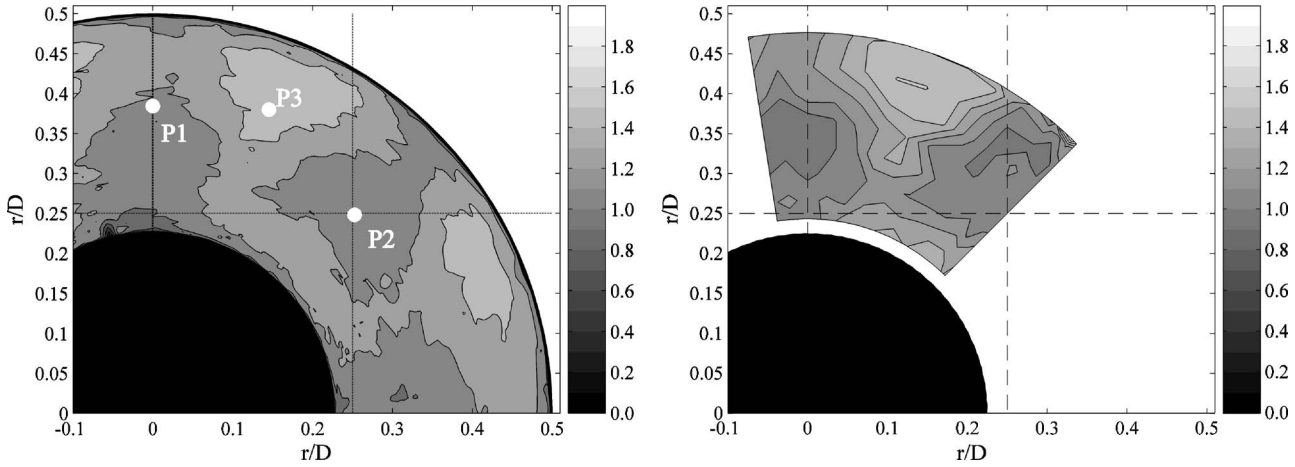

Fig. 6 Comparison of the predicted and measured distribution of the mean streamwise velocity normalized by the inflow velocity in the reference plane behind the turbulence generator. The dashed lines indicate the position of the struts of the turbulence generator.

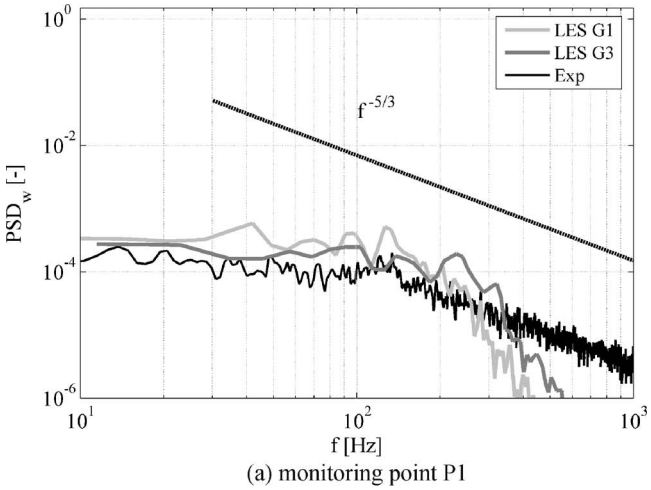

(a) monitoring point P1

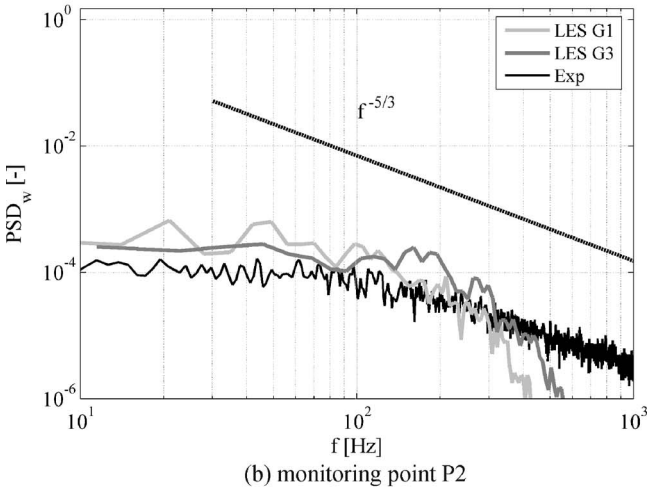

(b) monitoring point P2

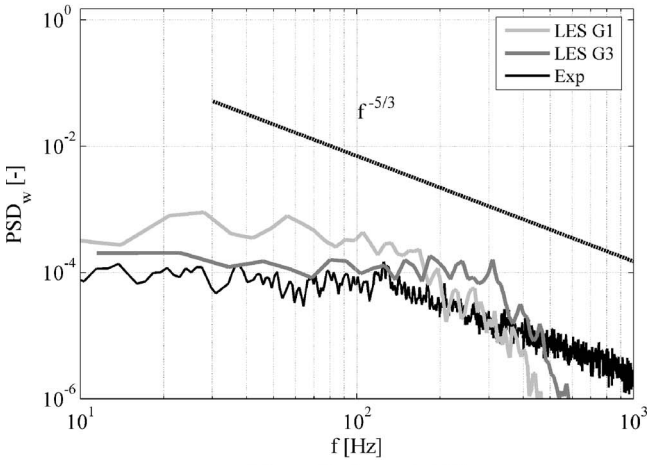

(c) monitoring point P3

Fig. 7 Comparison of the predicted and measured power spectral density (PSD_w) of the nondimensional axial velocity fluctuations at three monitoring points in the reference plane

The choice of seven sections (instead of ten corresponding to the number of the impeller's revolutions) avoids synchronous signal averaging. Namely, those events that are in phase with the blade rate are not enhanced, by contrast to the data processing in [19]. The reference pressure in the sound pressure levels is taken as $p_0 = 2 \times 10^{-5}$ Pa.

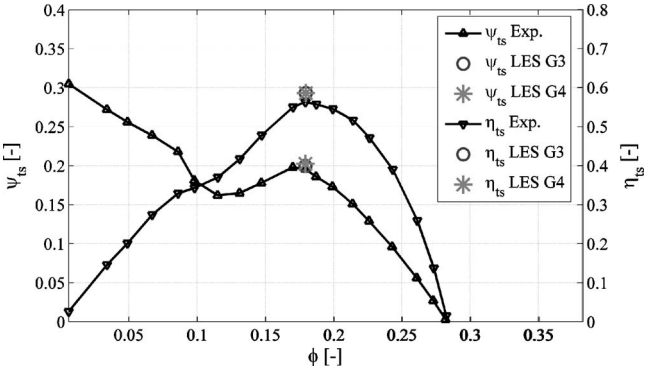

Fig. 8 Comparison of predicted total to static pressure rise and efficiency with measurements [16]; G3=2.9 million, G4 =3.3 million grid elements

5.2 Unsteady Flow Field and Blade Surface Pressure Fluctuations. Figure 10 depicts distributions of the root-mean-square (rms) values of the static pressure coefficient $c_p = \bar{p}/(0.5\rho\pi^2 D^2 n^2)$ on the blade surface. A characteristic difference between clean inflow (CI, left in Fig. 10) and turbulent inflow (HT, right) can be observed in the blade leading edge region. Compared to the CI case HT yields significantly higher rms values. However, the influence of the incident turbulence tends to vanish towards the trailing edge and in the tip region where fluctuations become large, irrespective of the inflow conditions. This trend agrees well with the measured surface pressure response of an isolated NACA0012 airfoil to ingested turbulence as reported by Paterson and Amiet [20] and our own measurements on a rotating fan blade surface [21,22].

In order to further illustrate the effects of the incident turbulence on the flow field, Fig. 11 shows instantaneous distributions of the static pressure coefficient and the surface streamlines on a blade surface and the velocity magnitude in the rotating frame of reference on the mid-span plane. The velocity is normalized with the impeller's tip speed. Each time instant corresponds to 3.6 deg rotating angle of the impeller. At time T_1 the solid arrow points at a surface streamline that is more or less parallel to the main flow direction. This indicates that the flow angle coincides with the camber angle at the leading edge. At time T_2 the region of high velocities at the suction side just downstream of the leading edge is expanding, and the surface streamline is now perpendicular to the main flow direction. Obviously, at this time instant (T_2) the ingested turbulent eddy is convected with a reduced velocity,

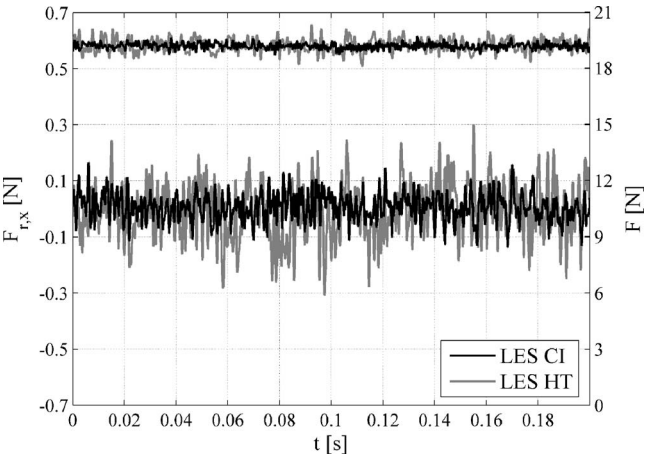

Fig. 9 Predicted fluctuations of impeller forces in a fully developed state

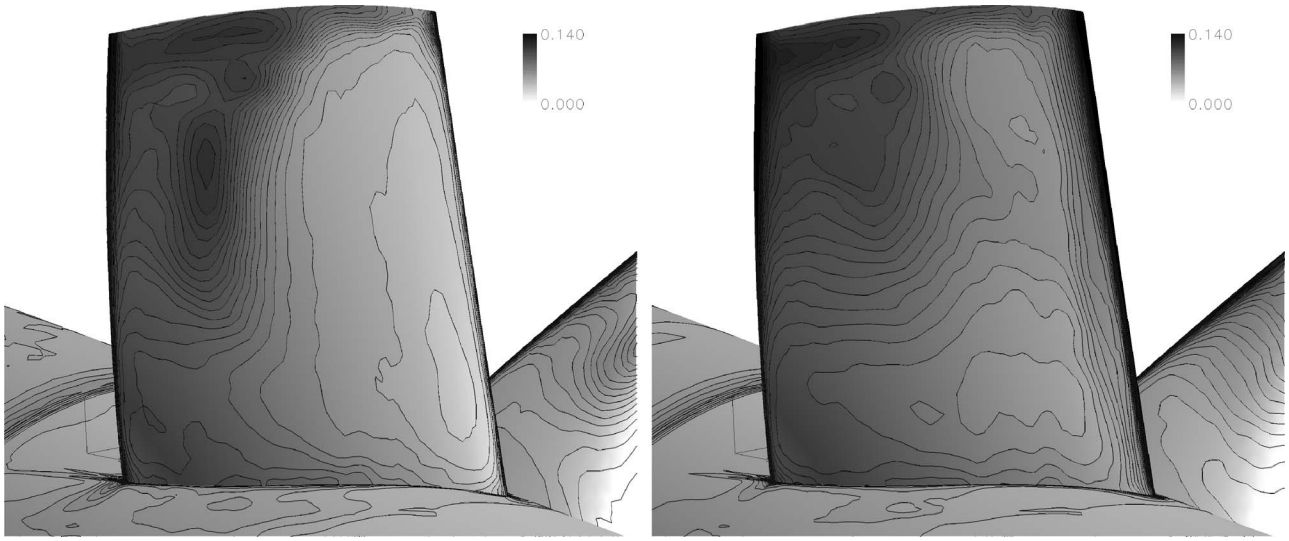

Fig. 10 Root mean square values of static pressure coefficient c_p; left: clean inflow (CI), right: highly turbulent inflow (HT)

which causes a change of incidence and thus a partial flow separation. The separation bubble generates a pressure foot print on the blade surface. As the region of high velocity is convected downstream (T_3 and T_4), the separation bubble vanishes and the pressure foot print moves downstream along the blade surface. Downstream approximately of the mid-chord the stretched spots of constant wall pressure disintegrate into many smaller spots. A similar streamwise stretching of structures on the suction side on a blade was observed by Opiela et al. [23], who investigated the interaction of the wake from an upstream cylinder with a turbine blade. Their LES showed that the boundary layer on the turbine blade is strongly affected by the periodic wake of the cylinder.

Figure 12 depicts the predicted and measured [22] power spectral density levels of the wall pressure fluctuations $\mathrm{PSDL}_{sp} = 10 \log [d(\bar{p}'^2_{sp}/p_0^2)/df]$ dB on the blade suction-side at approximately mid-span. Two monitoring points, P4 close to the leading edge and P5 near mid-chord, are selected for comparison. The predicted power spectra from all six blades are averaged in order to reduce statistical uncertainty. When comparing with measurements from [22], one has to keep in mind that the experimental data contain effects that were not present in the LES. Namely, the tonal peaks are attributed to a large-scale stationary nonuniformity of the inflow in the circumferential direction that is due to a slightly asymmetric inflow condition in [22]. Also, the bandwidth of the power spectra are $\Delta f_B = 3.125$ Hz and 17.52 Hz for the measurements and calculations, respectively. The relatively large bandwidth is selected for the calculations in order to reduce statistical uncertainty of the spectra that are estimated from time history data for a relatively short period.

At the leading edge monitoring point P4, the predicted and measured spectra agree very well for the HT case (see Fig. 12(*a*)). For the CI case the computed spectrum is overpredicted. At mid-chord point P5 all surface pressure spectra are more or less overpredicted (see Fig. 12(*b*)). One reason for the systematic overprediction by the LES method could be the relatively coarse numerical grid in the near-wall region of the blade. Although we used the finest possible grid within this study (G4), the cell density allowed us to resolve only *large* scale turbulent structures either from the inflow or those generated in the near-wall region of the blades. The breakdown of these large structures into smaller eddies is numerically limited by the (chosen) size of the grid elements in the near-wall region. The overpredicted turbulence downstream of the turbulence generator (see Fig. 5, numerical grid G2) may have also contributed to the observed differences to some smaller extent.

Figure 13 shows predicted time-average distributions of the static pressure coefficients on the blade suction-side for the CI case. In the outer blade region $\xi_3/(r_2 - r_1) > 0.5$, a local separation seems to occur at around 30% to 40% chord length downstream of the leading edge. This separation bubble, and any resulting pressure fluctuation, does not seem to be physical and again they are most likely attributed to the poor resolution of the computational grid in the near-wall region.

5.3 Unsteady Blade Forces and Radiated Sound. The unsteady overall forces are evaluated from the blades' surface pressure fluctuations following two different methods:

i. The unsteady pressures are integrated over each blade separately and subsequently the blade forces are averaged over all the six blades. This yields the unsteady force on a representative *blade*.
ii. The unsteady pressures are integrated over the entire impeller. This yields the unsteady force on *the complete impeller*.

The idea behind the first integration method is that each blade is considered as an incoherently radiating, acoustically compact sound source; the broadband sound radiated from the complete impeller is merely a sum of the sound radiated from each of the blades. By contrast the latter force contains all phase effects of the individual blade forces.

Figure 14 shows the power spectral density of the computed forces $\mathrm{PSD}_F = dF^2/df$. Again, a clear influence of the inflow condition is visible. HT yields larger force fluctuations up to 1200 Hz than CI. For the HT case, each blade encounters with, during one revolution of the impeller, eight similar (but not identical) wakes due to the eight struts of the turbulence generator. The *blade* force spectrum thus has a peak at 400 Hz as seen in the upper part of the figure. In the overall impeller force the 400 Hz peak is cancelled out because of the $2/3\pi$ phase difference between the single blade forces.

A simple algebraic acoustic model proposed by Morfey [24] is employed to yield a first-order approximation of the radiated acoustic power associated with the unsteady blade forces. The spectral density of the acoustic power $\mathrm{PSD}_{Pac} \equiv d(P_{ac}/P_0)/df$ becomes:

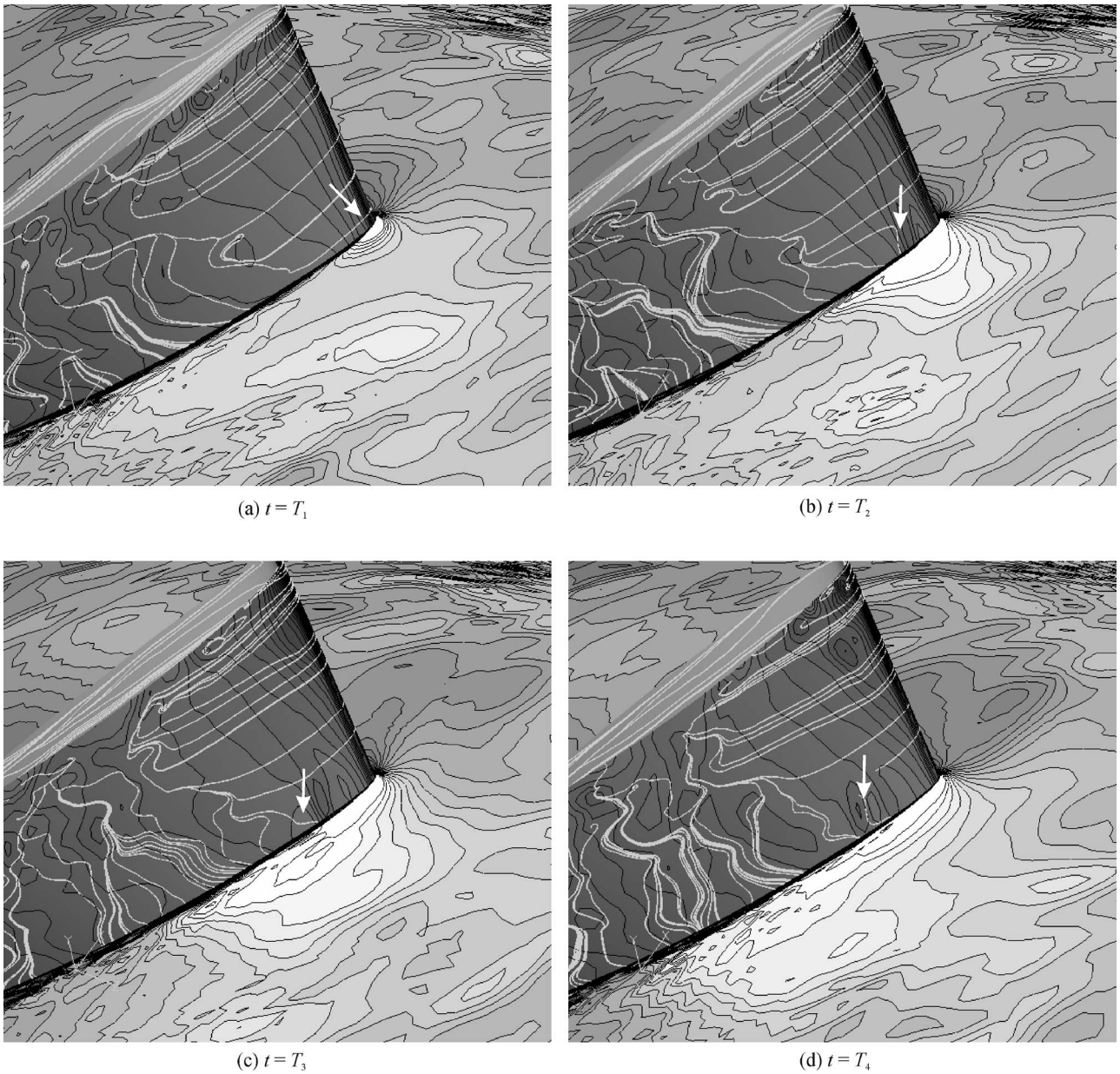

Fig. 11 Highly turbulent inflow (HT): instantaneous distributions of the static pressure coefficient (black lines) and surface streamlines (white lines) on a blade surface and relative velocity magnitude (black lines) on the mid-span plane $r=0.37D$ (normalized by the impeller's tip velocity) at four consecutive time instances

$$\mathrm{PSD}_{Pac}(f) = B\frac{\pi}{4}\frac{f}{\rho c_0^2 \frac{D}{2}\left(1-\left(\frac{r_1}{r_2}\right)\right)^2} A_{\pm}\mathrm{PSD}_F(f) \tag{9}$$

where $\mathrm{PSD}_F(f)$ is the spectral density of the unsteady blade forces, B is the number of the blades, D is the diameter of the impeller and duct, ρ is the density of the fluid, c_0 is the speed of sound, and $A_{\pm}$ is a radiation factor, which is 1 for flows with a Mach number smaller than 0.5. Strictly speaking, this model is valid only for acoustically compact noncorrelated blade forces.

Figure 15 shows a comparison of the predicted sound power spectral density with measurements from [25]. The sound power was measured by means of a microphone placed 3 m downstream of the rotor in the duct with an anechoic determination. In order to compensate for pseudo sound, the microphone was equipped with a slit tube and a nose cone. Since the thus-measured sound power corresponds roughly to half of the total sound power of the rotor, the values obtained with Eq. (9) are divided by 2 for comparison. The upper figure shows predictions by using the averaged unsteady force on *one blade* while the middle figure shows those obtained from the complete impeller force. As seen in Fig. 12 the measured blade surface pressure fluctuations contain tonal peaks at multiples of rotor shaft frequency due to effects not present in the LES. The sound power spectrum obtained from the force on one blade for HT (upper figure) shows the peak at 400 Hz as in the blade force spectrum in Fig. 14. However, the sound power spectrum obtained from the force on the complete impeller (middle figure), which includes the phase effects of the individual blade forces, does not show this peak, which is in better agreement to the measurements. The present LES predicts the absolute levels of the sound power and the differences between CI and HT cases reasonably well. The discrepancies between the predicted and measured sound power spectra can be attributed to (i) errors in the input source data (i.e., the surface pressure fluctuations), (ii)

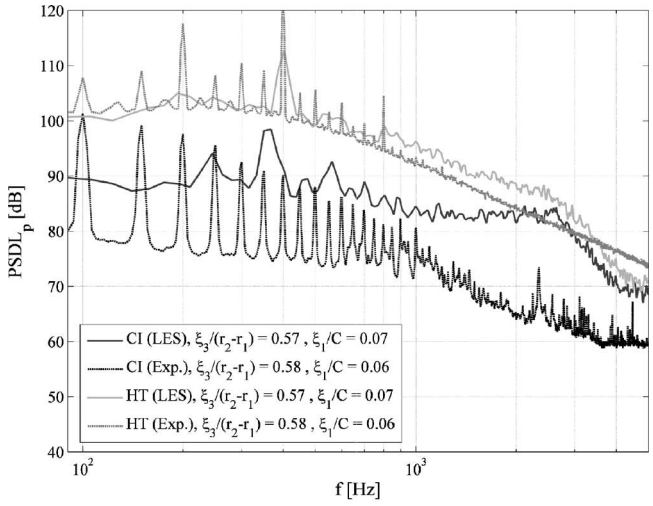

(a) near the leading edge (point P4)

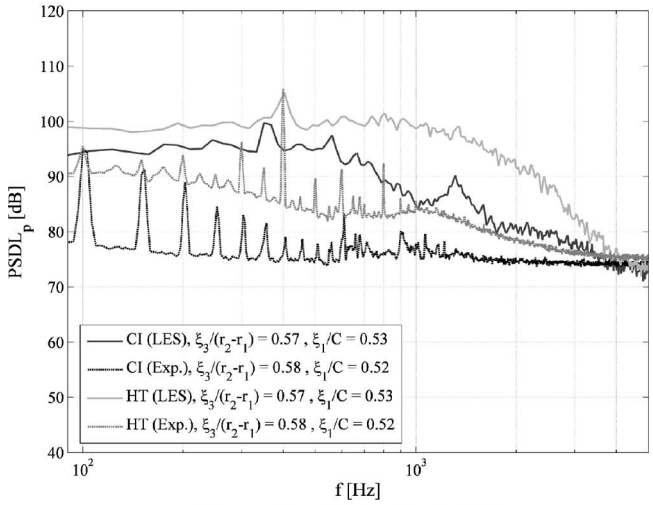

(b) near the mid chord (point P5)

Fig. 12 Comparisons of the predicted and measured [22] power spectral density levels of the wall pressure fluctuations on the blade suction-side at approximately mid span radius for clean (CI) and highly turbulent inflow (HT)

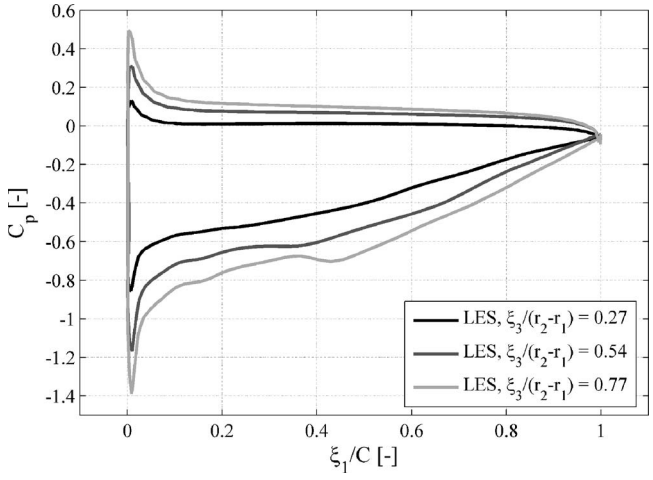

Fig. 13 Surface pressure coefficient at three blade sections predicted by LES with numerical grid G4

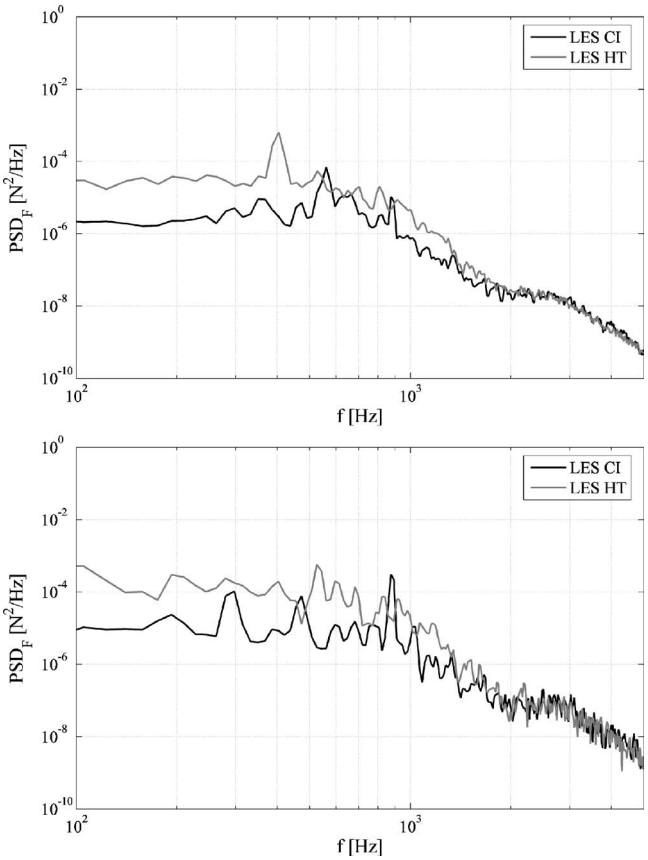

Fig. 14 Predicted power spectral density of the unsteady forces for clean inflow (CI) and highly turbulent inflow (HT) cases (upper: representative force on *one blade*, lower: force on the complete impeller)

the effects of the tip clearance, which are not included in the present simulations, and (iii) the limitations of the acoustical model, which assumes acoustically compact and incoherent sound sources.

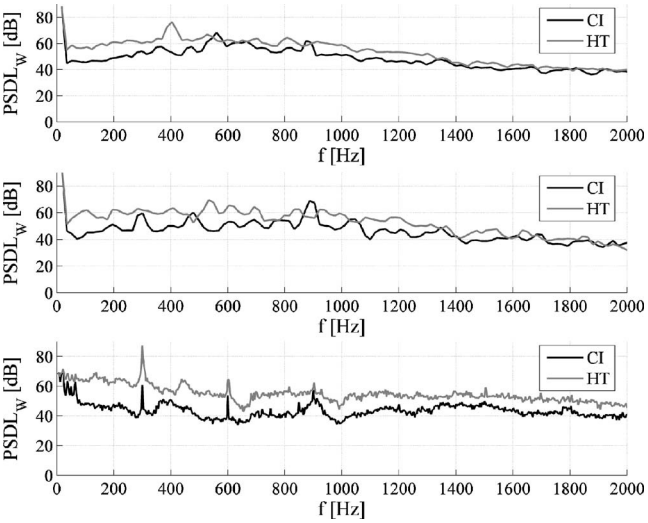

Fig. 15 Predicted and measured duct sound power spectral density (upper: predicted from the single blade force, middle: predicted from the overall impeller force, lower: measurements [25])

6 Conclusions

A large eddy simulation (LES) was applied to predict the unsteady flow in a complete low speed axial flow fan subjected to a highly "turbulent" inflow. The inflow turbulence was generated by a turbulence grid placed upstream of the impeller, being part of the computational domain. With the exception of neglecting the impeller tip clearance, no further geometrical simplifications were made.

The dynamic Smagorinsky model (DSM) was used as the subgrid scale (SGS) model. A streamwise-upwind finite element method (FEM) with second-order accuracy in both time and space was applied as the discretization method together with a multiframe of reference dynamic overset grid in order to take into account the effects of the blade-wake interactions. Based on a simple algebraic acoustical model for axial flow fans, the radiated sound power was also predicted by using the computed fluctuations in the blade force.

The LES yields phenomena associated with the steady and unsteady flow field, which seem very realistic. For instance, it accurately predicted the jet/wake structure downstream of the grid type turbulence generator. The fan performance and the computed results are consistent with the known fact that the influence of any incident turbulence tends to vanish towards the trailing edge of an airfoil, irrespective of the ingested turbulent structures. The predicted turbulence intensity and the turbulent length scale downstream of the turbulence generator agree reasonably well with the data measured by the hot-wire anemometry, when a large numerical grid with 3 million grid elements is employed. In terms of surface pressure fluctuations on a blade, the response of the blade to highly turbulent inflow is well predicted at the leading edge region. However, for clean, i.e., low, turbulent inflow, and further downstream, the surface pressure spectra are more or less overpredicted. The chosen cell density of the numerical grid in the near-wall region of the blades allows us to resolve only *large* scale turbulent structures. The large turbulent structures downstream of the turbulence generator are predicted reasonably well as confirmed by Figs. 5–7. But, the large structures computed in the near-wall region of the blades are not physical because smaller structures in the near-wall region, which play an essential role for the determination of the overall structures of the turbulent boundary layer, are not predicted by the present LES due to the limited number of the numerical grid points. To a lesser extent, the small overpredictions in the predicted turbulence downstream of the turbulence generator may also contributed to the observed differences. In order to overcome the grid deficiency in the near-wall region, it would be worthwhile to consider either a much finer numerical grid to resolve the near-wall turbulent structures or a hybrid numerical method (such as the detached eddy simulation).

Despite the above-mentioned deficiencies, the present LES reasonably well predicts the absolute level of the radiated sound power and the effects of the inflow turbulence on the radiated sound power. Although the tip clearance is as small as 0.18% of the rotor diameter and thus neglected in the present LES, it may affect the vortical structures near the tip and the resulting radiated sound. Therefore, further improvements in the sound prediction accuracy may probably achieved by (i) taking effects of the tip clearance into account and (ii) replacing the simple algebraic acoustical model by an acoustic field method in addition to the countermeasures to the poor grid resolution in the near-wall region already mentioned.

Acknowledgment

This work was supported by the German Academic Exchange Service (DAAD) and the German Research Foundation (DFG). We gratefully acknowledge this support.

Nomenclature

B = number of blades
C = chord length, m
c_0 = speed of sound, m/s
D = impeller diameter, m
f = frequency, Hz
$f_i (i=1,2,3)$ = inertial force, N
L_w = sound power level, dB
Ma = Mach number
n = revolutions per second, 1/s
P = power, W
P_0 = reference power (10^{-12} W), W
p = pressure, Pa
p_0 = reference pressure (2×10^{-5} Pa), Pa
r_1 = hub radius, m
r_2 = impeller radius, m
t = time, s
Tu = turbulence intensity
u,v,w = velocity components, m/s
u_i = velocity components ($i=1,2,3$), m/s
$\dot{V}$ = volume flow rate, m^3/s
$x_i (i=1,2,3)$ = Cartesian coordinates ($i=1,2,3$), m
x,y,z = Cartesian coordinates, m

Greek Symbols

ϕ = volume flow rate coefficient
η_{ts} = total to static pressure rise efficiency
Λ = integral length scale, mm
ν = kinematic viscosity, m^2/s
ρ = density of fluid, kg/m^3
Ω = angular velocity, rad/s
ψ_{ts} = pressure rise coefficient
ξ_i = blade coordinates, m

Sub- and Superscripts

$\overline{}$ = grid scale component
$'$ = subgrid scale component, fluctuation
$\sim$ = temporally averaged component

Abbrevations

CI = clean inflow
HT = highly turbulent inflow
LES = large eddy simulation
PSD = power spectral density

References

[1] Algermissen, G., Siegert, R., and Spindler, T., 2001, "Numerical Simulation of Aeroacoustic Sound Generated by Fans under Installation Conditions," 7th AIAA/CEAS Aeroacoustic Conference, AIAA Paper No. 2001-2174, Maastricht, Netherlands, 28-30 May 2001.

[2] Kouidri, S., Fedala, D., Belamri, T., and Rey, R., 2005, "Comparative Study of the Aeroacoustic Behaviour of two Axial Flow Fans with Different Sweep Angles," ASME Fluid Engineering Summer Conference, Paper No. FEDSM2005-77424, Houston, TX, 19–23 June 2005.

[3] Fowcs Williams, J. E., and Hawkings, D. L., 1969, "Sound Generated by Turbulence and Surfaces in Arbitrary Motion," Philos. Trans. R. Soc. London, **264**, pp. 321–342.

[4] You, D., Wang, M., Mittal, R., and Moin, P., 2003, "Study of Rotor Tip-Clearance Flow Using Large Eddy Simulation," 41st Aerospace Sciences Meeting and Exhibit, AIAA J. Paper No. 2003-0838, Reno, Nevada, 6–9 January 2003.

[5] Kato, C., Mukai, H., and Manabe, A., 2002, "Large Eddy Simulation of Unsteady Flow in a Mixed-Flow Pump," The 9th International Symposium on Transport Phenomena and Dynamics of Rotating Machinery (ISROMAC-9), Honolulu, HI, 10–14 February 2002.

[6] Kato, C., Kaiho, M., and Manabe, A., 2003, "An Overset Finite Element Large Eddy Simulation Method with Application to Turbomachinery and Aeroacoustics," ASME J. Appl. Mech., **70**, pp. 32–43.

[7] Yamanishi, N., Kato, C., and Matsumoto, Y., 2003, "LES Analysis of a Rocket Turbopump Inducer in Non-Cavitating and Cavitating Flows," 4th ASME/JSME Joint Fluids Engineering Conference, ASME FEDSM2003-45406, Honolulu, HI, 6–11 July 2003.

[8] Smagorinsky, J., 1963, "General Circulation Experiments with Primitive Equations," Mon. Weather Rev., **91**(3), pp. 99–164.

[9] Germano, M., Poimelli, U., Moin, P., and Cabot, W. H., 1991, "A Dynamic Subgrid-Scale Eddy Viscosity Model," Phys. Fluids A, **A 3**(7), pp. 1760–1765.

[10] Uddin, M. A., Kato, C., Taniguchi, N., Yamade, Y., and Tanahashi, M., 2004, "Comparative Study of Finite Element LES with Spectral DNS in Homogenous Isotropic Turbulence," 2nd BSME-ASME International Conference on Thermal Engineering, Dhaka, 2–4 January 2004.
[11] Kato, C., and Ikegawa, M., 1991, "Large Eddy Simulation of Unsteady Turbulent Wake of a Circular Cylinder Using the Finite Element Method," *Advances in Numerical Simulation of Turbulent Flows*, ASME, New York, ASME FED- Vol. 117, pp. 49–56.
[12] Tezduyar, T. E., and Hughes, T. J. R., 1983, "Finite Element Formulation for Convection Dominated Flows With Particular Emphasis on the Compressible Euler Equations," *Proceedings of AIAA 21st Aerospace Sciences Meeting*, AIAA Paper No. 83-0125, Reno, Nevada, 10–13 January 1983.
[13] Donea, J., et al., 1984, "Time Accurate Solution of the Advection-Diffusion Problems by Finite Elements," Comput. Methods Appl. Mech. Eng., **45**, pp. 123–145.
[14] Van der Vorst, H. A., 1992, "Bi-CGSTAB: A Fast and Smoothly Converging Variant of Bi-CG for the Solution of Nonsymmetric Linear Systems," SIAM (Soc. Ind. Appl. Math.) J. Sci. Stat. Comput., **13**, pp. 631–644.
[15] Kaiho, M., Ikegawa, M., and Kato, C., 1997, "Parallel Overlapping Scheme for Viscous Incompressible Flows," Int. J. Numer. Methods Fluids, **24**, pp. 1341–1352.
[16] Stremel, M., 2002, "Schaufelwechseldrücke und Schallabstrahlung bei einem Axialventilator unter turbulenter Zuströmung," Fortschr.-Ber. VDI Reihe 7 Nr. 439, VDI Verlag Düsseldorf.
[17] Schneider, M., and Carolus, T., 2003, "Calculation of Broadband Fan Noise due to Inflow Turbulence Employing Noise Prediction Models," Fan Noise 2003, Int. Symposium, Senlis, France, 22–25 September 2003.
[18] Roach, P. E., 1986, "The Generation of Nearly Isotropic Turbulence by Means of Grids," Int. J. Heat Fluid Flow, **8**(2), pp. 82–92.
[19] Washburn, K. B., and Lauchle, G. C., 1988, "Inlet Flow Conditions and Tonal Sound Radiation from a Subsonic Fan," Noise Control Eng. J., **31**(2), pp. 101–110.
[20] Paterson, R. W., and Amiet, R. K., 1977, "Noise and Surface Pressure Response of an Airfoil to Incident Turbulence," J. Aircr., **14**(8), pp. 729–736.
[21] Carolus, T. H., and Stremel, M., 2003, "Measurements of Surface Pressure Fluctuations—a Tool for Identifying Acoustic Sources in Fans," Fan Noise 2003, Int. Symposium, Senlis, France, 22–25 September 2003.
[22] Carolus, T. H., and Stremel, M., 2002, "Blade Surface Pressure Fluctuations and Acoustic Radiation from an Axial Fan Rotor Due to Turbulent Inflow," Acta. Acust. Acust., **88**, pp. 472–482.
[23] Opiela, M., Meinke, M., and Schröder, W., 2001, "LES of Wake-Blade Interaction," 4th European Conference on Turbomachinery, Paper No. ATI-CST-086/01, Florence, 20–23 March 2001.
[24] Morfey, C. L., 1972, "The Acoustic of Axial Flow Machines," J. Sound Vib., **22**(4), pp. 445–466.
[25] Schneider, M., 2006, "Der Einfluss der Zustrombedingungen auf das breitbandige Geräusch eines Axialventilators," Fortschr.-Ber. VDI Reihe 7 Nr. 478, VDI Verlag Düsseldorf.

Yoshiki Yoshida
Japan Aerospace Exploration Agency,
1 Koganezawa,
Kimigaya,
Kakuda, Miyagi 981-1525,
Japan
e-mail: kryoshi@kakuda.jaxa.jp

Kengo Kikuta
Research Student in JAXA
Tohoku University, 2-1-1 Katahira,
Aoba,
Sendai, Miyagi 980-8577,
Japan

Satoshi Hasegawa

Mitsuru Shimagaki
Japan Aerospace Exploration Agency,
1 Koganezawa,
Kimigaya,
Kakuda, Miyagi 981-1525,
Japan

Takashi Tokumasu
Tohoku University,
Institute of Fluid Science,
2-1-1 Katahira, Aoba,
Sendai, Miyagi 980-8577,
Japan

Thermodynamic Effect on a Cavitating Inducer in Liquid Nitrogen

For experimental investigations of the thermodynamic effect on a cavitating inducer, it is nesessary to observe the cavitation. However, visualizations of the cavitation are not so easy in cryogenic flow. For this reason, we estimated the cavity region in liquid nitrogen based on measurements of the pressure fluctuation near the blade tip. In the present study, we focused on the length of the tip cavitation as a cavitation indicator. Comparison of the tip cavity length in liquid nitrogen (80 K) *with that in cold water* (296 K) *allowed us to estimate the strength of the thermodynamic effect. The degree of thermodynamic effect was found to increase with an increase of the cavity length. The temperature depression was estimated from the difference of the cavitation number of corresponding cavity condition (i.e., cavity length) between in liquid nitrogen and in cold water. The estimated temperature depression caused by vaporization increased rapidly when the cavity length extended over the throat. In addition, the estimated temperature inside the bubble nearly reached the temperature of the triple point when the pump performance deteriorated.*
[DOI: 10.1115/1.2427076]

Introduction

For the rocket engine turbopump, the inducer is placed upstream of the main impeller to improve the cavitation performance. This inducer often suffers due to serious cavitating conditions at low inlet pressure. The propellants of Japanese rocket engines are liquid hydrogen (20 K), and liquid oxygen (90 K). The thermodynamic effect on cavitation appears notably in these cryogenic fluids, although it can be disregarded in cold water.

The thermodynamic effect on cavitation can be explained as follows. The vaporization requires latent heat to be supplied from the liquid to the interface. Heat transfer from the liquid to the bubble is possible only if the temperature inside the bubble (T_c) is less than that in the liquid bulk (T). Hence, the vapor pressure inside the bubble ($p_v(T_c)$) is also less than that in the liquid bulk ($p_v(T)$). Consequently, the pressure imbalance ($p_v(T_c)-p_{\mathrm{ref}}$) between the bubble and reference point at infinity decreases. Thus, it can be understood that the growth of the bubble with the thermodynamic effect is less than that without the thermodynamic effect, even under the same cavitation number (σ) at the reference point at infinity.

The first study on the thermodynamic effect in pumps was conducted by Stahl et al. [1]. They investigated the thermodynamic effect based only on the reduction of pump performance (i.e., the measurable cavitation effect of $\Delta H/H=3\%$) as a cavitation indicator. Although they assumed that "the same extent of cavitation is the same damage to the performance," they did not observe the cavitation phenomena. Franc et al. [2] recently investigated the thermodynamic effect based on the measurements of the development of leading edge cavitation using refrigerant R114 as a working fluid. They examined the thermodynamic effect and the onset of unsteady cavitations (i.e., alternate blade cavitation and rotating cavitation) based on comparison of the cavity length in R114 with that in cold water.

In the present study, we also adopted the cavity length of the tip cavitation as a cavitation indicator. It seems obvious to us that the tip cavitation plays an important role in cavitation performance, as well as in cavitation instabilities in inducers. To estimate the cavity length of the tip cavitation in liquid nitrogen, the pressure fluctuations were measured by using pressure sensors installed on the casing [3]. Examination of the relation of cavity length with the thermodynamic effect was done through comparison of the experimental results in liquid nitrogen with those in cold water.

Experimental Facility

The present study consisted of two types of experiments, experiments in water, in which the thermodynamic effect can be disregarded, and experiments in liquid nitrogen, in which the thermodynamic effect appears distinctly. Both type of experiment were conducted at the Kakuda Space Center (KSC) of the Japan Aerospace Exploration Agency (JAXA).

Experiment in Water. Experiments in water were conducted in the cavitation tunnel shown in Fig. 1. This tunnel is a closed-loop tunnel, and base pressure and hence cavitation number σ are adjusted by using the piston installed on the loop. The working fluid

Contributed by the Fluids Engineering Division of ASME for publication in the JOURNAL OF FLUIDS ENGINEERING. Manuscript received June 23, 2005; final manuscript received October 26, 2006. Assoc. Editor: Akira Goto.

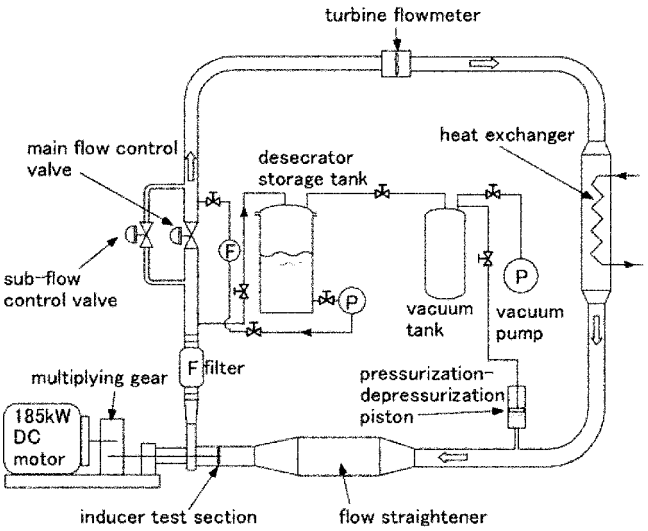

Fig. 1 Water cavitation tunnel

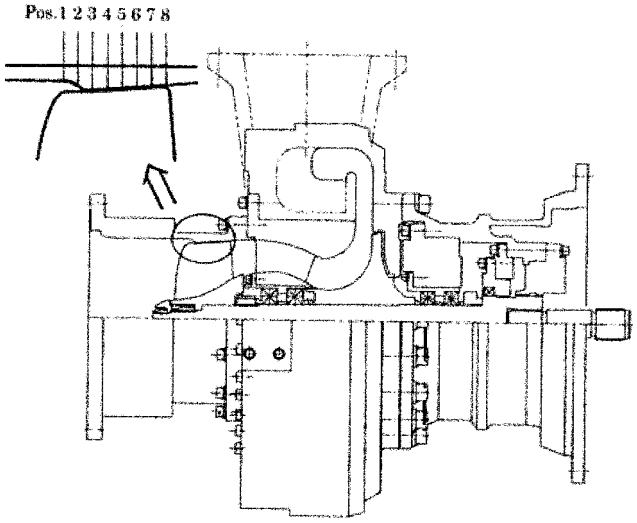

Fig. 3 Schematic diagram of the test inducer in liquid nitrogen showing the location of pressure taps

is cold water at room temperature (296 K) after degassing. The flow rate is set by a control valve installed downstream of the inducer. The inducer casing is made of transparent acrylic resin to permit visualization of the cavitation by use of a video camera. The rotational speed is 6000 rpm and the flow rate is $Q/Q_d = 1.00$ (Q_d=design flow rate). The rotational speed and the flow rate were kept constant in the experiment, and the cavitation number was changed by reducing the inlet pressure.

Experiment in Liquid Nitrogen. Experiments in liquid nitrogen were conducted at the Cryogenic Inducer Test Facility (CITF) [4] shown in Fig. 2. This facility is a blow-down cavitation tunnel, in which the working fluid is flushed from the run tank to the catch tank through the inducer test section. The flow control valve installed downstream of the inducer sets the flow rate, and the pressure in the run tank adjusts the inducer inlet pressure. The inducer casing is made of stainless steel, and thus visualization of the cavitating inducer is not possible. The rotational speed is 18,300 rpm (equal to that of an acutal turbopump and about three times that in the water experiment), and the flow rate is $Q/Q_d = 1.00$. Temperature of liquid nitrogen measured at the inducer inlet was 80 K.

Test Inducer. Figure 3 shows the inducer test section for the experiment in liquid nitrogen. The inducer used in the liquid nitrogen experiment has the same dimensions and geometric configuration as that in cold water. It has three blades with sweep cutback at the leading edge, and its solidity is about 1.9. The outlet diameter is 157 mm.

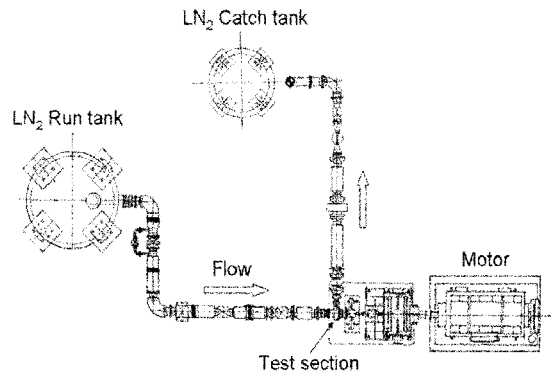

Fig. 2 Cryogenic inducer test facility

Estimation of Cavitating Region

In the experiment in liquid nitrogen, unsteady pressure sensors were installed on the casing to estimate the cavitation region. Figures 3 and 4 show the location of the pressure taps. There are eight sensors located from the leading edge to the trailing edge along the blade. The pressure sensors detect the unsteady pressure caused by the tip cavitation, which includes the tip leakage vortex cavitation, cavitation in the shear layer between the tip leakage flow and the main flow, and a part of the attached cavitation on the blade surface. The sensor is a charge mode pressure sensor (PCB Piezotronics Inc., model WH113A) with high resistance to shock (20,000 g), a wide range of the temperature for cryogenic fluid (~33 K), and high resonance frequency (250 kHz).

As the sensor cannot detect the DC component of unsteady pressure, the value of the vapor pressure cannot be measured. Thus, the vapor pressure was estimated based on the unsteady

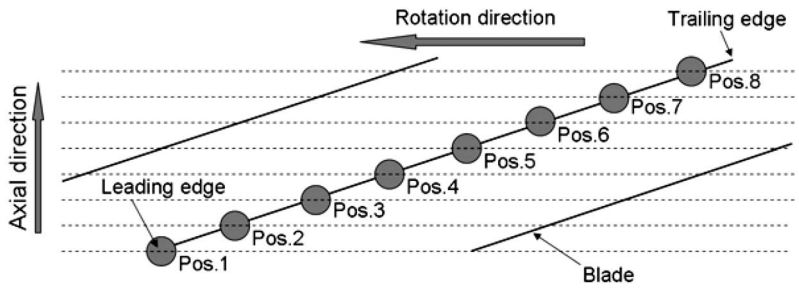

Fig. 4 Location of pressure taps along the blade

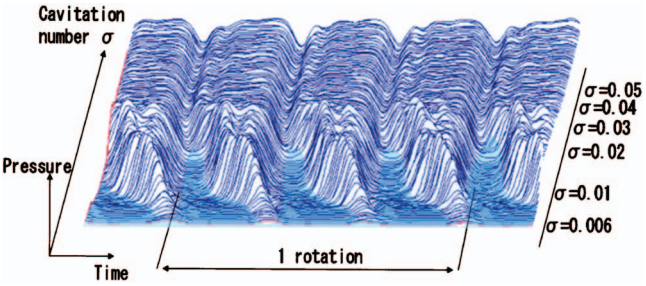

Fig. 5 Waterfall of unsteady pressure waveform at Pos. 4 (uncertainty in σ=0.001)

pressure wave form as follows. When cavitation develops on the suction side of the blade at the tip, the pressure sensor shows a particular wave form. Figure 5 shows the waterfall of a typical wave form measured at the location of Position 4 shown in Figs. 3 and 4. Wave forms of 50 rotations are averaged using the trigger signal of a rotation. The wave form clearly shows the pressure fluctuation caused by the blade passing at higher cavitation number. When the cavitation number becomes smaller, a flat region (colored by light blue) appears at the bottom of the wave form and extends from the suction side to the pressure side within the interblade. The pressure of this region can be considered to be the vapor pressure of the cavitation. Thus, we judged this domain as the region of cavitation.

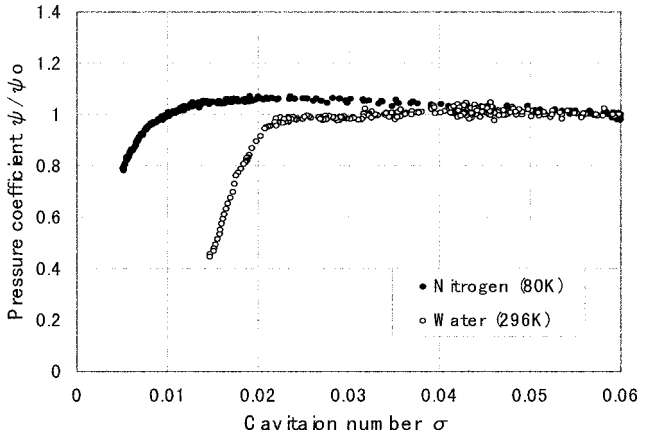

Fig. 6 Comparison of the cavitation performance between in cold water and that in liquid nitrogen (uncertainty in σ =0.001, ψ/ψ o=0.01)

Experimental Results

Cavitation Performance. Figure 6 shows a comparison of the cavitation performances between that in cold water (○) and that in liquid nitrogen (●). The horizontal axis is the cavitation number (σ), and the vertical axis is the normalized head coefficient (ψ/ψ_0). The inducer head in liquid nitrogen is maintained until the smaller cavitation number. The cavitation performance was greatly improved due to the thermodynamic effect in liquid nitrogen.

Regarding the pressure performance in liquid nitrogen, the inducer head trends to increases gradually as the cavitation number decreases; i.e., pump gain is negative ($d\psi/d\sigma<0$). The occurrence of unsteady cavitation, however, could not be confirmed from the fast Fourier transform (FFT) analysis of the pressure fluctuation. As opposed to the result in liquid nitrogen, the performance curve was almost flat ($d\psi/d\sigma\approx0$) in cold water. However, cavitation surge occurred within σ=0.028–0.045, resulting in the scatter of ψ in this range.

Cavitation surge is a kind of system instability and depends on the pump gain and unsteady characteristics of cavitation, i.e., mass flow gain factor and cavitation compliance. It also depends on the characteristics of the test loop. Unfortunately, full confirmation of the thermodynamic effect on the cavitation surge was not obtained in the present experiment. An extension of the experiment is underway with focus on the influence of the thermodynamic effect on the unsteady cavitation phenomena.

Observation of Cavitation. Figure 7 shows observations of the cavitating inducer in cold water. The cavity near the tip develops along the blade as the cavitation number decreases. At the critical point of the head break (σ=0.02), the cavity extends to a position near the trailing edge. The length of the cavity along the blade was measured from these pictures. On the other hand, cavitation also occurs in the backflow upstream of the inducer. However, the pressure sensor of the experiment in liquid nitrogen could not detect this backflow vortex cavitation.

Figure 8 shows the unsteady pressure distribution estimated from the pressure waveform in liquid nitrogen shown in Fig. 5. The estimated cavitation region (colored blue) develops along the blade from the leading edge to the trailing edge as the cavitation number decreases. It turned out that the cavitating region could be estimated indirectly by examination of the unsteady pressure wave form, although the kind of cavitation which can be detected by this method is limited.

Thermodynamic Effect

Stahl et al. [1] proposed liquid thermal cavitation criterion B (commonly called the B-factor)

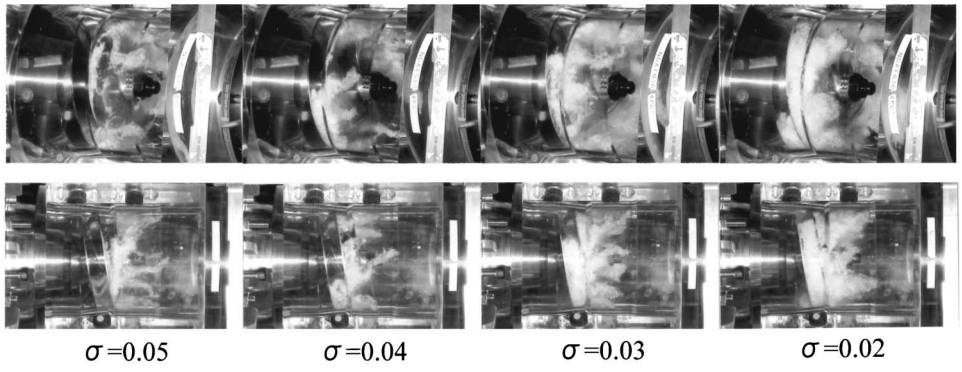

Fig. 7 Visualization of the cavitation in cold water (uncertainty in σ=0.001)

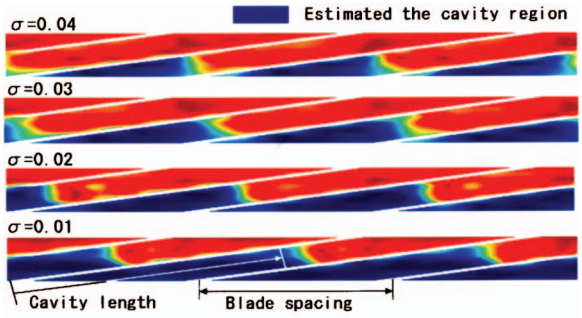

Fig. 8 Unsteady pressure distribution in liquid nitrogen showing the cavity region (uncertainty in σ=0.001)

$$B \equiv \frac{V_v}{V_l} = \frac{\rho_l c_{\mathrm{pl}} \Delta T}{\rho_v L} = \frac{\Delta T}{\Delta T^*} \left(\Delta T^* = \frac{\rho_v L}{\rho_l c_{\mathrm{pl}}} \right) \tag{1}$$

Stepanoff [5] stated that B is used merely as index of the "tendency" of the liquid to boil or its "readiness" to flash into vapor. To examine the tendency of the thermodynamic effect in terms of B, it is necessary to find the temperature depression $\Delta T(=T_\infty - T_c)$ between the liquid at infinity and the cavity region. ΔT^* is the characteristic temperature difference that depends only on the nature of the fluid. In the present study, ΔT was estimated by the same method employed in Franc's work [2]. Here, the present method is a simplification based only on Eulerian similarity condition and equal intensity of cavitation (quantified by the normalized cavity length), and is implicitly based on the assumption that no other effects significantly affect cavitation phenomena in nitrogen and in water, although the inducer Reynolds number $\mathrm{Re}=UD/\nu$ (D=diameter of inducer; U=peripheral speed of inducer tip) for the viscous effect are $\mathrm{Re}=7.3\times10^6$ in water and $\mathrm{Re}=1.1\times10^8$ in nitrogen, respectively.

First, the cavitation number σ is calculated from the vapor pressure at the liquid temperature at infinity T_∞

$$\sigma = \frac{p_{\mathrm{ref}} - p_v(T_\infty)}{\frac{1}{2}\rho_l U^2} \tag{2}$$

Second, the cavitation number σ_c is calculated from the actual cavity pressure p_c equal to the vapor pressure at the actual temperature of the cavity T_c

$$\sigma_c = \frac{p_{\mathrm{ref}} - p_c}{\frac{1}{2}\rho_l U^2} = \frac{p_{\mathrm{ref}} - p_v(T_c)}{\frac{1}{2}\rho_l U^2} \tag{3}$$

The temperature depression ΔT caused by the thermodynamic effect is obtained by Eqs. (2) and (3)

$$\frac{1}{2}\rho_l U^2(\sigma_c - \sigma) = \int_{T_c}^{T_\infty} \frac{dp_v}{dT} dT \quad \Delta T = T_\infty - T_c \tag{4}$$

From Eq. (4), the temperature depression ΔT can be calculated from the difference of the cavitation numbers, $\sigma_c - \sigma$, of two corresponding conditions. The value σ_c is obtained from the experimental result without the thermodynamic effect (i.e., in cold water), while the value σ is obtained from the experimental result with the thermodynamic effect (i.e., in liquid nitrogen).

Franc et al. [2] adopted the cavity length of the attached cavitation on the blade as a cavitation indicator concerning the corresponding cavitation numbers of σ_c and σ. They assumed that the cavity length is a function of only cavitation number σ_c regardless of the type of fluid. They observed the cavity length on the blade surface both in cold water and in refrigerant R114, and examined

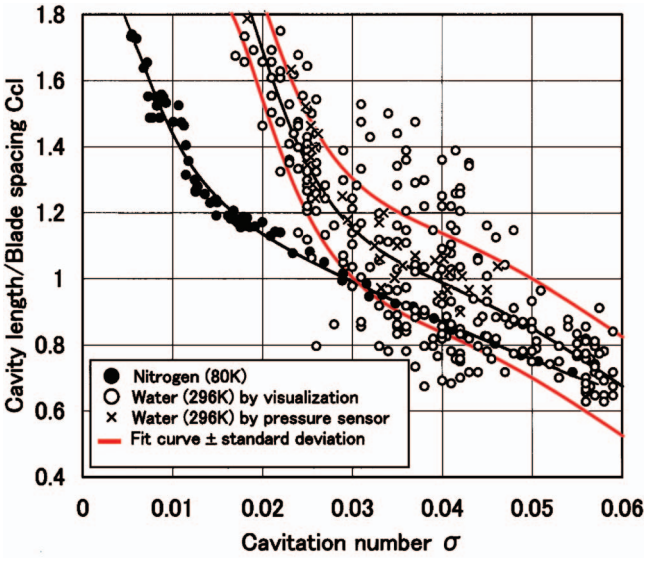

Fig. 9 Comparison of the cavity length of the tip cavitation between in cold water and that in liquid nitrogen (uncertainty in σ=0.001, Ccl=0.03)

the temperature depression from these two experiment results. In the present study, we also focused on the cavity length of the tip cavitation as a cavitation indicator.

Discussion

Cavity Length. Figure 9 shows the cavity length $C_{\mathrm{cl}}(L_c/h$, cavity length along the blade from the leading edge of the blade to the trailing edge of the cavity/blade spacing) versus cavitation number σ. The open circles (○) indicate the cavity lengths in cold water from the visualization shown in Fig. 7. One symbol shows a reading from one picture. There is wide scatter within $\sigma=0.028-0.045$ caused by cavitation surge. The cavity length fluctuates within $C_{\mathrm{cl}}=0.7-1.5$ around $C_{\mathrm{cl}}\approx1.1$. The standard deviation $S(C_{\mathrm{cl}})$ of those plots was 0.16. The best-fit curve (black line) obtained by the least square method, and best-fit curve ± standard deviation $S(C_{\mathrm{cl}})=0.16$ are also shown with red lines in the figure. In addition, the multis (×) show the cavity length in cold water measured by the indirect method using the pressure sensor, the same procedure as that in liquid nitrogen. From the comparison of the results by direct visualization with those by indirect observation using pressure sensor, we confirmed that the cavity length can be estimated by the present indirect method even in liquid nitrogen.

The closed circles (●) indicate the cavity length in liquid nitrogen from the estimated pressure distributions shown in Fig. 8. There is almost no scatter since one symbol shows the averaged value of 50 rotations. The unsteady cavitation phenomena (cavitation surge or rotating cavitation) were not observed in liquid nitrogen at all. Best-fit curves obtained by the least square method are also shown in the figure.

From comparison of the best-fit curves, it was found that the cavity length in nitrogen was shorter than that in cold water at the given cavitation number. The thermodynamic effect suppressed the growth of the cavity, and the difference between the cavity length in cold water and that in liquid nitrogen was smaller when C_{cl} was less than 1.0. However, the difference increased considerably when C_{cl} was larger than 1.0. Comparison with the cavitation performance curves in Fig. 8 shows that the inducer head decreased with $\Delta H/H=10\%$ when the cavity length became $C_{\mathrm{cl}}\approx1.6$ both in cold water and in liquid nitrogen. This result is

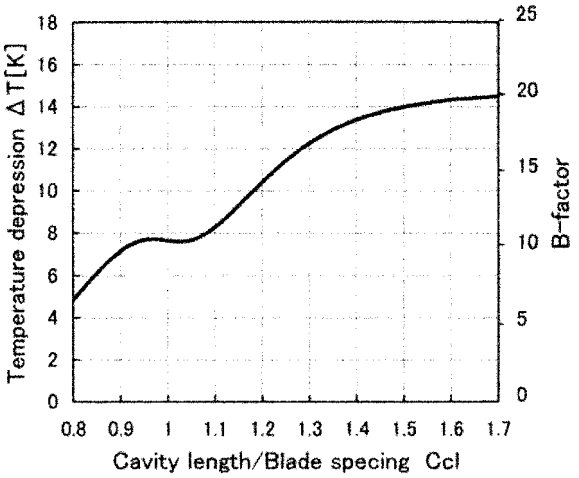

Fig. 10 Estimated temperature depression, and *B*-factor as a function of the cavity length

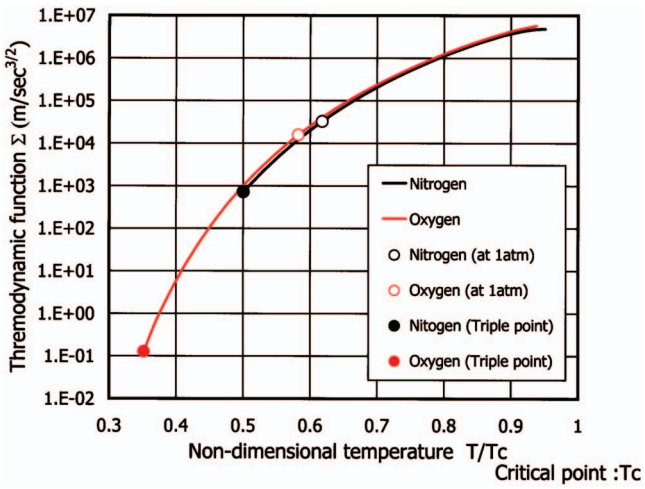

Fig. 11 Variation of the thermodynamic function $\Sigma(T)$ of nitrogen and oxygen

consistent with Stepanoff's assumption [1] that the same extent of cavitation is the same damage to the performance.

Temperature Depression. Figure 10 shows the temperature depression ΔT and B-factor versus the cavity length C_{cl} calculated from Eqs. (1) and (4). In the calculation, the difference of the cavitation number of $\sigma-\sigma_c$ is calculated based on a given cavity length using the best-fit curves in Fig. 9. It is interesting that the temperature depression changes with the cavity length. The temperature depression is smaller when the cavity length C_{cl} is less than 1.0. The increase of the temperature depression stagnates at $C_{cl}\approx 1.0$. When the cavity develops over the throat ($C_{cl}>1.1$), the temperature depression increases again. After that ($C_{cl}>1.4$), the slope of temperature depression decreases gradually. Finally, the temperature depression reaches 14 K. In this case, the estimated temperature in the cavity T_c is 66 K($=T_\infty(80\ \mathrm{K})-\Delta T(14\ \mathrm{K})$), a value is near the temperature of the triple point of nitrogen $T_t(63\ \mathrm{K})$.

The above-mentioned tendency differs from that in Franc et al. [2], who reported that the dependency of the B-factor on the development of the cavitation is nearly linear with the cavity length. Cavity length as a cavitation indicator and the kind of working fluid seem to result in this difference. The cavitation indicator is the cavity length of the tip cavitation, and the working fluid is liquid nitrogen (80 K) in the present experiment, as opposed to the cavity length of the attached cavitation on the blade and refrigerant R114 (293 ~ 313 K) in Franc's experiment. The tip cavitation is longer and larger than the attached cavitation and is more affected by the interaction of the leading edge of the adjacent blade, in particular, at the throat. This is the reason why the temperature depression stagnates at the cavity length $C_{cl}\approx 1.0$.

On the contrary, the temperature depression increases rapidly when the cavity length develops over the throat ($C_{cl}>1.1$). Yoshihara et al. [6] observed in the experiment of single hydrofoil that the ventilated cavity begins to oscillate and the ventilation flow rate increases steeply when the cavity length becomes larger than half of the chord length. It is because that the oscillating cloud cavitation at the rear part of the chord causes unsteady entrainment of the ventilated gas in addition to the entrainment of the stable cavitation. Even concerning natural cavitation in inducers, it seems that the similar phenomena occurs when the cavity length C_{cl} becomes larger than 1.1. On the larger cavities over the throat, the evaporation in the front part of cavity at the leading edge increases to compensate the losses in the rear part of the cavity at the blade channel. It might be the reason why the degree of thermodynamic effect increases when the cavity length develops over the throat. Thus, the throat design of the cascade plays an important role for the thermal effect in inducers.

In addition, the margin between the temperature of the fluid and that of the triple point is relatively smaller in liquid nitrogen than in refrigerant R114. This is the reason why there is a limitation of the increase of the temperature depression at $C_{cl}>1.4$ in liquid nitrogen. Figure 11 showed the thermodynamic function $\Sigma(T)$, proposed by Brennen [7], of nitrogen and oxygen as the function of T/T_c (T_c is the temperature of the critical point). The property of thermodynamic functions $\Sigma(T)$ of nitrogen is similar to that of oxygen. However, the margin between the temperature at 1 atm and the triple point of nitrogen is less than that of the oxygen. Thus, it is inferred that nitrogen has the limitation of the temperature depression due to the thermal effect.

Concluding Remarks

To obtain a fundamental understanding of the thermodynamic effect of the cavitating inducer, the relation between the temperature depression in the cavity and the cavity length of the tip cavitation was examined. The cavity length of the tip cavitation in the liquid nitrogen was estimated from the measurement of the unsteady pressure on the casing.

The temperature depression was estimated based on the comparison of the experimental results in cold water (296 K) with those in liquid nitrogen (80 K) with the cavity length as the cavitation indicator. It was found that the thermodynamic effect is a function of the cavity length. The temperature depression due to vaporization is small when the cavity length is short. The increase of the temperature depression immediately stagnates when the cavity length develops to the throat ($C_{cl}\approx 1.0$). When the cavity length develops over the throat, the temperature depression increases considerably. From these results, the interaction of the tip cavitation with the leading edge of the adjacent blade plays an important role in the degree of the thermodynamic effect.

In addition, the temperature depression is limited when the temperature in the cavity nearly reaches the temperature of the triple point. In this situation, the cavitation performance begins to deteriorate. It was inferred that the small margin between the temperature in the fluid and that of the triple point results in a limitation of the degree of the thermodynamic effect in inducers.

Acknowledgments

The authors would like to thank Mr. Yoshinobu Yasutomi of Ishikawajima-Harima Heavy Industries Co., Ltd. who made many

valuable suggestions as to the test inducer, and Shigemasa Yamashita and Yasumasa Ogura of Kobe Steel, Ltd. for providing support in the running of experiments.

Nomenclature

B = B-factor of Stepanoff
C_{cl} = cavity length/blade spacing
C_{pl} = liquid heat capacity
D = inducer diameter
h = blade spacing
L = latent heat of vaporization
L_c = cavity length
p_c = cavity pressure
p_{ref} = reference pressure
p_v = vapor pressure
Q = flow rate
Q_d = design flow rate
Re = inducer Reynolds number = UD/ν
$S(C_{cl})$ = standard deviation of C_{cl}
T_c = cavity temperature or temperature of the critical point
T_t = temperature of triple point
T_∞ = temperature at infinity
ΔT = temperature depression
ΔT^* = characteristic temperature
U = peripheral speed of inducer tip
V_l = volume flow rate of liquid
V_v = volume flow rate of vapor
ν = kinematic viscosity
ρ_l = liquid density
ρ_v = vapor density
σ = cavitation number
ψ = inducer head cofficient
ψ_0 = normal inducer head cofficient

References

[1] Stahl, H. A., and Stepanoff, A. J., 1956, "Thermodynamic Aspects of Cavitation in Centrifugal Pumps," ASME J. Basic Eng., **78**, pp. 1691–1693.
[2] Franc, J. P., Rebattet, C., and Coulon, A., 2004, "An Experimental Investigation of Thermal Effect In a Cavitating Inducer," ASME J. Fluids Eng., **126**, pp. 716–723.
[3] Yoshida, Y., Tsujimoto, Y., Kamijo, K., and Maekawa, Y., 1997, "Unsteady Interblade Pressure Distributions and Fluid Forces Under Rotating Cavitation," *Proceedings of the 5th Asian International Conference on Fluid Machinery*, Oct. 1997, Seoul, Korea, pp. 457–464.
[4] Yoshida, Y., Watanabe, M., Hashimoto, H., Shimagaki, M., Yamada, H., and Shimura, T., 2004, "Verification Results of Cryogenic Inducer Test Facility in JAXA," (in Japanese), *Proceedings JSME Fluids Engineering Conference*, Nov. 2004, Fukuoka, Japan, OS-12-6, No. 127.
[5] Stepanoff, A. J., 1964, "Cavitation Properties of Liquids," ASME J. Eng. Power, **86**, pp. 195–200.
[6] Yoshihara, K., Kato, H., Yamaguchi, H., and Miyanaga, M., 1988, "Experimental Study on the Internal Flow of a Sheet Cavity," *Proceedings Cavitation and Multiphase Flow Forum*, July, 1988, Cincinnati, Ohio, ASME, FED-Vol. 64, pp. 94–98.
[7] Brennen, C. E., 1973, "The Dynamic Behavior and Compliance of a Stream of Cavitating Bubbles," J. Fluids Eng., **98**, pp. 533–541.

Numerical Prediction of Cavitating Flow on a Two-Dimensional Symmetrical Hydrofoil and Comparison to Experiments

Olivier Coutier-Delgosha[1]
ENSAM Lille/LML Laboratory,
8 bld Louis XIV,
59046 Lille Cedex,
France
e-mail: olivier.coutier@lille.ensam.fr

François Deniset
e-mail: deniset@ecole-navale.fr

Jacques André Astolfi
e-mail: astolfi@ecole-navale.fr

Jean-Baptiste Leroux[2]
e-mail: jean-baptiste.leroux@ensieta.fr

Institut de Recherche,
l'Ecole Navale – EA3634,
BP 600,
29240 Brest Naval,
France

This paper presents comparisons between two-dimensional (2D) CFD simulations and experimental investigations of the cavitating flow around a symmetrical 2D hydrofoil. This configuration was proposed as a test case in the "Workshop on physical models and CFD tools for computation of cavitating flows" at the 5th International Symposium on cavitation, which was held in Osaka in November 2003. The calculations were carried out in the ENSTA laboratory (Palaiseau, France), and the experimental visualizations and measurements were performed in the IRENav cavitation tunnel (Brest, France). The calculations are based on a single-fluid approach of the cavitating flow: the liquid/vapor mixture is treated as a homogeneous fluid whose density is controlled by a barotropic state law. Results presented in the paper focus on cavitation inception, the shape and the general behavior of the sheet cavity, lift and drag forces without and with cavitation, wall pressure signals around the foil, and the frequency of the oscillations in the case of unsteady sheet cavitation. The ability of the numerical model to predict successively the noncavitating flow field, nearly steady sheet cavitation, unsteady cloud cavitation, and finally nearly supercavitating flow is discussed. It is shown that the unsteady features of the flow are correctly predicted by the model, while some subtle arrangements of the two-phase flow during the condensation process are not reproduced. A comparison between the peer numerical results obtained by several authors in the same flow configuration is also performed. Not only the cavitation model and the turbulence model, but also the numerical treatment of the equations, are found to have a strong influence on the results. [DOI: 10.1115/1.2427079]

Introduction

The simulation of cavitating flows is a challenging task because it requires a coupling between the resolution of the Navier-Stokes equations, a physical model of cavitation, and also a model of turbulence, since cavitation often occurs in high-speed flows. Moreover, such flows are systematically unsteady at some scale; their behavior is usually characterized by permanent more or less pronounced fluctuations. In the case of cavitation around a hydrofoil, these fluctuations affect either the whole cavitating area, with large and sometimes periodical vapor cloud shedding, or only the rear part of the liquid/vapor mixture, as reported for example by Kawanami et al. [1], Pham et al. [2], Laberteaux and Ceccio [3], and Leroux et al. [4].

An effective physical cavitation model is thus supposed to take correctly into account these different types of unsteadiness. This is the reason why the models that do not consider the flow inside the cavitation areas, predicting only the external shape of the attached cavity on a profile, can only be applied in some particular configurations where no more than the mean flow around the cavitation sheet is investigated.

For other cases, several physical models that compute all the flow including the liquid/vapor medium have been proposed for about 15 years by Delannoy and Kueny [5], Chen and Heister [6], Singhal et al. [7], Kunz et al. [8], and Song and Qin [9]. They are nearly systematically based on the assumption that the mixture can be considered as only one fluid: only one momentum equation is used (which means that the vapor is supposed to be perfectly carried out by the liquid flow) and the model of turbulence is also applied to the whole medium composed of both liquid and vapor. The models mainly differ by the treatment of the mass fluxes between vapor and liquid; they are managed either by a barotropic state law derived from the model proposed by Delannoy and Kueny [5], by a supplementary equation that controls the convection/production of vapor [8,10], or by the evolution of a cluster of bubbles according to a simplified Eulerian form of the Reyleigh-Plesset equation [7,11].

The model of turbulence was recently found to be also of first importance to predict accurately the unsteady process [12]. For example, using a Reynolds average Navier-Stokes equations (RANS) approach with a standard 2-equation model, such as k-ε or k-ω, usually leads to unrealistic stabilizations of the flow [13–15]. Corrections are usually applied to these models to obtain unsteady sheet cavitation. Wu et al. [16] propose to apply a filter-based k-ε model initially developed by Johansen et al. [17]. In this approach, the filter depends on the grid size, in order to avoid excessive dissipation in small-scale motions, without altering the large-scale flow characteristics. In the case of the barotropic state law, taking into account the effects of compressibility on the turbulence structure in the two-phase medium was shown by Coutier-Delgosha et al. [18] to be necessary to obtain oscillatory cavitation behaviors. These effects lead to a slight reduction of the

[1]Corresponding author.
[2]Now at ENSIETA - Laboratoire MSN, 2 rue François Verny, 29806 Brest Cedex 9, France.

Contributed by the Fluids Engineering Division of ASME for publication in the JOURNAL OF FLUIDS ENGINEERING. Manuscript received August 11, 2005; final manuscript received August 4, 2006. Assoc. Editor Georges L. Chahine.

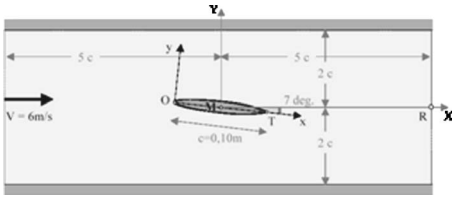

Fig. 1 Flow configuration proposed in the Workshop on physical models and CFD tools for computation of cavitating flows

turbulent viscosity in the liquid/vapor mixture. Alternatively, the use of large eddy simulation (LES) or detached eddy simulation (DES) models may overcome some of the classic limitations of the RANS approach, such as its deficiency in the case of substantial flow separation. It is expected that this category of model may yield improved simulations of large scale turbulent eddies, leading to better predictions of the large-scale flow unsteadiness. Promising results have been obtained in recent works by Kunz et al. [19] and Arndt et al. [20] with such type of approach.

In the present study, a modified k-ε turbulence model is coupled to a physical cavitation model based on a barotropic state law for the two-phase medium. The numerical resolution is derived from the SIMPLE algorithm, with significant modifications to treat highly compressible flows.

This numerical model has been applied to the two-dimensional (2D) configuration proposed as a test case in the numerical workshop of the 5th International Symposium on cavitation, which was held in Osaka in November 2003. (Fig. 1). Several cavitation numbers have been investigated, to obtain successively a noncavitating flow field, nearly steady sheet cavitation, unsteady cloud cavitation, and finally, nearly supercavitating flow. The calculations have been carried out in the ENSTA laboratory (Palaiseau, France) with the model "IZ", which was developed previously in the LEGI laboratory (Grenoble, France), with the support of the CNES (French Space Agency).

Measurements of the cavitating flow have been performed in the IRENAV tunnel of cavitation (Brest, France) for nearly the same flow configuration as the numerical simulations.

This joint experimental and numerical study of the test case completes the results presented during the workshop, focusing on the following information:

i. The experimental behavior of the 2D foil section, from cavitation inception to unsteady cloud cavitation
ii. The capability of the present numerical model to reproduce successively the different flow configurations, from nearly steady sheet cavitation to large vapor cloud shedding
iii. The distinction of two different periodical unsteady behaviors characterized by different values of Strouhal numbers, as shown previously in similar configurations by Arndt et al. [20] and Leroux et al. [21],
iv. The comparison between the present numerical results with the peer numerical simulations presented for the same test case at the 5th International Symposium on cavitation

1 Description of the Numerical Model

1.1 Physical Model of Cavitation. The present work applies a single-fluid model: the fluid density ρ varies in the computational domain according to a barotropic state law $\rho(P)$ that links the density to the local static pressure (Fig. 2). When the pressure in a cell is higher than the neighbourhood of the vapor pressure P_{vap} $[P > P_{vap} + (\Delta P_{vap}/2)]$, the fluid is supposed to be purely liquid. The entire cell is occupied by liquid, and its density ρ_l is calculated by the Tait equation [22],

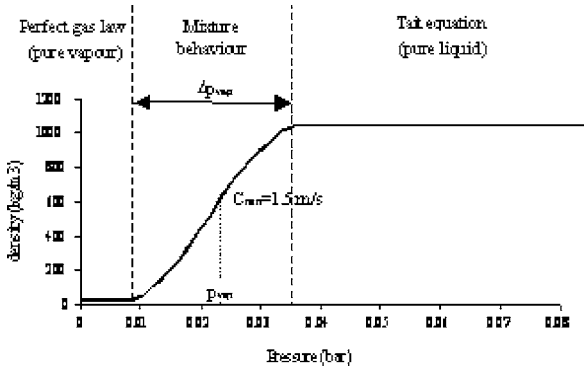

Fig. 2 Barotropic state law ρ(P). Water 20°C.

$$\frac{\rho}{\rho_{ref}} = \sqrt[n]{\frac{P + P_0}{P_{ref}^T + P_0}} \tag{1}$$

where $P_{ref}^T = P_{outlet}$ and $\rho_{ref} = \rho_{loutlet}$ are reference pressure and density considered at the outlet of the computational domain, and for water $P_0 = 3 \times 10^8$ Pa, $n = 7$.

If the pressure is lower than the neighborhood of the vapor pressure $(P < P_{vap} - (\Delta P_{vap}/2))$, the cell is full of vapor and its density ρ_v is given by the perfect gas law,

$$\frac{p}{\rho} = \text{cons} \tag{2}$$

The thermal effects are neglected in the present study. This is a usual assumption in the case of cavitation in cold water, because the variation of P_{vap} due to the slight cooling of the flow in the vaporized areas (~1.4 Pa, according to [23]) is negligible in front of the Δp_{vap} range represented in Fig. 2 (~3000 Pa).

Between purely vapor and liquid states, the cell is occupied by a liquid/vapor mixture, which is considered as one single fluid with a variable density ρ. This one is directly related to the void fraction $\alpha = (\rho - \rho_l)/(\rho_v - \rho_l)$ corresponding to the local ratio of vapor contained in this mixture.

To model the mixture state, the barotropic law presents a smooth link in the vapor pressure neighborhood, in the interval $\pm(\Delta P_{vap}/2)$. In direct relation with the range ΔP_{vap}, the law is characterized mainly by its maximum slope $1/C_{min}^2$, where $C_{min}^2 = \partial P/\partial \rho$. C_{min} can thus be interpreted as the minimum speed of sound in the mixture. Its calibration was done in previous studies [12,14]. The optimal value was found to be independent of the hydrodynamic conditions, and is ~1.5 m/s for cold water, with $P_{vap} = 0.023$ bar, and corresponding to $\Delta P_{vap} \approx 0.06$ bar. That value is applied for the computations presented hereafter.

In this approach, noncondensable gas present in the flow, such as air, is not taken into account. It is expected that this assumption may have only little effects in the upstream part of the sheet cavity, where the structure of the two-phase flow is mainly controlled by intense liquid vaporization. Conversely, it may induce significant discrepancies in the cavity wake, where the volume of air inclusion is not negligible because the void fraction is much lower.

Mass fluxes resulting from vaporization and condensation processes are treated implicitly by the barotropic state law; these mass fluxes are associated with the local variations of the mixture density, which result directly from the pressure variations. No supplementary assumptions are required. A pressure increase and decrease of the same amount dP make opposite variations of ρ, according to the barotropic state law, so vaporization and condensation fluxes are identical. Concerning the momentum fluxes, the model assumes that locally velocities are the same for liquid and for vapor; in the mixture regions vapor structures are supposed to be perfectly carried by the main flow. This hypothesis is often

assessed to simulate sheet-cavity flows, in which the interface is considered to be in dynamic equilibrium [10]. The momentum transfers between the phases are thus strongly linked to the mass transfers.

1.2 Numerical Resolution. The simulations are based on two-dimensional calculations of the flow. The mass and momentum equations are solved in the orthogonal frame of curvilinear coordinates (ξ, η), which leads to the following system of four equations:

$$S\frac{\partial}{\partial t}(\rho\Phi) + \nabla_\xi\left(\rho u\Phi - \Gamma_\Phi\frac{\partial\Phi}{\partial\xi}\right) + \nabla_\eta\left(\rho v\Phi - \Gamma_\Phi\frac{\partial\Phi}{\partial\eta}\right) = S_\Phi$$

$$\rho = F(C_p, \sigma) \tag{3}$$

where Φ stands either for 1, u, or v, Γ_Φ is the diffusion coefficient, u and v are the velocity components along coordinates ξ and η respectively, ∇_ξ and ∇_η are the physical components of the divergence operator along the curvilinear coordinates, S_Φ is the source term, C_p is the nondimensional pressure coefficient, and σ is the cavitation number. The energy equation is not solved, since thermal effects are presently neglected.

A finite volume discretization of these equations is used: the diffusive terms are calculated in a purely central manner, while the convection terms are calculated with the nonoscillatory second-order HLPA (hybrid linear/parabolic approximation) scheme proposed by Zhu [24]. This is a second-order scheme, which locally switches to first order, to prevent numerical oscillations in critical high-pressure or high-density gradient areas. The time integration is performed with a second-order implicit scheme

$$\frac{\partial(\rho\Phi)}{\partial t} = \frac{1.5\rho^{n+1}\Phi^{n+1} - 2\rho^n\Phi^n + 0.5\rho^{n-1}\Phi^{n-1}}{\Delta t} \tag{4}$$

The basis of the numerical resolution is the SIMPLE algorithm proposed by Patankar [25] for incompressible flow. Each physical time step is composed of successive iterations, which march the solution toward convergence. The initial scheme has been modified to treat as well the nearly incompressible parts of the flow as the highly compressible ones in the liquid/vapor mixture [5,14]. The main steps of a single iteration are listed hereafter:

- Resolution of the transport equations for the turbulent variables, and calculation of the turbulent viscosity ν_t
- Calculation of the estimated velocities $\mathbf{U}^*(u^*, v^*)$ from the momentum balance equations
- Calculation of the density ρ^* and its derivative $(\partial\rho/\partial P)$, according to the barotropic state law
- Resolution of the pressure correction equation. It is derived from the mass balance equation, which is discretized in each cell according to the following expression:

$$1.5\frac{S}{\Delta t}\rho_p^{n+1} = -\rho_e^{n+1}u_e^{n+1}\Delta\xi_e + \rho_w^{n+1}u_w^{n+1}\Delta\xi_w - \rho_n^{n+1}v_n^{n+1}\Delta\eta_n + \rho_s^{n+1}v_s^{n+1}\Delta\eta_s + S_\rho^n \tag{5}$$

where S is the cell area, P denotes the current cell, and e, w, n, and s denote the east, west, north, and south neighboring cells, respectively. S_ρ^n contains the explicit source terms resulting from the time discretization.

To obtain the final pressure correction equation, velocities u and v are replaced by u^*+du, v^*+dv, respectively, while ρ is replaced by $\rho^*+d\rho$. Thus, the expression of the pressure correction equation yields not only velocity variations $\mathbf{dU}(du, dv)$, but also supplementary terms involving variations $d\rho$. The term $\mathbf{dU}$ is derived from a simplified differential form of the momentum balance equation, while $d\rho$ is written as

$$d\rho_{i,j} = \left(\frac{\partial\rho}{\partial P}\right)_{i,j} dP_{i,j} \tag{6}$$

- When the pressure correction dP is obtained, not only the velocity and the pressure, but also the density values are corrected, according to the following expression:

$$\rho = \rho^* + \left(\frac{\partial\rho}{\partial P}\right)dP \tag{7}$$

Densities obtained from Eq. (7) may be outside from the physical range [0, 1], because of the high local values of $\partial\rho/\partial P$ in the two-phase mixture. Nonphysical values are thus corrected, and a supplementary loop over the pressure correction step is performed until all values of the void ratio are obtained inside their physical range [0, 1].

1.3 Turbulence Model. Most of the simulations of cloud cavitation in turbulent flow require a special attention to the model of turbulence to be paid [12–15]. Indeed, using a standard two-equation turbulence model leads to a complete stabilization of the flow, whereas in experiments a periodical self-oscillation behavior involving large vapor cloud sheddings is observed. This discrepancy is mainly due to the overestimation of the turbulent dissipation in the cavity downstream end, which stops prematurely the reentrant jet and thus inhibits the flow unsteadiness. In the case of the present physical cavitation model, Coutier-Delgosha et al. [18] have suggested that taking into account the effects of the mixture compressibility in the turbulence model may be necessary to obtain the correct periodical behavior of the cavity. A simple correction of the k-ε RNG model, initially proposed by Reboud et al. [12], was shown to enable a substantial improvement of the simulations. This correction can be applied directly in the expression of the turbulent viscosity by writing it $\mu_t = f(\rho)\ C_\mu\ k^2/\varepsilon$ instead of $\mu_t = C_\mu\ k^2/\varepsilon$ for a single phase flow. The function $f(\rho)$ is expressed as follows:

$$f(\rho) = \rho_v + (1-\alpha)^n(\rho_l - \rho_v) \tag{8}$$

with $n=10$.

The function f is then equal to ρ_v or ρ_l in the regions containing, respectively, pure vapor or pure liquid, but it decreases rapidly toward ρ_v for intermediate void ratios. This modification was applied previously in several configurations (Venturi type sections, foil sections, cascade of hydrofoils) and the results of the simulations were found in fair agreement with the unsteady flow properties obtained in experiments [26]. A similar improvement was achieved by using the corrections proposed by Wilcox [27] in his k-ω model to modelize compressible fluids.

The modified k-ε RNG turbulence model is applied in the computations presented hereafter. All parameters of the model, excepted the function $f(\rho)$, are set to the value proposed by Orszag [28].

1.4 Grid, Boundary, and Initial Conditions. The computational domain is consistent with all the indications given in the workshop (Fig. 3(*a*)). The shape of the 2D foil section is given by

$$\frac{y}{c} = a_0\sqrt{\frac{x}{c}} + a_1\frac{x}{c} + a_2\left(\frac{x}{c}\right)^2 + a_3\left(\frac{x}{c}\right)^3 + a_4\left(\frac{x}{c}\right)^4 \tag{9}$$

with $a_0=0.11858$, $a_1=-0.02972$, $a_2=0.00593$, $a_3=-0.07272$, and $a_4=-0.02207$.

A 630×50 C-type orthogonal mesh is used. Most of the cells are located around the foil, and a contraction of the grid is applied in its upstream part, to obtain an especially fine discretization of the areas where cavitation is expected (Fig. 3(*b*)). The nondimensional distance to solid walls y^+ is imposed between 30 and 50, since standard "log-law" wall functions are applied.

Standard boundary conditions for incompressible flow are applied: the velocity is imposed at the inlet ($V_{\text{ref}}=6$ m/s in the

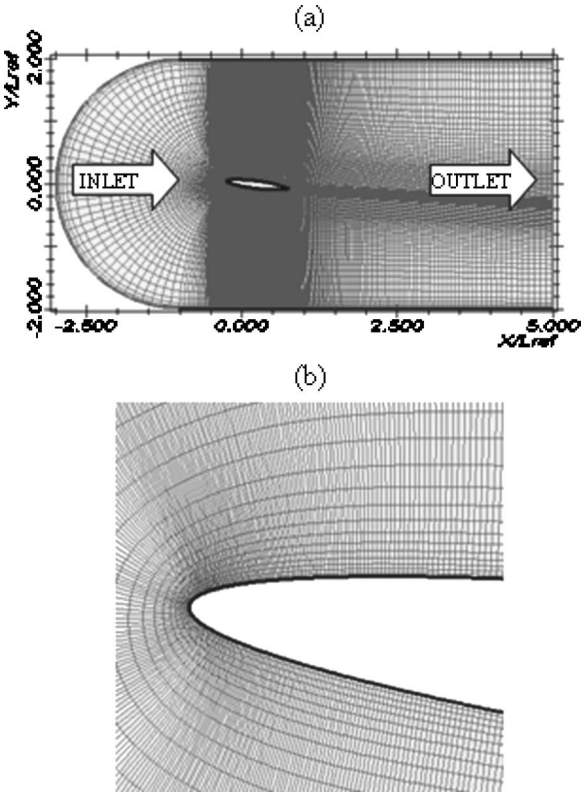

Fig. 3 (*a*) **Computational domain,** (*b*) **Zoom at the foil leading edge**

present case) and the pressure is fixed at the domain outlet. To start unsteady calculations, the following numerical procedure is applied: first of all, a stationary step is carried out, with an outlet pressure high enough to avoid any vapor in the whole computational domain. The flow obtained at convergence is the noncavitating result that will be detailed hereafter. Then, the pressure is lowered slowly at each new time step, down to the value corresponding to the desired cavitation number σ. Vapor appears during the pressure decrease. The cavitation number is then kept constant throughout the computation.

1.5 Numerical Parameters. Calculations are performed with nondimensional variables based on the following reference parameters:

$$\mathbf{U_a} = \frac{\mathbf{U}}{\mathbf{V_{ref}}} \quad V_{\text{ref}} = 6 \text{ m/s}$$

$$\rho_a = \frac{\rho}{\rho_{\text{ref}}} \quad \rho_{\text{ref}} = \rho_{\text{liquid}} = 1000$$

$$C_p = \frac{P - P_{\text{out}}}{1/2\rho_{\text{ref}} V_{\text{ref}}^2} \quad P_{\text{out}} = P_{\text{domain outlet}}$$

$$\sigma = \frac{(P_{\text{ref}} - P_{\text{vap}})}{1/2\rho_{\text{ref}} V_{\text{ref}}^2} \quad P_{\text{vap}} = 2000 \text{ Pa}$$

$$T_a = \frac{T}{T_{\text{ref}}} \quad T_{\text{ref}} = \frac{l_{\text{ref}}}{V_{\text{ref}}} = \frac{0.1}{6} = 0.0167 \text{ s}$$

The physical and numerical parameters applied for the simulations are given in Table 1. The choice of the minimum speed of sound $C_{\min}=1.5$ m/s, which determines the shape of the barotropic state law, has been validated in previous studies [12], on the basis of comparisons between calculations and experimental visualizations of a sheet cavity at the throat of a Venturi-type section. The ratio ρ_v/ρ_l used in the simulations has been also discussed previously in [14]; several values have been tested from 10^{-3} to 10^{-1}, and the influence of this parameter has been found negligible for values lower than 10^{-2}. This value is thus systematically used. The value of the nondimensional time step Δt is discussed in Sec. 1.6.

Table 1 Physical and numerical parameters

$C_{\min}$	Re	ρ_v/ρ_l	Inlet turbulence level	Δt
1.5 m/s	$0.6\ 10^6$	0.01	1%	0.005

1.6 Influence of Numerical Parameters. The effects of the numerical parameters on the results have been investigated in detail in a previous publication [14], devoted to the validation of the physical and numerical model. Influence of the grid size, of the time step, of the time order discretization, of the ratio ρ_v/ρ_l, of the turbulence model, and also of the minimum speed of sound $C_{\min}$ has been studied in a configuration of unsteady cavitation in a Venturi-type section. The values of the numerical parameters presented in Sec. 1.5 are consistent with the conclusions of this previous work.

To confirm that the results depend neither on the mesh size nor on the time step value in the present test case, the influence of these two parameters has been tested. Four C-type grids have been used, with respective sizes 200×30, 410×40, 630×50, and 1000×80. All other parameters are set to the value given in Sec. 1.5. Three time steps were also tested with the 630×50 grid. A single case has been considered, with $\sigma=0.9$, $\alpha=7$ deg, and $V_{\text{ref}}=6$ m/s. These conditions lead to unsteady cloud cavitation with periodical large vapor cloud shedding, as will be detailed in Sec. 3.3. The duration of the simulations is $75T_{\text{ref}}$, where T_{ref} is representative for the time necessary for the flow to cover a distance equal to the foil length with the speed V_{ref}. The attention is focused here on the influence of the two numerical parameters on the mean vapor volume, its standard deviation, and also on the mean frequency of the vapor shedding. These three values are obtained from the last $65T_{\text{ref}}$ of simulation: the first $10T_{\text{ref}}$ are not taken into account to avoid the influence of the initial transient growing of the cavity.

Additional short calculations have been performed to estimate for each grid size and each time step the cavitation number $\sigma_{\text{inception}}$ corresponding to cavitation inception on the foil suction side. Only the case $\alpha=7$ deg, and $V_{\text{ref}}=6$ m/s has been considered for this test.

The results are presented in Table 2. Nearly no influence of the numerical parameters on $\sigma_{\text{inception}}$ is observed, thus far the mesh is not too coarse: for the three finest meshes and the three time steps, $\sigma_{\text{inception}}=3.6$ is obtained. The tests performed at $\sigma=0.9$ exhibit a more significant influence of both parameters: the mean vapor volume for example increases continuously with the grid size. However, the difference between the values obtained with the two finest grids is $<10\%$. This is also the case for the standard deviation, which confirms that the mesh composed of 650×50 cells is a reasonable choice. The oscillation frequency is nearly constant, with the exception of the very coarse mesh configuration. Concerning the time step Δt, decreasing its value does not influence the frequency, but it leads to an increase of both the mean vapor volume and its standard deviation. However, the difference between the values obtained with $\Delta t=0.005$ and $\Delta t=0.002$ does not exceed 12%, which makes $\Delta t=0.005$ a convenient choice.

2 Experimental Setup

The experiments were carried out in the Ecole Navale Cavitation Tunnel, fitted with a 1 m long and $h=0.192$ m wide square cross test section. The geometry of the hydrofoil is the one pro-

Table 2 Influence of the grid size and the time step on the results (V_{ref}=6 m/s, α =7 deg)

Grid size	Time step Δt	σ = 0.9			$\sigma_{inception}$
		Mean vapour volume ($\times 10^{-4}$ m^3)	Standard deviation ($\times 10^{-4}$ m^3)	Oscillation frequency (Hz)	
200×30	0.005	1.04	0.76	7.7	3.4
410×40	0.005	2.24	1.23	6.7	3.6
630×50	0.005	2.52	1.47	6.5	3.6
1000×80	0.005	2.45	1.54	6.6	3.6
630×50	0.01	2.31	1.08	6.6	3.6
630×50	0.002	2.62	1.65	6.4	3.6

posed for the numerical workshop (see Eq. (5)), and its material is polished stainless steel. The chord length is l_{ref}=100 mm, and the test section dimension is $h \times b = 192 \times 192$ mm^2. This leads to a confinement parameter h/l_{ref}=1.92 different from h/l_{ref}=4 suggested for the workshop and applied in the numerical simulations. The axis of rotation is 37.5 mm downstream from the leading edge, and the distance between the inlet of the test section and the center of rotation is 420 mm. A regulation system sets the pressure and the velocity in the test section to prescribed values, in order to obtain the desired cavitation number σ. In the experiments, a 7 deg incidence angle was applied. The velocity was set to a constant value of 6 m/s, and the pressure P_{ref} was varied to obtain various values of σ in the range 0.5–3.5. The reference pressure P_{ref} was measured from a wall-pressure transducer located upstream of the hydrofoil at a distance of 215 mm from the axis of rotation.

Most of the experimental uncertainty concerns the flow conditions, i.e., the inlet mean flow velocity, the reference pressure in the test section, and the angle of attack. The conditions are regulated with 2% and 3% precision, respectively, for V_{ref} and P_{ref}, which leads to a relative uncertainty $\Delta\sigma/\sigma = \pm 7\%$. Moreover, during the experiments, care was taken to record the samples at the prescribed values of σ, with a variability $\Delta\sigma = \pm 0.02$. The uncertainty on the angle α is mainly due to the uncertainty on the zero angle of incidence (taken as a reference), which is $\Delta\alpha = \pm 0.1$ deg.

The inception (desinence) condition was determined by progressively increasing the angle of incidence (with σ constant) until cavitation appeared (totally disappeared). The criterion for cavitation detection was to obtain a thin band extending all along the span of the hydrofoil. In some cases, cavity lengths were measured using the laser sheet of the PIV system (Fig. 4). The uncertainty on the cavity length is due to the sheet cavity fluctuation during image capture. It is found to be $\Delta l/1 - 5\%$ for stable sheet cavities ($l/l_{ref} < 0.2$), and $\Delta l/1 - 10\%$ in the case of unsteady cloud cavitation.

Lift and drag were also measured in noncavitating conditions using a resistive gauge hydrodynamic balance calibrated in the laboratory.

PIV (particle image velocimetry) measurements were performed around the foil section in noncavitating conditions. The region of interest (above the foil suction side) was illuminated by a vertical laser light sheet (YAG laser). Two images of tracer particles are recorded successively with a CCD camera, and a cross correlation is performed with the DANTEC software. Each interrogation area is composed of 32×32 pixels. The mean velocities are derived from 400 pairs of images.

Unsteadiness of the sheet cavity was studied by spectral analysis of wall pressure fluctuations downstream from the foil section. Pressure fluctuations were recorded with a PCB Piezotronics transducer model 106B50 (15.69 mm dia) mounted flush on one of the tunnel vertical walls in the foil wake, 650 mm downstream from the trailing edge.

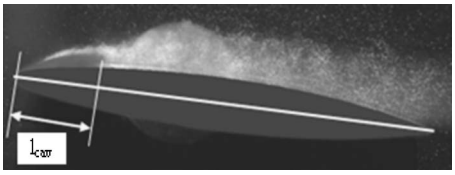

Fig. 4 Measurement of the cavity length, from the distance between the inception point and the closure of the cavity, both projected on the chord. (Here, σ=2.0 and l/l_{ref}=0.175).

3 Results

For a 7 deg angle of attack, the flow around the foil has been investigated both numerically and experimentally for a large range of inlet pressure. Additional measurements and short calculations have been also performed for various angles of attack, in order to focus on cavitation inception. At 7 deg incidence, four main flow configurations have been observed, as well in the experiments as in the simulations. They are given hereafter with the corresponding ranges of σ derived from the numerical simulations:

- Noncavitating conditions ($\sigma > 3.5$)
- Nearly steady sheet cavitation, with no periodical oscillations ($2 \leq \sigma \leq 3.5$)
- Unsteady behavior with large periodic cloud sheddings ($0.8 \leq \sigma \leq 1.7$)
- Severe cavitating conditions close to supercavitation (σ =0.5)

The results obtained in these different situations are presented in the present section, and the ability of the numerical model to simulate the experimental cavitating flow is discussed.

3.1 Noncavitating Flow Field. The noncavitating pressure field (Fig. 5(*a*)) exhibits a much localised low-pressure area on the foil suction side. A slight flow detachment can be seen at the leading edge (Fig. 5(*b*)). The velocity magnitude field obtained in the simulation is compared in Fig. 6 to the one obtained with the PIV measurements. Identical color scales are applied in Figs. 6(*a*) and 6(*b*). Several disagreements can be observed: the flow detachment at the leading edge is not obtained with the PIV measurements, and small-scale structures seem to be detected close to the foil surface only in the experiments. However, the PIV measurements close to the foil wall must be considered, circumspectly, because of the lack of data and too large interrogation areas. Apart from this discrepancy, a fair general agreement is obtained. This is confirmed by the comparison of the lift coefficients: C_L=0.65 was found experimentally for a 7 deg incidence angle and V_{ref} =6 m/s, versus C_L=0.66 given by the model. It suggests that the flow around the foil section in non cavitating conditions is satisfactorily predicted by the calculation.

3.2 Nearly Steady Sheet Cavitation. When the cavitation number is decreased in the simulations below 3.7, a small vaporized area is observed on the foil suction side. This cavity remains nearly stable until its length reaches at least 0.2 l_{ref}, for $\sigma \approx 2$. In the experiments, cavitation inception is observed when the cavitation number equals 3.5. It consists of separate vapor bubbles,

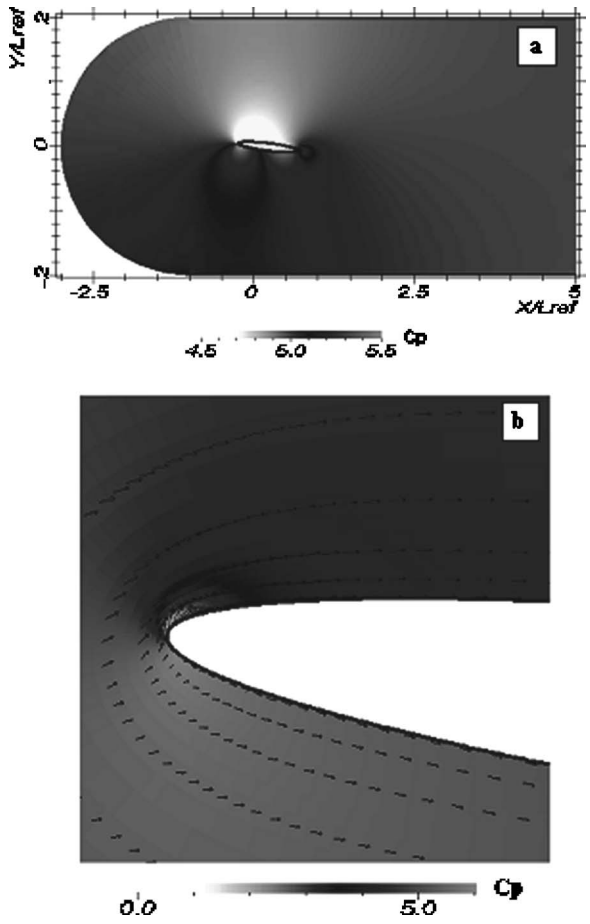

Fig. 5 Pressure fields around the foil in non-cavitating conditions. (Velocity vectors drawn only 1 cell over 5 along the foil, and 1 cell over 3 perpendicularly to the foil.)

which rapidly turn into a small strip along the foil span at the leading edge when the pressure is still slightly decreased. Figure 7 shows the shape of the sheet cavity for $\sigma=3.5$ and $\sigma=3$. A general view of the experimental situation is given first, and then two side views focusing on the foil leading edge are derived from the simulation and from the experiments, respectively. Significant discrepancies are observed concerning the inception point (more upstream in the simulation than in the experiments) and the cavity wake (which can be seen in the experiments, but not in the calculation). The first discrepancy may be related to the surface roughness, which is not taken into account in the simulation. It may also be related to the cavitation model, which does not incorporate any relaxation time for the vaporization process (the density is directly related to the pressure level). The second discrepancy suggests that the present cavitation model, although it reproduces well the physical mechanisms of unsteady cavitating flows (see the next section), is not so efficient to predict the subtle features of the cavity wake. Indeed, this flow area is characterized by a very low void fraction, and a significant influence of the air inclusions is expected, but the numerical model does not take it into account.

Inception and desinence cavitation numbers have been measured for other incidence angles ranging between 4 deg and 8 deg. The experiments have been conducted successively in the case of positive and negative angles of attack, in order to detect some differences between the two sides of the foil. The same tests have been performed numerically, for cavitation inception and top side cavities, only. All the results are reported in Fig. 8. No significant difference between bottom side and top side cavities is obtained. A small hysteresis effect is observed for angles of attack higher

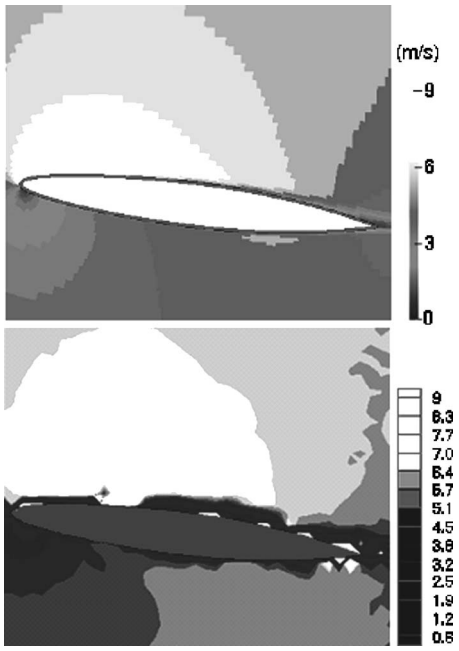

Fig. 6 Velocity magnitude obtained by simulation (top view) and PIV measurements (bottom view), $\alpha=7$ deg, $V_{ref}=6$ m/s, $\sigma=4$

than 6 deg, but it may be related to the visual detection of cavitation inception and desinence. A fair agreement between the experiments and the simulations is obtained at all incidence angles. It confirms that the pressure level on the foil suction side, which mainly governs the inception of cavitation, is correctly reproduced by the numerical model.

3.3 Cloud Cavitation. Unsteady cavitation including large vapor cloud shedding is obtained when the cavitation number is decreased below 1.7. These flow conditions, which are usually called partial cavity oscillations, are observed until the cavity downstream end becomes close to the foil trailing edge, i.e., until the cavitation number is decreased down to ~0.7. The results presented hereafter correspond to $\sigma=0.9$. The simulation was performed during $75T_{ref}$, i.e., 1.25 s. The frequency of the oscillations is ~6.5 Hz, which gives a period $T=0.15$ s and a Strouhal number (based on the maximum length l of the attached cavity) $St_l=0.076$.

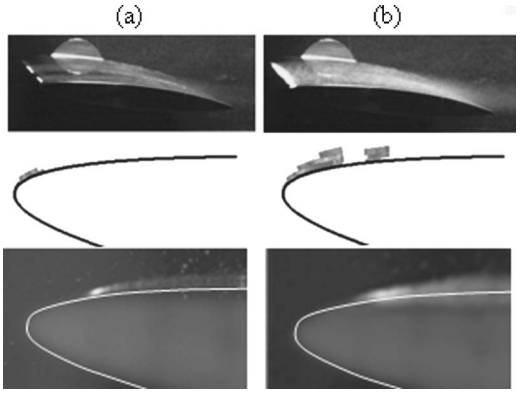

Fig. 7 Size of sheet cavitation for (*a*) $\sigma=3.5$, (*b*) $\sigma=3$, $V_{ref}=6$ m/s, $\alpha=7°$. From top to bottom: general view of the foil (experiment), side view at the leading edge (simulation), side view at the leading edge (experiment).

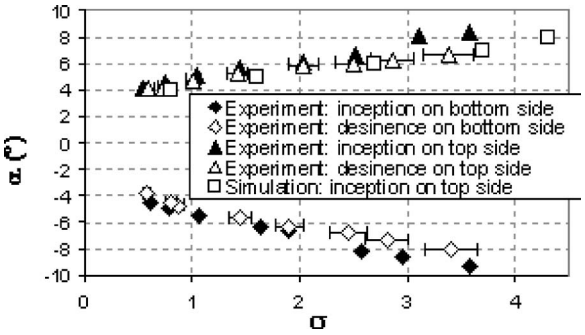

Fig. 8 Conditions of cavitation inception and desinence

Figure 9 presents the time evolution of both the cavity shape and the vapor volume in the computational domain. The upper image shows the minimum density (indicated by the color) in each section (denoted by the position X/l_{ref} in ordinate) as a function of the time (in abscissa). The example on the left corresponds to the time $T/T_{ref}=38.2$. Thus, this image illustrates the oscillatory behavior of the cavitation sheet, including the vapor cloud shedding. Although the evolution of the vapor volume is not so regular, the same periodical evolution can be observed.

One complete cycle is detailed in Fig. 10, to show the successive steps of the unsteady process. The flow arrangement at step 6 is compared in Fig. 11 with an experimental visualization performed in similar flow conditions ($V_{ref}=6$ m/s, $\sigma=1$), to display

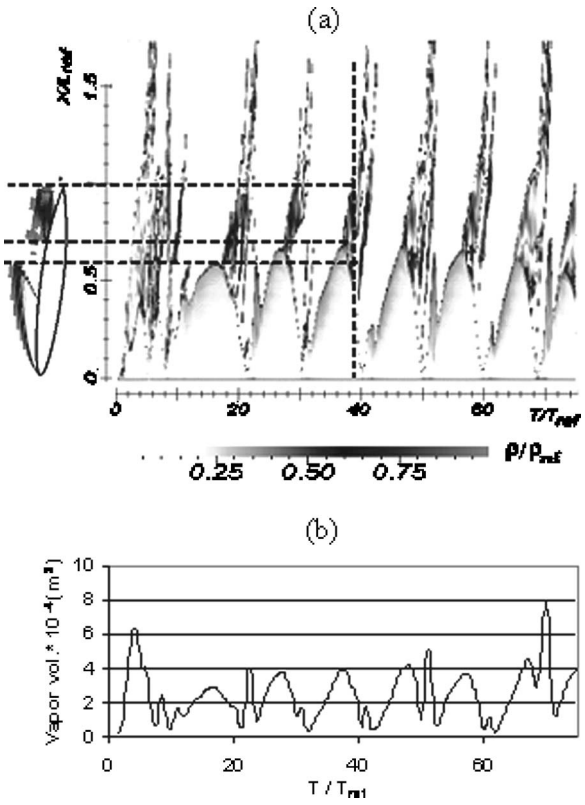

Fig. 9 Cloud cavitation ($V_{ref}=6$ m/s, $\alpha=7$ deg, $\sigma=0.9$). (*a*) Time evolution of the cavity length: the time is reported in abscissa, and the X position in the cavitation tunnel is graduated in ordinate. The grey levels represent the density values, as indicated under the figure (pure liquid and pure vapor are both in white). At a given point in time and position, the grey level indicates the minimum density in the corresponding cross section of the cavitation tunnel. (*b*) Time evolution of the vapor volume.

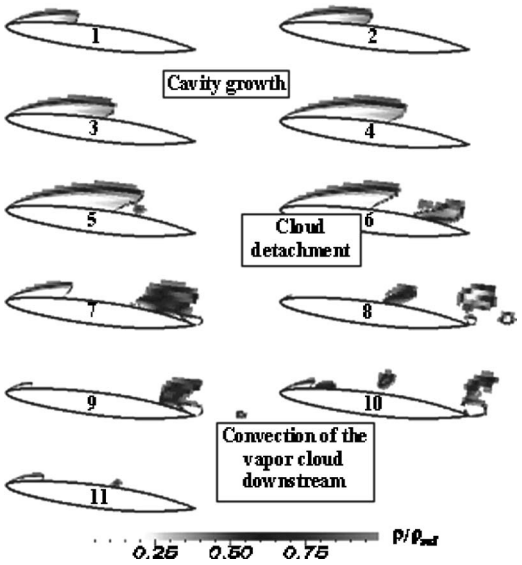

Fig. 10 One cycle of cloud cavitation (14 ms between two pictures, $V_{ref}=6$ m/s, $\alpha=7$ deg, $\sigma=0.9$, pure liquid and pure vapor both in white)

the satisfactory qualitative agreement between the two results. Discrepancies can still be observed in the transition between the attached cavity and the cloud of vapor, which is very sharp in the simulation, whereas it is indistinct in the experiments. It confirms that the numerical model does not reproduce correctly, during the collapsing process of the bubbles, the flow areas characterized by a very low void fraction. However, the mechanisms of the unsteady behavior are well simulated.

The maximum length of the attached cavity can be estimated to $l/l_{ref}=0.7$ and the maximum cavity thickness is almost equal to the foil maximum thickness (considering that the interface of the cavitation sheet corresponds to a void ratio $\alpha_v=10\%$). This maximum thickness is obtained almost at mid chord of the foil section, just before the detachment of the cavity rear part. The mean vapor volume per unit meter span (after the initial transient) equals 2.5×10^{-4} m^3.

The evolutions of the lift and drag coefficients are drawn in Fig. 12. The variations of the pressure coefficient on the foil suction side are also reported for three positions: $x/l_{ref}=0.1$, 0.5, and 0.9. The two main sequences of the cycle (growth of the cavity, and convection of the detached cloud of vapor) can be easily seen on the five charts. Sequence 1 corresponds to a low pressure at $x/l_{ref}=0.1$, and a progressive decrease of the pressure at $x/l_{ref}=0.5$, as soon as the cavity length increases. On the contrary, the pressure remains high at $x/l_{ref}=0.9$, since the maximum length of

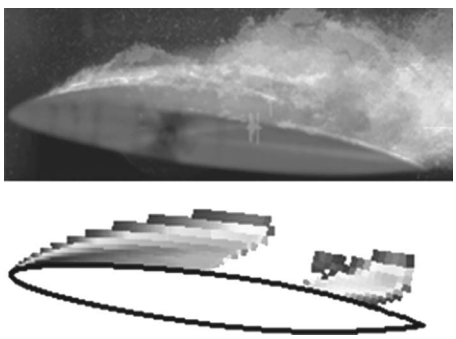

Fig. 11 Step 6 of the cloud cavitation cycle. Comparison between the experiment (top view) and the simulation (bottom view).

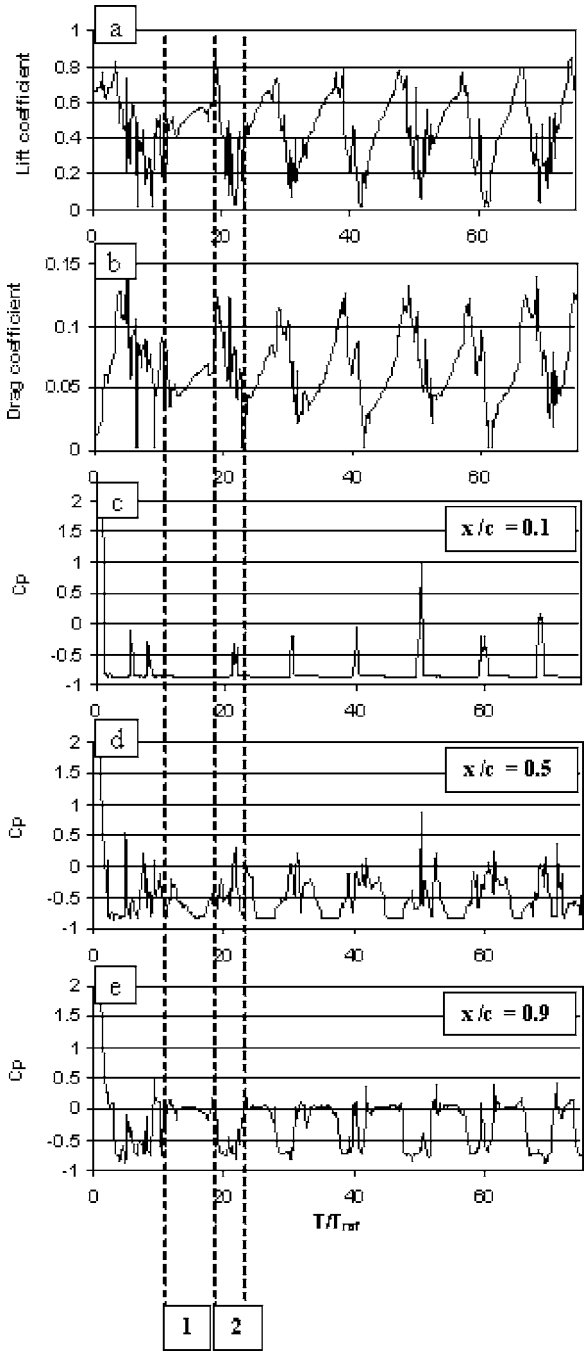

Fig. 12 Evolution of (*a*), (*b*) the lift and drag coefficients and (*c*), (*d*), (*e*) the pressure coefficients on the foil suction side at stations x/c=0.1, 0.5, 0.9. (Numerical result, V_{ref}=6 m/s, α=7 deg, σ=0.9). The dashed lines delimit one sequence "1" (cavity growth) and one sequence "2" (convection of the vapor cloud).

the cavity is x/l_{ref}=0.7. During sequence 2 the pressure increases in the first part of the foil (because no vapor is present anymore), while the passage of the cloud of vapor is detected in x/l_{ref}=0.9.

The lift and drag coefficients both slowly increase during the development of the sheet cavity. Then, C_L suddenly drops at the beginning of sequence 2, whereas C_D falls a bit later, during the convection of the vapor cloud. Indeed, the lift is directly linked to the length of the attached cavity on the foil section, while detached sheddings continue to affect the drag. Time-averaged values of C_L and C_D are respectively 0.45 and 0.07. This exhibits a

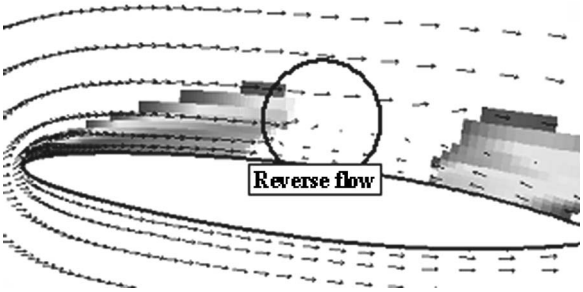

Fig. 13 Reverse flow during the cavity break-off. (Numerical result, V_{ref}=6 m/s, α=7 deg, σ=0.9.)

significant decrease of the foil efficiency in cavitating conditions: the values in noncavitating conditions were C_L=0.66 and C_D=0.015.

The unsteady behavior observed in the present case is due to a re-entrant jet that flows periodically upstream close to the foil and progressively detaches the rear part of the cavity from its upstream part (Fig. 13). It results in the cavity break-off and the convection of the cloud of vapor that was observed in Fig. 10.

Figure 14 shows successively the evolutions of the nondimensional parameters l/l_{ref}, St_c, and St_l according to the parameter $\sigma/2\alpha$, which was proposed by Acosta [29] in his linearized theory of partial cavitation on flat plate hydrofoils. More recently, Arndt et al. [20] have shown that the value $\sigma/2\alpha$=4 was the limit between two different types of partial cavity oscillations, characterized by different evolutions of the Strouhal numbers St_c and St_l: for $\sigma/2\alpha>4$, these authors found that the flow instability was mainly governed by the reverse flow under the cavity, leading to Strouhal numbers $St_l \approx 0.3$, as often reported for cloud cavitation. On the other hand, for $\sigma/2\alpha<4$, they found much lower frequencies, relatively insensitive to the variations of σ, and leading to Strouhal numbers St_c close to 0.2/0.25. In this situation, Arndt et al. suggested that shock wave phenomena were predominant in the mechanisms of the flow instability. In the present study, a similar behavior is obtained, as well in the simulations as in the experiments: for small cavities, corresponding to $\sigma/2\alpha>4$, the frequency increases nearly linearly with σ, and Fig. 14(*c*) shows that St_l remains close to 0.2/0.3. Figure 14(*b*) displays a fair agreement between the present results and Arndt's experiments for this situation. For larger cavities, i.e., $\sigma/2\alpha<4$, a nearly constant frequency is obtained in the simulations and in the experiments, leading to $St_c \approx 0.1$. This value is much lower than in the previous case of small cavities, which indicates a modification of the periodical oscillation cycle. This effect has been investigated recently by Leroux et al. [21], and it has been shown that the modification consists of a supplementary step in the cycle: after the main vapor cloud shedding a second growth and decrease of the cavity is observed, without any substantial shedding. This step delays the next shedding and thus makes the instability frequency notably decrease. This is slightly observed in the present simulation for σ=0.9 (i.e., $\sigma/2\alpha$=3.7) in Fig. 9: a fast pulsation of the cavity occurs after each cloud shedding, for example at t/T_{ref}=40, 50, 60. It is also obtained on the pressure signal at station x/c=0.5, and on the drag coefficient evolution (see Fig. 12).

The value St_c=0.1 is significantly lower that the one reported by Arndt et al. [20], which was about 0.2/0.25. It suggests that the geometry of the foil (which is slightly different in the present case from the NACA 0015 tested by Arndt) and /or the flow confinement have some influence on the instability frequency for $\sigma/2\alpha<4$. Conversely, $St_l \approx 0.25/0.3$ is systematically obtained for $\sigma/2\alpha>4$, whatever the foil geometry is [3,30–32].

3.4 Severe Cavitating Conditions. For a cavitation number of <0.7, nearly the whole foil surface is covered by sheet cavita-

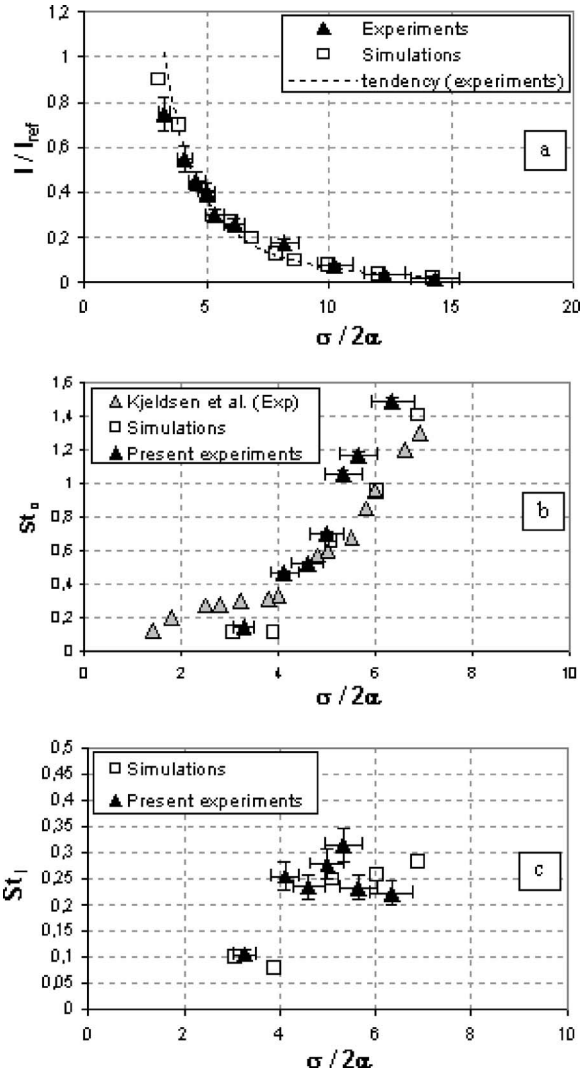

Fig. 14 Comparison between the experiments and the simulations, V_{ref}=6 m/s, α=7 deg. (*a*) Maximum cavity length l/l_{ref} (*b*) Strouhal number St_c based on the chord l_{ref} (*c*) Strouhal number St_l based on the maximum cavity length *l*.

tion on the suction side. For σ=0.55, cavitation is obtained also on the foil pressure side. It is localised on the rear part of the foil and its behavior is almost stable (Fig. 15(*a*)). On the suction side the cavity entirely covers the foil. Although the cavitation sheet is more stable than in the previous case, significant small-scale fluctuations are predicted by the model in its rear part (Fig. 15(*b*)). The simulation was performed during $50T_{ref}$.

No characteristic frequency can be observed here. Nevertheless, little vapor cloud shedding occurs more or less regularly at the foil trailing edge. Figure 16 presents the successive shapes of the cavitation sheet during such a shedding. The maximum cavity length is $l \approx l_{ref}$, and its maximum thickness (still considering that the interface corresponds to α_v=10%) is ~1.5 the maximum thickness of the foil.

The evolutions of the lift and drag coefficients are reported in Fig. 17. They only slightly fluctuate around their time-averaged value, respectively C_L=0.2 and C_D=0.065. In comparison with the values obtained in Sec. 3.3, the decrease of the cavitation number has almost no influence on C_D, while on the contrary C_L is considerably reduced again.

The pressure coefficients on both sides of the foil are almost constant even at the trailing edge, as can be seen on the evolution of C_p at x/l_{ref}=1 reported in Fig. 17. However, the time evolution

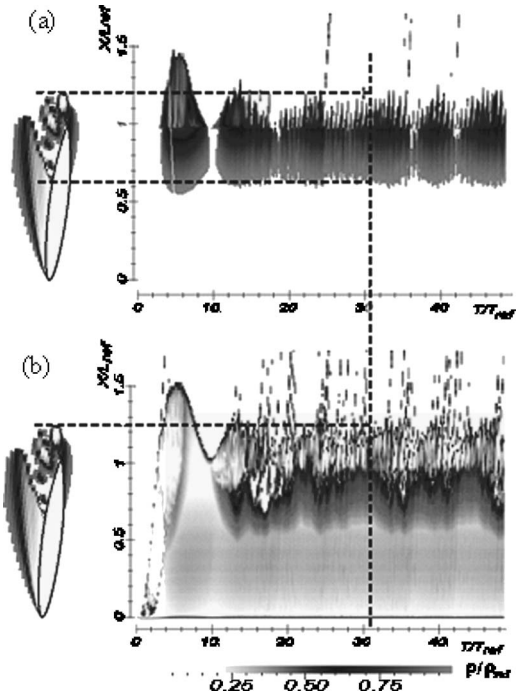

Fig. 15 Time evolution of large cavity (V_{ref}=6 m/s, α=7 deg, σ=0.55): (*a*) on the foil pressure side, (*b*) on the foil suction side

of the vapor volume confirms that the flow is not steady: the magnitude of the vapor volume variations remains of the same order of magnitude ($\pm 10^{-4}$ m^3) than in the previous configuration of cloud cavitation.

The time-averaged value of the vapor volume is notably higher than previously: 7.1×10^{-4} m^3 versus 2.5×10^{-4} m^3 reported in Sec. 3.3. This is mainly due to the stabilization of a large part of the sheet cavity.

The small-scale unsteadiness of the flow is also detected on the vorticity field (Fig. 18). Regular vortices appear in the wake of the trailing edge. It suggests that a periodical shedding of vortices may be associated with the apparently nonorganized fluctuations of the cavity downstream part. The evolution of the vorticity downstream from the trailing edge at x/l_{ref}=1.3 confirms that the phenomenon is periodical, although the magnitude of the vortices is rather irregular (Fig. 19). The oscillation frequency results in a Strouhal number equal to 1.6, much higher than in the previous configuration of cloud cavitation.

4 Comparison to the Peer Numerical Results

4.1 Overview of Models. Eight contributions have been proposed in the numerical workshop of the 5th International Symposium on cavitation. All the results, including the present ones, were obtained without the knowledge of the experimental cavitating behavior of the foil. Several cavitation models were applied,

Fig. 16 Fluctuations of the cavity shape (V_{ref}=6 m/s, α=7 deg, σ=0.55). (30< T/T_{ref} <32, 0.5T_{ref} between two pictures.)

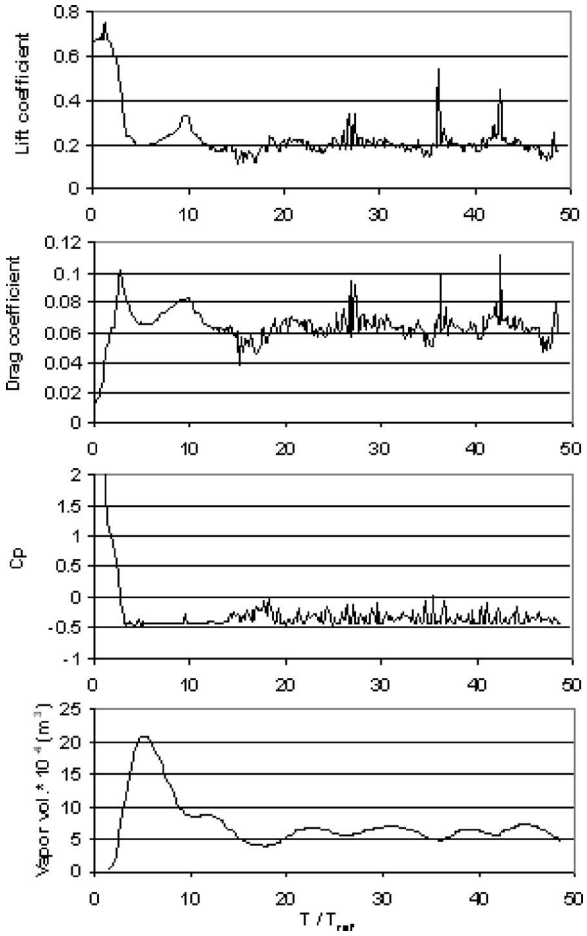

Fig. 17 Time evolutions of the lift and drag coefficients, the pressure coefficient at $x/l_{ref}=1$, and the vapor volume ($V_{ref}=6$ m/s, $\alpha=7$ deg, $\sigma=0.55$)

in association with several turbulence models. Various results were obtained at $\sigma_{downstream}=0.8$ and $\sigma_{downstream}=0.4$, ranging from completely steady sheet cavity to unsteady cyclic cloud cavitation. In the following discussion, "steady sheet cavity" means that no fluctuation is obtained in the cavitating flow, while "stable sheet cavity" means that the flow may fluctuate, but no periodical cavitation cycle is obtained, in opposition with "cyclic cloud cavitation."

A technical summary of the workshop is given in Table 3. Most of the quantitative results indicated in the eight papers are reported here, with the exception of the parameters that were almost identical in all the simulations. Some parameters, such as the mean vapor volume, are missing, because they were not systematically indicated in the papers. Some Strouhal numbers are not given because the sheet cavity fluctuations are not periodic (np) or because the sheet cavity is completely steady (s).

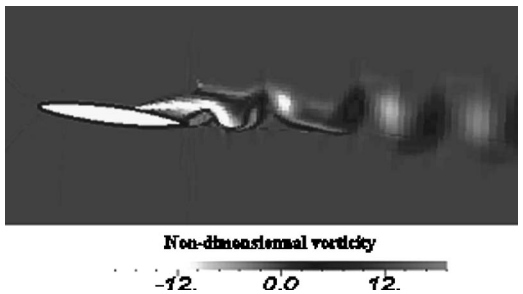

Fig. 18 Vorticity field at $T/T_{ref}=30$ ($V_{ref}=6$ m/s, $\alpha=7$ deg, $\sigma=0.55$)

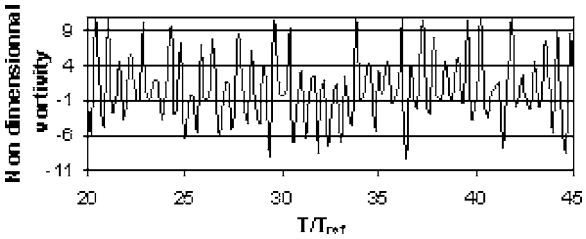

Fig. 19 Evolution of the vorticity at $x/l_{ref}=1.3$, $y=0$ ($V_{ref}=6$ m/s, $\alpha=7$ deg, $\sigma=0.55$)

Four main types of cavitation models have been applied:

- The homogeneous approach associated with a barotropic state law was used by Qin et al. [33], Pouffary et al. [15], and also in the present simulations. The state law is either in the two last cases the simple one initially proposed by Delannoy and Kueny [5], or in [33] the polynomial one developed by Song and He [34]. In [15], the pure liquid is considered as fully incompressible, while compressible effects are taken into account in [33] and also in the present work.
- The homogeneous approach associated with a convection/production equation for the void fraction α was applied by Saito et al. [35], Wu et al. [16], and Kunz et al. [19], with various formulations of the production term (see Table 3). Note that in [16] and [19], the classical expression $\rho=\alpha\rho v+(1-\alpha)\rho l$ is used to derive the mixture density from the void fraction, whereas Saito et al. adopt a more complex state law involving not only α but also the local pressure.
- Kawamura and Saokoda [36] use a so-called sheet cavity model that is a combination of a level-set approach (to obtain the position of interfaces, which delimit areas characterized by a pressure equal to P_{vap}) with a homogeneous approach (in the rest of the domain). In the areas governed by the homogeneous model, the void fraction is obtained from the resolution of a simplified Rayleigh-Plesset equation.
- Kinnas et al. [37] use a boundary element method (BEM): the cavity shape is obtained iteratively by applying kinematic and dynamic boundary conditions at the cavity interface. This method is significantly different from the three previous ones because it focuses on the mean characteristics of the sheet cavity, whereas the other ones are supposed to reproduce the unsteady features of the flow, including cavitating areas detached from the foil.

In addition with these distinctions, various turbulence models have been also used:

- Most of the simulations are based on a RANS approach and a two-equation turbulence model such as k-ε [15,16,19], k-ε RNG (present work), or k-ω [36]. In most of the cases, modifications are applied to the standard model: the diminution of the turbulent viscosity initially proposed by Reboud et al. [12] is used by Pouffary et al. [15], and also for the present simulations. A filtered version of k-ε is applied by Wu et al. [16], and compared to the standard version from Launder and Spalding.
- An algebraic Baldwin-Lomax model is used by Saito et al. [35].
- Large eddy simulations (LES) models are used by Qin et al. [33] and Kunz et al. [19]. In this last case, it is associated with a RANS k-ε approach, yielding to a detached eddy simulation (DES) model. The DES model is an LES in the

Table 3 Results of the numerical workshop of the 5th International Symposium on Cavitation, Osaka, Nov. 2003

Authors	Cavitation model	Turbulence model	Type of result
Qin et al.	Barotropic state law ρ (P) (Song / compressibility of pure liquid)	LES	σ=0.8: Stable sheet cavity σ=0.4: Stable sheet cavity
Pouffary et al.	Barotropic state law ρ (P) (Delannoy)	RANS: k-ε model with modifications for cavitation	σ=0.8: cyclic cloud cavitation σ=0.4: Steady sheet cavity
Saito et al.	Equation of convection / production of α (production term from Sone and Sugimoto) + ρ = f(α, P)	Baldwin-Lomax with Degani-Schiff modification	σ=0.8: cyclic cloud cavitation σ=0.4: cyclic cloud cavitation
Wu et al.	Equation of convection / production of α (production term from Kunz or Senocak)	RANS: k-ε Launder and Spalding RANS: filtered k-ε	σ=0.8: cyclic cloud cavitation σ=0.4: cyclic cloud cavitation
Kawamura et al.	Sheet cavity model (see the paper)	RANS: k-ω	σ=0.8: cyclic cloud cavitation σ=0.4: stable sheet cavity
Kinnas et al.	Boundary Element Method	Potential solver + Boundary layer model	σ=0.8: steady sheet cavity σ=0.4: steady sheet cavity
Kunz et al.	Equation of convection / production of α (production term from Kunz)	RANS: k-ε DES (LES / RANS k-ε)	σ=0.8: cyclic cloud cavitation σ=0.4: cyclic cloud cavitation
Present results	Barotropic state law ρ (P) (Delannoy + compressibility of pure liquid and vapor)	RANS: k-ε RNG model with modifications for cavitation	σ=0.8: cyclic cloud cavitation σ=0.4: stable sheet cavity

Authors	No cavitation		$\sigma_{downstream}$ = 0.8						$\sigma_{downstream}$ = 0.4					
	C_L	C_D	l_l/l_{sf}	l/l_{sf}	C_L	C_D	St_l	V_{vap} (10^{-4} m^3)	l_l/l_{sf}	l/l_{sf}	C_L	C_D	St_l	V_{vap} (10^{-4} m^3)
Qin et al.	0.646		3.7%	22%	0.359		np		5.6%	62%	0.183		np	
Pouffary et al.	0.62	0.029	0	57%	0.456	0.078	0.091	1.85	0	150%	0.291	0.086	s	21.1
Saito et al.			0.17%	76%	0.417	0.064	0.25		0.37%	130%	0.160	0.057	0.25	
Wu et al.	0.060	0.007	0.75%	60%	0.52	0.008	0.09		0.98%	101%	0.256	0.009	0.21	
	0.052	0.005	0.74%	65%	0.46	0.007	0.08		0.85%	106%	0.208	0.008	0.22	
Kawamura et al.	0.67	0.014	0.5%	97%	0.537	0.086	0.15	3.17	0.3%	129%	0.22	0.23	np	10
Kinnas et al.			0	110%	0.73	0.146	s		0.7%	125%	0.24	0.08		
Kunz et al.	0.624	0.024	0.45%	103%	0.49	0.080	0.11	2.74	0.77%	128%	0.198	0.068	0.09	5.66
			0.5%	110%	0.50	0.097			0.84%	136%	0.171	0.069		7.53
Present results	0.66	0.015	0	70%	0.45	0.07	0.076	2.52	0	120%	0.2	0.065	np	7.1
Experiments	0.65		3%	70%			0.105		3.5%	> l_{sf}				

areas where the grid is fine enough, and it turns to the classical RANS approach elsewhere.

- Kinnas et al. [37] use a potential solver associated with a boundary layer model to include the viscous effects.

4.2 Results in Noncavitating Conditions. The lift coefficients obtained in noncavitating conditions are most of the time close to the experimental measurement C_L=0.65: all the results but one are in the range 0.6–0.67. Only the value obtained in [16] with the filtered k-ε model is significantly lower. It suggests that the results obtained in cavitating conditions with this model should be considered circumspectly. Concerning the draft coefficients, the results are spread over a larger range 0.005–0.029. It can be noticed that some results obtained with the same turbulence model are notably different: for example, the values C_D =0.029, 0.024, and 0.007 are obtained in [15,16,19] with the same standard k-ε model. It shows that the numerical treatment of the equations, i.e., the discretization and the algorithm, play also an essential role in the simulations. In this example, the calculations performed by [15] and [19] are based on dual time-stepping and preconditioning methods, whereas a pressure based method is used in [16]. Accordingly, the values obtained in [15] and [19] are relatively close, while the value reported in [16] is notably lower.

4.3 Results for $\sigma_{downstream}$=0.8. This first flow condition imposed in the numerical workshop corresponds in the present calculations to the case σ=0.9 reported in Sec. 3.3, i.e., $\sigma/2\alpha$=3.7. In the experiments performed in the IRENav cavitation tunnel, this outlet condition is obtained for $\sigma \approx 0.85$, i.e., $\sigma/2\alpha \approx 3.5$.

The results presented in the workshop generally exhibit a periodical unsteady behavior for $\sigma_{downstream}$=0.8. Two exceptions can be noted: Kinnas et al. [37] modelize a steady cavity, but this is inherent to the boundary element method that they use; thus, attention should focus on the comparison between their results and the mean characteristics of the sheet cavity. Qin et al. [33] obtain a stable cavity with only nonorganized fluctuations. It should be noted that these authors have obtained with their numerical model unsteady cyclic behaviors in a configuration of NACA0015 foil section, in close agreement with the experimental measurements [38]. The cavitation model used in [33] is similar to the one applied in the present study, so the turbulence models may be mostly responsible from the disagreement between the two results.

Figure 20 presents the spectral analysis of the pressure fluctuations in the foil wake for two values of $\sigma/2\alpha$. In the configuration $\sigma/2\alpha$=3.5, Fig. 20(a) shows that the behavior of the sheet cavity in the present experiments is clearly periodic with a Strouhal number $St_c = f \times l_{ref}/V_{ref}$=0.15, i.e., $St_l = f \times l/V_{ref}$ close to 0.1. In the configuration $\sigma/2\alpha$=4.1, Fig. 20(b) shows a shift of St_c, which becomes close to 0.45. Such a transition for $\sigma/2\alpha$=4 has been obtained previously with other foil sections by Arndt et al. [20] and Leroux et al. [21] as well in experiments as in simulations.

In the St. Anthony Falls Laboratory (SAFL) cavitation tunnel, strong periodic oscillations were measured in the range $3 < \sigma/2\alpha < 4$, with a Strouhal number $St_c \approx 0.2$, as reported by Qin [38]. Conversely, no significant periodic unsteadiness was clearly detected for $\sigma/2\alpha > 4$.

The reason for such a disagreement between the two cavitation tunnels is difficult to handle. However, the question of the flow confinement should be addressed, since it may have some significant influence on the flow behavior.

Most of the numerical simulations reported in Table 3 are in fair agreement with St_l=0.1: values obtained in [15,16,19,36] and also in the present work are in the range 0.075–0.15. The higher value

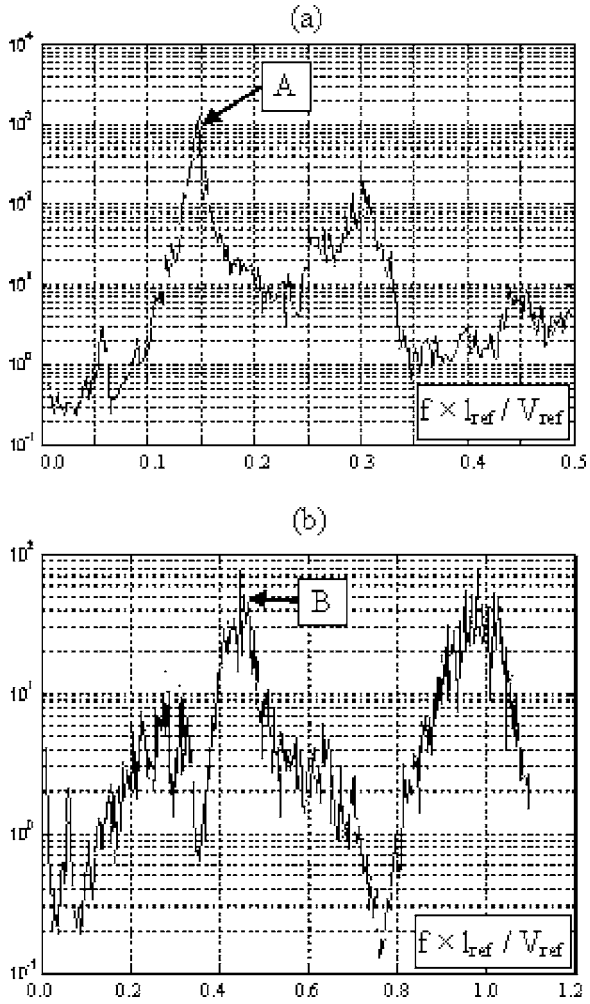

Fig. 20 Spectral analysis of the pressure fluctuations sampled at 6.5 chords downstream the foil trailing edge (*a*) $\sigma/2\alpha=3.5$, (*b*) $\sigma/2\alpha=4.1$

$St_l=0.25$ obtained by Saito et al. [35] may correspond to the experimental behavior observed in the present experiments for $\sigma/2\alpha>4$.

The values obtained for the maximum cavity length and the lift and drag coefficients are scattered into large ranges: 22–110% for l/l_{ref}, 0.36–0.73 for C_L, and 0.007–0.146 for C_D. The dispersion of l/l_{ref} is not surprising, since the attached part of the sheet cavity is sometimes difficult to separate from the detached cloud of vapor, particularly if time-averaging of the flow is performed to obtain this information. Indeed, there was some confusion in the papers between the length of the time-averaged cavity and the maximum cavity length. However, most of the values fall inside the range 57–76%, which is consistent with the experimental length $l/l_{ref}=70\%$. The small cavity obtained by Qin et al. [33] may be associated with the stable flow that is obtained by the authors. Conversely, the large values 103%, 110%, and 97% reported in [19] and [36], respectively, are based on time-averaged shapes of the sheet cavity, which include the detached clouds of vapor. It is expected that the estimation of the maximum length of the attached cavity would give values of l/l_{ref} consistent with the experiments.

Concerning the lift and drag coefficients C_L and C_D, mean values close to 0.5 and 0.08, respectively, can be derived from the numerical results. The values reported in [37] are notably higher, which suggests that the boundary element method may be inappropriate in configurations of pronounced flow oscillations. On the other hand, the value of C_L reported in [33] is also significantly lower, in accordance with the stable sheet cavity obtained by the authors. It can be noticed than significant differences of the mean drag coefficient C_D in the numerical results may be associated with slightly different values of σ, for a given $\sigma_{downstream}=0.8$. This may partially explain some disagreements between the results, since the present flow condition is close to the transition observed in the experiments for $\sigma/2\alpha=4$.

It can be finally remarked that nearly all the simulations predict a detachment point of the cavity located at the foil leading edge, i.e., $l_d/l_{ref}\approx 0$, whereas l_d/l_{ref} can be estimated from flow observations to $\sim 3\%$ for the present flow condition in the experiments. Only Qin et al. [33] obtain a sheet cavity detachment in reasonable agreement with this value. Their cavitation model is analogous to the one used in the present work, so this discrepancy illustrates again the influence of the turbulence model on the results.

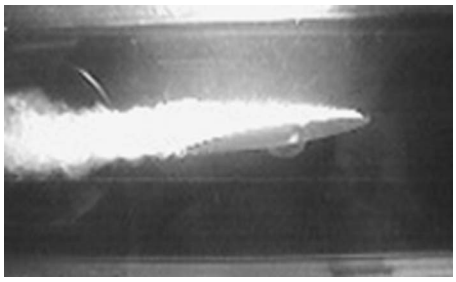

Fig. 21 Sheet cavity for $\sigma_{downstream}=0.4$

4.4 Results for $\sigma_{downstream}=0.4$. This second flow condition imposed in the numerical workshop corresponds in the present calculations to the case $\sigma=0.55$ reported in Sec. 3.4, i.e., $\sigma/2\alpha=2.25$. Like in Sec. 3.3, the sheet cavity detachment point is well predicted only by Qin et al. [33], while other simulations exhibit a nearly zero distance l_d/l_{ref}.

Various results are obtained for $\sigma_{downstream}=0.4$: periodical oscillations are still obtained by [16,19,35], whereas a stable cavity with only small-scale fluctuations is simulated in [33,36] and also in the present work. This second behavior is in agreement with the experiments performed in the SAFL cavitation tunnel [38], which exhibit a stable sheet cavity with no characteristic frequency. A completely steady sheet cavity is obtained in [15] and, of course, in [37], because of the cavitation model used by Kinnas et al. In nearly all cases, the maximum sheet cavity is longer than the chord. This point is in accordance with the present experiments (see Fig. 21), although the maximum length is difficult to estimate precisely.

The lift coefficient is obtained in the range 0.16–0.29, most of the results being close to 0.2/0.22. The drag coefficient is spread over a much larger range 0.008–0.23, but most of the simulations indicate a value close to 0.07/0.08. Concerning these two coefficients and also the mean vapor volume, a remarkable agreement can be noted between the present simulations and the ones performed by Kunz et al. [19] and Saito et al. [35], for both values of $\sigma_{downstream}$.

Conclusion

The foil section proposed in the numerical workshop of the 5th International Symposium on cavitation was investigated numerically and experimentally for several cavitating conditions. Nearly stable sheet cavitation, unsteady cloud cavitation, and severe cavitating conditions close to supercavitation were successively obtained by decreasing the cavitation number. These results were also compared to the peer numerical simulations of the same test case performed by other authors with various cavitation models and turbulence models.

Five main conclusions can be drawn from this study:

i. The numerical model, which consists of a single fluid approach based on the use of a barotropic state law for the liquid/vapor mixture, reproduces correctly the different global behaviors of the sheet cavitation, according to the cavitation number.
ii. The inception point at the foil leading edge is located more upstream in the simulations than in the experimental visualizations. This may be partially due to the surface roughness, which seems to have in the experiments a notable effect on the cavitation pattern at the leading edge, but is not taken into account in the numerical simulations.
iii. Several discrepancies have been observed concerning the two-phase flow structure in the cavity wake: the code predicts systematically sharp transitions between the cavitation area and the liquid flow, whereas in the experiments the downstream part of the cavity has an indistinct shape. Regions of flow condensation, characterized by a very low void fraction in the experiments, are not reproduced by the model. This may be related to the physical model itself, which links directly the density to the pressure. This is probably a reasonable assumption in the cavity upstream end, where the vaporization rate is governed by the local pressure gradient, whereas during the condensation process, other mechanisms, such as slip velocity between the phases, or surface tension may have a significant effect on the condensation rate. The fact that no inclusion of air is presently taken into account in the calculations may also notably modify the void fraction in the cavity wake. However, it can be noted that the other models applied in the peer simulations, such as the homogeneous approach based on the transport equation for α_v, do not significantly improve this point; it suggests that the development of an appropriate model for the condensation process in the cavity wake requires some further work.
iv. The two different unsteady behaviors reported previously by Arndt et al. [20] have been also obtained in the present study, both in the simulations and in the experiments: St_c is constant for $\sigma/2\alpha<4$, close to 0.15, whereas St_l is constant for $\sigma/2\alpha>4$, close to 0.25/0.3. $St_l \approx 0.25$ is consistent with many previous experimental studies, in various configurations of foil sections and Venturi-type sections (see, for example, [20,21,31,32]). Conversely, the value $St_c \approx 0.15$ is lower than the one reported by Arndt in the case of the NACA0015 foil section ($St_c \approx 0.2/0.25$), and also slightly lower than the value measured in the SAFL cavitation tunnel [38] in the present configuration ($St_c \approx 0.2$). This disagreement is difficult to handle. However, the question of the flow confinement and more generally of the influence of the test facilities should be addressed.
v. Peer numerical results obtained by [15,16,19,33,35–37] exhibit various behaviors for $\sigma_{downstream}=0.8$ (i.e., $\sigma/2\alpha \approx 3.7<4$), from steady sheet cavitation to periodic cloud cavitation. Most of the predicted Strouhal numbers agree neither with $St_c=0.15$ (present experiments) nor with $St_c=0.2$ (SAFL experiments). It suggests that the flow instability for $\sigma/2\alpha<4$ is not governed only by 2D mechanisms, but also by 3D effects that are not taken into account in the 2D simulations, leading to this dispersion of the results. Conversely, for $\sigma/2\alpha>4$, the correct value $St_l=0.25/0.3$ has been usually obtained in previous simulations [18,20,21,26], which implies that the physics of the unsteadiness is correctly reproduced by 2D models. It was shown for example in [21] that the flow instability in this case is mainly governed by the periodic reentrant jet, whereas other effects such as pressure wave propagation play also a significant role for $\sigma/2\alpha<4$. Three-dimensional calculations may be necessary in these more complex situations.

Acknowledgment

The numerical model "IZ" was developed for 15 years in the LEGI laboratory with successive work by Y. Delannoy (currently associate professor at the Institut National Polytechnique, Grenoble) and J.-L. Reboud (currently professor at Joseph Fourier University, Grenoble). This research was performed in the framework of collaboration between the LEGI and the CNES (Centre National d'Etudes Spatiales). The authors wish to express their deep appreciation for the continuous support of the Ecole Navale, Ministry of Defense (France) and of the technical staff (SEF) of the IRENav for the experiments.

Nomenclature

C_{min} = minimum speed of sound in the medium (m/s)
f = cavity self-oscillation frequency (Hz)
l_{ref} = reference length (chord of the foil) (m)
l = maximum length of the attached part of the cavity (m)
l_d = distance between the leading edge and the detachment point (m)
P = static pressure (Pa)
P_{ref} = reference pressure (inlet static pressure) (Pa)
P_{vap} = vapor pressure (Pa)
St_l = $f \times l / V_{ref}$ (Strouhal number based on the cavity length)
St_c = $f \times l_{ref} / V_{ref}$ (Strouhal number based on the chord)
T_{ref} = l_{ref} / V_{ref} (s)
$\mathbf{U}(u,v)$ = local velocity (m/s)
$\mathbf{U}^*(u^*,v^*)$ = first estimation of the velocity in the SIMPLE algorithm (m/s)
$\mathbf{dU}(du,dv)$ = correction of the velocity in the SIMPLE algorithm (m/s)
V_{ref} = reference velocity (inlet velocity) (m/s)
α = incidence angle of the foil (°)
α_v = local void fraction
ρ = fluid density (kg/m^3)
ρ^* = first estimation of the density in the SIMPLE algorithm (kg/m^3)
$d\rho$ = density correction in the SIMPLE algorithm (kg/m^3)
ρ_l, ρ_v = liquid/vapor density (kg/m^3)
ρ_{ref} = reference density=ρ_l (kg/m^3)
σ = $(P_{ref}-P_{vap})/(\rho V_{ref}^2/2)$ cavitation number
$\sigma_{downstream}$ = σ based on the outlet static pressure
$\sigma_{inception}$ = value of σ corresponding to inception of cavitation

References

[1] Kawanami, Y., Kato, H., Yamaguchi, H., Tagaya, Y., and Tanimura, M., 1997, "Mechanism and Control of Cloud Cavitation," ASME J. Fluids Eng., **119**, pp. 788–795.
[2] Pham, T. M., Larrarte, F., and Fruman, D. H., 1999, "Investigation of Unsteady Sheet Cavitation and Cloud Cavitation Mechanisms," ASME J. Fluids Eng., **121**, pp. 289–296.
[3] Laberteaux, K. R., and Ceccio, S. L., 2001, "Partial Cavity Flows. Part 1. Cavities Forming on Models Without Spanwise Variation," J. Fluid Mech., **431**, pp. 1–41.
[4] Leroux, J.-B., Astolfi, J.-A., and Billard, Y., 2004, "An Experimental Study of Unsteady Partial Cavitation," ASME J. Fluids Eng., **126**, pp. 94–101.
[5] Delannoy, Y., and Kueny, J. L., 1990, "Two Phase Flow Approach in Unsteady Cavitation Modeling," *Cavitation and Multiphase Flow Forum*, ASME, New York, ASME-FED Vol. 98, pp. 153–158.
[6] Chen, Y., and Heister, S. D., 1995, "Modeling Hydrodynamic Non-Equilibrium in Bubbly and Cavitating Flows," ASME J. Fluids Eng., **118**, pp. 172–178.
[7] Singhal, A. K., Ly, H. Y., Athavale, M. M., and Jiang, Y., 2001, "Mathematical

Basis and Validation of the Full Cavitation Model," ASME FEDSM 01, New Orleans.
[8] Kunz, R., Boger, D., Stinebring, D., Chyczewski, T., Lindau, J. W., Gibeling, H. J., Venkateswaran, S., and Govindan, T. R., 2000, "A Preconditioned Implicit Method for Two-Phase Flows with Application to Cavitation Prediction," Comput. Fluids, **29**(8), pp. 849–875.
[9] Song, C. C. S., and Qin, Q., 2001, "Numerical Simulation of Unsteady Cavitating Flow," *Proceedings of the Fourth International Symposium on Cavitation*, California Institute of Technology, Pasadena, June 20–23 (available on http://cav2001.library.caltech.edu/).
[10] Merkle, C. L., Feng, J., and Buelow, P. E. O., 1998, "Computational Modelling of the Dynamics of Sheet Cavitation," *Proc. of 3rd Intl. Symp. On Cavitation*, J. M. Michel and H. Kato, eds., Editions, Grenoble, Vol. 2, pp. 307–314.
[11] Kubota, A., Kato, H., and Yamaguchi, H., 1992, "A New Modelling of Cavitating Flows: A Numerical Study of Unsteady Cavitation on a Hydrofoil Section," J. Fluid Mech., **240**, pp. 59–96.
[12] Reboud, J.-L., Stutz, B., and Coutier, O., 1998, "Two Phase Flow Structure of Cavitation: Experiment and Modeling of Unsteady Effects," *Proc. of 3rd Int. Symp. on Cavitation*, J. M. Michel and H. Kato, eds., Editions, Grenoble, pp. 39–44.
[13] Yuan, W., and Schnerr, G. H., 2002, "Optimization of Two-Phase Flow in Injection Nozzles–Interaction of Cavitation and External Jet Formation," *Proc. of ASME Fluids Engineering Division, Summer Meeting*, Montreal, July 14–18, ASME, New York, CD-ROM.
[14] Coutier-Delgosha, O., Reboud, J.-L., and Delannoy, Y., 2003, "Numerical Simulations in Unsteady Cavitating Flows," Int. J. Numer. Methods Fluids, **42**, pp. 527–548.
[15] Pouffary, B., Fortes-Patella, R., and Reboud, J. L., 2003, "Numerical Prediction of Cavitating Flow Around a 2D Hydrofoil: A Barotropic Approach," Fifth Int. Symp. on Cavitation (Cav2003), Osaka, Nov. 1–4, Paper No. cav03-OS-1-5.
[16] Wu, J., Utturkar, Y., and Shyy, W., 2003, "Assessment of Modeling Strategies for Cavitating Flow Around a Hydrofoil," Fifth Int. Symp. on Cavitation (Cav2003), Osaka, Nov. 1–4, Paper No. cav03-OS-1-7.
[17] Johansen, S., Wu, J., and Shyy, W., 2003, "Filter-Based Unsteady RANS Computations," Technical Report, University of Florida (unpublished).
[18] Coutier-Delgosha, O., Fortes-Patella, R., and Reboud, J.-L., 2003, "Evaluation of the Turbulence Model Influence on the Numerical Simulations of Unsteady Cavitation," ASME J. Fluids Eng., **125**, pp. 38–45.
[19] Kunz, R. F., Lindau, J. W., Kaday, T. A., and Peltier, L. J., 2003, "Unsteady RANS and Detached Eddy Simulations of Cavitating Flow over a Hydrofoil," 5th Int. Symp. on Cavitation (Cav2003), Osaka, Nov. 1–4, Paper No. cav03-OS-1-12.
[20] Arndt, R. E. A., Song, C. C. S., Kjeldsen, M., He, J., and Keller, A., 2000, "Instability of Partial Cavitation: A Numerical/Experimental Approach," *Proc. of 23rd Symposium on Naval Hydrodynamics*, Office of Naval Research, Val de Reuil, France, National Academic Press, Washington, DC, pp. 599–615.
[21] Leroux, J. B., Coutier-Delgosha, O., and Astolfi, J. A., 2005, "A Joint Experimental and Numerical Study of Mechanisms Associated to Instability of Partial Cavitation on Two-Dimensional Hydrofoil," Phys. Fluids, **17**(5), 052101.
[22] Knapp, R. T., Daily, J. T., and Hammit, F. G., 1970, *Cavitation*, McGraw-Hill, New York.
[23] Charles, N., 1994, "Modélisation d'Écoulements Cavitants Avec Effets Thermodynamiques," Ph.D. thesis, Institut National Polytechnique de Grenoble, France.
[24] Zhu, J., 1991, "A Low Diffusive and Oscillation-Free Convection Scheme," Commun. Appl. Numer. Methods, **7**, pp. 225–232.
[25] Patankar, S. V., 1981, *Numerical Heat Transfer and Fluid Flow*, Hemisphere, New York.
[26] Coutier-Delgosha, O., Fortes-Patella, R., and Reboud, J. L., 2002, "Simulation of Unsteady Cavitation With a Two-Equations Turbulence Model Including Compressibility Effects," J. Turbul., **3**, 058, http://jot.iop.org.
[27] Wilcox, D., 1998, *Turbulence Modeling for CFD*, DCW Industries, La Canada, CA.
[28] Orszag, S. A., 1993, *Renormalization Group Modelling and Turbulence Simulations, Near Wall Turbulent Flows*, Elsevier, Amsterdam.
[29] Acosta, A. J., 1955, "A Note on Partial Cavitation of Flat Plate Hydrofoils," California Institute of Technology, Report No. E-19.9.
[30] Le, Q., Franc, J. P., and Michel, J. M., 1993, "Partial Cavities: Global Behaviour and Mean Pressure Distribution," ASME J. Fluids Eng., **115**, pp. 243–248.
[31] Joussellin, F., Delannoy, Y., Sauvage-Boutar, E., and Goirand, B., 1991, "Experimental Investigation on Unsteady Attached Cavities," *Cavitation'91*, ASME, New York, Vol. 116, pp. 61–66.
[32] Stutz, B., and Reboud, J.-L., 1997, "Two-Phase Flow Structure of Sheet Cavitation," Phys. Fluids, **9**, pp. 3678–3686.
[33] Qin, Q., Song, C. C. S., and Arndt, R. E. A., 2003, "A Virtual Single-Phase Natural Cavitation Model and Its Application to Cav2003 Hydrofoil," Fifth Int. Symp. on Cavitation (Cav2003), Osaka, Nov. 1–4, Paper No. cav03-OS-1-4.
[34] Song, C. C. S., and He, J., 1998, "Numerical Simulations of Cavitating Flows With a Single-Phase Approach," *Proc. of 3rd International. Symposium on Cavitation*, J. M. Michel and H. Kato, eds., April 7–10, Song and He, Grenoble, pp. 295–300.
[35] Saito, Y., Nakamori, I., and Ikohagi, T., 2003, "Numerical Analysis of Unsteady Vaporous Cavitating Flow Around a Hydrofoil," 5th Int. Symp. on Cavitation (Cav2003), Osaka, Nov. 1–4, Paper No. cav03-OS-1-6.
[36] Kawamura, T., and Saokoda, M., 2003, "Comparison of Bubble and Sheet Cavitation Models for Simulation of Cavitating Flow Over a Hydrofoil," 5th Int. Symp. On Cavitation (Cav2003), Osaka, Nov. 1–4, Paper No. cav03-OS-1-8.
[37] Kinnas, S. A., Sun, H., and Lee, H., 2003, "Numerical Analysis of Viscous Flow Around the Cavitating CAV2003 Hydrofoil," Fifth Int. Symp. On Cavitation (Cav2003), Osaka, November 1–4, Paper No. cav03-OS-1-10.
[38] Qin, Q., 2004, "Numerical Modeling of Natural and Ventilated Cavitating Flows," Ph.D. thesis, University of Minnesota.

A Numerical Study of Entrainment Mechanism in Axisymmetric Annular Gas-Liquid Flow

Huawei Han
PostDoc
Faculty of Engineering & Applied Science,
University of Ontario
Institute of Technology,
Oshawa, Ontario, L1H 7K4,
Canada
e-mail: colin.han@uoit.ca

Kamiel Gabriel
Associate Provost, Research
University of Ontario
Institute of Technology,
Oshawa, Ontario, L1H 7K4,
Canada
e-mail: kamiel.gabriel@uoit.ca

The main purpose of this study is to investigate liquid entrainment mechanisms of annular flow by computational fluid dynamics (CFD) techniques. In the modeling, a transient renormalization group (RNG) k-ε model in conjunction with an enhanced wall treatment method was employed. In order to reconstruct the two-phase interface, the volume of fluid (VOF) geometric reconstruction scheme was adopted. Simulation results indicated that disturbance waves were generated first on the two-phase interface and that their evolution eventually resulted in the liquid entrainment phenomena. The most significant accomplishment of this work is that details of the entrainment mechanism are well described by the numerical simulation work. In addition, two new entrainment phenomena were presented. One entrainment phenomenon demonstrated that the evolution of individual waves caused the onset of liquid entrainment; the other one showed that the "coalescence" of two adjacent waves (during the course of their evolution) played an important role in the progression of liquid entrainment. Further analysis indicated that the two entrainment phenomena are inherently the same entrainment mechanism. The newly developed entrainment mechanism is based on conservation laws.
[DOI: 10.1115/1.2427078]

Keywords: entrainment mechanism, CFD, k-ε model, VOF model, waves

1 Literature Review

Gas-liquid annular flow is an important two-phase flow regime. It frequently occurs in thermal management and thermal control systems in terrestrial and nonterrestrial energy transport systems, such as nuclear reactors, power plants, boilers, heat exchangers, and space station's thermal management systems. In annular flow, excessive liquid entrainment could lead to catastrophic events caused by "dry-out" conditions in which the liquid film is completely removed from contact with the channel's walls. It is very important to be able to predict such conditions to avoid its actual occurrence, particularly in situations where the effects could be quite disastrous (such as the breakdown of a nuclear reactor). However, the onset of the entrainment process and its progress through the formation of what is known as "disturbance waves" is poorly understood. This study is aimed at an improved understanding of this process by means of a numerical investigation.

Generally, there are three well-known mechanisms by which the liquid film is entrained into the gas core in vertical upward annular flow; these are: (a) wave entrainment, (b) entrainment by bubble burst, and (c) entrainment by droplet impingement. It is widely accepted that after disturbance waves are generated in the flow, wave entrainment is the most dominant liquid entrainment mechanism, while the other two types of mechanisms are generally neglected. This, in fact, is supported by the findings of Van Rossum [1], Hall-Taylor et al. [2], Woodmansee and Hanratty [3], and Schadel and Hanratty [4]. Their research work showed that significant liquid entrainment cannot be measured until after disturbance waves appear in the annular flow. Conventionally speaking, when the liquid entrainment mechanism is mentioned in annular flow, it usually refers to the wave entrainment mechanism. Thus, the wave-induced entrainment mechanism is the focus of this simulation work.

When disturbance waves appear at the liquid-gas interface, the wave entrainment mechanism is the dominant one that shears off droplets into the gas core. The relation between the disturbance waves and droplet entrainment has been clearly established since the 1960s by photographic and visual studies [3,5–7]. However, the exact mechanism for how the liquid droplets are generated out of a disturbance wave is still controversial. The fundamental recognition is that liquid entrainment is due to the disturbance wave crest being sheared off into the gas core. Several wave entrainment mechanisms were proposed to interpret this shearing-off process based on various studies, which include wave undercut, wave rolling, ripple wave shearing off, and wave coalescence. Thus far, there is no solid and direct evidence to favor any particular one.

Hewitt and Hall-Taylor [8] and Whalley [9] were the first to introduce the wave undercut entrainment mechanism as shown in Fig. 1. In this mechanism, part of the liquid in the disturbance wave peak region is "stretched" and sheared off by the incoming high-speed gas flow in the core. The sheared-off liquid eventually breaks up into droplets of various sizes. The wave undercut entrainment mechanism was derived from the droplet breakup mechanism. The fundamental work on this entrainment mechanism can be traced back to Lane [10].

The wave rolling entrainment mechanism has been described in a way similar to the breakup of beach waves in high winds and was initially introduced by Hewitt and Hall-Taylor [8]. Under the action of high-speed gas, the tips of disturbance waves will be rolled forward and subsequently break up into liquid droplets. The process is schematically shown in Fig. 2. This mechanism was developed from the breakup mechanism of liquid jets and liquid sheets. However, just as the authors [8] questioned, it is doubtful if the conclusions on the work of liquid jets and sheets could be directly applied to disturbance waves in annular flow since the latter case is far more complicated than the former.

Hall-Taylor et al. [2] investigated the motion and frequency of the disturbance waves in a vertical annular two-phase flow (Tube i.d.=31.25 mm). Using high-speed cine films, they observed that the collision and combination of two disturbance waves lead to liquid droplet entrainment. This, in effect, describes the wave coa-

Contributed by the Fluids Engineering Division of ASME for publication in the JOURNAL OF FLUIDS ENGINEERING. Manuscript received October 26, 2005; final manuscript received August 9, 2006. Assoc. Editor: Surya P. Vanka.

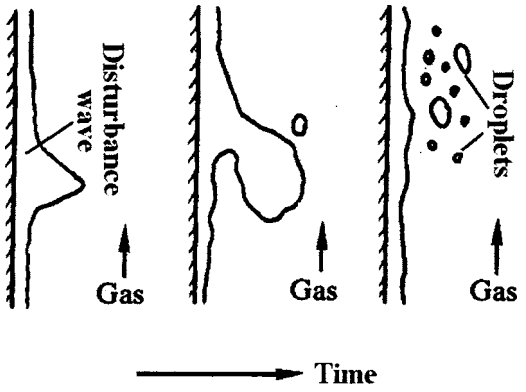

Fig. 1 Wave undercut entrainment mechanism [9]

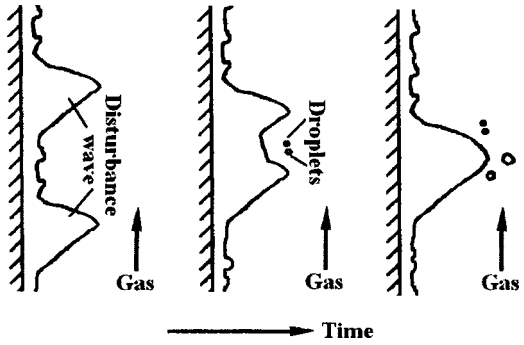

Fig. 3 Wave coalescence entrainment mechanism [2,11]

lescence entrainment mechanism, as illustrated in Fig. 3. However, no photographs were presented to show how this process happened. In the study, they defined three types of wave collisions. Based on that mechanism, Wilkes et al. [11] derived a wave coalescence model by which the entrainment fraction due to the wave coalescence was predicted. Comparison of the modeling results with the experimental data indicated that the liquid entrainment fraction due to the wave coalescence could be a significant portion of the total liquid entrainment. This model was based on the Monte Carlo techniques.

The ripple wave shearing-off entrainment mechanism was proposed by Woodmansee and Hanratty [3]. They investigated the liquid entrainment mechanism of a stratified flow in a horizontal rectangular channel. Their high-speed photographs revealed that liquid entrainment occurs by the removal of small wavelets that exist on top of the disturbance waves in the liquid film. The authors further pointed out that it is the Kelvin-Helmholtz instability that caused the removal of ripples from the surface of the disturbance wave. The process is shown schematically in Fig. 4. It is noted that the importance of disturbance waves in this mechanism is to provide a "platform" from which liquid entrainment is triggered. It is similar to all previously discussed types of wave entrainment mechanisms in that the liquid carried by the disturbance waves provides the entrained liquid droplets.

From the above survey, it is clear that there exist different theories and explanations for the wave entrainment mechanisms of annular flow, but a full understanding of such mechanisms is at best incomplete and uncertain at present. In addition, there are no sufficient details about any of the above mechanisms to favor one over the others due to the lack of consistency in the results. This is partially due to the limitations of current instrumentation methods, but also due to the extreme complexity of the liquid entrainment process itself. With such limitations and complexity of the experimental procedure, and with the significant progress in CFD techniques, several studies have attempted using numerical modeling to get clues into the process.

Thus far, there exist a few models to study the wave entrainment mechanisms. In addition to the work by Wilkes et al. [11] on the wave coalescence mechanism, Holowach et al. [12] presented a model to study wave entrainment, which was based on the work of Ishii and Grolmes [13] for the wave breakup. The latter was adapted from the work of Sevik and Park [14] on shattering of a droplet caused by resonance from gas-phase turbulence. Basically, the model was based on a force balance and interfacial instability. The forces considered in the model were the wave-crest drag force, gravitational force, and surface tension force.

The limitations of these models could be summarized as follows: (i) they are highly dependent on dimensionless groups and sometimes experimental correlations; and (ii) they have more or less dependency on the physical process of the targeted mechanism. These limitations reduce the usefulness of these existing models. According to the authors' best knowledge, no CFD model for liquid entrainment was found to be reported in the open literature.

2 Modeling

2.1 Model Formulations. The annular flow in this study is a vertical upward cocurrent air-water flow in a small diameter tube with an inner diameter of 9.525 mm. For annular flow in a small-diameter tube (i.d. $<$ 58 mm [15]), the liquid film is uniformly distributed around the tube circumference [16], and disturbance waves appear circumferentially coherent [2], [17], [18], two-dimensional [19], and circumferentially symmetrical [8], [20]. The observations by Martin [21] indicated that waves were highly regular in tubes with an inside diameter of 10 mm, which corresponds to the present study. These characteristics of disturbance

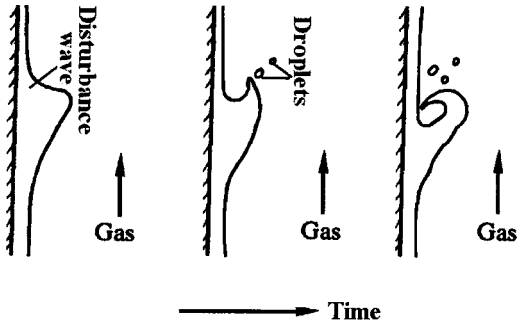

Fig. 2 Wave rolling entrainment mechanism [8]

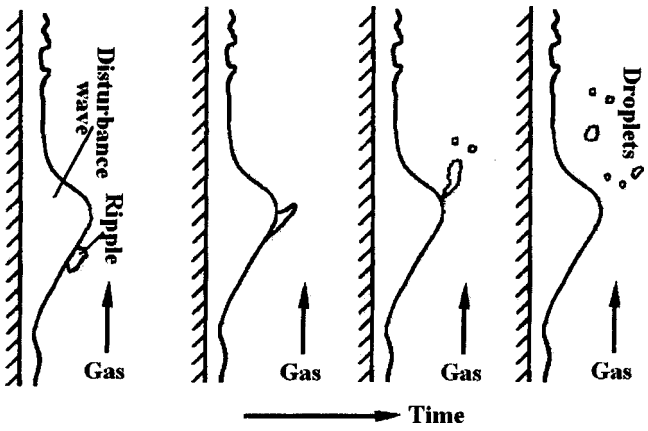

Fig. 4 Ripple shearing-off entrainment mechanism [3]

Table 1 Summary of the model configuration

Item		Model configuration
Phases in VOF model	Air Water	Primary phase Secondary phase
Relaxation factors for all variables		1.0
Discretization schemes of convective terms in governing equations	Pressure	Body force weighted
	Pressure-velocity coupling	PISO
	Momentum equation	First order upwind
	Turbulent kinetic energy	First order upwind
	Turbulence dissipation rate	First order upwind

waves are obviously important in modeling of waves and the flow phenomena associated with them. They indicate that a two-dimensional model is sufficient for CFD modeling of annular flow in a small-diameter tube.

Based on the work of Han [22], the gas core of annular flow in this study is in the turbulent state while the liquid film has strong features of the near-wall region flow. The RNG k-ε model, employing a scheme to consider the near-wall flow effects, is used in the simulation. The enhanced wall treatment method is used to deal with the near-wall flow effects. With this method, a coarser mesh than that of low Re k-ε model is allowed in the viscosity-affected near-wall region with little impact on the accuracy of simulation in that region. In order to reconstruct the gas-liquid interface of annular flow, the VOF geometric reconstruction scheme is adopted. Becuase of the flow axisymmetry, a two-dimensional model is constructed. The model in this simulation is a transient model.

FLUENT® 6.18 is used as the solution tool. For the model, the package uses a segregated solver that solves the governing equations sequentially, and implicit discretization schemes for the momentum k and ε transport equations. However, the package uses a first-order explicit time-marching scheme to solve the time-dependent continuity equations for the volume of fractions. In the modeling, the surface tension is included and its value is set to that of the air-water surface tension, i.e., 0.072 N/m. Some other information on the model configuration is listed in Table 1. The convergence criterion is set such that the residuals of all the variables are $\leqslant 10^{-3}$.

As shown in Table 1, air is set as the primary phase and water is the secondary phase. In FLUENT® 6.18, the results are not affected by the selection of which phase is chosen as the primary phase. The only difference is the solution methods for their volume fractions.

2.2 Overview of Experimental Work. It should be noted that in this simulation the simulation parameters are determined according to the experimental work of MacGillivray and Gabriel [23]. They measured the film thickness in air-water annular flow. In the experiments, the air-water two-phase mixture entered into a 9.525 mm i.d. stainless-steel tube and was allowed to develop over a length of 0.72 m (76 D). The liquid superficial velocity ranged from 0.076 m/s to 0.315 m/s, and the gas superficial velocity ranged from 15.8 m/s to 29.4 m/s. The measured average liquid film thickness ranged from 0.2 mm to 0.8 mm. Further details of the experimental work can be found in MacGillivray and Gabriel [23].

In addition, another experimental analysis work was carried by Zhao and Rezkallah [24] is used to compare to the simulation results, which is to prove that the simulation work is reliable. Zhao and Rezkallah [24] achieved a microgravity flow map based on the experimental measurements and observations in a simulated zero-gravity condition aboard the NASA's Zero-gravity KC-135 aircraft. The liquid superficial velocity ranged from 0.09 m/s to 3.73 m/s, and the gas superficial velocity from

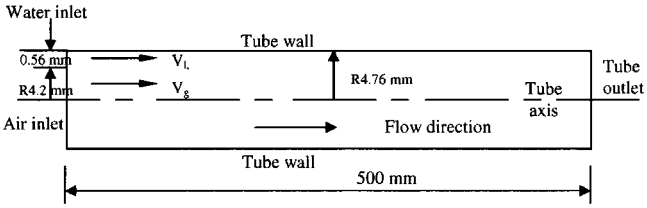

Fig. 5 Schematic of the simulation domain

0.2 m/s to 29.9 m/s. Bubble, slug, frothy slug-annular, and annular flows were observed to exist. They used a dimensionless number, the Weber number (We), as the correlating parameter for the different flow regimes in a similar tube size and shape. According to their study, when the gas-phase Weber number was larger than 20, $We_g > 20$, the flow at microgravity condition was annular flow. When $We_g < 1$, the flow was bubble or slug flow, and for values of We between 1 and 20, the flow was transitional.

The Weber number is defined as

$$We_g = \frac{V^2 D \rho}{\sigma} \tag{1}$$

where σ is the air-water surface tension and ρ is the density of the gas phase.

2.3 Simulation Domain. The simulation domain is shown in Fig. 5. Only half of the tube domain is simulated since the flow is axisymmetric. The simulation domain is bounded by the tube wall, tube axis, and the tube inlet and outlet sections. Air and water enter the inlet section with the air inlet radius set to 4.2 mm, and the water annulus width at the inlet section is set to 0.5625 mm. These values are chosen based on the range of measured liquid film thickness in a channel of 9.525 mm i.d. [23]. In the simulation, the tube length is set to 500 mm, shorter than the actual development length used by MacGillivray and Gabriel [23]. This length is chosen because it can satisfy the simulation objective with a minimum computational time.

2.4 Boundary and Initial Conditions. *Boundary conditions:* As shown in the experimental study, water is supplied through the tube's inlet at a constant velocity V_l. In the simulation, the water velocity ranges from 0.7 m/s to 1.1 m/s, corresponding to the actual measured liquid velocity [23]. The volume fraction of water at the inlet was set to 1, meaning only water is flowing at the water annulus inlet section. As to the turbulence boundary conditions, the turbulence intensity and hydraulic diameter are used to specify the turbulence parameters. The turbulence intensity I is defined as the ratio of the root-mean-square of the velocity fluctuations u' to the mean flow velocity u, i.e., $I = u'/u$. Commonly, for low intensity turbulent flow, $I \leqslant 1\%$, and for high-intensity turbulent flow, $I > 10\%$. This principle is used to estimate the turbulence intensity at the inlet. Because in this study the liquid film of annular flow has the features of near-wall flow, a low value for I is appropriate for this simulation. At the water inlet, the turbulence intensity of the water is set in a range of 0.2–1.2 %, corresponding to the different water inlet velocities. The hydraulic diameter is kept the same as the two times width of the water annulus inlet (0.5625 mm).

Air is supplied through the gas portion of the inlet section at a constant velocity V_g, as shown in Fig. 5. In the simulation, V_g ranges from 0.5 m/s to 15 m/s, which is, in fact, lower than the actual measured gas velocity. This arrangement is mainly to save on computational time and prevent the potential liquid flow breakdown at higher gas velocities. The volume fraction of water at this portion of the inlet was set to 0, meaning no water flow. As to the turbulence boundary conditions, the turbulence intensity of the air was set in the range from 1% to 10% corresponding to various air

Table 2 Boundary conditions at tube inlet (air and water inlets)

Boundary condition		Water inlet	Air inlet
Constant velocity inlet (m/s)		0.7–1.1	0.5–15
Turbulence specification	Turbulence intensity (%)	0.2–1.2	1–10
	Hydraulic diameter (mm)	1.125	8.4
Volume fraction of secondary phase (water)		1 (with water flow)	0 (no water flow)

velocities. The hydraulic diameter remains the same as the diameter of the air inlet section of 8.4 mm. The boundary conditions at the tube inlet are summarized in Table 2.

The gas and liquid Reynolds numbers corresponding to the simulated conditions are listed in Table 3, in which V is the actual velocity of the gas or liquid phase; V_s is the superficial velocity; Re is the actual Reynolds number based on the gas or liquid inlet dimension; and Re_s is the superficial Reynolds number based on the inner tube diameter. According to the work of Andreussi et al. [25], the critical liquid Reynolds number for disturbance wave formation is ~280. It can be seen from the Table 3 that the liquid Reynolds numbers in this work exceed the critical value.

A no-slip boundary condition is assumed at the tube wall. The flow is axisymmetric with the gradient of all the variables about the axis being zero, i.e., $\partial\phi/\partial r=0$ (ϕ can be the velocity, k, or ε). An outflow boundary condition is assumed at the tube outlet.

Initial conditions: The initial conditions in the simulation are the same as those in the experiments. At $t=0$ s, the tube is full of air. This means the volume fraction of the secondary phase, i.e., water, is zero everywhere in the tube. The initial pressure in the tube is 1 atm. As far as the velocities, both radial and axial velocities in the tube are set to 0 m/s at $t=0$ s. The same applies to the initial k and ε values.

2.5 Material Properties. The air and water properties are listed in Table 4.

2.6 Additional Considerations. Additional considerations dealing with the effects of changing the gravity level, the mesh size, and the time step in the simulation are addressed here.

Gravity level: Gravity has a destabilizing effect on the flow. In this simulation, the gravity is set to zero.

Mesh size: The mesh size contributes to the computational time and the accuracy of the results. A finer mesh has the potential to improve the accuracy of the simulation results, but this improvement comes in many cases at the expense of computational time. Thus, a balance between the accuracy of the results and the computing time should be always sought. The mesh size, shown in Table 5, attempts to meet this principle. A quadrilateral mesh is used for this simulation.

Table 3 Gas and liquid (water and air) Reynolds number in the simulation

	V (m/s)	V_s (m/s)	Re	Re_s
Liquid	0.7–1.1	0.16–0.24	788–1238	1482–2328
Air	0.5–6–15	0.39–4.7–11.7	287–3444–8610	253–3037–7593

Table 4 Phase properties

Phase	Density ($\mathrm{kg/m^3}$)	Viscosity ($\mathrm{kg/(m\,s)}$)
Air	1.23	1.8×10^{-5}
Water	1000	10^{-3}

In Table 5, $\Delta r_{\max}$ and $\Delta r_{\min}$ are the maximum and minimum mesh sizes in the radial direction, respectively; and Δx is the mesh size in the axial direction. In addition, 20 mesh nodes are arranged on the tube radius (nearly half of these nodes are distributed in the region between the tube wall and estimated interface) and 101 nodes on the tube axis or tube wall.

The mesh is evenly distributed in the axial direction while an uneven distribution of the mesh is used in the radial direction in such a way as to satisfy the goals of the simulation. It is known that the wave-induced entrainment phenomenon occurs on the gas-liquid interface. This also requires a finer mesh near the tube wall region in order to capture the features of this process in the simulation. Therefore, in this research, the mesh distribution in the radial direction is designed in such a way that the mesh is fine near the wall but as it gets closer to the tube axis, it becomes coarser.

Time step: The time step depends on two-phase velocities and mesh sizes. The higher the two-phase velocities and the smaller the mesh sizes, the smaller is the time step. Once the mesh sizes are set, the initial time step is determined by two-phase inlet velocities. The initial time step is the one that works throughout the whole simulation if a smooth interface is generated between the two phases. For this simulation work, the initial time step is set at 10^{-7} s. In the simulation, once a wave is generated on the interface, the gas velocity will increase due to the contraction of the gas core near the wave peak region and the time step should be refined accordingly.

3 Results and Discussions

Various meshes were designed and mesh-independent calculations were conducted. Comparisons, as shown in Table 6, indicated that the base mesh already produced mesh-independent results. The wave parameters around a position of $x=190$ mm at $t=2.163$ s for each mesh are obtained, and the comparisons are conducted in terms of wave parameters. The results of comparing the wavelength and wave height from the four meshes are summarized in Table 6. It can be seen that the wave height appears not to be influenced by the different meshes. The standard and the finer meshes produce almost the same wavelengths, whereas those of the two coarser meshes are different. These results show that the base mesh meets the requirement to generate mesh-independent results.

The simulation results are presented in this section. In the contours, the other symmetrical part of the calculation domain is added using the "mirror" function of FLUENT® 6.18 In the figures, the dark color always represents the liquid phase, while the gray color represents the gas phase (air in this case). Based on the mesh described above, two annular flow cases (see Table 7) were simulated and their results are presented and discussed.

Table 5 Mesh size for the simulations

Mesh size (mm)			Mesh node numbers		Domain dimensions (mm)	
$\Delta r_{\max}$	$\Delta r_{\min}$	Δx	Tube radius	Tube length	Tube radius	Tube length
0.476	0.138	5	20	101	4.7625	500

Table 6 Comparison of wave parameters: wave height and wavelength

Mesh	Nodes in radial direction	Nodes in axial direction	Node number	Wavelength (mm)	Wave height (mm)
Base mesh	20	101	2,020	25.4	1.1
Finer mesh	21	106	2,226	25.3	1.1
Coarser mesh I	19	81	1,539	29.6	1.1
Coarser mesh II	17	73	1,241	31.6	1.1

3.1 Comparisons to Experimental Work. The purpose of this section is to compare the simulation results to those obtained from the experimental work by Zhao and Rezkallah [24] to validate the simulation techniques used in this study. It includes a study of the flow patterns arising from the simulation and compares them with the experimental flow regimes.

3.1.1 Flow Patterns From Simulations. In the former sections, it was mentioned that two annular flows were simulated at V_g =6 m/s and V_g=15 m/s. In both cases, the liquid velocity V_l was kept constant at 1 m/s. In this study, a slug flow was obtained by decreasing the gas velocity from its initial value to 0.5 m/s, while keeping the liquid velocity at 1 m/s. Restricted by the simulation domain, only one complete slug is obtained, which is shown in Fig. 6. It can be seen from the figure that a second slug is forming downstream.

Thus, two types of flow patterns are obtained from the present simulations: two annular flows (cases I and II), and one slug flow when the gas velocity is reduced.

3.1.2 Comparison of Flow Patterns. The results of the flow pattern simulation are similar to those obtained from the experimental analysis work conducted earlier by Zhao and Rezkallah [24]. In the simulation, the two types of flow patterns are obtained with gravity set to zero. The We_g for the three simulation cases have been calculated and the results are listed in Table 8.

According to the criteria of Zhao and Rezkallah [24], the simulation flow patterns from cases II and III agree well with the microgravity flow map, while the result from case II should have been slug-annular flow instead of annular flow. The discrepancy of case II can be explained in that, based on a sensitivity study, it is known that the presence of gravity greatly influences the flow patterns since the gravitational force acts as a destabilizing force. In the simulation, gravity is set to zero and its influence on the flow is therefore excluded. However, in the microgravity experiments, although it is significantly reduced, the influence of the gravitational force still exists due to residual gravity effects. Thus, a lower Weber number in the simulation could sustain an annular flow. This is not the case in actual microgravity conditions.

3.1.3 "Disturbance Waves" on the Two-Phase Interface. The main purpose of this study is to explore the liquid entrainment mechanism in annular flow. However, due to the strong role of waves in the entrainment process, they need to be considered. Figure 7 shows an individual wave on the two-phase interface.

Figure 7 shows that a fully developed wave has a wavelength of 25 mm, approximately three times the tube diameter; and a wave peak of ~1.1 mm, slightly larger than the average liquid film thickness. Simulation also shows the waves are propagating downstream in the tube axial direction, further indicating that the simulation waves are axially coherent. These features are typical of disturbance waves. In addition, just as in the case of a disturbance wave, the wave crest on the leeward side is relatively steep, whereas the part on the windward side is relatively smooth. Therefore, it can be concluded that the waves generated on the interface can be classified as disturbance waves. However, as clearly observed from the numerical results, the "disturbance wave" images are less irregular and much less chaotic than those observed from experiments (e.g., [3,4,25]). This is mainly due to features of k-ε model. The model yields time-averaged or ensemble-averaged results, which leads to more smooth and orderly wave shape. For convenience, the waves obtained in this work are still called disturbance waves.

The other wave characteristic that could be seen in the simulation is that the waves are dynamic. That is, they are continually

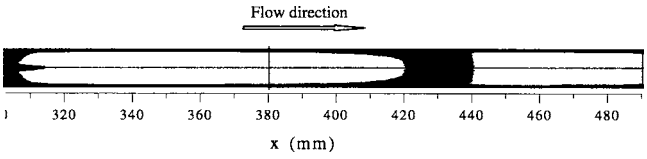

Fig. 6 Slug flow at V_g=0.5 m/s; V_l=1 m/s; and t=1.7268 s

Table 7 Annular flow cases for simulation

Cases	V_l (m/s)	V_g (m/s)	Re_l	Re_g	Flow regime
I	1	15	1125	8610	Annular flow
II	1	6	1125	3444	Annular flow

Table 8 Weber number values for the three simulation cases

Cases	Flow pattern in simulation	V_g (m/s)	We_g
I	Annular flow	15	6
II	Annular flow	6	37
III	Slug flow	0.5	0.04

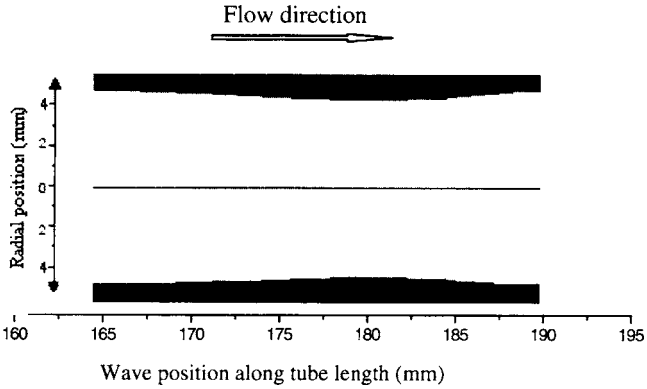

Fig. 7 Wave shape and dimensions in the fully developed region; Case II (V_g=6 m/s; V_l=1 m/s) at t=2.163 s

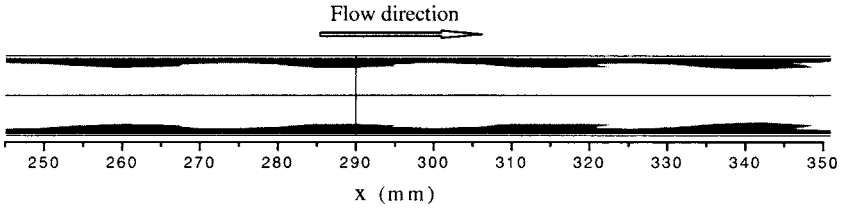

Fig. 8 Waves in the enlarged wavy region of case II (V_g=6 m/s; V_l=1 m/s); t =2.163 s

developing over time and changing their shapes under the action of the gas flow from the moment of their inception. Figure 8 shows a number of interfacial waves in the wavy region. By careful examination of the wave shapes at the upstream locations of 250 mm – 280 mm, and their shapes at the downstream locations of 310 mm – 350 mm, the reader can deduce that these waves are different. In particular, it can be seen that the last two waves downstream started to protrude into the gas core as demonstrated by the shape of the wave crests. The protruding part is due to the action of the gas flow on the wave crest and, as it develops further, it will finally be sheared off from the wave crest and entrained in the form of droplets in the gas core.

The gas-phase velocity in the simulation is lower than known annular flows in the literature and it is impossible to make meaningful comparisons. However, the wave parameters obtained from numerical simulation are listed in Table 9, in which V_w is the wave velocity; H_w, wave peak height; L_w, wave length; F_t, mean film thickness; and f_w is the wave frequency. It should be noted, when F_t was calculated, the liquid film containing the deformed waves was not considered. Because the waves in the simulation are dynamic waves, their wave length and wave peak height are changing during their evolution in the flow. Thus, H_w and L_w, as presented in the table, are wave parameters around a position of x =290 mm at t=2.163 s for each annular flow.

3.2 Liquid Entrainment Mechanisms. From this study, two types of liquid entrainment phenomena are identified: one phenomenon (from case I with comparatively higher gas velocity) shows that an individual wave continues to develop and deforms until its crest is finally sheared off by the incoming gas phase. The other phenomenon, as demonstrated from case II with comparatively lower gas velocity, shows "wave coalescence" as the source of the waves' breaking off into the gas core. The two entrainment phenomena are presented and discussed below.

3.2.1 Entrainment Mechanism at Higher Gas Velocity. This mechanism is identified based on the analysis of the simulation results of case I (the gas velocity is set to 15 m/s). It is found that individual waves in the simulation are generated and, in the process of evolving, part of the liquid in the wave crest gains extra momentum from the incoming high-speed gas phase. This causes a protruding part to be formed in the wave front. During this process, the wave grows in both the radial and axial directions, absorbing the liquid from the film in front of it and behind it. The protruding part continues to be stretched forward by the incoming high-speed gas phase. It draws most of the liquid from the wave crest to maintain its growth. Finally, it is cut off by the higher-speed gas phase and is entrained into the gas core. Figures 9(*a*)–9(*j*) depict the entire liquid entrainment process and demonstrate how the evolution of an individual wave eventually leads to liquid entrainment.

Table 9 Wave parameters from simulated annular flows, V_l =1 m/s

Annular flow case	V_w (m/s)	H_w (mm)	L_w (mm)	F_t (mm)	f_w
V_g=15 m/s	1.1	1.1	30	1.01	14.0
V_g=6 m/s	0.9	1.2	25	1.07	12.5

Figure 9(*a*) shows that an individual wave has already grown to become a disturbance wave at t=3.00 s. After 0.02 s, it can be seen in Fig. 9(*b*) that the wave front becomes shorter and steeper. This indicates that the liquid in the wave crest moves relatively fast under the influence of the gas phase and absorbs part of the wave front. Figure 9(*c*) further confirms this trend. After another 0.02 s, as shown in Fig. 9(*d*), the faster liquid in the wave crest moves ahead of the wave front and protrudes into the gas core. With time, the protruding part of the wave further develops while at the same time the liquid film before and after the wave becomes thinner. The wave crest is stretched in both the axial and radial directions. This indicates that the wave draws the liquid phase from the film. In addition, due to the lift of the interfacial shear stress exerted on the wave by the gas phase, the tip of the protruding part is stretched toward the tube axis (Figs. 9(*e*)–9(*g*)). The protruding part continues to be stretched and becomes longer and thinner. It eventually loses its connection to the wave crest and is ultimately broken off and entrained into the gas core. In this process, because the gas phase cannot provide sufficient lift to the protruding part, it finally reaches a "balanced" position and its surface is flattened, as seen in Figs. 9(*h*)–9(*j*). Figure 9(*i*) shows that the protruding part is barely connected with the wave body. Figure 9(*j*) indicates that the protruding part has broken off from the wave body and is entrained into the gas core.

3.2.2 Entrainment Mechanism at Lower Gas Velocity. The second entrainment phenomenon is identified based on the analysis of the simulation results of case II with the gas velocity set to 6 m/s. It was found that during the evolution process, consecutive waves on the interface first "coalesce" before being entrained into the gas core. The entire entrainment process in this case is shown in Figs. 10(*a*)–10(*k*).

Figure 10(*a*) shows two adjacent waves at t=2.0709 s. In both cases, the waves resemble the characteristics of a disturbance wave. It can be clearly seen that the downstream wave has already started to protrude into the gas core, whereas the upstream wave's short and steep front indicates it is ready to grow a protruding part. The wave amplitudes in both cases are similar. After 0.01 s, the two waves move to new positions, each with a slight change in the appearance of the protruding part at the leading edge, as shown in Fig. 10(*b*). With time, the two waves continue to develop. Figures 10(*c*)–10(*h*) show that the upstream wave seems to be "catching up" with and merging into the downstream one. Because of the higher shear stress and higher pressure exerted on the surface of the upstream wave, the liquid in the body of the upstream wave moves relatively faster and continues to "catch" up with and merge into the downstream wave. The lower shear stress and lower pressure exerted on the surface of the downstream wave also allow it to further develop. Thus, the downstream wave continues to be strengthened in its amplitude, and its protruding part continues to grow larger. During this process, the liquid film near the front region of the downstream wave becomes much thinner. This suggests that the downstream wave also absorbs liquid from the film to support its evolution. Figure 10(*i*) shows that the up-

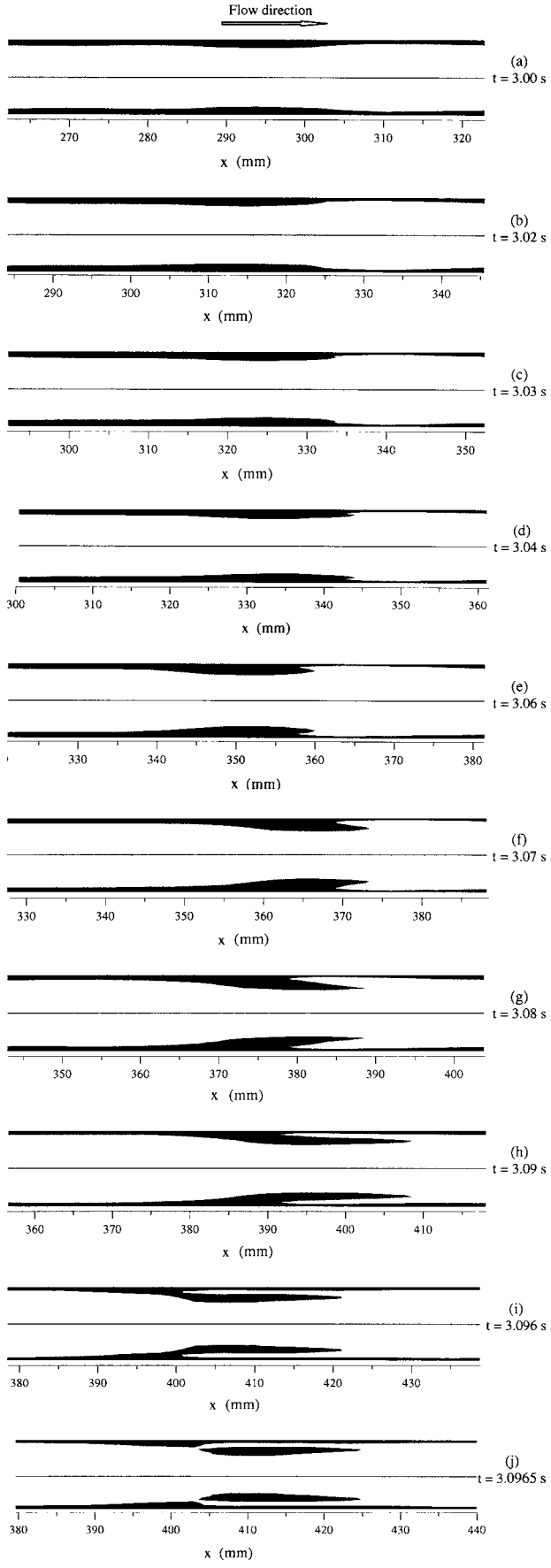

Fig. 9 Details of wave evolution and liquid entrainment; Case I: V_g=15 m/s; V_l=1 m/s

stream wave is totally absorbed by the downstream wave and the protruding part of the downstream wave continues being lifted towards the tube axis and being stretched in the flow direction. Such changes are due to the following actions exerted on the wave. Around the wave peak region of the downstream wave, due to the contraction of flow passage, the wave peak region in the gas core is a low-pressure region and tends to draw in the liquid wave. The wave peak region also has most acute interfacial shear stress distribution, which indicates a strong shearing force in that region. The gas flow with the maximum velocity near the wave peak region also impacts the interfacial waves and presses an effect as shoveling the wave peak into the gas core. The comprehensive effects of these factors caused above changes. Figures 10(*j*) and 10(*k*) clearly show that the protruding part is finally sheared off from its wave body and into the gas core.

In summary, Figs. 9(*a*)–9(*j*) and 10(*a*)–10(*k*) clearly demonstrate the onset and evolution of the liquid entrainment mechanism in annular flow. The results from both cases show that in both phenomena, it is the wave crests that are sheared off eventually by the gas flow. But there are some subtle differences between the two phenomena. For the phenomenon from case I, it is the individual wave that develops and deforms under the action of the faster-moving gas phase. In order to provide enough liquid phase to sustain the wave, the wave draws additional mass from the liquid film. For the entrainment phenomenon of case II, the upstream wave is involved in the evolution of the downstream wave. Because of the higher shear stress and higher pressure on the surface of the upstream wave, it is gradually absorbed by the downstream wave and thus provides material for further development of the downstream wave. The wave crest of the downstream wave is eventually sheared off by the gas core. Therefore, although there exist small differences in the process of the wave evolution, both cases present the same liquid entrainment mechanism.

3.2.3 Comparisons to Other Mechanisms in the Literature. The entrainment mechanism arising from the present simulations with those available in the open literature is compared. Earlier, four types of wave entrainment mechanisms were introduced to interpret the process of wave crest shearing, namely: (i) wave undercut, (ii) wave rolling, (iii) ripple wave shearing-off, and (iv) wave coalescence. It is interesting to note that the entrainment mechanism arising from the present simulations is closer to the ripple wave shearing-off mechanism than any other mechanism. Almost in all previous work, researchers interpret the entrainment mechanism as the liquid shearing off from the tops of disturbance waves. However, there are distinct differences between the two mechanisms. In the ripple wave shear-off mechanism, the Kelvin-Helmholtz ripples on the surface of the disturbance waves are removed from the wave crests. In the present simulation, part of the liquid phase in the wave crests is stretched forward in the flow direction until it is broken off by the incoming gas phase.

The entrainment phenomenon from case II displays a wave "coalescence-like" process. But this coalescence process is different from other wave coalescence mechanisms found in the literature in that the wave "coalescence" in this case does not directly cause the onset of the liquid entrainment process. It provides the liquid material to trigger the occurrence of the entrainment phenomenon. According to the studies reported in the literature, the wave coalescence entrainment mechanism claims that the liquid droplets are generated when two disturbance waves collide and coalesce. That is, the direct interaction between the two waves causes the liquid phase to be entrained into the gas core.

4 Conclusions

Disturbance waves play a major role in the entrainment process in annular, two-phase flow. A numerical study was conducted to simulate the dynamic wave formation process for a two-dimensional (2D) wave in a small diameter tube. This type of

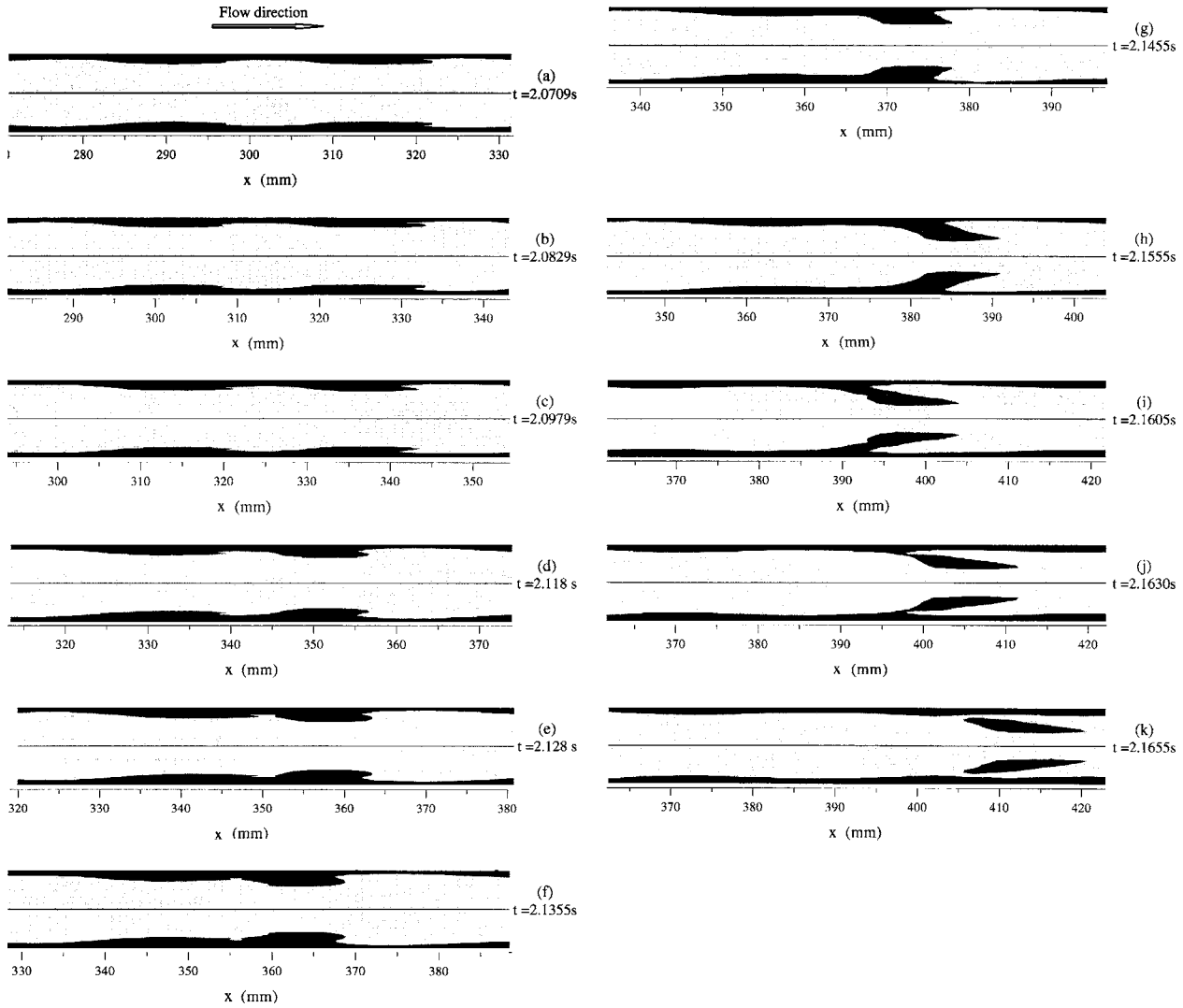

Fig. 10 Details of wave development and liquid entrainment; Case II: V_g=6 m/s; V_l=1 m/s

wave is very dynamic in that it is continually changing from initial growth to further development. Eventually, the crest breaks off by the incoming gas phase, resulting in entrained liquid into the gas core.

From the study, two types of wave evolution phenomena were identified in annular flow and their onset and evolution were presented. One phenomenon shows that an individual wave, once formed, continues to deform and develop under the action of the faster-moving gas phase until its crest is finally sheared off into the gas core. In this process, the wave draws liquid from the film during its evolution. The other one shows that the upstream wave is absorbed by the downstream one, and it provides material for further development of the downstream wave. Eventually, the wave crest of the downstream wave is sheared off by the incoming gas phase.

The simulation results confirm the disturbance waves' role in the liquid entrainment process. It also supports a common recognition by other researchers that liquid entrainment is mainly due to the wave crest being sheared off. However, comparisons to other liquid entrainment mechanisms indicate that the two wave entrainment phenomena from simulation are inherently the same entrainment mechanism although there is a small difference in that one mechanism involves only one wave while the other is based on the interaction of two adjacent waves.

Finally, the flow patterns arising from the simulations were compared to those from experiments. Comparisons indicate that the results of the flow pattern simulations are similar to those of the experimental work, thus increasing confidence in the simulation results.

References

[1] Van Rossum, J. J., 1959, "Experimental Investigation of Horizontal Liquid Films-Wave Formation, Atomization, Film Thickness," Chem. Eng. Sci., **11**(1), pp. 35–52.

[2] Hall-Taylor, N., Hewitt, G. F., and Lacey, P. M. C., 1963, "The Motion and Frequency of Large Disturbance Waves in Annular Two-Phase Flow of Air-Water Mixtures," Chem. Eng. Sci., **18**(8), pp. 537–552.

[3] Woodmansee, D. E., and Hanratty, T. J., 1969, "Mechanism for the Removal of Droplets from a Liquid Surface by a Parallel Air Flow," Chem. Eng. Sci., **24**(2), pp. 299–307.

[4] Schadel, S. A., and Hanratty, T. J., 1989, "Interpretation of Atomization Rates of the Liquid Film in Gas-Liquid Annular Flow," Int. J. Multiphase Flow, **15**(6), pp. 893–900.

[5] Cooper, K. D., Hewitt, G. F., and Pinchin, B., 1964, "Photography of Two-Phase Gas-Liquid Flow," J. Photogr. Sci., **12**, pp. 269–278.

[6] Jacowitz, L. A., and Brodkey, R. S., 1964, "An Analysis of Geometry and Pressure Drop for the Horizontal Annular Two-Phase Flow of Water and Air in the Entrance Region of a Pipe," Chem. Eng. Sci., **19**(4), pp. 261–274.

[7] Arnold, C. R., and Hewitt, G. F., 1967, "Further Developments in the Photography of Two-Phase Gas-Liquid Flow," J. Photogr. Sci., **15**, pp. 97–114.

[8] Hewitt, G. F., and Hall-Taylor, N. S., 1970, *Annular Two-Phase Flow, Pergamon Press*, London, pp. 136–139.

[9] Whalley, P. B., 1987, *Boiling, Condensation, and Gas-Liquid Flow*, Clarendon Press, Oxford, pp. 92–93.

[10] Lane, W. R., 1951, "Shatter of Drops in Streams of Air," Ind. Eng. Chem., **43**(6), pp. 1312–1317.
[11] Wilkes, N. S., Azzopardi, B. J., and Thompson, C. P., 1983, "Wave Coalescence and Entrainment in Vertical Annular Two-Phase Flow," Int. J. Multiphase Flow, **9**(4), pp. 383–398.
[12] Holowach, M. J., Hochreiter, L. E., and Cheung, F. B., 2002, "A Model for Droplet Entrainment in Heated Annular Flow," Int. J. Heat Fluid Flow, **23**(6), pp. 807–822.
[13] Ishii, M., and Grolmes, M. A., 1975, "Inception Criteria for Droplet Entrainment in Two-Phase Concurrent Film Flow," AIChE J., **21**(2), pp. 308–318.
[14] Sevik, M., and Park, S. H., 1973, "Splitting of Drops and Bubbles by Turbulent Fluid Flow," ASME J. Appl. Mech. **95**(1), pp. 53–60.
[15] Pols, R. M., Hibberd, S., and Azzopardi, B. J., 1998, "Discontinuous Wave Solutions in Stratified and Annular Two-Phase Flows," 3rd International Conference on Multiphase Flow, Lyon, France, June 8–12.
[16] Asali, J. C., Hanratty, T. J., and Andreussi, P., 1985, "Interfacial Drag and Film Height for Vertical Annular Flow," AIChE J. **31**(6), pp. 895–902.
[17] Hewitt, G. F., and Lovegrove, P. C., 1969, "Frequency and Velocity Measurements of Disturbance Waves in Annular Two-Phase Flow," AKAEA Report No. AERE-R4304.
[18] Asali, J. C., and Hanratty, T. J, 1993, "Ripples Generated on a Liquid Film at High Gas Velocities," Int. J. Multiphase Flow, **19**(2), pp. 229–243.
[19] Zhu, Z., 2004, "A Study of the Interfacial Features of Gas-Liquid Annular Two-Phase Flow," Master's thesis, University of Saskatchewan, Saskatoon, Saskatchewan, Canada.
[20] Ohba, K., and Nagae, K., 1993, "Characteristics and Behavior of the Interfacial Wave on the Liquid Film in a Vertically Upward Air-Water Two-Phase Annular Flow," Nucl. Eng. Des., **141**(1–2), pp. 17–25.
[21] Martin, C. J., 1983, "Annular Two Phase Flow," Ph.D. thesis, Oxford University.
[22] Han, H., 2005, "An Entrainment Study for Two-Phase Upward Cocurrent Annular Flow in a Vertical Tube," Ph.D. thesis, University of Saskatchewan, Saskatoon, Saskatchewan, Canada.
[23] MacGillivray, R., and Gabriel, K. S., 2002, "Annular Flow Film Characteristics in Variable Gravity. Microgravity Transport Processes in Fluid, Thermal, Biological, and Material Sciences," Ann. N.Y. Acad. Sci., **974**, pp. 306–315.
[24] Zhao, L., and Rezkallah, K. S., 1993, "Gas-Liquid Flow Patterns at Microgravity Conditions," Int. J. Multiphase Flow, **19**(5), pp. 751–763.
[25] Andreussi, P., Asali, J. C., and Hanratty, T. J., 1985, "Initiation of Roll Waves in Gas-Liquid Flows," AIChE J., **31**(1), pp. 119–126.

Stability of Taylor–Couette Magnetoconvection With Radial Temperature Gradient and Constant Heat Flux at the Outer Cylinder

R. K. Deka
Department of Mathematics,
Gauhati University,
Guwahati-781 014,
India
e-mail: rkdg@sify.com

A. S. Gupta
Department of Mathematics,
Indian Institute of Technology,
Kharagpur-721 302,
India

An analysis is made of the linear stability of wide-gap hydromagnetic (MHD) dissipative Couette flow of an incompressible electrically conducting fluid between two rotating concentric circular cylinders in the presence of a uniform axial magnetic field. A constant heat flux is applied at the outer cylinder and the inner cylinder is kept at a constant temperature. Both types of boundary conditions viz; perfectly electrically conducting and electrically nonconducting walls are examined. The three cases of $\mu<0$ (counter-rotating), $\mu>0$ (co-rotating), and $\mu=0$ (stationary outer cylinder) are considered. Assuming very small magnetic Prandtl number P_m, the wide-gap perturbation equations are derived and solved by a direct numerical procedure. It is found that for given values of the radius ratio η and the heat flux parameter N, the critical Taylor number T_c at the onset of instability increases with increase in Hartmann number Q for both conducting and nonconducting walls thus establishing the stabilizing influence of the magnetic field. Further it is found that insulating walls are more destabilizing than the conducting walls. It is observed that for given values of η and Q, the critical Taylor number T_c decreases with increase in N. The analysis further reveals that for $\mu=0$ and perfectly conducting walls, the critical wave number a_c is not a monotonic function of Q but first increases, reaches a maximum and then decreases with further increase in Q. It is also observed that while a_c is a monotonic decreasing function of μ for $N=0$, in the presence of heat flux ($N=1$), a_c has a maximum at a negative value of μ (counter-rotating cylinders).
[DOI: 10.1115/1.2427080]

1 Introduction

The problem of the stability of an incompressible viscous flow between two concentric rotating circular cylinders (Couette flow) was first studied by Taylor [1]. He found experimentally that for narrow gap between the cylinders, the flow becomes unstable when the speed of the inner cylinder exceeds some critical value, the outer cylinder being at rest. The instability produced a steady secondary motion in the form of cellular toroidal vortices spaced regularly along the common axis of the cylinders. This problem was extended by Chandrasekhar [2] to the case when the fluid is electrically conducting and a uniform magnetic field acts along the common axis of the cylinders. He took the disturbances to be axisymmetric and formulated the problem under the assumption of narrow gap between the cylinders and a conducting fluid of very small magnetic Prandtl number P_m. It was found that for perfectly electrically conducting or insulated cylinder walls, the effect of the magnetic field is to inhibit the onset of instability. This inhibiting effect becomes more and more pronounced as the Hartmann number $Q=\mu_e^2 H^2 d^2 \sigma/(\rho\nu)$ is increased, where ρ, μ_e, d, σ, H, and ν denote the density of the fluid, magnetic permeability, gap width, electrical conductivity of the fluid, the magnetic field strength and the kinematic viscosity of the fluid, respectively. Experimentally, Donnelly and Ozima [3] and Donnelly and Caldwell [4] confirmed the results of Chandrasekhar [2] using mercury contained between Perspex and stainless-steel cylinders. Although not much differences in the results concerning stability were found in the two cases of perfectly conducting and insulating boundaries, the boundary conditions in the hydromagnetic stability problems are nevertheless nontrivial. These are described with clarity by Roberts [5] who extended the theoretical studies of Chandrasekhar on the hydromagnetic stability of Couette flow in the presence of a uniform axial magnetic field to include the cases of finite gap width and finitely conducting cylinders. He also investigated the nonaxisymmetric modes of instability.

It may be noted that the velocity distribution in the unperturbed state for circular Couette flow is always the same, regardless of whether the boundaries are electrically nonconducting or conducting or whether there is any axial magnetic field imposed at all or not. However one specific example where the boundary conditions do make a big difference is in the flow of an electrically conducting fluid confined in a spherical shell with the inner sphere rotating and the outer sphere at rest. A strong magnetic field is imposed parallel to the axis of rotation. While studying the flow and stability of this configuration, Hollerbach and Skinner [6] showed that the axisymmetric basic state depends strongly on the electromagnetic boundary conditions, with insulating boundaries yielding a shear layer, but conducting boundaries giving rise to a counter-rotating jet.

Chen and Chang [7] investigated the hydromagnetic dissipative Couette flow in the presence of a uniform axial magnetic field. The small-gap equations with respect to nonaxisymmetric disturbances were derived and solved for both stationary and oscillatory critical mode. Prior to this study, Chang and Sartory [8] investigated this problem with small-gap approximation, perfectly conducting cylinders, and axisymmetric stationary and oscillatory

Contributed by the Fluids Engineering Division of ASME for publication in the JOURNAL OF FLUIDS ENGINEERING. Manuscript received November 5, 2005; final manuscript received October 12, 2006. Assoc. Editor: Malcolm J. Andrews.

modes. It was shown by them that for sufficiently high magnetic field, axisymmetric oscillatory disturbances might become more critical than stationary disturbances. Other papers in this field are by Niblett [9] and Kurzweg [10], who investigated Chandrasekhar's problem [2] by different methods, assuming a narrow-gap, small magnetic Prandtl number, co-rotating, and counter-rotating cylinders, and electrically nonconducting or conducting cylinders. However, a fully numerical solution using the method of Harris and Reid [11] of the hydromagnetic Couette flow instability problem was presented by Takhar et al. [12] using narrow-gap approximation.

The combined effect of a radial temperature gradient and constant heat flux at the outer cylinder on the stability of Couette flow between two concentric rotating circular cylinders in the hydrodynamic case was studied by Ali et al. [13]. However their analysis is confined to narrow gap approximations. On the other hand Soundalgekar et al. [14] investigated the linear stability of wide-gap hydromagnetic Couette flow between two concentric circular cylinders in the presence of an axial magnetic field under isothermal condition. Note that the authors in this paper (Ref. [14]) did not consider magnetorotational instability (MRI) since they assumed that the electrically conducting fluid is of very small magnetic Prandtl number P_m. By contrast MRI was discovered by Velikhov [15] who showed that in the limit of large magnetic Prandtl number, a magnetic field can destabilize a rotating velocity field in which the angular momentum increases outwards. This result is significant to accretion disks in the astrophysical context [16]. Destabilization at large P_m was also studied by Rüdiger and Zhang [17] and Willis and Barenghi [18].

In this paper we present a linear stability analysis for wide-gap hydromagnetic dissipative Couette flow of an electrically conducting fluid (of very small magnetic Prandtl number) between two rotating concentric circular cylinders in the presence of a uniform axial magnetic field. The study of the present problem in the context of the papers by Ali et al. [13] and Soundalgekar et al. [14] is interesting for the following considerations: (i) while the analysis in Ref. [13] is restricted to hydrodynamic Couette flow with narrow-gap approximations, the problem studied here deals with hydromagnetic stability of Taylor–Couette flow with wide-gap approximations. (ii) In the problem investigated by Soundalgekar et al. [14], no thermal effects are considered and cylinder walls are assumed electrically nonconducting. But in our present study, Taylor–Couette magnetoconvection is investigated with radial temperature gradient and a constant heat flux at the outer cylinder. Further both the cases of perfectly electrically conducting and electrically nonconducting walls are examined. It may be noted that uniform heat flux condition at the wall may be more realistic than isothermal condition at the wall in some physical situation. For example if heat is supplied at the wall in the form of an electric current through a thin metallic foil (see Sparrow et al. [19]), uniform heat flux condition will hold at the wall. The study of the influence of temperature stratification on a Taylor–Couette flow system is important for different applications (see Mutabazi et al. [20]). Further a stabilized laminar motion of an electrically conducting fluid is essential in gaseous core nuclear reactors and power-generating devices where thermal effects are likely to be important.

The main motivation for the present study is that the results are likely to have bearing on the current hydromagnetic dynamo experiments using liquid sodium and gallium (which have very small magnetic Prandtl number). The dynamo process has recently been studied in the laboratory experiments by Gailitis et al. [21] and Steiglitz and Müller [22]. Due to the fact that dynamo action is associated with sheared or spiral flow, hydromagnetic Taylor–Couette flow is a suitable candidate for dynamo simulation. This explains the importance of our present study where the magnetic Prandtl number of the fluid is assumed to be very small (e.g., mercury or liquid sodium).

The paper is organized as follows. Section 2 presents the formulation of the linear stability problem, the governing equations, the boundary conditions, the various dimensionless parameters and the solution procedure for the eigenvalue problem. Section 3 contains results and discussion. Results for three typical cases are compared. These pertain to the flow between (i) a rotating inner wall with a stationary outer wall; (ii) counter-rotating walls; and (iii) co-rotating walls. In Sec. 4 conclusions are presented.

2 Linear Stability Analysis

Let r, θ, and z denote the cylindrical coordinates with the z axis coinciding with the common axis of two long concentric circular cylinders. The radii and the angular velocities of the inner and outer cylinder are R_1, R_2 and Ω_1, Ω_2, respectively.

2.1 Governing Hydromagnetic Equations. The momentum equation for an incompressible viscous and electrically conducting fluid is (Chandrasekhar [2])

$$\frac{\partial \vec{\mathbf{q}}}{\partial t} + (\vec{\mathbf{q}} \cdot \nabla)\vec{\mathbf{q}} = -\nabla\left(\frac{p}{\rho} + \mu_e \frac{|\vec{\mathbf{H}}|^2}{8\pi\rho}\right) + \upsilon\nabla^2\vec{\mathbf{q}} + \frac{\mu_e}{4\pi\rho}(\vec{\mathbf{H}} \cdot \nabla)\vec{\mathbf{H}} \tag{1}$$

The equation of continuity is

$$\nabla \cdot \vec{\mathbf{q}} = 0 \tag{2}$$

With the displacement currents neglected, Maxwell's equations are

$$\nabla \cdot \vec{\mathbf{H}} = 0 \tag{3}$$

$$\nabla \times \vec{\mathbf{H}} = 4\pi\vec{\mathbf{J}} \tag{4}$$

and

$$\nabla \times \vec{\mathbf{E}} = -\mu_e \frac{\partial \vec{\mathbf{H}}}{\partial t} \tag{5}$$

In the above equations, $\vec{\mathbf{q}}$, p, ρ, and ν denote the fluid velocity, pressure, density, and the kinematic viscosity, respectively. In electromagnetic units, $\vec{\mathbf{E}}$ and $\vec{\mathbf{H}}$ are the intensities of the electric and magnetic fields; $\vec{\mathbf{J}}$ is the current density; and μ_e is the magnetic permeability. The fluid is assumed to be nonmagnetic so that μ_e is taken as unity in all applications; it is retained only to identify units. Further we have Ohm's law relating the current density to the electric field, which is expressed as

$$\vec{\mathbf{J}} = \sigma(\vec{\mathbf{E}} + \mu_e\vec{\mathbf{q}} \times \vec{\mathbf{H}}) \tag{6}$$

where σ is the electrical conductivity of the fluid.

Elimination of $\vec{\mathbf{J}}$ and $\vec{\mathbf{E}}$ from Eqs. (4)–(6) gives on using Eq. (3), the following magnetic induction equation

$$\frac{\partial \vec{\mathbf{H}}}{\partial t} = \nabla \times (\vec{\mathbf{q}} \times \vec{\mathbf{H}}) + e\nabla^2\vec{\mathbf{H}} \tag{7}$$

where σ is assumed to be uniform and the magnetic diffusivity e is given by

$$e = \frac{1}{4\pi\mu_e\sigma} \tag{8}$$

Notice that the magnetic diffusivity differs from the usual definition by a factor $(1/4\pi)$. This is due to the fact that the electromagnetic variables are all measured in electromagnetic units.

The energy equation is

$$\rho C_p\left[\frac{\partial T}{\partial t} + (\vec{\mathbf{q}} \cdot \nabla)T\right] = k\nabla^2 T \tag{9}$$

where T, C_p, and k denote the temperature, specific heat at constant pressure, and the thermal conductivity of the fluid, respec-

tively. Further the variation of density with temperature is given by the equation of state

$$\rho = \rho_0[1 - \alpha(T - T_0)] \tag{10}$$

where α is the coefficient of thermal expansion and ρ_0 is the density at the reference temperature T_0.

2.2 Unperturbed Solution. For an electrically conducting fluid between two rotating co-axial circular cylinders with a constant magnetic field H applied in the axial (i.e., z direction) direction, the hydromagnetic Eqs. (1)–(3), (7), and (9) give the following stationary solution for velocity, magnetic field and temperature as

$$u = w = 0, \quad v = V(r), \quad f = g = 0, \quad h = H = \text{constant}, \quad T = \bar{T}(r) \tag{11}$$

Here (u,v,w) are the r, θ, and z components of velocity $\vec{\mathbf{q}}$ and (f,g,h) are the corresponding components of the magnetic field $\vec{\mathbf{H}}$. The solution Eq. (11) holds provided that

$$\frac{1}{\rho}\frac{ds}{dr} = \frac{V^2}{r} \tag{12a}$$

$$\nabla^2 V - \frac{V}{r^2} = 0 \tag{12b}$$

$$\frac{d^2\bar{T}}{dr^2} + \frac{1}{r}\frac{d\bar{T}}{dr} = 0 \tag{12c}$$

where $s(r)$ is the sum of the fluid pressure p and the magnetic pressure $\mu_e|\vec{\mathbf{H}}|^2/8\pi$ given by

$$s = p + \frac{\mu_e|\vec{\mathbf{H}}|^2}{8\pi} \tag{13}$$

in the unperturbed state. The solution of Eq. (12b) is consistent with the boundary conditions

$$V = \Omega_1 R_1 \quad \text{at } r = R_1; \quad V = \Omega_2 R_2 \quad \text{at } r = R_2 \tag{14}$$

is

$$V = Ar + \frac{B}{r} \tag{15}$$

where, as pointed out at the beginning of Sec. 2, Ω_1 and Ω_2 are the constant angular velocities of the inner and outer cylinder, respectively. The constants A and B are given by

$$A = \frac{\mu - \eta^2}{1 - \eta^2}\Omega_1, \quad B = \frac{R_1^2(1-\mu)}{1-\eta^2}\Omega_1, \quad \eta = \frac{R_1}{R_2}, \quad \mu = \frac{\Omega_2}{\Omega_1} \tag{16}$$

The steady temperature distribution $\bar{T}(r)$ given by Eq. (12c) satisfies the following boundary conditions

$$\bar{T} = T_1^0 \quad \text{at } r = R_1 \tag{17}$$

and

$$\frac{d\bar{T}}{dr} = \frac{q}{k} \quad \text{at } r = R_2 \tag{18}$$

where T_1^o is constant and q (>0) is the constant heat flux at the outer cylinder. The solution of Eq. (12c) obeying Eqs. (17) and (18) is

$$\bar{T} = T_1^0 + \frac{qR_2}{k}\ln\frac{r}{R_1} \tag{19}$$

2.3 Perturbation Equations. Denoting the disturbances in the velocity field by (u',v',w'), that in magnetic field by (f',g',h') and those in temperature, density, and pressure by T',ρ',s', respectively, the perturbed state of the fluid is described by

$$u', V + v', w', f', g', H + h', \bar{T} + T', \rho + \rho', s + s' \tag{20}$$

The disturbances are assumed to be axisymmetric about the z axis, and so they are independent of θ but dependent on r, z, and t only. Substituting these quantities Eq. (20) into the MHD Eqs. (1)–(10), and neglecting all terms that involve products and powers greater than one of the disturbance quantities, we obtain the following linearized equations

$$\rho\frac{\partial u'}{\partial t} - 2\rho\frac{V}{r}v' - \rho'\frac{V^2}{r} - \frac{\mu_e}{4\pi}H\frac{\partial f'}{\partial z} = -\frac{\partial s'}{\partial r} + \rho\nu\left(\nabla^2 u' - \frac{u'}{r^2}\right) \tag{21}$$

$$\rho\frac{\partial v'}{\partial t} + \rho\left(\frac{\partial V}{\partial r} + \frac{V}{r}\right)u' - \frac{\mu_e}{4\pi}H\frac{\partial g'}{\partial z} = \rho\nu\left(\nabla^2 v' - \frac{v'}{r^2}\right) \tag{22}$$

$$\rho\frac{\partial w'}{\partial t} - \frac{\mu_e}{4\pi}H\frac{\partial h'}{\partial z} = -\frac{\partial s'}{\partial z} + \rho\nu\nabla^2 w' \tag{23}$$

$$\frac{\partial f'}{\partial t} - H\frac{\partial u'}{\partial z} = e\left(\nabla^2 f' - \frac{f'}{r^2}\right) \tag{24}$$

$$\frac{\partial g'}{\partial t} - \left(\frac{\partial V}{\partial r} - \frac{V}{r}\right)f' - H\frac{\partial v'}{\partial z} = e\left(\nabla^2 g' - \frac{g'}{r^2}\right) \tag{25}$$

$$\frac{\partial h'}{\partial t} - H\frac{\partial w'}{\partial z} = e\nabla^2 h' \tag{26}$$

$$\frac{\partial u'}{\partial r} + \frac{u'}{r} + \frac{\partial w'}{\partial z} = 0 \tag{27}$$

$$\frac{\partial f'}{\partial r} + \frac{f'}{r} + \frac{\partial h'}{\partial z} = 0 \tag{28}$$

$$\frac{\partial \bar{T}}{\partial t} + \frac{\partial \bar{T}}{\partial r}u' = \frac{k}{\rho C_p}\nabla^2 T' \tag{29}$$

$$\rho + \rho' = \rho_0[1 - \alpha(\bar{T} + T' - T_0)] \tag{30}$$

Owing to the smallness of the thermal expansion coefficient α, a small temperature variation will lead to a small variation in the density. We shall assume that the density ρ is a constant except when multiplied by the centrifugal acceleration term V^2/r. This is the usual Boussinesq approximation. In view of Eq. (30), the term $\rho' V^2/r$ in Eq. (21) can be replaced by $-\rho\alpha T' V^2/r$.

By analyzing the disturbances into normal modes, we seek solutions of Eqs. (21)–(29) in the form

$$u' = u(r)e^{\sigma t}\cos\lambda z \; v' = v(r)e^{\sigma t}\cos\lambda z \; w' = w(r)e^{\sigma t}\sin\lambda z$$

$$f' = f(r)e^{\sigma t}\sin\lambda z \; g' = g(r)e^{\sigma t}\sin\lambda z \; h' = h(r)e^{\sigma t}\cos\lambda z$$

$$s' = s(r)e^{\sigma t}\cos\lambda z \; T' = T(r)e^{\sigma t}\cos\lambda z \tag{31}$$

where the disturbances are assumed to be axisymmetric and the axial wavelength λ is real. In view of the physical similarity of this problem with the stability of Taylor–Couette flow, it is likely that in the present problem the onset of instability will also be a steady secondary flow. Thus when the marginal state is stationary, we may put $\sigma=0$ in Eq. (31).

Substituting Eq. (31) with $\sigma=0$ in Eqs. (21)–(29) and replacing

$(dV/dr+V/r)$ by $2A$, $(dV/dr-V/r)$ by $-2B/r^2$, and $d\bar{T}/dr$ by its value from Eq. (19), we obtain the following perturbation equations

$$\nu\left(\frac{d^2}{dr^2}+\frac{1}{r}\frac{d}{dr}-\lambda^2-\frac{1}{r^2}\right)u=\frac{1}{\rho}\frac{ds}{dr}-2\frac{V}{r}v+\alpha\frac{V^2}{r}T-\frac{\lambda\mu_e}{4\pi\rho}Hf \tag{32}$$

$$\nu\left(\frac{d^2}{dr^2}+\frac{1}{r}\frac{d}{dr}-\lambda^2-\frac{1}{r^2}\right)v=2Au-\frac{\lambda u_e}{4\pi\rho}Hg \tag{33}$$

$$\nu\left(\frac{d^2}{dr^2}+\frac{1}{r}\frac{d}{dr}-\lambda^2\right)w=-\frac{\lambda}{\rho}s+\frac{\lambda\mu_e}{4\pi\rho}Hh \tag{34}$$

$$e\left(\frac{d^2}{dr^2}+\frac{1}{r}\frac{d}{dr}-\lambda^2-\frac{1}{r^2}\right)f=\lambda Hu \tag{35}$$

$$e\left(\frac{d^2}{dr^2}+\frac{1}{r}\frac{d}{dr}-\lambda^2-\frac{1}{r^2}\right)g=2Hv+2\frac{B}{r^2}f \tag{36}$$

$$e\left(\frac{d^2}{dr^2}+\frac{1}{r}\frac{d}{dr}-\lambda^2\right)h=-\lambda Hw \tag{37}$$

$$\left(\frac{d}{dr}+\frac{1}{r}\right)u=-\lambda w \tag{38}$$

$$\left(\frac{d}{dr}+\frac{1}{r}\right)f=\lambda h \tag{39}$$

$$\frac{k}{\rho C_p}\left(\frac{d^2}{dr^2}+\frac{1}{r}\frac{d}{dr}-\lambda^2\right)T=\frac{qR_2}{rk}u \tag{40}$$

Eliminating s from Eqs. (32) and (34), we can rewrite the above equations as

$$(DD^*-\lambda^2)\left(\frac{1}{\lambda}Dw+u\right)=-\frac{2}{\nu}\frac{V}{r}v+\frac{a}{\nu}\frac{V^2}{r}T-\frac{\lambda\mu_e}{4\pi\nu\rho}H\left(f-\frac{1}{\lambda}Dh\right) \tag{41}$$

$$(DD^*-\lambda^2)v=\frac{2A}{\nu}u-\frac{\lambda\mu_e}{4\pi\nu\rho}Hg \tag{42}$$

$$(DD^*-\lambda^2)f=\frac{\lambda}{e}Hu \tag{43}$$

$$(DD^*-\lambda^2)g=\frac{\lambda}{e}Hv+2\frac{B}{er^2}f \tag{44}$$

$$(D^*D-\lambda^2)h=-\frac{\lambda}{e}Hw \tag{45}$$

$$D^*u=-\lambda w \tag{46}$$

$$D^*f=\lambda h \tag{47}$$

$$(D^*D-\lambda^2)T=\rho C_p\frac{qR_2}{rk^2}u \tag{48}$$

where

$$D=\frac{d}{dr},\quad D^*=\frac{d}{dr}+\frac{1}{r},\quad DD^*=\frac{d^2}{dr^2}+\frac{1}{r}\frac{d}{dr}-\frac{1}{r^2}$$

$$D^*D=\frac{d^2}{dr^2}+\frac{1}{r}\frac{d}{dr} \tag{49}$$

Using Eqs. (43), (46), and (47) and eliminating w, f, and h, we obtain from Eq. (41)

$$\left[(DD^*-\lambda^2)^2+\frac{\lambda^2\mu_e H^2}{4\pi e\rho\nu}\right]u=2\frac{\lambda^2}{\nu}\frac{V}{r}v-\frac{\alpha\lambda^2}{\nu}\frac{V^2}{r}T \tag{50}$$

It was shown by Chandrasekhar (Ref. [2], p. 403) that for flow of liquid metals like mercury for which the magnetic Prandtl number $P_m(=\nu/e)$ is very small, the second term on the right-hand side of Eq. (44) in comparison with the first term can be neglected. An alternative explanation for this result can be given as follows. Since the flow takes place under laminar conditions in the presence of a magnetic field (which has a tendency to stabilize the flow), a typical Reynolds number Re for the flow can be taken as $(\Omega_1 R_1)d/\nu)$ which is of order one. Hence the magnetic Reynolds number $\mathrm{Re}_m=(P_m.\mathrm{Re})$ is very small since $P_m\ll 1$. Thus the second term on the right hand side of Eq. (44) which is a measure of the induced magnetic field can be neglected in comparison with the first term (involving H), which is a measure of the imposed field.

Thus we get

$$(DD^*-\lambda^2)g=\frac{\lambda}{e}Hv \tag{51}$$

Operating by $(DD^*-\lambda^2)$ on Eq. (51) and eliminating v by using Eq. (42), we obtain

$$\left[(DD^*-\lambda^2)^2+\frac{\lambda^2\mu_e H^2}{4\pi e\rho\nu}\right]g=2\frac{\lambda AH}{e\nu}u \tag{52}$$

Further elimination of v from Eqs. (50) and (51) gives

$$\left[(DD^*-\lambda^2)^2+\frac{\lambda^2\mu_e H^2}{4\pi e\rho\nu}\right]u=2\frac{Ve\lambda}{\nu Hr}(DD^*-\lambda^2)g-\frac{\alpha\lambda^2V^2T}{\nu r} \tag{53}$$

We now introduce the dimensionless quantities

$$x=\frac{r-R_1}{d},\quad a=\lambda d,\quad \xi=\frac{r}{R_2},\quad \bar{u}=\frac{ud}{\nu},\quad \bar{g}=\frac{g}{H},\quad Q=\frac{\mu_e H^2d^2}{4\pi e\rho\nu}$$

$$G(x)=\frac{V}{r\Omega_1}=A_1+\frac{B_1}{\xi^2},$$

$$\theta=\frac{k}{qd}T,\quad A_1=\frac{\mu-\eta^2}{1-\eta^2},\quad B_1=\frac{\eta^2(1-\mu)}{1-\eta^2} \tag{54}$$

Here Q is the Hartmann number representing the strength of the imposed magnetic field and d is the gap width R_2-R_1.

Further the dimensionless operators $\bar{D}$ and $\bar{D}^*$ are defined by

$$D=\frac{1}{d}\bar{D},\quad D^*=\frac{1}{d}\bar{D}^* \tag{55}$$

Then using Eq. (54), the governing equations for the perturbations $\bar{u}$, $\bar{g}$, and θ given by Eqs. (48), (52), and (53) can be written in dimensionless form after dropping the bars over the operators as

$$(D^*D-a^2)\theta=\frac{\mathrm{Pr}}{\xi}\bar{u} \tag{56}$$

$$[(DD^*-a^2)^2+Qa^2]\bar{g}=\frac{2\lambda Ad^3}{e}\bar{u} \tag{57}$$

$$[(DD^*-a^2)^2+Qa^2]\bar{u}=\frac{2ad^2\Omega_1 Ge}{\nu^2}(DD^*-a^2)\bar{g}-\frac{a^2d^4\alpha\Omega_1^2G^2\xi R_2q}{\nu^2k}\theta \tag{58}$$

Now with the transformations

$$\bar{g} = \frac{2\lambda A d^3}{e} \cdot \overline{g_1}, \quad \theta = \mathrm{Pr} \cdot \overline{\theta_1} \tag{59}$$

Eq. (57) becomes

$$[(DD^* - a^2)^2 + Qa^2]\overline{g_1} = \bar{u} \tag{60}$$

while Eq. (58) reduces to

$$[(DD^* - a^2)^2 + Qa^2]\bar{u} = -a^2 T_1 G(x)[(DD^* - a^2)\overline{g_1} + N\xi G(x)\overline{\theta_1}] \tag{61}$$

Here T_1 is Taylor number given by

$$T_1 = -\frac{4A\Omega_1 d^4}{\nu^2} \tag{62}$$

and N stands for

$$N = -\frac{\alpha\Omega_1 R_2 q \mathrm{Pr}}{4kA} \tag{63}$$

Note that A as defined by Eq. (16) is negative because $\mu < \eta^2$ in view of the instability of flow and $\eta^2 < 1$. Thus $T_1 > 0$ and N is the ratio of Rayleigh number Ra and Taylor number T_1, where

$$\mathrm{Ra} = \frac{\alpha\Omega_1^2 R_2 q d^4 \mathrm{Pr}}{\nu^2 k} \tag{64}$$

Notice that Rayleigh number defined above does not contain the factor g (the acceleration due to gravity). In fact g is replaced by outward directed centrifugal force generated by the rotation of the cylinders. This also means that the effective gravity which is related to $G(x)$ varies with r. It may further be observed that the parameter N may be regarded as the ratio of thermal to rotational driving.

Equation (56) for θ now becomes

$$(D^*D - a^2)\overline{\theta_1} = \frac{\bar{u}}{\xi} \tag{65}$$

Thus Eqs. (60), (61), and (65) are the perturbation equations for $\bar{u}$, g_1, and θ_1. These equations are to be solved with requisite boundary conditions for $\bar{u}$, $\overline{g_1}$, and $\overline{\theta_1}$.

2.4 Boundary Conditions. First, the boundary conditions on the velocity components require that they vanish on the walls (no-slip conditions). According to Eq. (46), the condition $w=0$ at the walls can be replaced by $D^*u=0$ at $x=0$ and $x=1$. Further since $u=0$ at the walls, we must have $Du=0$ at $x=0$ and $x=1$. This in turn implies from Eq. (54) that $D\bar{u}=0$ at $x=0$ and $x=1$. From Eqs. (51), (54), and (59), the condition $v=0$ at the walls implies $(DD^*-a^2)\overline{g_1}=0$ at $x=0$ and $x=1$.

Secondly, the boundary conditions on the magnetic field depend on the electrical properties of the cylinders confining the fluid. We shall consider two cases:

1. Electrically nonconducting cylinders; and
2. Perfectly conducting cylinders.

In case (1), no currents in the fluid can cross the cylinders so that $J_r=0$ at the cylinders, where J_r is the radial component of the current density $\vec{\mathbf{J}}$. Using this, Maxwell's equation $\nabla\times\vec{\mathbf{H}}=4\pi\vec{\mathbf{J}}$ and the normal mode resolution Eq. (31), we get $g=0$ at $x=0$ and $x=1$. This in turn implies from Eqs. (53) and (59) that $\overline{g_1}=0$ at $x=0$ and $x=1$.

For perfectly conducting cylinders, no magnetic field can cross the boundary and we must have $f=0$ and $J_z=0$ on the cylinders. The second condition implies $(\nabla\times\vec{\mathbf{H}})_z=0$ which for the form of the solutions assumed requires $D^*g=0$ at the cylinder walls. It then follows from Eqs. (54) and (59) that $D^*\overline{g_1}=0$ at $x=0$ and $x=1$.

Finally, we consider the boundary conditions on the temperature. Since temperature is fixed on the inner cylinder and the heat flux is prescribed on the outer cylinder, we must have $\theta=0$ at $x=0$ and $D\theta=0$ at $x=1$. Using Eqs. (54) and (59), this implies $\overline{\theta_1}=0$ at $x=0$ and $D\overline{\theta_1}=0$ at $x=1$. It may be noted that uniform heat flux condition at the walls may be more realistic than isothermal conditions at the walls in some physical situations as pointed out earlier by Sparrow et al. [19].

Thus the boundary conditions on the cylinder walls are

1. For perfectly conducting cylinders

$$\bar{u} = D\bar{u} = D^*\bar{g}_1 = (DD^* - a^2)\overline{g_1} = \overline{\theta_1} = 0 \quad \text{at } x = 0 \tag{66}$$

$$\bar{u} = D\bar{u} = D^*\bar{g}_1 = (DD^* - a^2)\overline{g_1} = D\overline{\theta_1} = 0 \quad \text{at } x = 1 \tag{67}$$

2. For electrically nonconducting cylinders

$$\bar{u} = D\bar{u} = \bar{g}_1 = (DD^* - a^2)\overline{g_1} = \overline{\theta_1} = 0 \quad \text{at } x = 0 \tag{68}$$

$$\bar{u} = D\bar{u} = \bar{g}_1 = (DD^* - a^2)\overline{g_1} = D\overline{\theta_1} = 0 \quad \text{at } x = 1 \tag{69}$$

Note that the boundary condition $f=0$ at $x=0$ and $x=1$ on perfectly conducting cylinders is not needed for the solution of the eigenvalue problem although this condition will be required for determining the radial component of the magnetic field.

2.5 Numerical Solution of the Eigenvalue Problem. The homogenous system of Eqs. (60), (61), and (65) with the boundary conditions Eqs. (66) and (67) for perfectly conducting cylinders and Eqs. (68) and (69) for electrically nonconducting cylinders determine an eigenvalue problem of the form

$$F(\mu, Q, \eta, N, a, T_1) = 0 \tag{70}$$

For given values of μ, Q, N, and η we seek the minimum real positive values of the Taylor number T_1 for which there is a nontrivial solution of Eq. (70). This gives the critical Taylor number T_c for assigned values of μ, Q, N, and η. The wave number a_c corresponding to T_c determines the critical wave number at the onset of instability. We solve the aforementioned eigenvalue problem by a shooting technique together with a unit disturbance method. The method used in the present study has been widely used by several workers for similar hydrodynamic stability problems, for example, Chen and Chang [7]. For details, the reader is referred to Harris and Reid [11]. In order to obtain a faster convergence of the iteration, we use a modified algorithm developed by Chen and Chang [7] for this eigenvalue problem.

3 Numerical Results and Discussion

In the numerical study, the Hartmann number Q is varied from 10 to 650 for a range of values of η from 0.95 to 0.1 and for a range of values of $\mu < \eta^2$. For $\mu > \eta^2$, the flow is known to be stable to axisymmetric disturbances of the form Eq. (31). For $\eta = 0.4$ (wide-gap) values of μ are considered in the range $-0.4 \leq \mu \leq 0.4$.

3.1 Verification of Computer Code. To verify our computer code, we check the results in terms of a_c and T_c and compare these values with the corresponding values derived by Takhar et al. [23] who studied the stability of hydrodynamic Couette flow ($Q=0$) between concentric rotating cylinders under wide gap approximations in the absence of constant heat flux at the wall ($N=0$) (see Table 1). There is an excellent agreement between the two results. This shows that our computer code can be used with great confidence.

3.2 Effect of Constant Heat Flux at the Outer Cylinder. To study the effect of the supply of constant heat flux at the outer cylinder, small as well as large values of N are considered. It follows from the definition of A in Eq. (16) that for μ very near η^2, it is possible to have large values of N. Numerical results are given in Table 2 for $\eta=0.95$, 0.8, 0.6, 0.4, 0.2, 0.1, $\mu=0$, $Q=0$,

Table 1 Comparison of the values of a_c and T_c calculated in the present study (A) with those of Takhar et al.[a] (B) when $N=0$, $Q=0$ for various values of μ and η

		A	B	A	B
η	μ	a_c		T_c	
0.9	−1.5	5.579	5.58	69,641.69	69,640.82
0.9	−1.0	4.407	4.41	27,142.11	27,135.50
0.75	−0.75	4.316	4.312	27,981.06	27,973.68
0.5	−0.50	4.798	4.8	52,235.44	52,217.36
0.4	−0.25	3.810	3.811	30,115.48	30,110.89
0.3	−0.1	3.364	3.361	22,120.76	22117.03
0.2	−0.1	4.248	4.250	82,111.54	82,090.37
0.1	−0.01	3.424	3.424	87,867.43	87,873.32

[a]See Ref. [23].

50, 100, and $N=0$, 5, and 10 for both perfectly conducting and electrically nonconducting walls and further illustrated in Figs. 1–6.

3.3 Inhibiting Influence of Magnetic Field on Stability. Table 2 shows that for a given value of heat flux parameter N, an increase in Hartmann number Q results in increase in T_c. Thus the magnetic field has an inhibiting effect on the onset of instability. The physical reason for this is that in addition to dissipation of mechanical energy due to viscosity arising out of shearing of fluid between the rotating cylinders, there will be dissipation of magnetic energy due to Joule heating. In a conducting fluid where the effect of electrical resistance is important (fluid of small magnetic Prandtl number P_m as in our present problem), the effect of the magnetic force can be regarded as giving rise to a strong magnetic viscosity in the presence of a magnetic field. This tends to destroy motion across the magnetic lines of force. This in turn prevents an easy closing of the streamlines required for the onset of instability. Thus a magnetic field exerts a stabilizing influence on the flow. An

Table 2 The values of T_c and a_c, for assigned values of N, Q, η, $\mu=0$ for both conducting and nonconducting walls. The values within brackets are for nonconducting walls

η	Q	N	a_c	T_c
0.95	0	0	3.127	3509.65
		5	2.819	843.09
		10	2.771	478.01
	50	0	3.492(2.367)	16,090.92 (11,788.95)
		5	2.256 (2.191)	1460.78 (1392.83)
		10	2.216 (2.183)	759.19 (740.22)
	100	0	3.414 (1.728)	34,880.34 (22,037.59)
		5	1.951 (1.903)	1890.83 (1813.67)
		10	1.932 (1.907)	966.55 (945.88)
0.8	0	0	3.132	3988.59
		5	2.837	1041.83
		10	2.785	597.78
	50	0	3.477 (2.379)	18,090.67 (13,345.04)
		5	2.262 (2.193)	1832.34 (1741.33)
		10	2.218 (2.185)	957.27 (931.50)
	100	0	3.399 (1.739)	39,089.66 (24,926.25)
		5	1.949 (1.897)	2377.56 (2272.81)
		10	1.927 (1.900)	1219.17 (1190.88)
0.6	0	0	3.148	5143.08
		5	2.879	1557.65
		10	2.821	915.40
	50	0	3.436 (2.406)	22,650.64(16,975.77)
		5	2.285 (2.208)	2816.84 (2661.78)
		10	2.234 (2.192)	1489.18 (1444.04)
	100	0	3.350 (1.769)	48,506.64 (31,600.28)
		5	1.952 (1.892)	3676.45 (3492.21)
		10	1.926 (1.896)	1899.43 (1848.77)
0.4	0	0	3.183	7996.05
		5	2.957	3011.82
		10	2.897	1849.87
	50	0	3.345 (2.462)	32,997.60 (25,562.51)
		5	2.347 (2.247)	56,99.07 (5347.31)
		10	2.277 (2.228)	3093.30 (2984.72)
	100	0	3.205 (1.834)	69,143.20 (47,178.45)
		5	1.976 (1.904)	7540.40 (7096.92)
		10	1.944 (1.908)	3965.95 (3838.98)
0.2	0	0	3.263	20,715.32
		5	3.128	11,208.48
		10	3.060	7649.97
	50	0	3.148 (2.589)	73,212.88 (61,485.44)
		5	2.546 (2.405)	23,172.90 (21,665.43)
		10	2.448 (2.372)	13,680.76 (13,130.19)
	100	0	2.806 (1.988)	14,3770.00 (110,970.7)
		5	2.104 (1.987)	32,014.22 (29,835.64)
		10	2.043 (1.983)	17,957.25 (17,243.80)
0.1	0	0	3.345	64,602.20
		5	3.268	46,706.11
		10	3.229	36,411.24
	50	0	3.076 (2.725)	197,020.30 (178,029.1)
		5	2.809 (2.641)	105,268.91 (99,345.38)
		10	2.722 (2.584)	71,522.31 (68,700.57)
	100	0	2.695 (2.177)	36,0115.60 (313,202.1)
		5	2.385 (2.152)	154,925.40 (145,212.5)
		10	2.281 (2.152)	98,545.90 (94471.9)

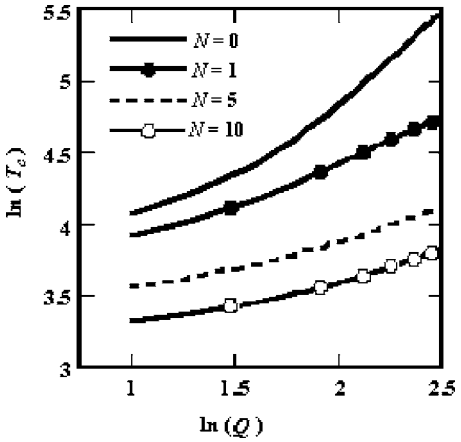

Fig. 1 The variation of T_c with Q for η=0.4, μ=0, and N (conducting walls)

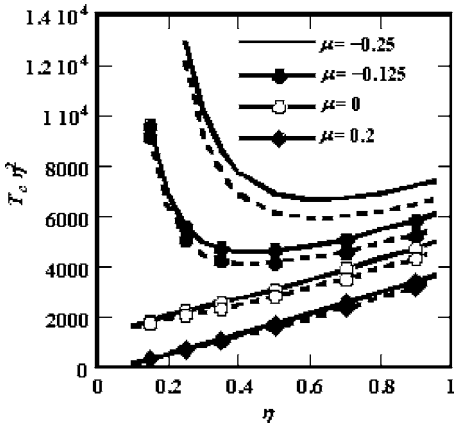

Fig. 4 The variation of T_c with η for N=1.0, Q=50, and μ. The solid curves are drawn for conducting walls, while the dashed ones are for nonconducting walls.

interesting result which is observed from Table 2 is that for given values of η, Q, and N, the critical values of Taylor number T_c for conducting walls is greater than the corresponding value for electrically nonconducting walls. Thus we see that the insulating walls are more destabilizing than the conducting walls. It may be further noticed from Table 2 that as the gap width between the cylinders increases (i.e., η decreases), the critical Taylor number T_c progressively increases for given values of Q and N. For example, with Q=100 and N=5, we find that T_c=1890.83 for η=0.95 (narrow gap) but T_c=32,014.22 when η=0.2 (wide gap). Hence we find that the wider the gap, the more stable is the flow. A novel result emerging from the analysis (see Table 2) is that for given values of η and Q, T_c gradually decreases with increase in N.

Figure 1 shows the variation of T_c with the magnetic parameter Q for several values of N when μ=0 and η=0.4 in the case of perfectly conducting walls. It is observed that for given values of η and N, T_c increases with the increase in Q, which shows that the magnetic field is stabilizing. Figure 2 displays the variation of T_c with N for a given value of Q (=50) and several values of μ (both positive and negative) when η=0.4 and the walls are perfectly conducting. The progressive decrease in T_c with increase in N shows that increase in heat flux at the outer cylinder has a destabilizing influence on the flow. This result may be physically explained as follows. As defined in Eq. (63) and (64), the parameter N can be regarded as the ratio of thermal to rotational driving. Hence for a given Taylor number, N is a measure of thermal force, which in turn depends on the heat flux at the outer cylinder. Now when the heat flux q ($>$0) is increased, a stage will be reached when the radial temperature gradient across the cylinders becomes positive since the temperature of the inner cylinder is held fixed. The stability of this flow system with respect to axisymmetric disturbances has an analogy with the stability of a horizontal layer of quiescent fluid heated from below in a field of gravity as in Rayleigh–Benard flow. So long as only axisymmetric perturbations are considered, one may ignore the flow and think of the fluid as being subject to a radially outward gravitational field which in the analogy is towards the heated wall. This is what leads

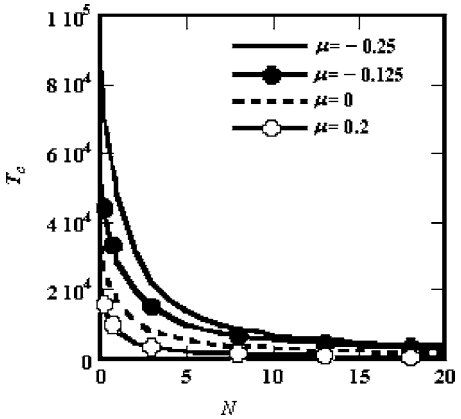

Fig. 2 The variation of T_c with N for η=0.4, Q=50, and μ (conducting walls)

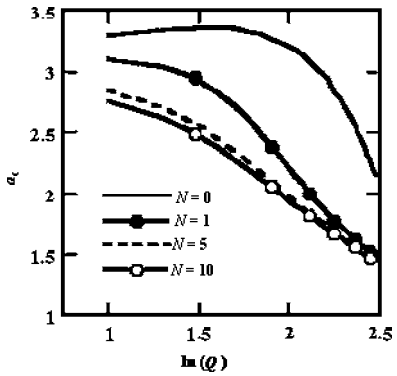

Fig. 3 The variation of a_c with Q for η=0.4, μ=0, and N (conducting walls)

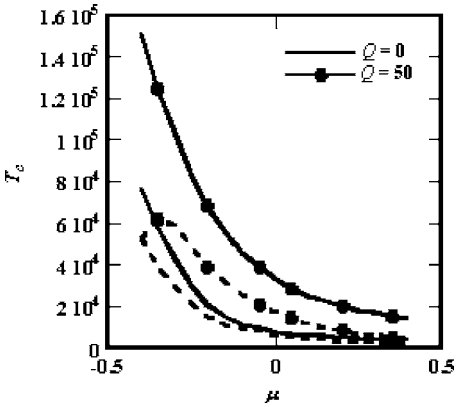

Fig. 5 The variation of T_c with μ for η=0.4 and Q (conducting walls). The solid curves are drawn for N=0, while the dashed ones are for N=1.

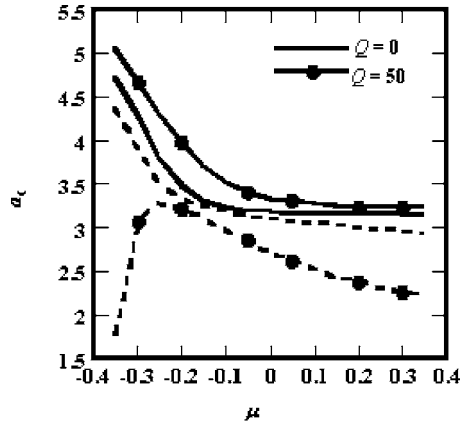

(*a*)

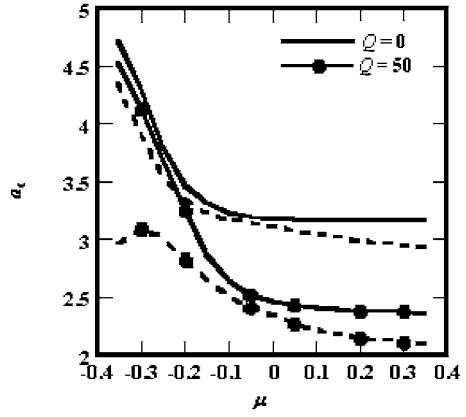

(*b*)

Fig. 6 (*a*) The variation of a_c with μ for $\eta=0.4$ and Q (conducting walls). The solid curves are drawn for $N=0$, while the dashed ones are for $N=1$. (*b*) The variation of a_c with μ for $\eta=0.4$ and Q (nonconducting walls). The solid curves are drawn for $N=0$, while the dashed ones are for $N=1$.

to the positive radial temperature gradient to be stabilizing.

Figure 3 shows the variation of the critical wave number a_c with Q in the case of perfectly conducting walls for several values of N when $\eta=0.4$ (wide-gap case) and $\mu=0$. Note that the value of T_1 in this figure is in fact the critical Taylor number T_c at the onset of instability. Since in Fig. 3, $\mu=0$, $\eta=0.4$, and the walls are conducting, it follows from the eigenvalue problem Eq. (70) that for given values of Q and N, Taylor number T_1 is a function of the wave number a only. The minimum positive value T_c is found for $a=a_c$. Thus for every pair of values of Q and N in Fig. 3, we can find a_c which corresponds to a particular T_c. It is observed that for $N=0$, there is an initial increase in a_c with an increase in Q but for Q greater than about 50, a_c starts decreasing with further increase in Q. A plausible physical explanation for this is as follows. With the increase in Q (with $N=0$) Taylor cells become narrower (see Chandrasekhar [2]) resulting in an increase in a_c (disturbances being assumed axisymmetric). But when Q becomes fairly large, nonaxisymmetric instability modes prevail and this explains the anomalous behavior of a_c with change in Q for $N=0$. Chen and Chang [7] also obtained similar results in their study of dissipative Couette flow with nonaxisymmetric disturbances. The variation of a_c with Q for higher values of N is also shown in Fig. 3.

Figure 4 displays the variation of $T_c\eta^2$ with η for $N=1.0$, $Q=50$, and for several positive and negative values of μ. It is observed that for given values of η, N, and Q, the critical Taylor number T_c decreases with increase in μ (>0). The solid curves shown in this figure correspond to conducting walls, while the dashed curves correspond to electrically insulating walls. It is interesting to observe that the behavior of $T_c\eta^2$ can be predicted linearly with respect to η from η close to 1, with deviation from linearity occurring for $\eta<0.5$. Thus the wide gap effects are sensible for $\eta<0.5$ and negative values of μ. Finally using similar arguments as in the case of Fig. 3, we may say that the values of a in Figs. 1, 2, and 4 correspond to critical wave number a_c at the onset of instability, which corresponds to the values of T_c in these figures.

Variation of T_c with μ for $\eta=0.4$ and perfectly conducting walls and for assigned values of Q (=0 and 50) is shown in Fig. 5 in two cases: $N=0$ and $N=1$. It is interesting to note that in the presence of magnetic field ($Q=50$) and constant heat flux ($N=1$) at the outer cylinder, the variation of T_c with μ is not a monotonic decreasing function of μ. Instead T_c has a maximum at a negative value of μ (counter-rotating cylinders) such that $|\mu|\sim 0.3$. In the absence of heat flux ($N=0$), however, T_c is a monotonic decreasing function of μ. On the other hand the variation of a_c with μ for $\eta=0.4$ and for $Q=0$ and 50 is depicted in Fig. 6(*a*) for perfectly conducting walls and in Fig. 6(*b*) for nonconducting walls. It is observed that for no heat flux at the outer cylinder ($N=0$), a_c is a monotonic decreasing function of μ for any value of Q. But in the presence of a magnetic field ($Q=50$) and heat flux ($N=1$), a_c is not a monotonic function of μ. In this case a_c has a maximum at a negative value of μ (counter-rotating cylinders). The physical reason for both T_c and a_c to behave in this anomalous way for nonzero heat flux perhaps lies in the circumstance that when μ is sufficiently large and negative (counter-rotating cylinders), the disturbances which manifest themselves at the onset of instability in the hydromagnetic case and for nonzero heat flux are nonaxisymmetric. In this connection mention may be made of the analysis of Chen and Chang [7] who found that for MHD dissipative Couette flow between two concentric cylinders whose walls are nonconducting, the critical disturbance at the onset of instability is a nonaxisymmetric mode as the value of μ is sufficiently negative and the domain of Q for which axisymmetric modes prevail is rather limited. They also obtained similar results for perfectly conducting walls at a low Hartmann number.

4 Conclusions

A linear stability analysis is presented for wide-gap hydromagnetic (MHD) dissipative Couette flow of an incompressible electrically conducting fluid between two concentric circular cylinders in the presence of a uniform axial magnetic field and with a constant heat flux at the outer cylinder. It is shown that for given values of the radius ratio η and the heat flux parameter N, the critical Taylor number T_c at the onset of instability increases with increase in Hartmann number Q for both electrically conducting and electrically insulating walls. It is also found that insulating walls are more destabilizing than the conducting walls. The analysis reveals that the wider the gap, the more stable the flow. It is observed that for given values of η and Q, increase in N results in a decrease in T_c. It is found that for a stationary outer cylinder and perfectly conducting walls, the critical wave number a_c first increases, reaches a maximum, and then decreases with further increase in Q. The analysis further reveals that although a_c is a monotonic decreasing function of μ ($=\Omega_2/\Omega_1$, where Ω_1, Ω_2 are the angular velocities of the inner and outer cylinder) for $N=0$, in the presence of heat flux ($N=1$), a_c has a maximum at a negative value of μ (counter-rotating cylinders).

Acknowledgments

The authors thank the referees for their useful comments, which enabled an improved presentation of the paper. One of the authors (R.K.D.) was supported by University Grants Commission (Research & Award Bureau), New Delhi while the other (A.S.G.)

acknowledges the financial assistance of Indian National Science Academy, New Delhi for carrying out this research.

References

[1] Taylor, G. I., 1923, "Stability of a Viscous Liquid Contained Between Two Rotating Cylinders," Philos. Trans. R. Soc. London, Ser. A, **223**, pp. 289–343.
[2] Chandrasekhar, S., 1961, *Hydrodynamic and Hydromagnetic Stability*, Clarendon Press, Oxford, UK.
[3] Donnelly, R. J., and Ozima, M., 1962, "Experiments on the Stability of Flow Between Rotating Cylinders in the Presence of a Magnetic Field," Proc. R. Soc. London, Ser. A, **226**, pp. 272–286.
[4] Donnelly, R. J., and Caldwell, D. R., 1963, "Experiments on the Stability of Hydromagnetic Couette Flow," J. Fluid Mech., **19**, pp. 257–263.
[5] Roberts, P. H., 1964, "The Stability of Hydromagnetic Couette Flow," Proc. Cambridge Philos. Soc., **60**, pp. 635–651.
[6] Hollerbach, R., and Skinner, S., 2001, "Instabilities of Magnetically Induced Shear Layers and Jets," Proc. R. Soc. London, Ser. A, **457**, pp. 785–802.
[7] Chen, C. K., and Chang, M. H., 1998, "Stability of Hydromagnetic Dissipative Couette Flow With Nonaxisymmetric Disturbance," J. Fluid Mech., **366**, pp. 135–158.
[8] Chang, T. S., and Sartory, W. K., 1967, "On the Onset of Instability by Oscillatory Modes in Hydromagnetic Couette Flow," Proc. R. Soc. London, Ser. A, **301**, pp. 451–471.
[9] Niblett, E. R., 1958, "The Stability of Couette Flow in an Axial Magnetic Field," Can. J. Phys., **36**, pp. 1509–1525.
[10] Kurzweg, U. H., 1963, "The Stability of Couette Flow in the Presence of an Axial Magnetic Field," J. Fluid Mech., **17**, pp. 52–60.
[11] Harris, D. L., and Reid, W. H., 1964, "On the Stability of Viscous Flow Between Rotating Cylinders, Part 2 Numerical Analysis," J. Fluid Mech., **20**, pp. 95–101.
[12] Takhar, H. S., Ali, M. A., and Soundalgekar, V. M., 1989, "Stability of MHD Couette Flow in a Narrow Gap Annulus," Appl. Sci. Res., **46**, pp. 1–24.
[13] Ali, M. A., Takhar, H. S., and Soundalgekar, V. M., 1992, "Stability of Flow Between Two Rotating Cylinders in the Presence of a Constant Heat Flux at the Outer Cylinder," J. Appl. Mech., **59**, pp. 464–465.
[14] Soundalgekar, V. M., Ali, M. A., and Takhar, H. S., 1994, "Hydromagnetic Stability of Dissipative Couette Flow: Wide-Gap Problem," Int. J. Energy Res., **18**, pp. 689–695.
[15] Velikhov, E. P., 1959, "Stability of an Ideally Conducting Liquid Flowing Between Cylinders Rotating in a Magnetic Field," Sov. Phys. JETP, **36**, pp. 1398–1404.
[16] Balbus, S. A., and Hawley, J. F., 1991, "A Powerful Local Shear Instability in Weakly Magnetized Disks. I. Linear Analysis," Astrophys. J., **376**, pp. 214–222.
[17] Rüdiger, G., and Zhang, Y., 2001, "MHD Instability in Differentially-Rotating Cylindric Flows," Astron. Astrophys., **378**, pp. 302–308.
[18] Willis, A. P., and Barenghi, C. F., 2002, "Magnetic Instability in a Sheared Azimuthal Flow," Astron. Astrophys., **388**, pp. 688–691.
[19] Sparrow, E. M., Goldstein, R. J., and Jonsson, U. K., 1964, "Thermal Instability in a Horizontal Fluid Layer: Effect of Boundary Conditions and Nonlinear Temperature Profiles," J. Fluid Mech., **18**, pp. 513–528.
[20] Mutabazi, I., Goharzadeh, A., and Dumouchel, F., 2001, "The Circular Couette Flow With a Radial Temperature Gradient," *Proceedings 12th International Couette-Taylor Workshop*, Evanston, IL, September 6–8.
[21] Gailitis, A. et al., 2001, "Magnetic Field Saturation in the Riga Dynamo Experiment," Phys. Rev. Lett., **86**(14), pp. 3024–3027.
[22] Stieglitz, R., and Müller, U., 2001, "Experimental Demonstration of a Homogeneous Two-scale Dynamo," Phys. Fluids, **13**(3), pp. 561–564.
[23] Takhar, H. S., Ali, M. A., and Soundalgekar, V. M., 1989, "Stability of the Flow Between Rotating Cylinders-Wide Gap Problem," J. Fluids Eng., **111**, pp. 97–99.

Small Scale Modeling of Vertical Surface Jets in Cross-Flow: Reynolds Number and Downwash Effects

K. Shahzad

B. A. Fleck[1]
e-mail: brian.fleck@ualberta.ca

D. J. Wilson

Department of Mechanical Engineering,
University of Alberta,
Edmonton,
Alberta, Canada T6G 2G8

Jet-crossflow experiments were performed in a water channel to determine the Reynolds number effects on the plume trajectory and entrainment coefficient. The purpose was to establish a lower limit down to which small scale laboratory experiments are accurate models of large scale atmospheric scenarios. Two models of a turbulent vertical surface jet (diameters 3.175 mm *and* 12.7 mm*) were designed and tested over a range of jet exit Reynolds numbers up to* 10^4*. The results show that from Reynolds number 200–4000 there is about a 40% increase in the entrainment coefficient, whereas from Reynolds number 4000–10,000, the increase in entrainment coefficient is only 2%. The conclusion is that Reynolds numbers significantly affect plume trajectories when the model Reynolds numbers are below 4000. Changing the initial turbulence in the exit flow from 12% to 2% without changing its mean velocity profile caused a less than one source diameter increase in the final plume rise.* [DOI: 10.1115/1.2427084]

Keywords: jet-crossflow, plume-rise, LIF, PLIF, downwash entrainment

1 Introduction

There are three distinctly different factors that influence jet plume trajectories. The first, and most obvious, is the vertical momentum flux of the exit jet from the hole. The second is the pressure and entrainment induced downwash of the plume back toward the surface. Finally, the third effect is the influence of Reynolds number on the jet exit flow, and the subsequent turbulent jet on the rate of entrainment of cross-stream fluid into the jet.

These effects all act at the same time, and all vary together as the velocity of the plume of cross-flow is changed. The goal of our study was to separate the influence of each of these parameters, attributable to momentum, surface pressure, and viscosity.

A typical and generally accepted method for modeling large scale atmospheric plumes is through small scale modeling in wind tunnels or water channels. The question arises as to the lower size limitations for such models, if one wishes to maintain similitude. The initial hypothesis of this work was that a certain lower Reynolds number threshold could be found above which experiments must be maintained when accurate modeling is intended. In this study, density weighted velocity ratio and jet exit Reynolds number effects on the plume trajectory were investigated.

In a similar vein, it was also postulated that since small scale model tests are often done using laminar sources, it would be interesting to see if jet exit turbulence affects results. A jet source was created that could generate nozzle jets of varying turbulence intensity while maintaining a relatively flat inlet mean profile. Because the bulk of the inlet vorticity would always emanate from the inlet shear layer, it is hoped that the effect of the additional turbulence in the core would have only a small effect on the jet trajectory and entrainment, allowing the common practice of using low exit turbulence model to simulate high exit turbulence prototypes.

The trajectories of a turbulent jet in a cross-flow have been studied by numerous investigators [1–7]. They have shown that the main parameter influencing the trajectory is the density weighted velocity ratio between the jet and the cross-flow.

The centerline trajectory of a plume seeded with fluorescing dye was determined from the average light intensity of 1800 images of the jet illuminated with a laser sheet. These images were recorded with a digital video camera at the rate of 6 images/s for 300 s. The plume trajectory was found using the loci of light intensity (concentration) maxima in the bent over plume as was done previously [5,8].

2 Plume Rise Model

The plume rise model for a momentum jet used here was developed by Briggs [9]. This approach to derive the plume rise equation has continued to be used [10–12,5]; the well known assumptions for this model are

1. The plume is "fully bent over" with its axis parallel to wind direction for its entire rise; and has a circular cross section in the plane perpendicular to its axis;
2. The density difference between the plume fluid and the ambient fluid is small enough to have a negligible effect on the jet trajectory through either buoyancy forces or turbulent entrainment coefficients;
3. The free stream (cross-flow) velocity is constant, and the bent-over plume is carried downstream at the ambient fluid speed, U_a;
4. Plume trajectory is not affected by the ambient turbulence; and
5. Entrainment coefficient, β, is constant for all plume cross-section locations. This is therefore a trajectory averaged value between a value of 0.1 at the jet exit to 1.0 very far downstream. The emphasis in this study was to determine laboratory simulation limits for modeling of ground level toxic or flammable releases into the atmosphere. In environmental modeling of plume trajectories, a single constant in the closed form solution is usually used to characterize the "entrainment." This simplification is desirable in the formulation of dispersion models for hazardous releases that must

[1]Corresponding author.

Contributed by the Fluids Engineering Division of ASME for publication in the JOURNAL OF FLUIDS ENGINEERING. Manuscript received February 8, 2006; final manuscript received August 3, 2006. Assoc. Editor: Timothy J. O'Hern.

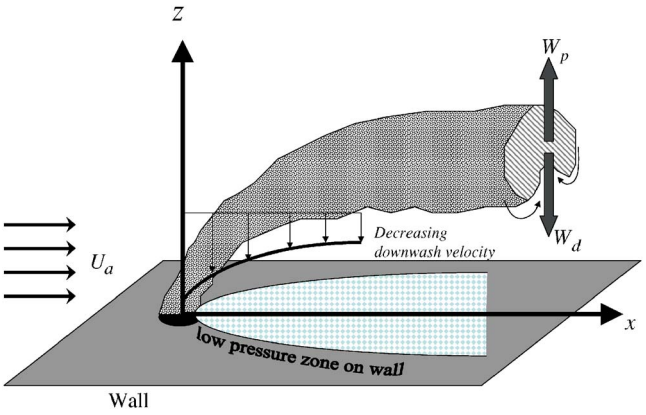

Fig. 1 Continuous downwash velocity distribution along the plume. Downwash velocity W_d decreasing with x as rising plume increases space for entrainment into bottom of bent-over plume.

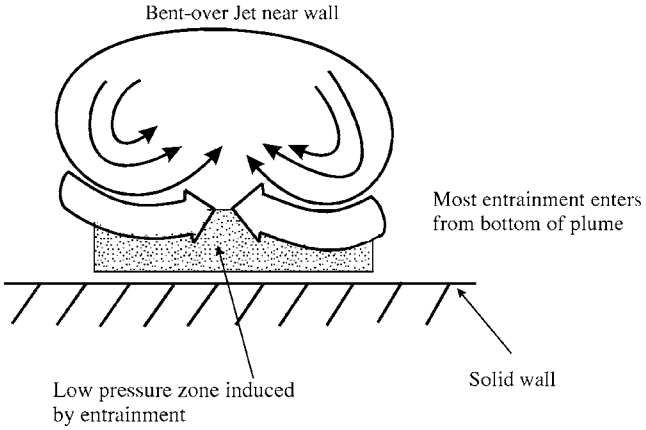

Fig. 2 Low pressure on the wall is induced as free stream fluid accelerates toward the jet centerline before it is entrained

be able to handle a great many atmospheric conditions in searching for a worst case.

This set of assumptions leads to an equation for the final rise h_m known as the 1/3 law [9,13]

$$h_m = \left(\frac{3}{\beta^2} \frac{F_m}{U_a^2} x \right)^{1/3} \tag{1}$$

where F_m is the inlet momentum flux; x is the downstream coordinate; and β is defined as the trajectory averaged entrainment coefficient, which is the ratio of the entrainment velocity to the vertical momentum rise velocity.

Using a density weighted velocity ratio M, defined according to

$$M \equiv \alpha^{1/2} \left(\frac{\rho_s}{\rho_a} \right)^{1/2} \frac{W_s}{U_a} \tag{2}$$

where α is the momentum correction factor used for nontophat jet inlet profiles. In this work the density ratio was one and α was found by integrating the momentum of the LDV measured source jet exit momentum profiles and comparing them to the top-hat case with equal mass flow. A modified version of Eq. (1) can be derived

$$\frac{h_m}{d_s} = \left(\frac{3}{4\beta^2} M^2 \frac{x}{d_s} \right)^{1/3} \tag{3}$$

where β, the trajectory averaged entrainment coefficient, is obtained from a best fit 1/3 power law of Eq. (3) to the data.

2.1 Downwash Velocity Correction. A model was used in the present study to account for the influence of the low pressure zone on the wall downstream of the plume when the source flow issues from a hole in a flat plate parallel to the crossflow (see schematic in Fig. 1). A physically realistic spatially varying downwash velocity model is introduced in the plume rise equation. The explanation for downwash is that the low-pressure area behind the plume affects the plume's ability to rise. The emerging vertical jet produces a low-pressure wake which acts like an obstacle in the path of the ambient fluid. Figure 1 illustrates this downwash concept and other basic quantities. As the figure shows, the plume is induced into the low-pressure zone by an effective downwash velocity W_d. This downwash velocity decreases with x as the low pressure decreases downstream. However, it must be noted that the low-pressure zone due to the plume–wall interaction appears to exist further downstream than typical wakes due to the bending over of the plume that extends the zone of the plume–wall proximity.

In Fig. 2 a schematic shows how when the plume is near the wall, the entrainment into the plume causes the low pressure zone to form behind the jet exit hole. This distributed pressure downwash model for the surface jet was inspired by the work of Ref. [5] in wakes behind circular stack jets. The plume downwash velocity can be written in terms of pressure differences, consistent with Fearn and Weston [14] who observed lower pressure on the wall downstream of a jet exit

$$W_d = \left. \frac{dh}{dt} \right|_{\text{downwash}} \propto \left[\frac{2(P_a - P_{\text{wall}})}{\rho} \right]^{1/2} \tag{4}$$

where P_{wall} is the wake pressure behind the jet at downstream distance x and P_a is the pressure in undisturbed flow. The pressure loss can be related to the source radius and downstream distance as a dynamic pressure coefficient that is assumed to decay as

$$(P_a - P_{\text{wall}}) = C_P \left(\frac{\rho U_a^2}{2} \right) \left(\frac{d_s}{2x} \right)^{2n} \tag{5}$$

where C_P is a dynamic pressure coefficient and n is the downwash velocity exponent (which appears in the next equation, the factor 2 is intentionally added for simplicity). Substituting Eq. (5) into Eq. (4), one obtains

$$W_d = B' U_a \left(\frac{d_s}{2x} \right)^n \tag{6}$$

where B' is a constant of proportionality. For unimpeded plume rise, the plume upward momentum rise velocity, W_p, with no downwash is

$$W_p = \left. \frac{dh}{dt} \right|_{\text{no downwash}} \tag{7}$$

From Fig. 2 it is clear that

$$W_{\text{net}} = W_p - W_d \tag{8}$$

which, after substitution, gives

$$\frac{dh}{dt} = \left. \frac{dh}{dt} \right|_{\text{no downwash}} - \left. \frac{dh}{dt} \right|_{\text{downwash}} \tag{9}$$

$$\frac{dh}{dt} = \left. \frac{dh}{dt} \right|_{\text{no downwash}} - B' U_a \left(\frac{d_s}{2x} \right)^n \tag{10}$$

Integrating Eq. (10) yields

$$\frac{h}{d_s} = \left(\frac{3}{4\beta^2} M^2 \frac{x}{d_s} \right)^{1/3} - B \left(\frac{x}{d_s} \right)^{1-n} \tag{11}$$

where $B \equiv 2^{-n} B'/(1-n)$ is the downwash coefficient. Equation (11) is the nondimensional plume rise equation for a fully bent-

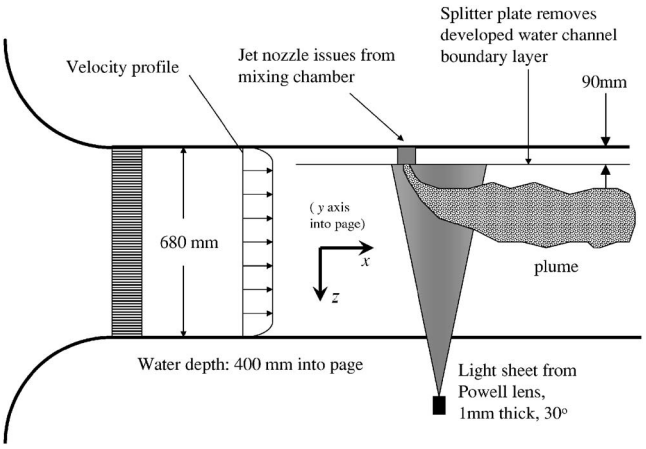

Fig. 3 Schematic view of the water channel facility, looking down through the free water surface

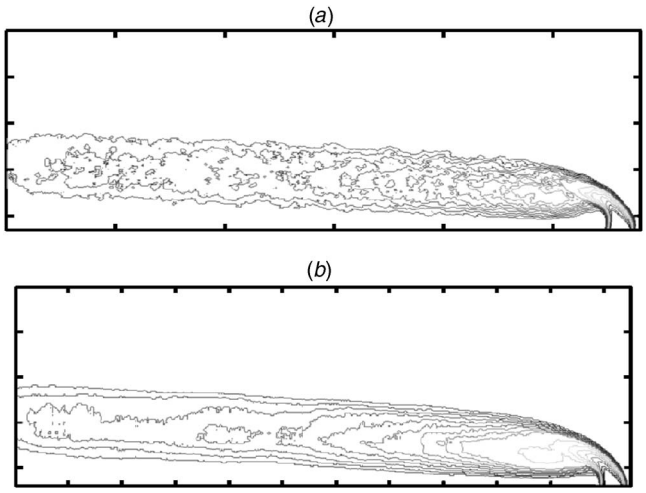

Fig. 4 Contour profiles of average images for the source, produced from 200 (top) and from 1200 (bottom) consecutive images. M=4.0, Re_d=9100. The images are averages of 1/30 s video frames taken 1/6 s apart (6 frames/s), in a crossflow with velocity U_a=180 mm/s, which is 14 source diameters/s.

over nonbuoyant momentum jet, accounting for jet wake pressure-induced downwash.

The value of the exponent n is expected to depend on the behavior of the near-wake recirculation region downstream of the jet exit. In the far wake behind a two-dimensional solid body, the wake width grows like $n=1/2$, and in an axisymmetric solid-body wake $n=1/3$. Our experiments will show that either of these exponents is reasonable, with $n=1/2$ fitting the downwash near the jet exit hole somewhat better.

3 Experiments

The experiments in this study were conducted in the water channel at the Mechanical Engineering Building at the University of Alberta, shown schematically in Fig. 3. The cross stream velocity profile was essentially uniform (±1%) making the determination of the appropriate choice for the ambient cross-flow velocity U_a easy.

Measurements of stream-wise jet plume cross sections for calculating plume trajectory were obtained using a horizontally oriented source with the laser sheet illumination from the other side, whereas measurements of jet velocity and turbulence characteristics were performed using a vertically oriented jet. The dyed source water had the same temperature (and density) as the cross-flow water. The dye itself is of very low concentration, and thus has a negligible effect on the source water density.

The PLIF technique was calibrated using a series of known dye concentrations mixed in a glass tank exposed to the laser sheets. The distribution of laser light intensity was adjusted for laser sheet divergence angle and losses through the calibration tank walls. Beer's law path extinction was negligible for these experiments due to low dye concentrations and short beam paths. The calibration was fitted with camera response and dye-fluorescence nonlinearity. The fluorescence from background emissions was measured and subtracted from the images.

3.1 Plume Trajectory. Measurements of the jet trajectory were made by injecting a nonbuoyant momentum jet from the turbulent source into a cross-flow at the same water temperature. The source fluid had a known concentration of fluorescence dye which emits at 520 nm when excited by the 488 nm light from the argon ion laser. The laser line at 514 nm can be a confounding signal, and so the laser was always tuned to maximize the 488 nm line (thus significantly reducing the 514 nm line).

Images were collected by a Hitachi KP-M1 charge-coupled device (CCD) monochrome video camera using a filter to attenuate the laser sheet light while allowing most of the fluorescing light to pass. The analog signal from the camera was digitized by a computer video board (Matrox Pulsar version 1.0) to produce images with a light intensity resolution of 10 bits (1024 intensity levels) and spatial resolution of 640 pixels horizontally and 480 pixels vertically.

As shown in Fig. 4 the contour profiles of the average image produced from 200 images were not sufficiently well defined. There is still evidence of random motion associated with the largest (longest lived) eddies in the flow. The contour profiles of the average image produced from 1200 images were better but still there appeared to be inadequate smoothness in the contour profiles. The contour profiles of the average image produced from 1800 images compared to one from 2400 images were found to be qualitatively very similar, and so an averaging of 1800 independent images was chosen to be enough to obtain reliable plume trajectories.

All the images are an average of many 1/30 s video frames, taken 1/6 s apart (6 frames/s), in a cross-flow with velocity U_a =180 mm/s, which is 14 source diameter/s.

Figure 5 shows a typical image used for determining the trajectory from 1800 instantaneous images. The curves show how ver-

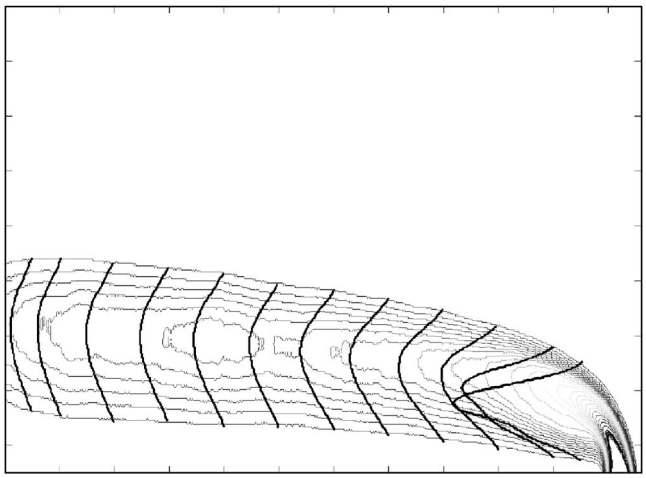

Fig. 5 Concentration and contour profiles are shown together. Jet trajectory was determined by joining the peaks of these concentration profiles.

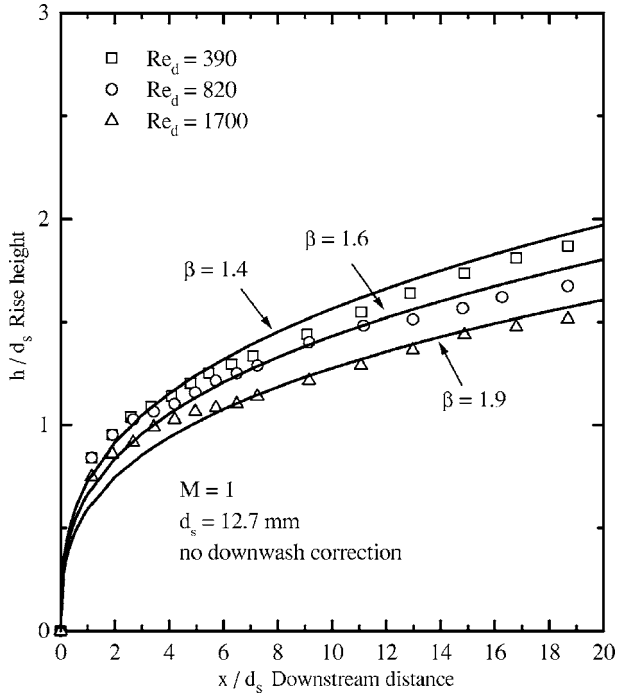

Fig. 6 Comparison between experimental data and the momentum rise equation (Eq. (3)) with no downwash correction for the large source diameter. The trajectory averaged entrainment coefficients, β, are much too large if no downwash correction is used.

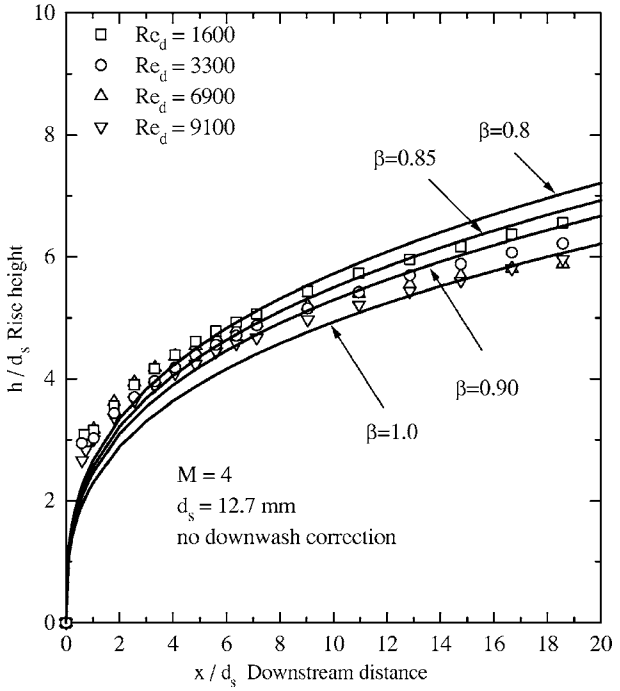

Fig. 7 Comparison between experimental data and the momentum rise equation (Eq. (3)) with no downwash correction for the large source diameter. The trajectory averaged entrainment coefficients, β, are large but acceptable for this momentum ratio M=4 but the slope does not match well without a downwash correction.

tical light intensity profiles through the plume show maxima. The peak values in each curve were used to form a curve that defined the experimental plume trajectory.

It is important to note also that when the plume is not entirely bent over (very early stage of plume development), the vertical slices are not normal to the trajectory line, and may give a less reliable estimate of the local maximum concentration. For this reason, the focus of the plume trajectory predictions was always on the far field data.

Another detail of interest is that these images were all acquired for relatively low dye concentration compared to the laser power, and so the plume emission could be assumed to be through an optically thin medium with minimal light extinction along both the path of the exciting and emitted light.

The plume profiles in Fig. 5 show a particular trait that was observed in almost all the experiments. The contours show an isolated "island" of higher concentration detached from the monotonic drop in concentration along the plume trajectory away from the source. Since these profiles were taken at the midplane of the mean plume, this shape is probably due to the time averaging of the jet oscillation. Upstream there are likely off-axis maxima in the left and right vortices of the plume, and as this phenomenon dies out, a single maximum at the centerline forms. Reference [5] found that the position of maximum on the centerline concentration profile was an accurate estimator of the centroid of a $y-z$ plume cross-sectional area even when there were off-axis maxima.

3.2 Jet Exit Velocity Profile. Jet exit velocity profiles, mean velocity, and turbulence intensity measurements were measured in the water channel using a two component LDV. Considerable effort was made to ensure a well mixed uniform velocity profile. The turbulence intensity was uniform through the jet core and highest in the circular shear layer at the edge. The intensity of the core turbulence could be reduced from 12–14% to 2–3% by inserting a screen in the outlet.

4 Results and Discussion

4.1 Trajectory Averaged Entrainment Coefficient. The observed plume trajectories were compared with Eq. (3) to obtain a best fit (least squares power law) over the range of the data observed within the field of view of the camera. The results are shown for two cases $M=1$ and $M=4$ in Figs. 6 and 7. For the lower velocity ratio M value, the required entrainment coefficient β to obtain reasonable fit is extremely high, between 1.4 and 1.9. For the higher velocity ratio M value, the fit is not excellent but the values of entrainment coefficient are more reasonable. Clearly, at the lower density weighted velocity ratios (and likewise, momentum ratios) and resulting smaller rise heights, the 1/3 law requires some adjustment to produce more realistic rates of entrainment.

4.2 Downwash Correction to Plume Trajectory. To correct for the poor fit of the 1/3 law results for cases of smaller M, the downwash model in Eq. (11) was used. Combinations of the values of B and n were determined by trial and error and used to obtain more reasonable entrainment coefficients and better fits for the data. After some experimentation with the numbers, the value of B was found to be near zero for low values of M and then increase asymptotically toward $B=0.5$ for greater values of M. The function

$$B = \tfrac{1}{2}(1 - e^{-M/2}) \tag{12}$$

fits the data well and was adopted as a step in the modeling process.

It is interesting to note that this function has the reverse trend to the observations of Ref. [5] who studied rigid tubular stack far above the surface and obtained higher values of B at lower M, with a decreasing asymptote to $B=0$ for the largest density weighted velocity ratios. Clearly the downwash mechanism is different for surface jets compared to stack jets than for stack jets.

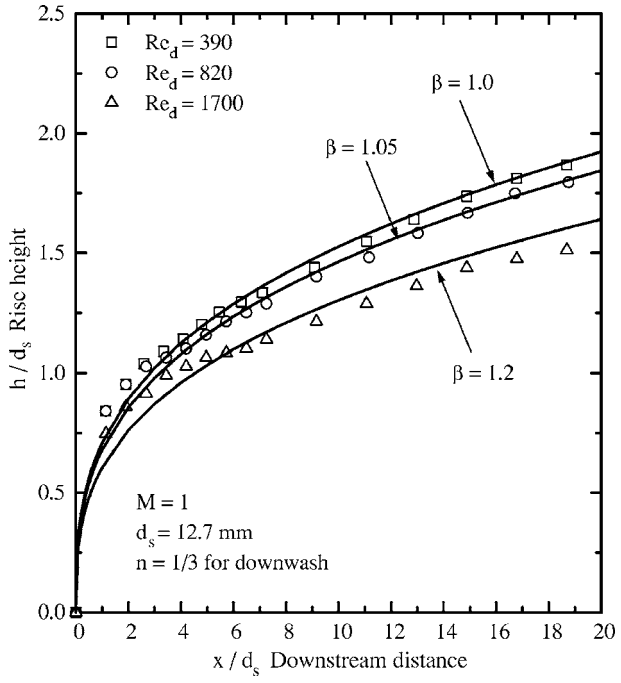

Fig. 8 Comparison between experimental data and the plume rise equation with downwash correction (Eq. (11)). Wall wake decay exponent $n=1/3$, $B=0.20$ at $M=1$.

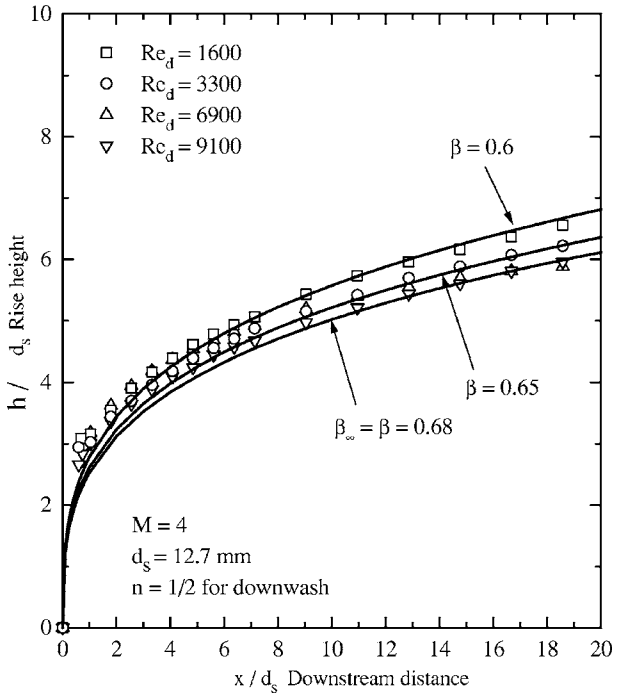

Fig. 10 Large source comparison between experimental data and the plume rise equation with downwash correction (Eq. (11)). $B=0.43$

Though the higher momentum jet is subject to greater downwash, clearly this effect is of relatively lesser importance because the stronger jets have greater overall momentum rise. However at high values of M, the downwash correction in Eq. (11) is very small relative to the first term that is proportional to M to the 2/3 power. Hasselbrink and Mungal [15] also found that the surface pressure effect on trajectory is negligible for high M.

Figures 8 and 9 show the comparison of the predicted plume trajectories and the experimental data of the large source at the more problematic $M=1$. In this case, the value predicted by Eq. (12) $B=0.2$ works well and $n=1/2$ fits the data well, particularly close to the jet exit. With the downwash effect estimated from Eq. (11) with $n=1/2$ and B from Eq. (12), the trajectories have very reasonable entrainment coefficients and also, as shown previously, is consistent with the assumption that the correction is the result of a pressure field effect.

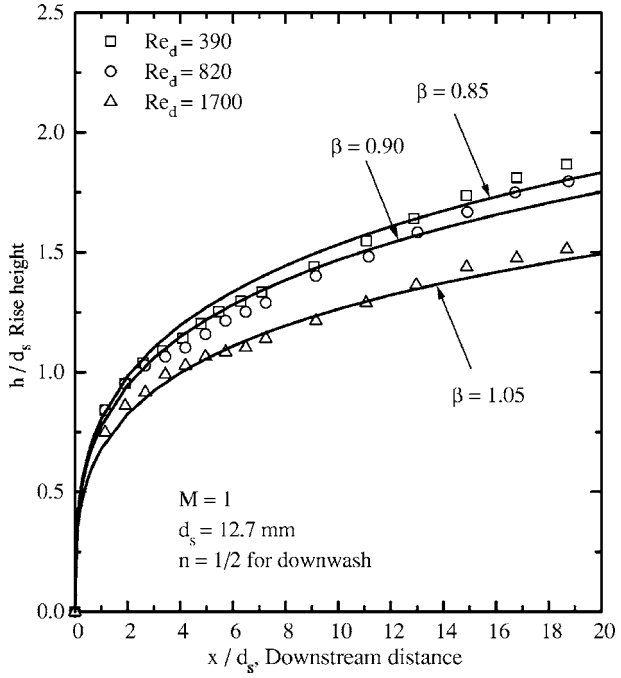

Fig. 9 Comparison between experimental data and the plume rise equation with downwash correction (Eq. (11)). Wall wake decay exponent $n=1/2$, $B=0.20$ at $M=1$.

Additional results show the validity of Eq. (12) and illustrate very reasonable fits for a range of parameters. For example, Figs. 10 and 11 show a comparison between small source data and the predicted plume rise trajectories. The β values are very realistic, compared to the values calculated without any downwash correction. The shape and fit of the curves are excellent for the full range of Re_d values tested in this work. The figures indicate decreasing entrainment with M, though a slight increasing trend with Re_d.

4.3 Jet Exit Reynolds Number Effects on Trajectory Averaged Entrainment Coefficient. To further bring order to the varying parameters in the plume rise, the Re_d effects on β were normalized by the entrainment coefficient obtained at the highest Re_d. To perform this normalization, entrainment coefficients at the highest jet exit Reynolds numbers for each density weighted velocity ratio were defined as β_∞ (see Table 1).

As shown in Fig. 12, the normalized entrainment coefficient β/β_∞ varies with Re_d. Note how five of the data points that lie exactly on the line β/β_∞ since these are the five data from Table 1 that were used to normalize the others. A simple empirical function that fits the data is

$$\frac{\beta}{\beta_\infty} = \frac{1}{1+\dfrac{150}{\mathrm{Re}_d}} \tag{13}$$

A slightly better fit was possible by changing the jet exit Reynolds number exponent but here the objective was to show the trend. Figure 12 shows that from $\mathrm{Re}_d=200$ to 4000 there is about a 40% increase in the entrainment coefficient, whereas from $\mathrm{Re}_d=4000$

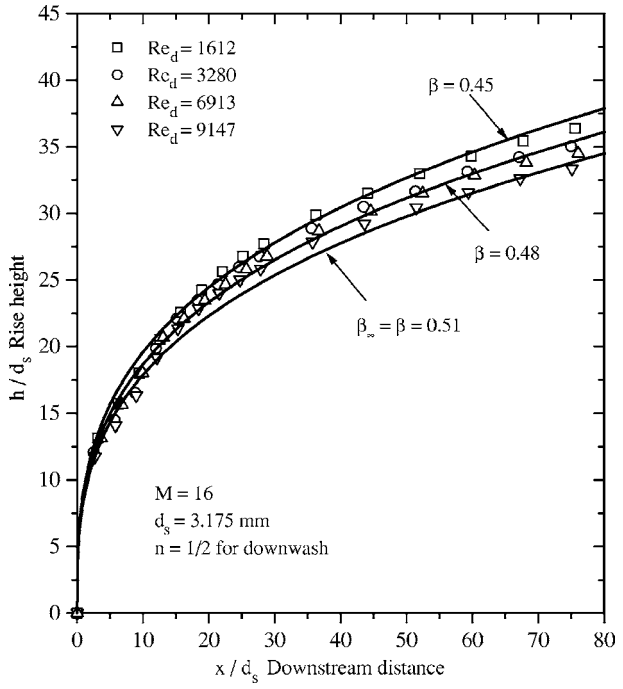

Fig. 11 Small source comparison between experimental data and the plume rise equation with downwash correction (Eq. (11)), B=0.50

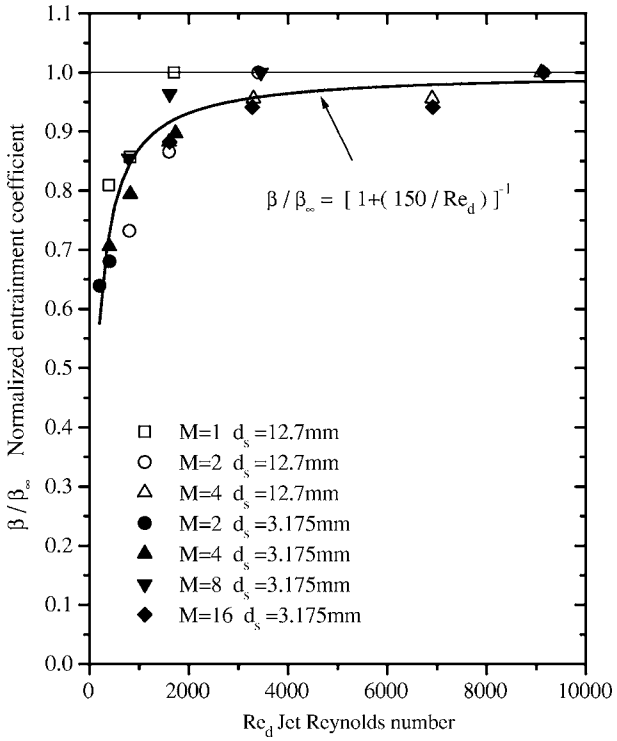

Fig. 12 Effect of Re_d on entrainment coefficient normalized by the high jet exit Reynolds number entrainment coefficient β_∞ at the largest measured Re_d for that M

to 10,000 the increase in entrainment coefficient is only 2%. Therefore it is obvious that at the higher Re_d range, viscous effects are negligible on the plume trajectory compared to cases with lower values of Re_d.

4.4 Trajectory Averaged Entrainment Coefficients at High Reynolds Number. An empirical equation for the relationship between β_∞ with M was chosen that would be continuous, monotonic, bounded and would tend asymptotically to a single value (0.5) for the highest M values. The equation chosen was

$$\beta_\infty = 1.1\left(\frac{1+0.063M^2}{1+0.14M^2}\right) \tag{14}$$

Clearly, this function was found by an empirical fit but it suits the desired characteristics noted above. From Eq. (14), β_∞=1.1 at M=0 and β_∞=0.51 at $M \geqslant 16$.

Figure 13 is a plot showing the entrainment data and the function used to model them. The empirical function used by Ref. [5], in their study of stack jets, is also shown. The difference for their stack jet and the surface jet in the present study was probably due to that fact that the Ref. [5] data were only for Re_d=1800, whereas in the present study, data were collected for a wide range of Re_d. The dotted curve in Fig. 13 is from Ref. [16] for stack jets. Briggs' curve comparison was done only after all functions were determined, and no adjustments were made to fit the present study β_∞ to Briggs equation. It was comforting to find that the curve from the Briggs equation is also a reasonable fit to the data (though it is unbounded at M=0).

Table 1 Maximum Re_d used for each value of M. The entrainment coefficients found at these jet exit Reynolds numbers were called β_∞ and were used to normalize entrainment coefficients for lower jet exit Reynolds numbers.

M	1	2	4	8	16
Re_d	1700	3400	9100	3450	9150

4.5 Jet Exit Reynolds Number Effects on Plume Rise. An estimate of the effect of Re_d on the trajectory-averaged entrainment coefficient β can be made by assuming very large x, so we can neglect the downwash term from Eq. (11). With this assumption

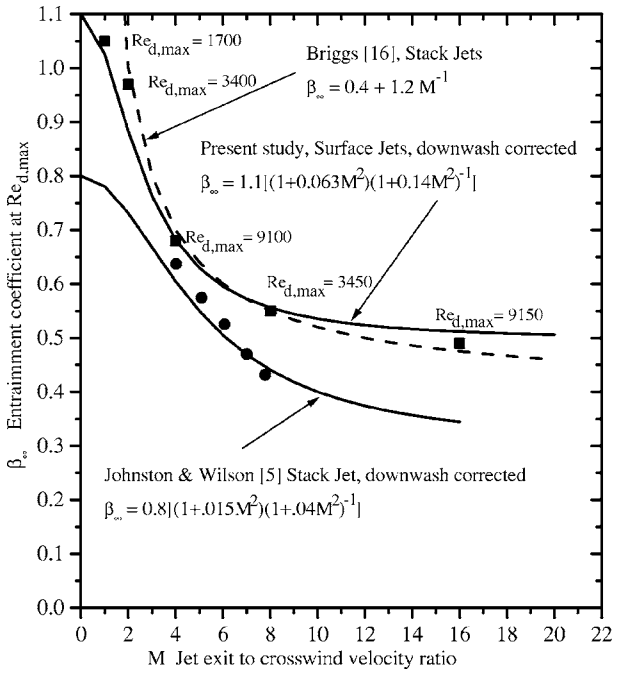

Fig. 13 Entrainment coefficient decreases as M increases. Previous measurements [5] shown as solid circle; present study as solid squares.

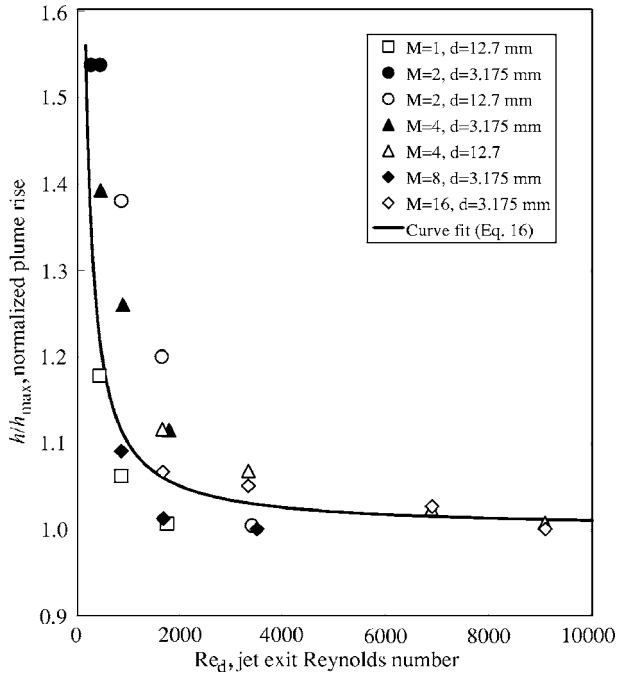

Fig. 14 Effects of Re_d on plume rise. The curve given is based on Eq. (16).

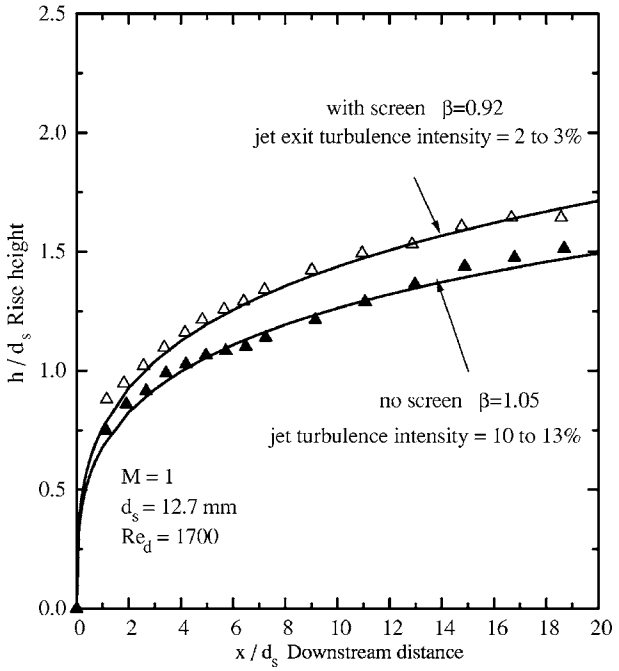

Fig. 15 Effects of jet exit turbulence on the plume trajectory at low density-weighted velocity ratio *M*

$$\frac{h}{h_{\max}} = \left(\frac{\beta}{\beta_\infty}\right)^{-2/3} \tag{15}$$

where $h_{\max}$ is the rise and β_∞ the trajectory averaged entrainment coefficient that would be expected for very large values of Re_d. Rewriting using the empirical relationship in Eq. (13) yields

$$\frac{h}{h_{\max}} = \left(1 + \frac{150}{\mathrm{Re}_d}\right)^{2/3} \tag{16}$$

Figure 14 shows that the curve obtained from Eq. (16) is in good agreement with the experimental data.

This gives an important quantitative scale model size limitation. If the exit Reynolds number of scale model jets remain above jet exit Reynolds numbers of 4000, most scaling of plume behavior will be maintained.

4.6 Effects of Initial Exit Jet Turbulence on Trajectory. Data were collected at different density weighted velocity ratios and various jet exit Reynolds numbers. Figures 15 and 16 show a comparison of the jet trajectories with and without the turbulence damping screen. The jet produced from the source with no screen had about 10–15% turbulence intensity, whereas the jet produced with the screen on the source had about 2–3% turbulence intensity; similar behavior was predicted by Ref. [6]. As expected, the jets with higher initial turbulence intensity have less plume rise, probably because they entrain more ambient fluid than jets with an exit screen that have low turbulence intensity. The difference between the two trajectories is roughly $\Delta h = 0.5 d_s$.

4.7 Boundary Layer Thickness. The boundary layer thickness in these measurements has not been factored into the models developed here. Though it has been suggested that this parameter should be considered in the scaling of these flows, we have left this out in this first attempt at finding practical guidelines for small scale modeling.

In all our experiments the boundary layer thickness was less than three source diameters and was in most cases on the order of one source diameter. In the early stage near the jet exit, the entrainment coefficient is small, so the net effect of the velocity of the cross-flow is smaller when the jet is not yet bent over.

Our focus on the bent over stage of plume rise is thus entirely outside of the boundary layer. We would expect that future correlations that incorporate boundary layer thickness as a parameter could potentially have corrections of up to a source diameter in plume rise.

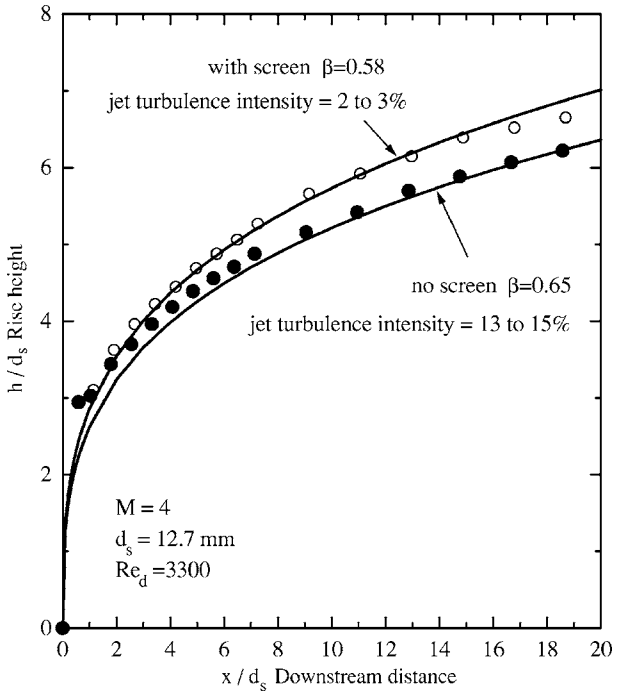

Fig. 16 Effects of jet exit turbulence on the plume trajectory at high density-weighted velocity ratio *M*

5 Conclusion

The standard Briggs plume rise model was enhanced to include the downwash effects for surface jets and was compared with the experimental data. It was found that the jet exit Reynolds number Re_d, h_{downwash}, M, and β had interrelated effects on plume rise.

The experimental data clearly show that the plume experiences downwash that must be considered when relative plume rise is otherwise low. The downwash velocity model was robust in its prediction of the plume trajectories, matching the experimental data very closely. Its importance was found to be greatest for jets with relatively low inlet velocity compared to the cross-flow. The downwash coefficient was found to be a function of M but overall the effect on plume rise was predicted to generally be less than one half a source diameter.

At low jet exit Reynolds number, Re_d=200–4000, there was up to a 40% increase in the entrainment coefficient but by $\mathrm{Re}_d \geqslant 4000$ the increase in entrainment coefficient was only 2%. In the higher Re_d range, viscous effects are negligible on the plume trajectory and at very low Re_d, entrainment coefficient is a strong function of Re_d.

Similarly, at lower jet exit Reynolds number, such as Re_d =200–4000, there was 50% decrease in the plume rise but at $\mathrm{Re}_d \geqslant 4000$ the decrease is only 5%. It was concluded from these results that for these greater jet exit Reynolds numbers, viscous effects have a negligible *relative* effect on plume rise at a fixed M.

Effects of initial turbulence on the plume trajectory were studied by reducing the initial turbulence in the jet from 10–15% to 2–3% with a fine mesh exit screen without changing the jet velocity profile. The results show that reducing the initial turbulence in the jet (as would be the case for very small laminar jets used in small scale experiments) without changing its velocity profile causes a less than 1 source diameter increase in the plume trajectory rise. This small increase suggests that the effect of increasing exit turbulence only affects the development of the jet core flow for a few diameters, and has no effect on the trajectory averaged entrainment coefficient. This has important implications for successful small scale experimental modeling of exhaust jets which are often turbulent in full scale and laminar in the model.

This study shows that the quantitative scale model jet exit Reynolds number limitation is about 4000, above which no correction is required to jet trajectory. In addition, in both full scale and model testing of surface jets the effect of plume trajectory downwash must be included to accurately predict near-source trajectories.

Practically this implies that the laboratory modeling of large scale phenomena such as gas well blowouts or momentum dominated jet releases from ruptured or cracked vessels can only be safely scaled down to a limited degree while still maintaining credibility for applications in safety or emergency response planning [17–20].

Nomenclature

h = vertical height of plume center line (m)
h_m = final momentum jet rise (m)
Δh = change in height (m)
F_m = momentum flux ($\mathrm{m}^4/\mathrm{s}^2$)
U = cross-flow velocity (m/s)
x = downstream coordinate (m)
z = vertical coordinate (m)
ρ = density (kg/m^3)
W = vertical velocity (m/s)
d = diameter (m)

Subscripts

m = momentum
∞ = far downstream
a = ambient (free stream)
s = source (from jet)
d = downwash
p = pressure

Dimensionless

Re_d = jet exit Reynolds number
M = density weighted velocity ratio
α = momentum correction factor
n = empirical downwash velocity exponent
B = empirical trajectory downwash constant
β = entrainment coefficient
max = extrapolated to large Reynolds number

References

[1] Keffer, J., and Baines, W., 1963, "The Round Turbulent Jet in a Cross Wind," J. Fluid Mech., **15**, pp. 481–496.
[2] Pratte, B., and Baines, W., 1967, "Profiles of the Round Turbulent Jet in a Cross Flow," J. Hydr. Div., **93**, pp. 53–63.
[3] Hoehne, V., and Luce, R., 1970, "The Effects of Velocity, Temperature and Molecular Weight on Flammability Limits in Wind-Blown Jets of Hydrocarbon Gases," American Petroleum Institute, **56–70**, pp. 1057–1081.
[4] Kamotani, Y., and Greber, I., 1972, "Experiment on a Turbulent Jet in a Cross Flow," AIAA J., **10**, pp. 1425–1429.
[5] Johnston, C., and Wilson, D., 1997, "A Vortex Pair Model for Plume Downwash Into Stack Wakes," Atmos. Environ., **31**, pp. 13–20.
[6] Yuan, L. L., and Street, R. L., 1998, "Trajectory and Entrainment of a Round Jet in Crossflow," Phys. Fluids, **10**(9), pp. 2323–2335.
[7] Muppidi, S., and Mahesh, K., 2005, "Study of Trajectories of Jets in Crossflow Using Direct Numerical Simulations," J. Fluid Mech., **530**, pp. 81–100.
[8] Smith, S., and Mungal, M., 1997, "Mixing Structure and Scaling of the Jet in Crossflow," J. Fluid Mech., **357**, pp. 83–122.
[9] Briggs, G., 1975, *Lecture on Air Pollution and Environmental Impacts Analysis*, D. A. Haugen, ed., American Metereology Society, pp. 59–111.
[10] Weil, J., 1988, *Lectures on Air Pollution Modelling*, A. Venkatram and J. C. Wyngaards, eds., American Metereology Society, pp. 119–166.
[11] Davidson, G., 1989, "Simultaneous Trajectory and Dilution Predictions From a Single Integral Plume Model," Atmos. Environ., **23**, pp. 341–349.
[12] Snyder, W. H., and Lawson, R. E., 1991, "Fluid Modeling Simulations of Stack Tip Downwash for Neutrally Buoyant Plumes. Atmospheric Environment," Atmos. Environ., **25A**, pp. 2837–2850.
[13] Weil, J., 1977, *Lectures in Air Pollution Modeling*, A. Venkatram and J. C. Wyngaard, eds., American Metereology Society, pp. 119–166.
[14] Fearn, R., and Weston, R., 1975, "Induced Pressure Distribution of a Jet in a Crossflow," NASA, Washington, D.C., Tech. Rep. No. TN D-7916.
[15] Hasselbrink, E., and Mungal, M., 2001, "Transverse Jets and Jet Flames. Part 1. Scaling Laws for Strong Transverse Jets," J. Fluid Mech., **443**, pp. 1–25.
[16] Briggs, G., 1984, *Atmospheric Science and Power Production*, D. Randerson, ed., U.S. Dept. of Energy, Washington, D.C., Vol. No. DOE/TIC-27601, pp. 327–366.
[17] Hasselbrink, E., and Mungal, M., 2001, "Transverse Jets and Jet Flames. Part 2. Velocity and Oh Field Imaging," J. Fluid Mech., **443**, pp. 27–68.
[18] Su, L., and Mungal, M., 2004, "Simultaneous Measurements of Scalar and Velocity Field Evolution in Turbulent Crossflowing Jets," J. Fluid Mech., **513**, pp. 1–45.
[19] Gopalan, S., Abraham, B., and Katz, J., 2004, "Effect of Velocity Ratio on the Structure of a Jet in Cross Flow," Phys. Fluids, **16**(6), pp. 2067–2087.
[20] New, T., Lim, T. T., and Luo, S., 2004, "A Flowfield Study of Elliptic Jets in Cross Flow Using dpiv Technique," Exp. Fluids, **36**(4), pp. 604–618.

Use of Bacterial Carpets to Enhance Mixing in Microfluidic Systems

Min Jun Kim[1]

Kenneth S. Breuer[2]
e-mail: kbreuer@brown.edu

Division of Engineering,
Brown University,
Providence, RI 02912

We demonstrate that flagellated bacteria can be utilized in surface arrays (carpets) to achieve mixing in a low-Reynolds number fluidic environment. The mixing performance of the system is quantified by measuring the diffusion of small tracer particles. We show that the mixing performance responds to modifications to the chemical and thermal environment of the system, which affects the metabolic activity of the bacteria. Although the mixing performance can be increased by the addition of glucose (food) to the surrounding buffer or by raising the buffer temperature, the initial augmentation is also accompanied by a faster decay in mixing performance, due to falling pH and oxygen starvation, both induced by the higher metabolic activity of the bacterial system.
[DOI: 10.1115/1.2427083]

Keywords: Serratia marcescens, microfluidics, mixing, diffusion bacterial carpet, glucose, temperature

1 Introduction

In a microfluidic environment, the small-scale and consequently low-Reynolds number flow regime leads to diffusion-limited, viscous-dominated dynamics. This has led to several engineering challenges, for example, how to pump fluids through a small system with optimum efficiency and how to enhance mixing between parallel streams of fluids. Mixing for chemical systems continues to be a challenge, although several concepts for laminar mixers have been proposed. Some of these techniques are associated with chaotic advection [1–3] in which the objective is to generate a chaotic cycle to stretch the two-fluid interface. Spatial methods [4–6] generate chaotic mixing using complex meandering channels, or ribbed channels. There have also been attempts at making temporal chaotic mixers at micro scale; however, these have tended to fail due to difficulties in finding a compact fluidic actuator that can be conveniently incorporated into a microfluidic system.

A novel approach for generating fluids mixing in small-scale devices is to employ the rotating flagella from bacteria as fluidic actuators [7]. Flagellated bacteria, such as *Escherichia coli* or *Serratia marcescens*, possess a remarkable motility system based on a reversible rotary motor [8,9]. Such bacteria typically have several flagella, each controlled by a separate, independent motor. When all the flagella rotate in a counterclockwise direction (its preferable sense of rotation), the flagella combine to form a bundle that propels the bacterium through the ambient fluid. A unique feature of bacterial flagellar motors is that they alternate between clockwise and counterclockwise rotation in a random manner, and this behavior leads to the execution of a random walk by bacteria as they move in the surrounding fluid. Thus, their natural behavior mimics, at the cellular level, the random motion of the classical chaotic mixer [1]. Freely swimming collections of bacteria have been observed to enhance diffusion and superdiffusive mixing has been measured [10,11].

If a large number of bacteria are encouraged to adhere to a substrate, then a bacterial carpet will be created with unique properties. This was observed by Darnton et al. [7], in which *S. marcescens* were observed to stick to a poly-dimethyl-siloxane (PDMS) film, where they were observed to generate fluid flow motions ("whirlpools" and "rivers") and to enhance the local diffusion of fluorescent tracer particles in the region above the carpet. We suspect that the flow inside a microchannel coated with a bacterial carpet may demonstrate similar properties and the successful demonstration of bacteria as microfluidic actuators in a designed system might be of value in future microfluidic systems. Exploring this possibility forms the central theme of the current paper.

Flagellated bacteria are also exquisitely sensitive to a wide variety of external stimuli. They respond to thermal and chemical gradients that directly influence their motility characteristics and form the basis for chemotactic and thermotactic responses [8]. Changes in temperature or the chemical environment can stimulate the bacteria's sensory system and alter the flagellar motor performance, including the counterclockwise and clockwise rotation intervals and the rotation frequency [12–14]. This sensitivity can be exploited to control the behavior and performance of a bacterial carpet.

One can imagine appliations where it is undesirable to introduce freely swimming bacteria into the working fluid, and thus, in this paper we extend the work of Kim and Breuer [11] to study the use of *bacterial carpets* (rather than freely swimming bacteria) to enhance mixing. Bacterial carpets are surfaces activated by the adhesion of bacteria [7], and thus, the biological cells are not mixed with the working fluid. The current paper is divided into two thrusts in which we (i) explore the possibility of using bacterial carpets to generate enhanced microfluidic mixing and (ii) examine the ability of chemical and thermal signals to control the device's performance by affecting the bacterial behavior. These investigations are conducted using simple microfluidic devices such as flow-through microchannels and sealed microfluidic chambers. This enables careful characterization and comparisons to theory, although the expectation is that these methods can be applied to more complex devices of practical interest.

2 Materials and Methods

2.1 Culturing Bacteria. *S. marcescens* were used in this study: ATCC 274 (American Type Culture Collection, wild type), provided by L. Turner and H. Berg of the Rowland Institute at Harvard University. For the best motility, the 100 μl frozen ali-

[1]Present address: Mechanical Engineering and Mechanics, Drexel University, Philadelphia, PA 19104.
[2]Corresponding author.
Contributed by the Fluids Engineering Division of ASME for publication in the JOURNAL OF FLUIDS ENGINEERING. Manuscript received February 5, 2006; final manuscript received September 7, 2006; Assoc. Editor: Ali Beskok.

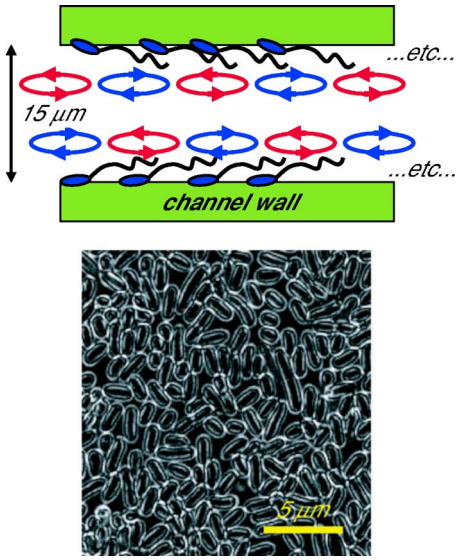

Fig. 1 Schematic of the bacterial mixing system and micrograph of the bacterial carpet as it develops inside the microfluidic system. The picture is taken 2000 s after the initiation of the flow deposition procedure. The scale bar is 5 μm.

quot of *S. marcescens* was put into 10 ml of LB growth medium and incubated for 4 h at 33 °C. The cultures were aerated by gently shaking the tube at ~180 rpm. The bacteria were removed from the incubator during the exponential phase of their growth for use in the experiments. After longer incubation times, the density of the culture saturates and motility quickly decreases. The *S. marcescens* were separated from the nutrient broth by centrifugation at 2200 g for 10 min and then resuspended in 0.5 ml of buffer. Buffer, consisting of 0.01 M KPO_4, 0.067 M NaCl, 10^{-4} M EDTA, (pH 7), was then added to bring the total volume to 10 ml. This separation process was repeated three times to ensure that all the growth medium were removed. The average size of *S. marcescens* is ~1 μm dia by 2 μm long, with 3–5 long (10 μm), thin (20 nm) helical filaments.

2.2 Microfabrication and Formation of Bacterial Carpets. The experiments were conducted using fluid devices fabricated using "soft lithography" techniques [15] in which a geometry is molded using poly-dimethyl-siloxane (PDMS) and then bonded to a glass substrate to form a microfluidic system. The geometries tested were long, wide channels, 15 μm high, 200 μm wide, and several millimeters long. Since these devices are closed, the bacterial carpets were formed on the inside surfaces using flow-deposition techniques rather than the blotting techniques of Darnton et al. [7]. Using a syringe pump, a buffer containing a high concentration ($2-5\times10^9$/ml) of motile *S. marcescens* was pumped through the channel at a low flow rate (0.05 μl/min). After 5 s, the pump was switched off, and the system was allowed to settle for 5 min. During this time, the bacteria swim randomly through the channel, sticking on contact to bare spots on both the PDMS and glass surfaces. *S. marcescens* form slimy durable coatings on the cell body and strongly adhere to the inside of the channel. The flow-and-settle cycle was repeated until the surfaces of the microchannel were coated to the desired density. The system must be rotated to ensure even coating and to counteract the natural tendency for the cells to preferentially coat the lower surface.

The formation of the carpet was tracked optically using differential interference contrast (DIC) microscopy. The DIC image was preprocessed by removing the static background image and then thresholding to enhance the outline of each cell body (Fig. 1). MATLAB-based image processing tools were used to determine the

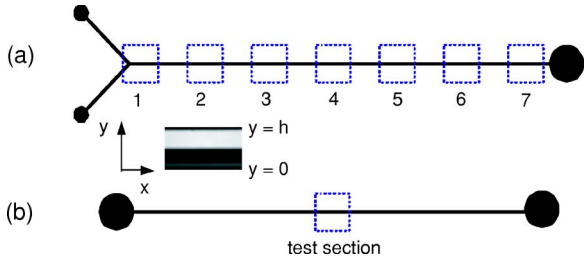

Fig. 2 Schematic of the test geometries: (*a*) the Y-junction microchannel and (*b*) the straight microchannel

cell density ("fill factor") and distributions of the cell orientation. The carpet was largely comprised of a bacterial monolayer, and examination of the carpet images indicated that 81% of the cells adhered to the surface as a single isolated cell, whereas 19% were in contact with or partially on top of another bacterial cell. The most probable orientation of the cells was observed to be parallel to the major axis (x) of the channel, and it was found that 55% of the cells were aligned between −30 deg and +30 deg with respect to the channel's x-axis. After 3000 s, the fill factor was measured to be 83% (±1.2%), and the average density of bacteria was 31/100 μm^2 (±2). Although a few cells were observed to stick to the surface by their flagella, most of the cells stuck to the surface by their bodies with their flagella free to rotate in the flow.

2.3 Experimental methods. The first experiment was designed to observe the mixing of two streams of fluid. This is an extension of the experiments of Kim and Breuer [11] in which freely swimming *E. coli* bacteria were observed to enhance laminar mixing. A PDMS Y-junction microchannel was fabricated, with two arms each feeding a stream of fluid into a main mixing channel that measured 28 mm long, 15 μm high and 200 μm wide (Fig. 2(*a*)). A *S. marcescens* carpet was flow deposited on the inside of the microchannel and then rinsed with motility buffer. During the experiment, one arm of the Y-channel carried a pure biological buffer solution, with a low concentration (0.02 vol. %) of FITC (Fluorescein isothiocyanate)-labeled Dextran (MW 77,000). The second arm contained the same buffer and Dextran, except that the Dextran was not fluorescently labeled. Images were captured at seven sections located at x=0.5, 4, 8, 12, 16, 20, 24 mm, and at four different flow rates (Q=0.468, 0.376, 0.282, 0.188 μl/min). As the two streams flow down the main channel, a clear boundary between the fluorescent and nonfluorescent streams is established at the Y-junction. The two streams mix together, generating an increasingly diffuse fluorescence profile at x stations further down the channel (Fig. 3). The intensity profile was monitored using a high resolution charged-coupled device (CCD) camera from which the diffusion profiles could be extracted.

Images were obtained using a Nikon TE200 inverted epifluorescent microscope with a 20× objective and recorded with an IDT SharpVision 12-bit cooled CCD camera (IDT, Tallahassee FL), with 1300×1080 pixels. Ten images were recorded at each x station and each flow rate. The intensity profiles across the channel were computed by averaging the ten frames and averaging over 300 pixels in the streamwise direction (corresponding to 107 μm). The maximum of the intensity profile was calculated by fitting the top five data points (two to either side of the peak intensity) to a quadratic polynomial $[y=y_0-a(x-x_0)^2]$. The width of the mixing zone was determined from the standard deviation of the gradient of the intensity distribution, computed by integrating the moments of the intensity gradient distribution using Simpson's rule.

A second experiment was also designed to assess diffusion enhancements in a sealed system. For these experiments, diffusion was measured from the dispersion of tracer particles. A straight

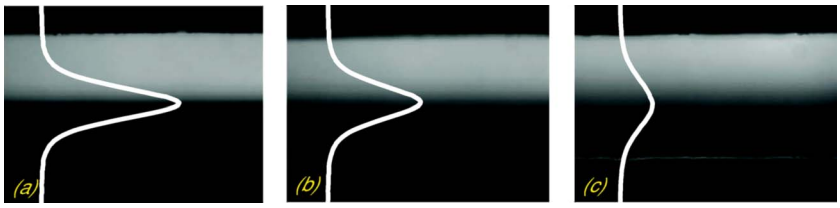

Fig. 3 The photographs illustrate typical intensity distributions in the Y-junction microchannel, showing the diffusion profiles ($\partial I/\partial y$) that is established between the labeled and unlabeled streams (x=24 mm, Q=0.188 μl/min): (*a*) the clean-walled microchannel, (*b*) the channel coated with nonmotile bacterial carpet, and (*c*) the channel coated with an active bacterial carpet. The enhancement of mixing is apparent.

PDMS microchannel (15 mm long) was fabricated with a single inflow and outflow (Fig. 2(*b*)). Following the formation of the bacterial carpet in the straight microchannel, the system was rinsed with the motility buffer to remove drifting bacteria and then seeded with a low concentration (0.04 vol. %) of neutrally buoyant fluorescent particles (490 nm dia Duke Scientific, Palo Alto CA). Finally, the inlet and the outlet were sealed using a drop of RTV silicone adhesive sealant (Permatex, Solon OH).

Mixing is quantified by measuring the effective diffusion coefficient. This is appropriate given the fact that mixing enhancements due to the bacterial carpet are isotropic, continuous, and distributed—all qualities of diffusive processes. Diffusion was determined using particle tracking velocimetry. Image pairs consisting of two successive CCD images (5 ms exposure, separated by 50 ms) were acquired using standard fluorescence microscopy techniques. The fluorescent particles were identified and tracked from the first image to the second, yielding a displacement vector. Approximately 3000 vectors were computed at each condition. Using a 100× objective, the image resolution is 64 nm/pixel, and assuming a tracking accuracy of 0.05 pixels, the displacement resolution is thus 3.2 nm. Typically, 100 image pairs were recorded at a fixed point in the channel in the course of several minutes. Effective diffusion coefficients were then computed from the width of the measured particle displacement distribution.

3 Results and discussion

3.1 Mixing enhancements in a Y-junction channel. Kim and Breuer [11] showed that freely swimming bacteria can enhance the mixing between two streams in a Y-junction microchannel. The present experiment repeats this experiment with the major difference that the bacterial are fixed to the device walls and do not need to be present in the two fluid streams. The evolution of the diffusion interface in the Y-channel can be modeled accurately using a quasi-one-dimensional theory [11] in which the concentration of the fluorescent tracer is represented by the fluorescence intensity, I,

$$\frac{\partial I}{\partial \tau} = D\frac{\partial^2 I}{\partial y^2} \tag{1}$$

where the pseudotime variable, τ, is defined as x/U (U is the average streamwise velocity) and D is the effective diffusion coefficient. This is Fick's second equation, satisfying the initial condition (I=0, $y>0$, and τ=0) and the boundary condition ($I=I_0$, y=0, and $\tau>0$). The solution to this equation is

$$I(\eta) = \mathrm{erfc}(\eta) \tag{2}$$

where η is a similarity variable

$$\eta = \frac{y}{\sqrt{Dx/U}} \tag{3}$$

Thus, the gradient of the intensity profile should behave like

$$\frac{\partial I}{\partial y} = \frac{1}{2\sqrt{\pi Dx/U}} \exp^{-(y/2\sqrt{Dx/U})^2} \tag{4}$$

from which one observes that the maximum in the intensity gradient should decay proportional to $(x/U)^{-1/2}$, and that the width of the diffusion zone, measured by the standard deviation of the intensity gradient, should grow proportional to $(x/U)^{1/2}$. Figure 4 shows the behavior of the maximum of the intensity gradient measured for three cases: (i) a baseline channel with clean walls, (ii) a channel coated with an inactive bacterial carpet, and (iii) a channel coated with an active (motile) bacterial carpet. Images of the intensity profile were obtained for several values of x and U, and the values of the effective diffusion coefficient D were extracted from the composite data using a least-squares regression analysis. Note that the collapse of the data with the similarity variable $\tau = x/U$ is excellent. For this particular carpet (83% fill factor), the effective diffusion coefficient D is observed to increase above the

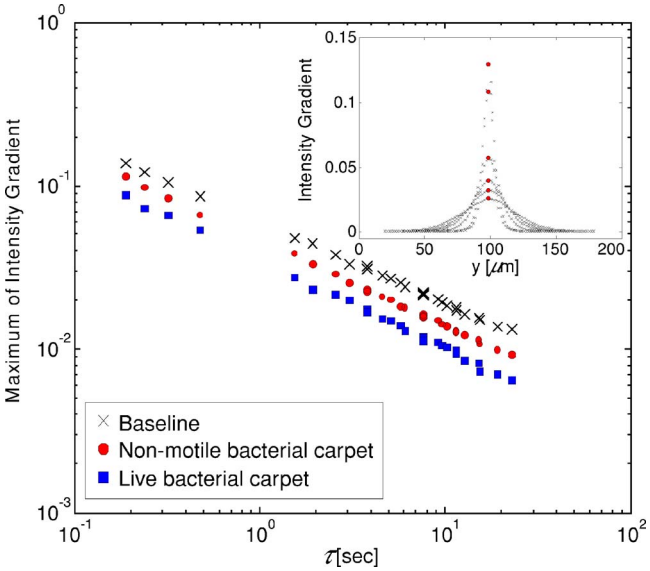

Fig. 4 The variation of the maximum of the intensity gradients, from all seven x locations and four different flow rates. Inset shows the gradient of the intensity profiles at different distance from the Y-junction, generated from images for Q =0.468 μl/min. Fluorescence intensity distributions are extracted from photographs shown in Fig. 3, and plotted against $\tau = x/U$, where U is the average flow velocity. Three sets of data are shown: (i) the clean-walled microchannel, (ii) the channel coated with nonmotile bacterial carpet, and (iii) the channel coated with an active bacterial carpet and the downward shift in each line indicates the increased diffusion due to presence and motion of bacterial flagella. The gradient of the intensity profile decays and spreads as $\tau = x/U$ increases.

baseline value by a factor of four, rising from 21.3 to 85.4 $\mu m^2/s$. After testing with the active bacterial carpet, 0.001% of FCCP (carbonylcyanide-p-trifluoromethoxyphenyl hydrazone) was added to the buffer, rendering the bacteria nonmotile. The channel coated with nonmotile bacterial carpet still resulted in an observed increase in D (to 41.8 $\mu m^2/s$), indicating that the mere presence of the passive flagella in the flow enhances fluid transport. Note that in the 15 μm high channel, the passive flagella (which are approximately 10 μm long) will extend throughout the flow system and their thermal motion will induce some additional transport. Darnton et al. [7] measured rise in the diffusion coefficient of 1 μm beads from 0.48 $\mu m^2/s$ in the bulk to 22.4 $\mu m^2/s$ at the carpet surface. The enhanced values in the present case are even larger, presumably due to the fact that the fluid streams are influenced by flagella from cells on both the top and bottom walls. Similar experiments conducted in a 40 μm deep channel did not show any enhanced transport when the cells were inactive.

The presence of freely swimming bacteria has also been observed to lead to the superdiffusive motion of passive tracer particles [10,11], which mix faster than the square-root dependence predicted by standard Fickian diffusion. Careful analysis of the data in Fig. 4 shows that the maximum in the intensity gradient does decays faster than $\sqrt{\tau}$. We can model the decay in the maximum intensity gradient, I_{max} (normalized by some initial value, I_0) as

$$\frac{I_{max}}{I_0} \propto \left[\frac{\tau^*}{\tau}\right]^{\gamma} \tag{5}$$

where γ is the diffusion exponent and τ^* is a reference time scale. For Fickian diffusion, γ is equal to 0.5, and τ^* is determined solely by the molecular diffusion coefficient D. Applying this model to the current data yields γ=0.499 for the baseline (clean channel) while γ=0.524 and 0.542 for the inactive and active carpets, respectively, indicating a mildly superdiffusive process, and comparable to the values found for freely swimming bacteria in a microchannel [11].

3.2 Mixing Enhancement in a Sealed System. The second series of experiments was designed to explore the dependence of the mixing enhancements on the elapsed time as well as on the composition of the fluid buffer. Since the mixing enhancement is due to the motion of living, motile bacteria, we would expect that the conditions of the buffer solution, its pH, oxygen content, etc., will have an effect on the bacterial carpet's effectiveness. For this experiment, tracer particles were introduced into a straight channel which was then sealed.

Immediately after the carpet creation, beads were observed to move rapidly, and over long distances, consistent with the observations over exposed bacterial carpets [7]. After long times, the bead motion was much more subdued. This motion was characterized by computing an effective diffusion coefficient D_p from the mean-square particle displacement statistics and by comparing D_p to the diffusion coefficient of the same particles due to Brownian motion D_b. This assay was repeated at regular intervals to determine the time-evolution of the carpet's effectiveness. We find that the diffusion enhancement, D_p/D_b, reaches its maximum value D_o immediately after the carpet's formation, after which time it decays exponentially, with a decay rate α (Fig. 5),

$$\frac{D_p}{D_b} = 1 + D_o \exp(-\alpha t) \tag{6}$$

For these conditions, diffusion enhancements in excess of 20 times that due to Brownian motion are achieved and the behavior over time is consistent with the behavior of bacterial carpets in open systems [7].

3.2.1 Effects of Glucose Concentration. These measurements were repeated for a variety of glucose concentrations (0, 2, 20, 60, and 120 mM), two of which are shown in Fig. 5, from which we see that the elevated glucose concentration serves to increase the initial diffusion enhancement D_o, but also to increase the subsequent decay rate α. Figure 6 shows the dependence of the initial diffusion enhancement D_o and the decay rate of the particle diffusion due to bacterial carpets in response to changes in concentration of glucose. A small increase in the buffer glucose concentration quickly increases the initial diffusion coefficient, although as the concentration increases the diffusion coefficient approaches a plateau. This behavior is due to the fact that, although the presence of small concentrations of glucose increases the metabolic rate of the bacteria, resulting in higher motor rotation rates [9,16], the glucose consumption rate per cell quickly saturates at a buffer concentration of ~20 mM, above which the increased concentration has no additional effect on the motor performance. Similar behavior is seen with the decay rate of the diffusion enhancement

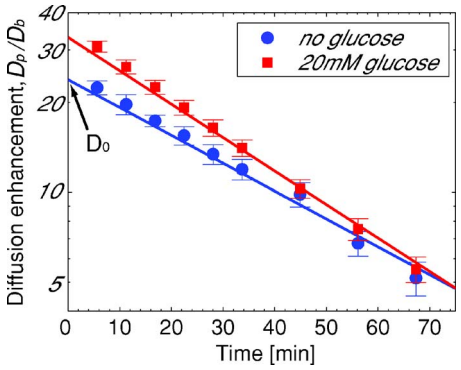

Fig. 5 Enhancement over Brownian motion of the tracer particle diffusion coefficient as a function of time. Two measurement series are shown: with the plain motility buffer (circles) and with 20 mM glucose added (squares). Error bars represent standard deviations based on five sets of measurement.

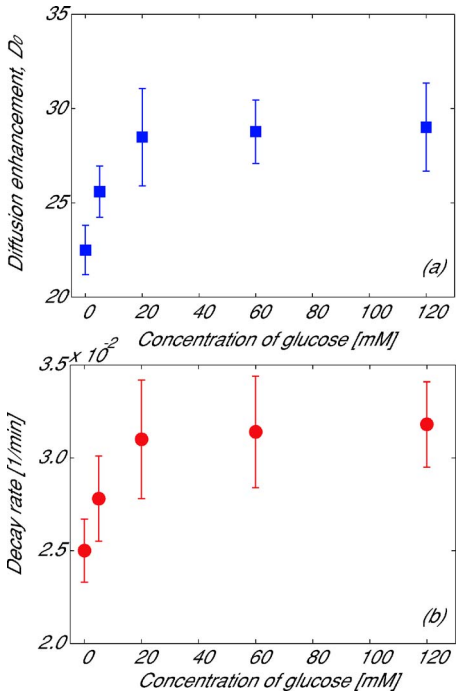

Fig. 6 Variation of (*a*) the initial diffusion enhancement factor and (*b*) the decay rate for flows above bacterial carpets in response to changes in concentration of glucose (0, 2, 20, 60, and 120 mM). Error bars represent standard deviations based on five sets of measurement.

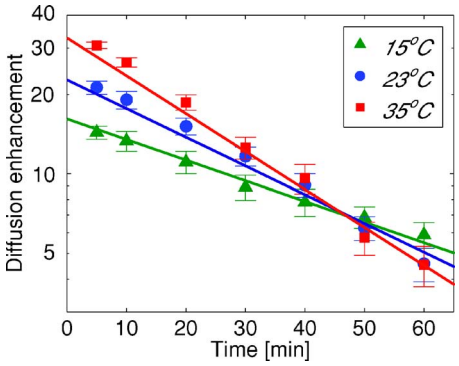

Fig. 7 Enhancement over Brownian diffusion as a function of time at different temperatures. The rising temperatures increase the metabolic activity of the cells resulting in increased diffusion enhancement. However, that increased activity also hastens the carpet's catabolic poisoning, resulting in a faster decay in the mixing activity. Error bars represent standard deviations based on five sets of measurement.

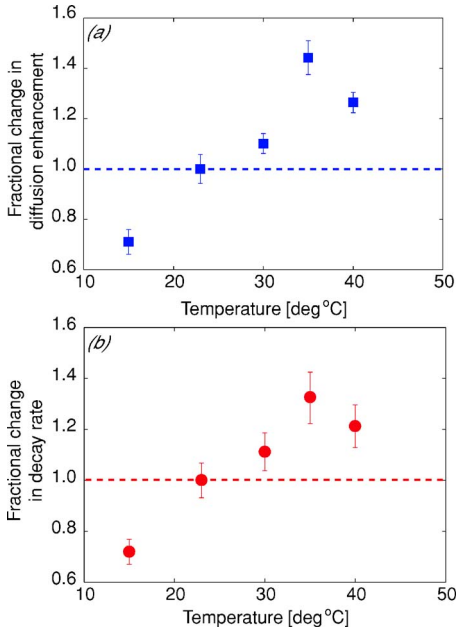

Fig. 8 Percent variation of (*a*) the initial diffusion enhancement and (*b*) the decay rate due to bacterial carpet motility as a function of temperatures. The increase in temperature of the buffer shows an increase in the initial motility and a increase in the decay rate up to 35 °C. The decline at *T*=40 °C may be related to changes in tumbling frequency for *S. marcescens* observed at higher temperatures [16]. Error bars represent standard deviations based on five sets of measurement.

factor. This may be explained by the fact that bacterial catabolism of glucose rapidly produces lactic, acetic, citric, and pyruvic acids in the buffer [17], and since the system is sealed, there is no mechanism to remove these waste products and they cause the buffer pH to drop. Cellular activity, including motor performance is driven by trans-membrane pH gradient and thus, as the pH drops, the cell motility (and thus the carpet motility) falls [8]. Thus in these sealed systems, the carpet's activity directly leads to its own decline and at the elevated metabolic rates induced by the superabundant glucose concentrations, this process is only made more extreme.

Another reason for the decay in the carpet's effectiveness over time may be due to oxygen starvation. For the bacterium, the power required to swim is about 8×10^{-18} W (8×10^{-11} ergs/s), which corresponds to the consumption of oxygen at a rate of $\sim$25 mol/s [18]. However, the introduction of a carbon source, such as glucose, enables cell growth, in which case the rate of oxygen consumption can rise by two orders of magnitude [18]. A reasonable estimate for the amount of dissolved oxygen in the buffer solution at 25°C is 1.6×10^{20} mol/l [19], and taking into account the amount of dissolved oxygen in the sealed microchannel ($\sim7\times10^{12}$ mol) and the number of bacteria that form the carpet ($\sim2\times10^{6}$, based on a fill factor of bacteria of 31.3/100 μm^2), we can estimate that, in the *absence* of any growth, the oxygen in the sealed system is sufficient to sustain the bacteria for close to 40 h. Thus, in the absence of glucose, the decay of the diffusion enhancement is likely not due to oxygen starvation. However, in the presence of glucose, if the oxygen consumption increases by only a factor of 50, then the bacterial metabolism will become oxygen limited, adding to (indeed dominating) the effects of catabolic poisoning, resulting in the increased decay rate of the diffusion enhancement observed in Fig. 5.

3.2.2 Effects of Temperature. The flagellar motion on the bacterial carpet is also quite sensitive to temperature because an individual bacteria's motility pattern is strongly influenced by the motor rotation frequency and the tumbling frequency, both of which are temperature sensitive [12,16]. Using the procedure described above, the evolution of the effective diffusion enhancements as a function of time were measured at different ambient temperatures (Fig. 7). The percentage deviation from the baseline measurement (at 23°C) of the initial diffusion enhancement D_o and of the decay rate ε is shown in Fig. 8.

In general, the initial diffusion enhancement increases with increasing temperature until it reaches a peak at 35°C. The dip at 40°C might be related to the observed fall in the tumbling frequency at higher temperatures [12], which may lead to reduced hydrodynamic effectiveness, although this needs to be studied further. As with the glucose dependence, the behavior of the diffusion coefficient decay rate follows closely the behavior of the initial diffusion coefficient and strengthens the hypothesis that the reduction in carpet effectiveness is directly caused by the production of metabolic side-products, and that at higher metabolic rates (either due to glucose or temperature effects), increased carpet activity is necessarily accompanied by a faster decline in motility.

4 Conclusions

We have demonstrated the use of a bacterial carpet as a convenient means to enhance mixing in a microfluidic system. The carpet can be easily formed using a flow deposition technique. The random rotation of the flagella acts as a mixer, increasing effective diffusion coefficients by factors in excess of thirty times the baseline diffusion coefficient. The performance of microfluidic devices powered by bacterial carpets has also been shown to be a sensitive function of the environment in which the bacteria live. Factors that enhance bacterial motility, such as the concentration of glucose and the system temperature, affect the carpet motility and hence influence the overall diffusion of the passive tracer. The decline of the device performance is thought to be related to the effects of catabolism in which by-products of the carpet metabolism reduces the buffer pH and hence leads to a reduction in motility and device performance. In addition, oxygen starvation can play a role in a sealed system, particularly when the level of metabolic activity is raised by the addition of a food source such as glucose.

Bacterial carpets are clearly not yet a mature technology. The purpose of this paper is not to suggest that bacterial carpets are ready to displace other more conventional techniques for mixing (such as moving surfaces or electrokinetic systems). Rather we aim to demonstrate that actuators from biological systems such as

bacteria can be effectively harnessed in engineered systems. Effective applications are still some years away and many issues need to be addressed. Comparisons between the *S. Marascens* carpet-based system discussed here, and the mixing achieved by freely-swimming *E. Coli* demonstrated in our earlier work [11] are difficult since the bacteria used have quite different metabolic characteristics. However, the system demonstrated here has many advantages over the free-flowing bacterial mixer, particularly because with the carpet, the cells are not part of the stream, but fixed to the device wall. Such bacterial systems are (to our knowledge) the first demonstrations of biological actuation of an engineered microfluidic system. The robustness, easy of manufacture and the ability to genetically modify their behavior make such systems highly attractive for powering microfluidic devices.

Acknowledgment

This work was supported by the DARPA BioMotors program and the Ostrach Graduate Fellowship (M.J.K.). The assistance and collaboration with Howard Berg, Linda Turner, Nicholas Darnton, Tom Powers, Greg Huber, and MunJu Kim are most gratefully acknowledged.

References

[1] Aref, H., 1984, "Stirring by Chaotic Advection," J. Fluid Mech., **143**, pp. 1–21.
[2] Oddy, M. H., Santiago, J. G., and Mikkelsen, J. C., 2001, "Electrokinetic Instability Micromixing," Anal. Chem., **73**, pp. 5822–5832.
[3] Strembler, M. A., Haselton, F. R., and Aref, H., 2004, "Designing for Chaos, Applications of Chaotic Advection at the Microscale," Philos. Trans. R. Soc. London, Ser. A, **362**, pp. 1019–1036.
[4] Liu, R. H., Stremler, M. A., Sharp, K. V., Olsen, M. G., Santiago, J. G., Adrian, R. J., Aref, H., Bebee, D. J., 2000, "Passive Mixing in a Three Dimensional Serpentine Microchannel," J. Microelectromech. Syst. **9**, 190–197.
[5] Strook, A. D., Dertinger, S. K. W., Ajdari, A., Mezic, I., Stone, A., and Whitesides, G. M., 2002, "Chaotic Mixer for Microchannels," Science, **295**, pp. 647–651.
[6] Tabeling, P., Chabert, M., Dodge, A., Jullien, C., and Okkels, F., 2004, "Chaotic Mixing in Cross-Channel Micromixers," Philos. Trans. R. Soc. London, Ser. A, **362**, 987–1000.
[7] Darnton, N., Turner, L., Breuer, K., and Berg, H., 2004, "Mixing Fluids With Bacterial Carpet," Biophys. J., **86**, pp. 1863–1870
[8] Berg, H. C., 2003, "The Rotary Motor of Bacterial Flagella," Annu. Rev. Biochem., **72**, 19–54.
[9] Manson, M. D., Tedesco, P., Berg, H. C., Harold, F. M., and Van der Drift, C., 1977, "A Protonmotive Force Drives Bacterial Flagella," Proc. Natl. Acad. Sci. U.S.A., **74**, pp. 3060–3064.
[10] Wu, X. L. and Libchaber, A., 2000, "Particle Diffusion in a Quasi-Two-Dimensional Bacterial Bath," Phys. Rev. Lett., **84**, pp. 3017–3020
[11] Kim, M. J. and Breuer, K. S., 2004, "Enhanced Diffusion Due to Motile Bacteria," Phys. Fluids, **16**(9), pp. 78–81.
[12] Maeda, K., Imae, Y., Shioi, J. I., and Oosawa, F., 1976, "Effects of Temperature on Motility and Chemotaxis of Escherichia coli," J. Bacteriol., **127**, pp. 1039–1046
[13] Macnab, R. M., Koshland, R. M., 1972, "The Gradient-Sensing Mechanism in Bacterial Chemotaxis," Proc. Natl. Acad. Sci. U.S.A., **69**, 2509–2512.
[14] Berg, H. C. and Turner, L., 1990, "Chemotaxis of Bacteria in Glass Capillary Arrays," Biophys. J., **58**, pp. 919–930.
[15] Duffy, D., McDonald, C., Schueller, O., and Whitesides, G., 1998, "Rapid Prototyping of Microfluidic Systems in Poly(dimethylsiloxane)," Anal. Chem., **70**, 4974–4984.
[16] Blair, D. F., 1991, "The Bacterial Rotary Motor," Nanotechnology, **2**, pp. 123–133.
[17] Solé, M., Rius, N., and Lorén, J. G., 2000, "Rapid Extracellular Acidification Induced by Glucose Metabolism in Non-Proliferating Cells of Serratia marcescens," Internatl Microbiol, **3**, pp. 39–43.
[18] Berg, H. C., 1993, *Random Walks in Biology* Exp. ed., Princeton University Press, Princeton.
[19] Cui, Y. Q., Van Der Lans, R. G. J. M., and Luyben, K. C. A. M., 2000, "Effects of Dissolved Oxygen Tension and Mechanical Forces on Fungal Morphology in Submerged Fermentation," J. Bacteriol., **57**, pp. 409–419.

Nanoscale Fluid Flow Over Two Side-by-Side Cylinders With Atomically Rough Surface

A. S. Ziarani
e-mail: zasabbag@ucalgary.ca

A. A. Mohamad
ASME Fellow
e-mail: mohamad@ucalgary.ca

Department of Mechanical and Manufacturing Engineering,
University of Calgary,
Calgary, Alberta,
Canada, T2N 1N4

A molecular dynamics simulation of flow over two side-by-side cylinders with atomically rough surfaces is presented. The model is two-dimensional with 3×10^5 *liquid argon atoms. The surface roughness is constructed by external protrusion of atoms on the surface of the cylinders with specified amplitude and width. Two cylinders, with diameters of* $d=79.44$ *(molecular units), are placed at a distance of D in a vertical line. The solids atoms are allowed to vibrate around their equilibrium coordinates to mimic the real solid structure. The influence of various parameters, such as roughness amplitude, topology, periodicity, and the gap between cylinders on the hydrodynamics of flow, especially drag and lift forces, is studied. It was noted that even very little surface roughness, with amplitude on the order of a few nanometers, can influence the drag forces. Both roughness texture and the number of roughening elements affects the drag and lift coefficients. The gap between the cylinders showed to be an effective parameter, especially on the lift force for flow over the nanoscale cylinders.* [DOI: 10.1115/1.2427087]

1 Introduction

The study of fluid flow behavior at the nanoscale has been a subject of interest in recent years. The understanding of the physical behavior and the hydrodynamics of flows has great importance on the theoretical study of fluid dynamics and many applications in engineering, physics, chemistry, and biosciences. The fluid flow instability or vortex shedding is a classical problem of fluid mechanics. Vortex shedding occurs in the wake behind bluff bodies and causes a fluctuation of flow field, lift, and drag forces. Numerous experimental and numerical investigations have been carried out to probe the hydrodynamics phenomenon at the macroscale, such as appearance and formation of eddies, separation of vortices, stability of vortex street, transition to turbulent wakes, forces involved, and the possibility of manipulating and suppressing the shedding process [1–5]. Although extensive experimental and numerical studies on two-dimensional (2D) and three-dimensional (3D) instabilities for conventional systems [6–13], namely, macroscale devices, have been reported, the microscopic ground of this phenomenon has not been well understood. Few works addressing this issue at the molecular scale have been cited [14–21].

The initial deviation from the Stokes flow starts at $\mathrm{Re}\cong5$, developing two counterrotating vortices behind the cylinder. The periodic shedding of vortices becomes stronger as the Reynolds number increases, and the von $K'_arm'_an$ vortex street can be observed at the range of $\mathrm{Re}=55-70$ [14]. At a higher Reynolds number of $\mathrm{Re}>200$, the flow shows three-dimensional and turbulent behaviors. For a flow over two aligned cylinders, the transition to turbulence decreases due to augmented characteristic length, when two cylinders are very close to each other. This suggests that the three-dimensional phenomena should emerge at a high Reynolds number and small gap, namely, about $\mathrm{Re}>100$ and $D^*=D/d<0.4$. Therefore, the two-dimensionality assumption would be an acceptable starting attempt for a numerical study of the wake behind two side-by-side cylinders at a low Reynolds number [22].

When the system size shrinks down to the nanoscale, the flow behavior is affected by the dynamics information and the structure of discrete particles. The molecular dynamics (MD) simulation is one of the most effective and powerful methodologies to describe the details of the hydrodynamics of flow at the nanolevel based on the statistical mechanics of nonequilibrium fluid. The advantages of molecular dynamics simulation over continuum hydrodynamics studies is that no artificial assumption, such as initial perturbation, is used. It also enables the study of the real source of instability originated from the motion of particles or fluctuations in atomic scale. Moreover, in the classical continuum theory, the transport coefficients are considered to be time and space independent. In MD, they are treated to be a function of time and space. This will affect the physical properties and the hydrodynamics of the nanoscale flows. Many fundamental nano- and microfluid flow problems, which might be extremely difficult in experimental studies, can be investigated by means of molecular dynamics.

Rapaport and Clementi [14] studied the evolution of eddies in a two-dimensional flow over a circular cylinder, which was further developed by Rapaport [15]. Liquid argon was used with Week-Chandler-Anderson (WCA) potential. No solid atoms were considered for the construction of the cylinder. In their model, the obstacle was treated as an internal boundary exposing the fluid atoms with slip condition. The development of a vortex behind the cylinder wake in time was investigated. Their results indicated that continuum hydrodynamics is applicable for the length scale as small as a few hundred nanometers.

The Rayleigh-Taylor phenomenon for a two-dimensional model of a Lennard-Jones molecular liquid was studied by Alda et al. [18]. The development of hydrodynamics instabilities was observed from two layers of fluid with different particle size and mass. The atomic unit mass of the heavier fluid was twice that of the lighter. They observed a fingering type of instability as a result of oscillations caused by the gravitational field. For equally mixed particles, a spontaneous "fluctuation driven" mixing with a long start-up time was observed. Although the development of the instability depends strongly on the different sizes of particles, it can be influenced by the mass ratio and the thickness of respective layers. The authors concluded that the initial perturbations generated at the microscale can be propagated into the macroscale.

This phenomenon was further investigated by Dzwinel et al. [16] using a 2D molecular dynamics simulation. It was noticed that the microscopic bubble-and-spikes stage of the mixing process is similar to that of the macroscale. The constant of mixing layer growth estimated from MD simulation was approximately

Contributed by the Fluids Engineering Division of ASME for publication in the JOURNAL OF FLUIDS ENGINEERING. Manuscript received April 18, 2006; final manuscript received August 29, 2006. Assoc. Editor: Dimitris Drikakis.

the same as that of the 2D simulation of the macroscale using the Navier-Stokes equations. In the closed particle system, the value of this constant remained stable with the change of the physical conditions, as observed at the macroscale. In the open particle system with a free surface, the value of the growth constant was 20% higher and reached the value of 0.07, which was the same as that of the experimental data.

The growth and decay of Taylor vortices in a fluid ($\rho=0.5$) confined between two concentric cylinders was studied using molecular dynamics by Hirshfeld and Rapaport [17]. The width of the annular region was on the order of 25 atomic diameters. The results indicated that the overall behavior of this microscopic system agrees with the macroscale experimental results.

Meiburg [23] compared the molecular dynamics method and the direct simulation of Monte Carlo (DSMC) in terms of their capability of simulating vorticity distribution. Gas flow over a flat plate at 45 deg incidence was simulated. Apart from statistical scatter, the result from both methods agreed quite well, provided that the dimension perpendicular to the plate of the cell in the DSMC simulation was small enough. A Strouhal number of 0.25 was reported which seemed too high for a Reynolds number as low as 78 when compared to experimental results for incompressible flows. The author believes that this discrepancy lies in the fact that the channel is fairly narrow, thus causing a strong acceleration of the flow above and below the plate, which, in turn, leads to the separation of the vortices before they reach full size. The results of both methods for the Rayleigh-Stokes problem were satisfactory. The DSMC did not show any periodic vortex shedding, whereas, as mentioned above, the MD simulation resulted in a vortex street. The difference was attributed to the loss of angular momentum on the particle level during the process of carrying out the collisions.

Even though there is no MD simulation directly addressing the calculation of drag and lift forces for molecular liquid flows, the kinetic theory of these forces for rarefied gas flows has been described by Beijeren and Dorfman [24,25]. Using the Boltzmann equation, they have derived the Stokes-Boussinesq form of equation for the frequency-dependent force on a sphere [24]. In their later work [25], they found Lamb's formula for the forces on a cylinder. The topic was further investigated by Dorfman et al. [26]. It was noted that for molecular gas flows, the drag force on the cylinders depends logarithmically on the inverse of the Knudsen number.

Because of the roughness effects, the microscopic behavior of nanoflows may be more complicated than thought. The influence of surface roughness is more pronounced because of the significantly high ratio of surface to volume in the nanoscale devices. Note that other factors, such as type of intermolecular interactions, especially fluid-solid interactions, and also physicochemical properties play an important role in nanoflows.

The focus of the present work is to study the effect of the external surface roughness on the hydrodynamics of flow, especially drag and lift forces. The molecular dynamics method is employed to investigate the influence of surface roughness amplitude, topology, and periodicity on the drag and lift coefficients. Also, the dependence of these forces on the cylinders' gap will be examined. To the best knowledge of the authors, this is the first study of its kind at the nanoscale level. In Sec. 2, the simulation approach is outlined, followed by the presentation of the results for the smooth models, the effect of other parameters as mentioned above and then the concluding remarks.

2 Simulation Approach

In a molecular dynamics simulation, a given number of atoms or molecules are positioned into a defined control volume. The construction of the initial configurations depends on the problem under consideration. For instance, the initial positions can be randomly distributed with overlaps avoided, or prescribed explicitly. It is customary to use lattice structures for the initial positions to avoid any overlap and computational errors. Similarly, the initialization of the particles' velocity depends on the problem. The initial velocities can be assigned randomly or based on the Maxwell-Boltzmann distribution at a specified temperature. With their individual positions and velocities subjected to certain boundary conditions and to the classical law of mechanics, i.e., Newton's equation, the particles start moving and bumping each other. The particles' new trajectories are updated according to their current velocities and also the forces exerted on them. Very small time steps, on the order of a few femtoseconds, are used to integrate the equations of motion. The calculations are usually performed for, at the most, a few hundred nanoseconds. When the particles approach the boundaries of the system, different treatments may be applied based on the physics of a problem. For the hard sphere model, the atoms can be specularly reflected, corresponding to a symmetric boundary condition. The alternative treatment is diffusive reflection of particles, which mimics a rigid wall. It is also possible to apply an accommodation coefficient, which takes into account to what extent particle's postcollision velocity depends on its previous history.

The molecular dynamics has the advantage of being a grid-free method. This enables the treatment of relatively complicated configuration, since, in principle, the only requirement to be satisfied is the geometry of the control volume or of a body in the flow. Therefore, it is easily feasible to model flow in and over complex objects as long as they can be composed of basic geometries [1].

The leap-frog algorithm is used to solve the equations of motion. The computationally demanding part in MD simulation is the calculation of forces among particles. A linked-list and cell subdivision approach proposed by Rapaport [27] is employed to accelerate the process of intermolecular force calculations. The linked list associates a pointer with a data item to provide a nonsequential path through the data. In the cell subdivision methodology, linked list associates atoms with their residing cells at any given instance. A one-dimensional array is required to store the list. This algorithm facilitates the search of neighboring molecules more efficiently and helps to reduce the order of calculation from $O(N^2)$ to $O(N)$, where N is the number of particles [28]. The flow is externally surrounded by periodic boundary conditions both in the x and y directions.

As mentioned in the introduction, two-dimensional modeling is a valid assumption for a flow over two cylinders with $\mathrm{Re}<100$ and $D/d\geqslant 0.4$. Therefore, a two-dimensional system with a total number of 3×10^5 particles is studied. Liquid argon with Lennard-Jones potential at a density of $\rho=0.8$ (number density, particles/unit area) is simulated. Both fluid-fluid and fluid-solid interaction were considered to be based on 12-6 Lennard-Jones potential, which was cut off at $r_c=2.5$,

$$V_{ij}(r)=4\varepsilon\left[\left(\frac{\sigma}{r}\right)^{12}-\left(\frac{\sigma}{r}\right)^{6}\right] \tag{1}$$

where σ is the molecular diameter, ε is the strength of interaction, and r is the distance between a pair of atoms.

Two cylinders, with diameters of $d=89.44$ (molecular units), were placed at a distance D from each other in a vertical line (see Fig. 1). The diameter is small enough, relative to the width of the simulation box, to avoid any excessive velocities on the sides of cylinders. The nondimensional gap between two cylinders is $D^*=D/d=2.5$. The dimensions of periodic simulation box enclosing the fluid are set to $a=704.36$ and $b=559.01$ (molecular units). At the entrance and exit of simulation regions, at every 40 time steps, the x and y velocity components of atoms are scaled to a desired temperature ($T=1.0$). Moreover, a constant velocity of 1.0 is added to x component of velocity to force the flow in x direction. This controls the temperature of system and drives the flow in x direction. It is necessary to mention that the alternative method could be the application of a constant external force on the system

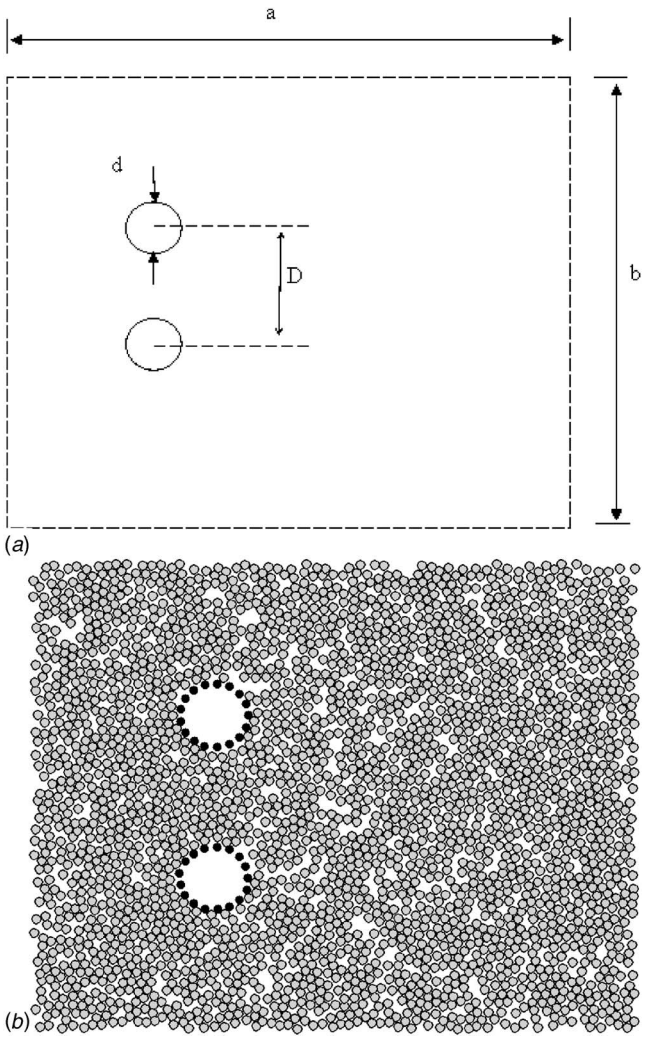

Fig. 1 Schematic of cylinders: (*a*) parameters and (*b*) a small molecular model with 2860 atoms at $t=20$

which is commonly used in molecular dynamics studies [27]. The simulation was performed for 4×10^5 time steps corresponding to 4.3 ns.

The code is composed of three subsections. In the first part, the initialization is performed. The second part, which is the main core of the code, is devoted to the force calculation and the integration of governing equations. In the last section, the statistical mechanics is employed to compute the desired flow parameters from the trajectories of individual molecules. A simulation run of a typical model with 3.04216×10^5 molecules takes ~151 hr on a Pentium IV with a CPU of 2.26 GHz.

Obviously, it is more desirable to use three-dimensional molecular dynamics simulation to capture all the physics of problem. For a 3D model, a hundred folds molecules, order of 10^7 molecules, are required to generate rich patterns for analysis. Such a kind of model will be computationally demanding and supercomputers must be used.

The grid methodology was employed to record the flow properties. The total of 90×75 grids (bins) were used for the sampling and averaging of interested properties. The results were averaged over at every 100 time steps and recorded in output files at every 4000 steps.

Reduced molecular units (dimensionless units) are used in the MD simulation. The molecular mass (m) and diameter (σ) of liquid argon are used as unit of mass and length, respectively. The ε, which is the strength of interaction for Lennard-Jones potential, is considered as unit of energy. Table 1 gives detail of the units and their equivalent in the cgs system.

Table 1 Molecular units

Quantity	Unit	Equivalent in cgs (for argon)
Length	σ	3.405×10^{-8} cm
Mass	M	6.634×10^{-23} gr
Energy	ε	1.657×10^{-14} erg
Time	$\tau=\sigma\sqrt{m/\varepsilon}$	2.16×10^{-12} s
Velocity	$\sigma/\tau=\sqrt{\varepsilon/m}$	1.58×10^{4} cm/s
Number density	σ^{-3}	4.206×10^{-2} mole/cm^3
Force	ε/σ	4.866×10^{-7} dyne
Viscosity	$\sigma^{-2}\sqrt{\varepsilon m}$	9.043×10^{-4} poise
Temperature	ε/k_B[a]	120 K

[a] k_B is the Boltzmann constant

3 Obstacles and Surface Roughness

The surface roughness is an important identifying factor on the condition of fluid at the solid interface. It has been proven to influence the slip condition in the internal micro- and nanochannel flows. Molecular dynamics studies shows that the no-slip condition can be achieved for a wall with very low or even zero adsorption. As far as external flows at the nanoscale concerned, no previous attempt has been made to study the role of surface irregularities on the drag and lift forces. The surface roughness can be modeled using a random distribution of solid molecules on the surface. Although this would be the case in the real surface structure, it is easier to consider a roughness with a specified pattern in terms of width, amplitude (A) and periodicity. In the current study, roughness with three general forms of rectangular, triangular, and random patterns are considered (see Fig. 2). The roughness elements are modeled as an external protrusion placed on the surface of the cylinders. The roughness molecules are treated the same as the cylinders' molecules. Both cylinder and roughness molecules are called solid molecules hereafter.

The cylinders are assumed to be long enough to allow the problem to be treated as a two-dimensional model. The structure of cylinders and surface roughness are represented by the solid molecules identical to that of fluid molecules for simplicity. Each solid atom is anchored to its lattice site by a linear Hookean spring. This allows the solid atoms to oscillate about their equilibrium positions, which mimics the real solid structure. The Hookean spring force on the solid atoms is based on

$$F=-k(r_i-r_i^{eq}) \tag{2}$$

where r_i^{eq} is the equilibrium position of atoms. The spring constant was set to $K=150$ [29]. A cutoff was applied for the vibration of solid atoms. This insures that the solid atoms are vibrating, rather than moving away from their positions. The Lindemann criterion for the melting of solid has been examined in the simulation. The present MD modeling does not violate this criterion, which means that the obstacles will not lose their solid state during the simulation if [30]

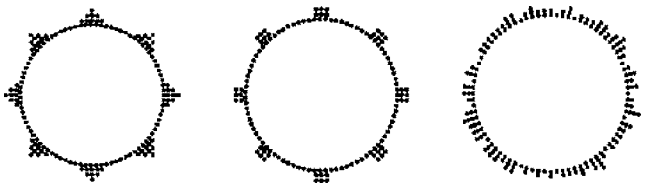

Fig. 2 Schematic of various surface roughness models

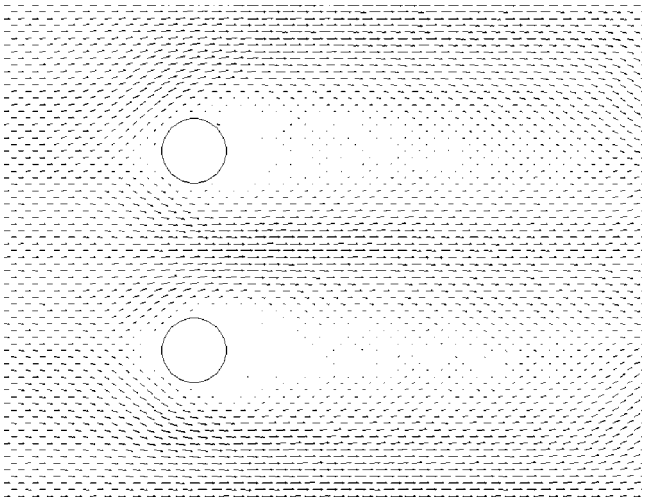

Fig. 3 Velocity vectors for smooth model $D^*=2.5$, Re=74.5 (*d*) $t=2000$

$$\theta = \frac{\langle (\Delta r)^2 \rangle}{d_{\min}} < 0.15 \tag{3}$$

where θ is called Lindemann ratio, $\langle (\Delta r)^2 \rangle$ is mean-square displacement of atoms and $d_{\min}$ is the nearest-neighbor distance.

4 Results and Discussion

In the conventional macroscale systems of two side-by-side cylinders, the flow characterized by mutual interaction between two single-cylinder wakes is governed by a nondimensional parameter; Reynolds number, $\mathrm{Re}=ud/\nu$, and nondimensional gap, $D^*=D/d$, where u is the freestream velocity, d is the cylinder diameter, ν is the kinematic viscosity, and D is the center-to-center distance between two cylinders. It is well established that for $D^* \geqslant 5$, the mutual interference between two wakes disappears and two independent single-cylinder wakes are observed [22]. Therefore, in the current study the value of D^* is kept at <5.

The code was verified by producing the published data. For this purpose, the vortex shedding behind a single cylinder studied by Rapaport [27] was duplicated. The wake formation behind a single cylinder was attempted elsewhere [31] to study the effect of surface roughness. The surface roughness was produced by the deviation of the cylinder molecules from the perimeter of the circle. It was found that when the amplitude of surface roughness is only a few percent of molecular diameter, maximum 50%, it does not have any significant influence on the stability of flow. Therefore, surface roughness with higher amplitudes should be investigated. For this purpose, the surface roughness as an external protrusion is presented in the current work.

It would have been very useful if we were able to presents the results of the simulation as movies of vortex shedding or albums of the images. Since this is not feasible, the flow patterns, velocity vectors, are presented along with some graphs for interested parameters.

4.1 Smooth Cylinders. The Stokes flow around cylinders can be observed at the start of simulation. The flow separation happens at $t=100$, and a wake forms behind cylinders. Then, a pair of counterrotating eddies appear at the downstream of cylinders. The vortices are visible at $t=500$ and become stronger as the time of simulation is preceded. Even though the flow reaches to a quasi-steady-state condition after about $t=1500$, the formation of vortices at the downstream of cylinders continues. The vortices behind cylinders at $t=2000$ are fully visible (Fig. 3). Note that this graph shows only the vortex shedding behind the cylinders; larger domains are required to allow the vortex street to be visible.

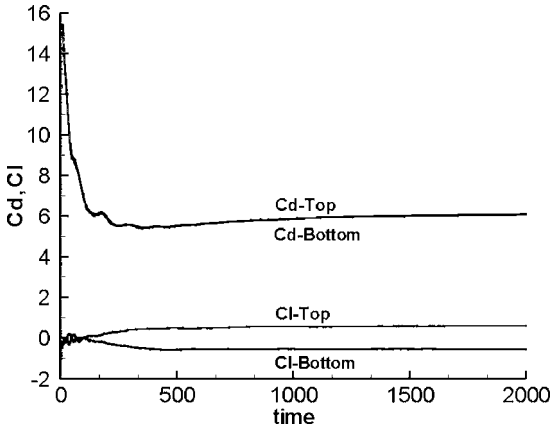

Fig. 4 Drag and lift coefficients for smooth model

The Reynolds number can be calculated based on the flow parameters and cylinders' diameters. For the current simulation, the velocity of the flow and the diameter of cylinders are $u=0.98$ and $d=89.44$, respectively. The kinematic viscosity, $\nu=\mu/\rho$, is available from previous two-dimensional molecular dynamics studies, $\nu=1.2$ [15,32]. These will give Re=74.5.

4.1.1 Drag and Lift Forces. The drag coefficient is defined as the ratio of drag force to dynamics force. Assuming an incompressible flow over a cylinder, it can be calculated from the following equation:

$$C_d = \frac{F_d}{\frac{1}{2}\rho d u^2} \tag{4}$$

where F_d is the drag force, ρ is the fluid density, d is the diameter of cylinder, and u is the freestream flow velocity. For two-dimensional model, Eq. (4) gives the drag coefficient per unit length of the cylinders. The drag force is directly calculated from the forces exerted on the cylinders' particles by fluid particles. It is the summation of forces applied on the solid molecules by the fluid molecules in the x direction. Similarly, the lift coefficient, C_l, can be calculated; the lift force, F_l, would be the total forces applied on the cylinders' molecules by the fluid molecules in the y direction.

Figure 4 shows the statistically averaged drag and lift coefficients versus time for smooth cylinders. Drag coefficients for both cylinders have a sharp drop at the start of simulation, which is due to relaxation from initial configuration. The same value of C_d is obtained for the top and bottom cylinders. It reaches a value of 6.00 at the steady-state condition. Unlike the drag forces, no significant drop was observed in lift forces at the start of simulation. This is due to the fact that the flow was forced in the x direction rather than the y direction. The lift coefficients differ for the top and bottom cylinders, as they should. For the top cylinder, C_l was found to be 0.60, whereas, a value of −0.56 was obtained for the bottom cylinder. The difference in C_l can be attributed to the interaction of flow between two cylinders.

4.2 Effect of Roughness Amplitude. As mentioned earlier, the surface roughness was modeled by the external protrusions of the atomic structures on the surface of the cylinders, with random, rectangular, and triangular geometries. Triangular and rectangular rough elements were constructed on the surface with a specified width, amplitude, and periodicity. Table 2 lists the details of triangular roughness models. The same width and amplitude are used for rectangular models. Note that for the last model, model with $A=3.4$ nm, the roughness amplitude is comparatively high.

Table 2 Surface roughness specifications

Model	Amplitude (nm)	Width (nm)
1	0 (smooth)	0
2	1.36	2.38
3	2.38	4.42
4	3.40	6.46

Therefore, this model can be considered as a model with distorted cylinders than cylinders with rough surface. Simulations were performed for various roughness amplitudes using triangular roughness model.

The results indicate that when the surface structure is changed from smooth to rough, it affects the stability of the flow. Even though, this might not be that significant in terms of the flow patterns, it has a significant effect on the drag and lift forces.

The drag and lift coefficients for the rough model with the amplitude of 3.4 nm have been depicted in Fig. 5. The trend of graphs is the same for all models. However, the drag coefficient for the top and bottom cylinder increases from 6.00 on the smooth model to 7.60 on the rough model. The value of lift coefficient for the top and bottom cylinders was found to be 0.83 and −0.80, respectively. The changes in these coefficients indicate that the surface roughness is an important factor influencing the hydrodynamics of flow. It should be mentioned that the base diameters of the cylinders are used to calculate the force coefficients of the rough models.

Figure 6 presents the vortex formed behind cylinders with the surface roughness of $A=3.4$ nm at $t=2000$. For a rough model, the deviation from the Stokes flow is visible even at the start of simulation, $t=20$. The flow separation happens at $t=100$, and later at $t=500$, the vortices appear behind the cylinders. The vortices become stronger as the simulation is performed for longer times. As it can be seen, the surface roughness does not show a significant influence on the flow pattern behind the cylinders.

Figure 7 presents the variations of the drag and lift coefficients versus the roughness amplitude. The magnitude of the drag coefficient shows a considerable increase as the surface pattern is changed from smooth to rough. However, the variations of lift coefficients are not that significant. A very small increase was observed for the lift coefficient of the top cylinder, and a slight decline was noted for the bottom cylinder as the amplitude of roughness was increased.

4.3 Roughness Topology and Periodicity. In his review of flow over circular cylinder, Zdravkovich [33] has listed the various types of surface roughness. Although, in practice, the roughness does not have any specific type of geometry and its topology can vary randomly, for simplicity, we study certain type of topologies with known geometry. The triangular roughness elements were used in all previous sections. For comparison, rectangular roughening elements as well as random patterns are adopted. Figure 8 shows the drag and lift coefficients for three types of rectangular, triangular, and random elements. The results indicate that the roughness texture is an important parameter that can change

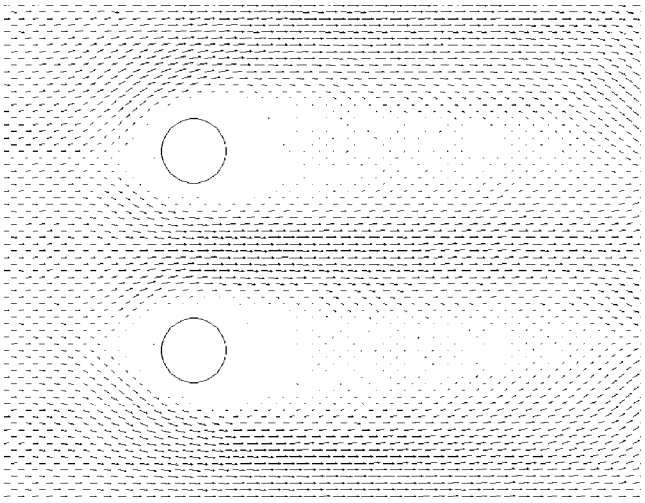

Fig. 6 Velocity vectors for rough model with $A=3.4$ nm and $D^*=2.5$, Re=74.5, $t=2000$

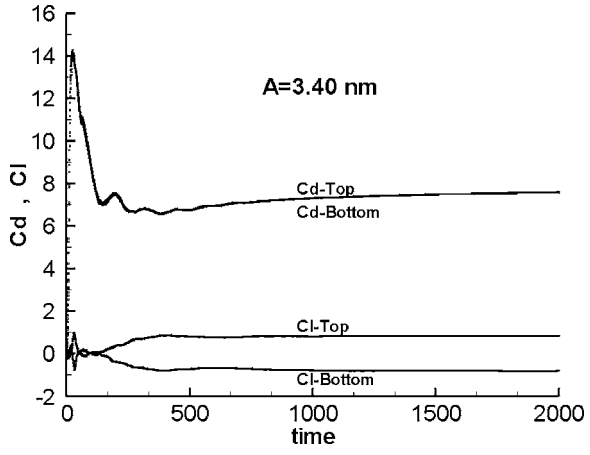

Fig. 5 Drag and lift coefficients for triangular roughness with $A=3.4$ nm

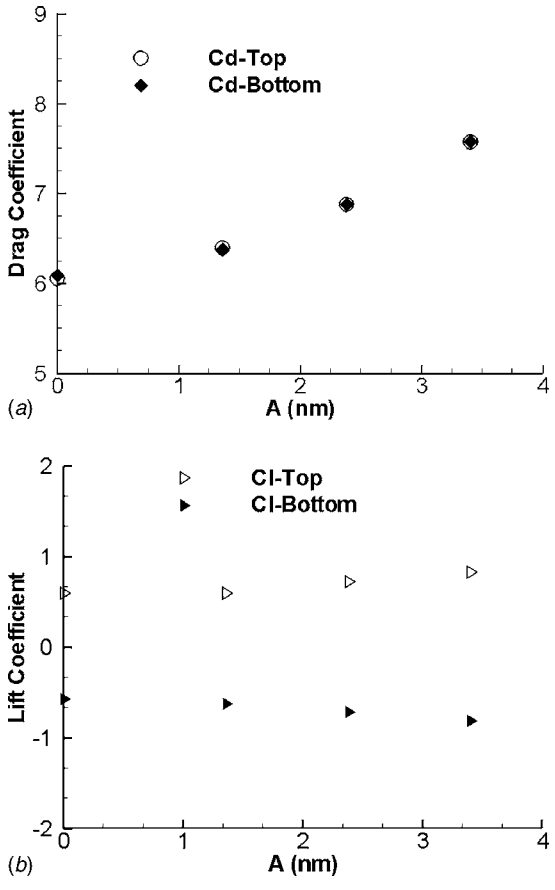

Fig. 7 Drag and lift coefficients versus roughness amplitude for a triangular roughness model, $A=0$ nm correspond to smooth surface

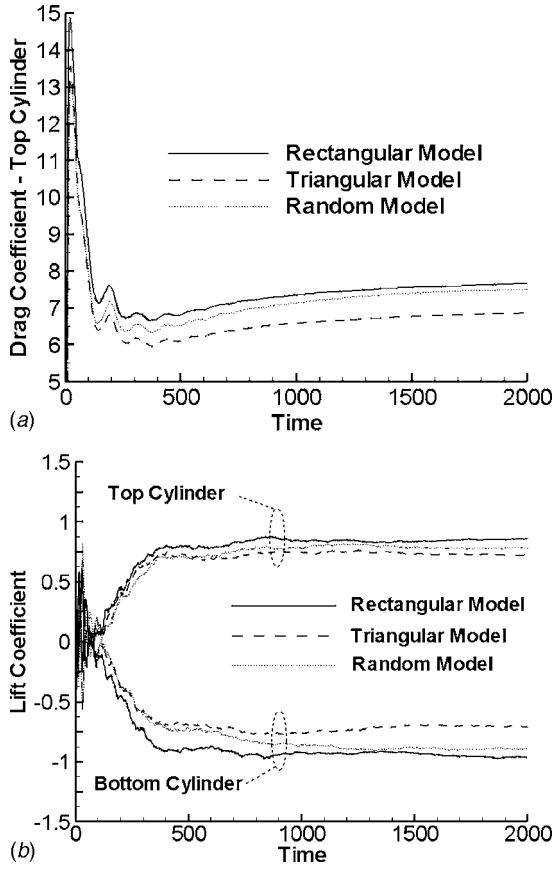

Fig. 8 Drag and lift coefficient for rectangular, triangular, and random rough models with $A=2.38$ nm

the magnitude of force exerted on the cylinders by the fluid. The drag force on the top cylinder (Fig. 8(a)), with a value that is the same as that of the bottom cylinder, increases from 6.87 on the triangular model to 7.68 on the rectangular model. The change of C_d is significant considering the fact that all roughness models have the same amplitude. As it can be seen, the drag coefficient for the random models lies within that of the rectangular and triangular models. The variation of lift coefficients for the top and bottom cylinders is illustrated in Fig. 8(b). The results show a noticeable difference between the rectangular and triangular models.

The periodicity (number of rough elements on the perimeter of cylinder) of rough arrays is the other parameter that might be important to study. Simulations with various numbers of triangular elements were performed. Figure 9 depicts cylinders with different numbers of rough elements. Four models with 4, 6, 8, and 12 rough arrays were considered. The variation of drag and lift coefficients for all four models has been presented in Fig. 10. Increasing the number of the roughening elements on the surface of cylinders resulted in increasing of drag force on the top cylinder (Fig. 10(a)). Note that the same drag forces are obtained for the bottom cylinder. Even though no significant change of C_d is

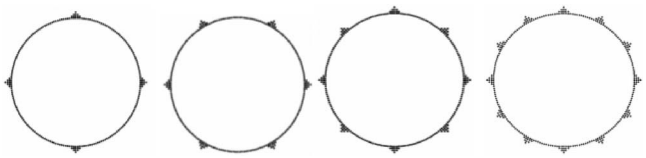

Fig. 9 Cylinders with various rough elements (from 4 to 12), triangular rough elements

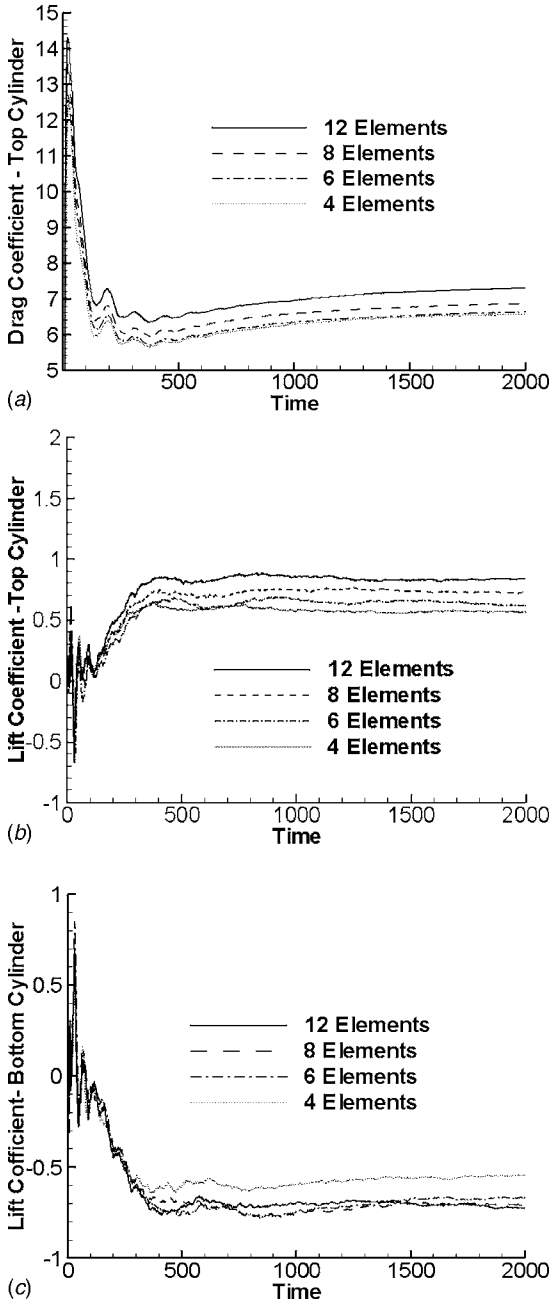

Fig. 10 Effect of the number of roughness elements on drag and lift coefficients for triangular rough elements $A=2.38$ nm

observed for models with 4 and 6 elements, the change in drag force is clearly visible for model with 8 arrays and especially 12 arrays. As far as the variations of the lift coefficient are concerned, for the top cylinder, C_l increases as the surface is covered with more rough elements. On the bottom cylinder, the magnitude of lift coefficient also increases, although for the case with 12 elements the lift force does not exceed that of model with 8 elements until $t=1500$. This can be partially attributed to the influence of the fluctuation of the vortices behind the cylinders, which affects the force applied on the bottom cylinder. The results shows that C_l increases from 0.73 to 0.86 on the top cylinder and the variation of lift on the bottom cylinder is found to be from −0.71 to −0.96.

4.4 Comparison of Results. Even though continuum equation might not be valid at the nanoscale, a comparison is made between the results obtained from molecular dynamics and mo-

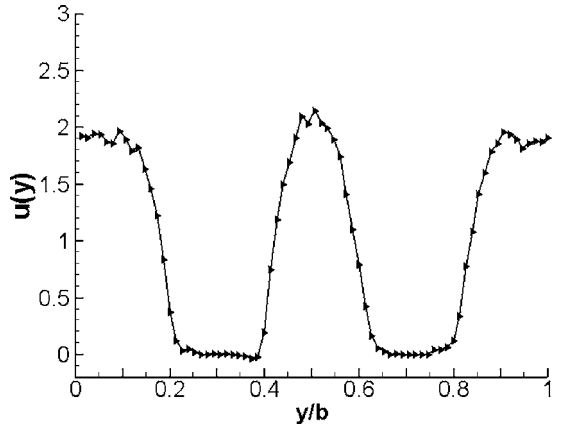

Fig. 11 Local velocity behind cylinders for smooth model

mentum conservation. The drag force on a cylinder can be determined using the velocity profile in the wake and the conservation of linear momentum [34]. The linear momentum conservation gives the drag force as follows:

$$F_D = \rho b \int u(U_\infty - u)dy \tag{5}$$

where b is the width of region, ρ is the density of fluid, u is the velocity of fluid behind cylinders, and U_∞ is the freestream velocity.

Figure 11 shows the local velocity profile behind the cylinders. Using the velocity profile, the drag force and the drag coefficients can be calculated. Table 3 summarizes the results for a few models both from molecular dynamics simulation and momentum equation. The difference between the results of two methodologies ranges from 25% to 29%. This discrepancy is partially attributed to the inaccuracy of continuum approach for the nanoscale flows.

Table 3 Drag coefficient from MD and momentum equation

A (nm)	MD results	Momentum results	Difference %
Smooth	6.06	4.30	29 %
1.36	6.38	4.76	25 %
2.38	6.87	4.98	27 %
3.40	7.57	5.50	27 %

4.5 Effect of Gap Between Cylinders. It is well known that the size of the gap between cylinders can influence the behavior of the flow around cylinders. In the side-by-side arrangement, the flow behind two cylinders can be divided into three regions [35]. When the spacing between cylinders is small, $1 \leqslant D^* = D/d \leqslant 1.2$, a single vortex street appears at downstream and the two cylinders behave as a single bluff body. When the gap between two cylinders is in the range of $1.2 \leqslant D^* \leqslant 2.2$, narrow and wide wakes will form, separated by a biased flow through the gap. It has been noted that the biased flow is bistable; the narrow and wide wakes can intermittently interchange between the two cylinders, and the frequency of vortex shedding is found to be different in the two wakes. As the spacing is further increased, both vortices shed behind the cylinders have the same frequency, but they are coupled in an out-of-phase mode. The vortices are simultaneously formed and shed on the gap side and then simultaneously on the outer side. The coupling gradually decreases and vanishes beyond $D^* > 4$. Eventually the two vortices are decoupled when $D^* > 5$ [35]. The gap spacing not only affects the vortex dynamic, but it

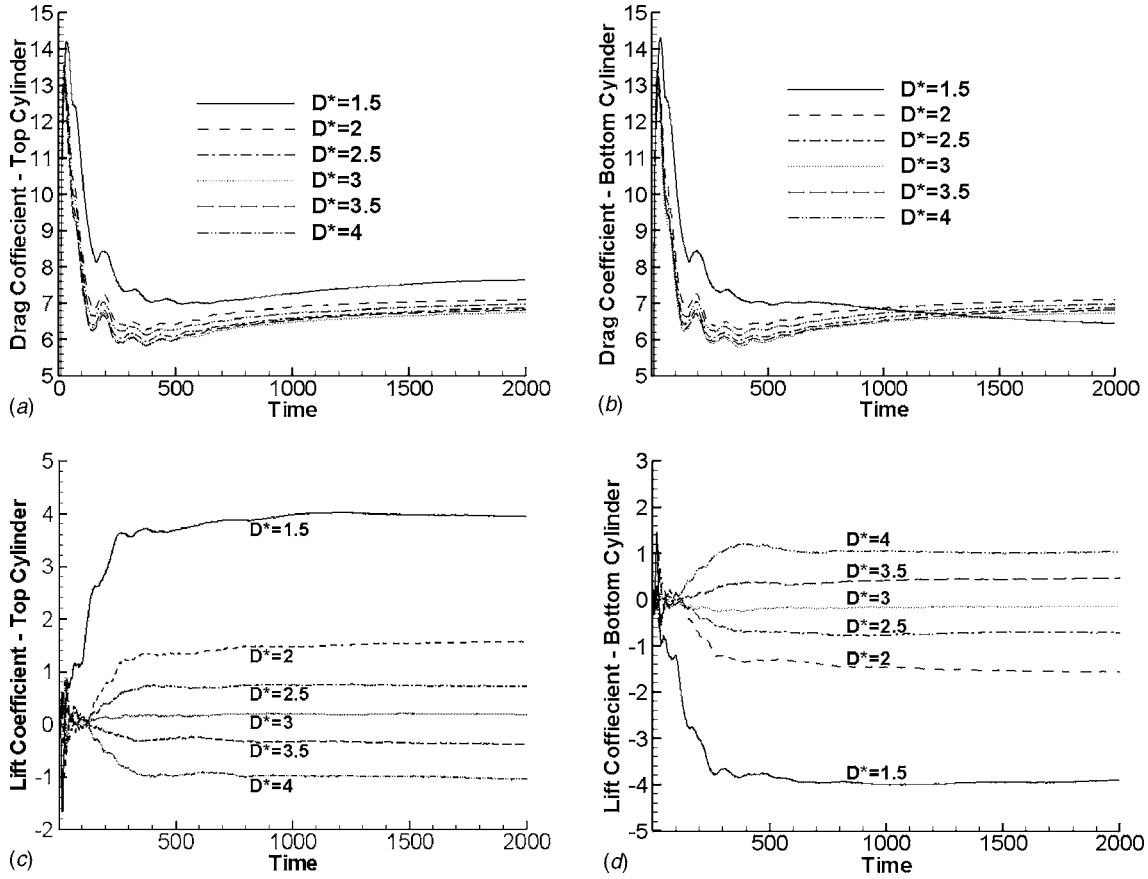

Fig. 12 Effect of gap spacing on the drag and lift coefficients for triangular model $A = 2.38$ nm

also influences the forces applied on cylinders. In all previous simulations, the gap between two cylinders was fixed at 2.5. In this section, the D^* will be varied from 1.5 to 4.0 and its effect on the drag and lift coefficients will be investigated.

Figure 12 presents the drag and lift coefficients for various gap sizes. As shown in Fig. 12(*a*), the drag coefficient for the top cylinder has a small variation when the D^* changes between 2.0 and 4.0. For the model with $D^*=1.5$, the increase of drag force is clearly visible. On the bottom cylinder, the drag coefficient shows similar behavior with the variation of gap spacing, except for the case with $D^*=1.5$ (Fig. 12(*b*)). In this case, the drag coefficient unexpectedly drops below to that of other models at $t=1300$. This indicates that the structure of vortices around the bottom cylinder, especially in the flow direction, is highly affected when the distance between cylinders becomes as small as 1.5. For the lift coefficients, Figs. 12(*c*) and 12(*d*), the results again shows a noticeable change for the case with $D^*=1.5$. All of these signify the fact that decreasing the space between cylinders from 2.0 to 1.5 significantly changes the flow behavior.

5 Conclusion

The flow over a pair of circular cylinders with rough surface was studied using molecular dynamics simulation of the Lennard-Jones atoms. The system was bounded by periodic boundary conditions, and the flow was driven by rescaling the velocity of particles in the x-direction at the inlet and exit. The roughness texture was modeled by placing atoms on the surface of the cylinders with specified patterns and dimensions. The results indicate that the surface roughness on the order of a few nanometers can influence the drag and lift coefficients. As the surface structure changes from smooth to rough, all of the force coefficients are increased. The topology of roughness is the other factor that influences the drag and lift forces. Also, the gap between cylinders significantly affects the forces on the cylinders, especially the lift forces. The comparison of continuum and molecular dynamics results for the drag coefficient shows a 25–30 % difference. This discrepancy is partially due to the fact that the Navier-Stokes equations are not valid at the nanoscale.

Acknowledgment

The authors acknowledge the financial support of the Natural Sciences and Engineering Research Council of Canada.

References

[1] Strykowski, P. J., and Sreenivasan, K. R., 1990, "On the Formation and Suppression of Vortex Shedding at Low Reynolds Numbers," J. Fluid Mech., **218**, pp. 71–107.
[2] Wu, J. Z., Tramel, R. W., Zhu, F. L., and Yin, X. Y., 2000, "Vorticity Dynamics Theory of Three-Dimensional Flow Separation," Phys. Fluids, **12**, pp. 1932–1954.
[3] Saffman, P. G., and Schatzman, J. C., 1982, "Stability of a Vortex Street of Finite Vortices," J. Fluid Mech., **117**, pp. 171–185.
[4] Jeon, D., and Gharib, M., 2004, "On the Relationship Between the Vortex Formation Process and Cylinder Wake Vortex Patterns," J. Fluid Mech., **519**, pp. 161–181.
[5] Homescu, C., Navon, I. M., and Li, Z., 2002, "Suppression of Vortex Shedding for Flow Around a Circular Cylinder Using Optimal Control," Int. J. Numer. Methods Fluids, **38**, pp. 43–69.
[6] Williamson, C. H. K., 1996, "Vortex Dynamics in the Cylinder Wake," Annu. Rev. Fluid Mech., **28**, pp. 477–539.
[7] Williamson, C. H. K., and Govardhan, R., 2004, "Vortex-Induced Vibrations," Annu. Rev. Fluid Mech., **36**, pp. 413–455.
[8] Oertel, H., 1999, "Wakes Behind Blunt Bodies," Annu. Rev. Fluid Mech., **22**, pp. 539–562.
[9] Zhou, Z., So, R. M. C., Liu, M. H., and Zhang, H. J., 2000, "Complex Turbulent Wakes Generated by Two and Three Side-by-Side Cylinders," Int. J. Heat Fluid Flow, **21**, pp. 125–133.
[10] Choi, S., Choi, H., and Kang, S., 2002, "Characteristics of Flow over a Rotationally Oscillating Cylinder at Low Reynolds Number," Phys. Fluids, **14**, pp. 2767–2777.
[11] Young, D. L., and Huang, J. L., 2001, "Simulation of Laminar Vortex Shedding Flow Past Cylinders Using a Coupled BEM and FEM Model," Comput. Methods Appl. Mech. Eng., **190**, pp. 5975–5998.
[12] Bailey, S. C. C., Martinuzzi, R. J., and Kopp, G. A., 2002, "The Effects of Wall Proximity on Vortex Shedding From a Square Cylinder: Three-Dimensional Effects," Phys. Fluids, **14**, pp. 4160–4177.
[13] Summer, D., Wong, S. S. T., Price, S. J., and Paidoussis, M. P., 1999, "Fluid Behavior of Side-By-Side Circular Cylinders in Steady Cross-Flow," J. Fluids Struct., **13**, pp. 309–338.
[14] Rapaport, D. C., and Clementi, E., 1986, "Eddy Formation of Obstructed Fluid Flow: A Molecular Dynamics Study," Phys. Rev. Lett., **57**, pp. 695–698.
[15] Rapaport, D. C., 1987, "Microscale Hydrodynamics: Discrete-Particle Simulation of Evolving Flow Patterns," Phys. Rev. A, **36**, pp. 3288–3299.
[16] Dzwinel, W., Alda, W., Pogoda, M., and Yuen, D. A., 2000, "Turbulent Mixing in the Microscale: A 2D Molecular Dynamics Simulation," Physica D, **137**, pp. 157–171.
[17] Hirshfeld, D., and Rapaport, D. C., 2000, "Molecular Dynamics Simulation of Taylor-Couette Vortex Formation," Phys. Rev. Lett., **80**, pp. 5337–5340.
[18] Alda, W., Dzwinel, W., Kitowski, J., Moscinski, J., Pogoda, M., and Yuen, D., 1998, "Complex Fluid-Dynamical Phenomena Modeled by Large-Scale Molecular-Dynamics Simulations," Comput. Phys., **12**, pp. 595–599.
[19] Hirshfeld, D., and Rapaport, D. C., 2000, "Growth of Taylor Vortices: A Molecular Dynamics Study," Phys. Rev. E, **61**, pp. R21–R24.
[20] Moscinski, J., Alda, W., Bubak, M., Dzwinel, W., Kitowski, J., Pogoda, M., and Yuen, D. A., 1997, "Moleculay Dynamics Simulations of Rayleigh-Taylor Instability," Annu. Rev. Comput. Phys., **5**, pp. 23–60.
[21] Kadau, K., Germann, T. C., Hadjiconstantinou, N. G., Lomdahl, P. S., Dimonte, G., Holian, B. L., and Alder, B. J., 2004, "Nanohydrodynamics Simulations: An Atomistic View of the Rayleigh-Taylor Instability," Proc. Natl. Acad. Sci. U.S.A., **101**, pp. 5851–5855.
[22] Kang, S., 2003, "Characteristics of Flow Over Two Circular Cylinders in a Side-By-Side Arrangement at Low Reynolds Numbers," Phys. Fluids, **15**, pp. 2486–2498.
[23] Meiburg, E., 1986, "Comparison of the Molecular Dynamics Method and the Direct Simulation Monte Carlo Technique for Flows Around Simple Geometries," Phys. Fluids, **29**, pp. 3107–3113.
[24] Beijeren, H. V., and Dorfman, J. R., 1980, "Kinetic Theory of Hydrodynamic Flows. I. The Generalized Normal Solution Method and Its Application to the Drag on a Sphere," J. Stat. Phys., **23**, pp. 335–402.
[25] Beijeren, H. V., and Dorfman, J. R., 1980, "Kinetic Theory of Hydrodynamic Flows. II. The Drag on a Sphere and on a Cylinder," J. Stat. Phys., **23**, pp. 443–461.
[26] Dorfman, J. R., Sengers, J. V., and McClure, C. F., 1986, "Kinetic Theory of the Drag Force on Objects in Rarefied Gas Flows," Physica A, **134**, pp. 283–322.
[27] Rapaport, D. C., 1995, *The Art of Molecular Dynamics Simulation*, Cambridge University Press, Cambridge, England.
[28] Allen, M. P., and Tildesley, D. J., 1987, *Computer Simulation of Liquids*, Oxford University Press, London.
[29] Gala, T. M., and Attard, P., 2004, "Molecular Dynamics Study of the Effect of Atomic Roughness on the Slip Length at the Fluid-Solid Boundary During Shear Flow," Langmuir, **20**, pp. 3477–3482.
[30] Hansen, J. P., and McDonald, I. R., 1976, *Theory of Simple Liquids*, Academic, London.
[31] Ziarani, A. S., and Mohamad, A. A., 2005, "Nanohydrodynamics: The Effect of Solid Surface Roughness on Stability Flow," *Proc. of 13th Annual (International) Conference of Mechanical Engineering*, May 17–19, Isfahan University of Technology, Isfahan, Iran, pp. 1–8.
[32] Heyes, D. M., Morris, G. P., and Evans, D. J., 1985, "Nonequilibrium Molecular Dynamics Study of Shear Flow in Soft Disks," Chem. Phys., **83**, pp. 4760–4766.
[33] Zdravkovich, M. M., 1985, "Flow Induced Oscillations of Two Interfacing Circular Cylinders," J. Sound Vib., **101**, pp. 511–521.
[34] White, F. M., 2003, *Fluid Mechanics*, 5th ed., McGraw-Hill, New York.
[35] Lam, K. M., Wong, P. T. Y., and Ko, N. W. M., 1993, "Interaction of Flows Behind Two Circular Cylinders of Different Diameters in Side-by-Side Arrangement," Exp. Therm. Fluid Sci., **7**, pp. 189–201.

Yiqing Yuan[1]
Eysion A. Liu
James Hill

DaimlerChrysler Corporation,
800 Chrysler Dr.,
Auburn Hills, MI 48326

Qian Zou
Oakland University,
Rochester, MI

An Improved Hydrodynamic Model for Open Wet Transmission Clutches

A mathematical model describing the hydrodynamics of the flow within a disengaged wet transmission clutch is presented. The primary improvement of this model over the existing ones is the inclusion of the surface tension effect, which is expressed in the pressure equation as an additional term. The drag torque predicted by the model correlates well with the test data for nongrooved clutch packs. The significance of the surface tension in this type of flows is discussed as well. [DOI: 10.1115/1.2427088]

Introduction

Reduction of parasitic loss in disengaged wet clutches is the focus of today's automatic transmission design because it is one of the potential areas where improvements can be made to increase transmission efficiency. This requires a good understanding of the physical phenomenon and drag characteristics of open wet clutches. However, a search of the literature reveals that a model that can provide predictions of engineering-level accuracy does not exist, although quite a large amount of work has been done in this area.

In 1984, the governing equations for the turbulent flow in a thrust bearing subject to centrifugal effect were presented by Hashimoto et al. [1]. These equations describe the flow between two adjacent flat rotating plates facing each other at an angle. Although this work is not directly applicable to clutches, it laid down a framework on which some subsequent clutch models were developed.

In a paper more specifically addressing the drag losses of wet clutches and brakes, Kato et al. [2] utilized Hashimoto's equations to derive the following equations that describe the pressure distribution and drag torque in the oil film between clutch plates:

$$P(r) = P(r_2) + \frac{\mu Q_s}{2\pi r_m h^3 N G_r}(r_2 - r) - \frac{\rho\omega^2}{2}(r_2^2 - r^2)\left(f + \frac{1}{4}\right) \quad (1)$$

$$T = 2\pi N \int_{r_c}^{r_2} \frac{\mu\omega r^3}{h}(1 + 0.0012\,\mathrm{Re}^{0.94})dr \quad (2)$$

However, Kato's equations fall short in predicting the pressure distribution and drag torque accurately, evidenced by the comparison shown in their publication. In fact, there are significant discrepancies between the calculated and experimental drag torques. There are two major shortcomings in their model. The first is that the cavitation is considered to be the only reason for the deficit of the oil film, and it starts from the inner radius. This is generally not true when the clutch speed is below 4000 rpm in a regular wet friction clutch of automatic transmissions for passenger cars because the pressure in the clutch can barely go low enough for cavitation to take place. In fact, some observations have shown that the deficit of the oil film starts from the outer radius. This is likely the reason that the torque peaks at a higher clutch speed than the experimental data. The second drawback is that the dominant factor in the dynamic equilibrium of the oil film, surface tension, is not addressed at all in their model.

In a more recent publication, the effects of various design factors, such as facing area, wave height, number of grooves, and flow rate, are studied and the following theoretical drag torque equation is presented by Kitabayashi et al. [3]:

$$T = \frac{N\mu\pi(r_2^2 - r_1^2)\omega r_m^2}{h} \quad (3)$$

Obviously, Eq. (3) can only represent the rising portion of a typical drag torque curve in the low-speed region. Refer to the test data in Figs. 6–9 for examples of the torque curves.

From the above review of the previous work, it is clear that the effect of capillary and surface tension forces in retaining the oil film in clutch clearances has not been revealed yet to date. The objective of this work is to introduce this important term into the pressure equation, to evaluate the effect of this factor on the torque prediction, and to validate the theory through comparison to available test data.

Theoretical Analysis

For the steady-state, incompressible oil film between nongrooved open clutch plates operating in turbulent regime subject to centrifugal effect, the governing equation can be expressed as [1]

$$-\frac{\rho V_\theta^2}{r} = -\frac{\partial p}{\partial r} + \frac{\partial \tau_{rz}}{\partial z} \quad (4)$$

$$0 = -\frac{1}{r}\frac{\partial p}{\partial \theta} + \frac{\partial \tau_{\theta z}}{\partial z} \quad (5)$$

$$\frac{1}{r}\frac{\partial (rV_r)}{\partial r} + \frac{1}{r}\frac{\partial V_\theta}{\partial \theta} + \frac{\partial V_z}{\partial z} = 0 \quad (6)$$

A typical gear-shifting clutch is shown in Fig. 1. These types of clutches usually operate in a near atmospheric environment, with minimal differential pressure between the inlet (inner diameter) and outlet (outer diameter). The oil motion in the radial direction between the plates is essentially driven by the centrifugal force, whereas the viscous and surface tension forces tend to resist this motion.

The importance of surface tension force with respect to viscous and hydrodynamic forces can be characterized by such dimensionless quantities as the capillary number Ca and the Weber number We, along with the Reynolds number Re. The capillary number, the ratio of viscous force to surface tension force, is defined as

[1]Corresponding author.

Contributed by the Fluids Engineering Division of ASME for publication in the JOURNAL OF FLUIDS ENGINEERING. Manuscript received May 9, 2006; final manuscript received September 5, 2006. Assoc. Editor: Yu-Tai Lee.

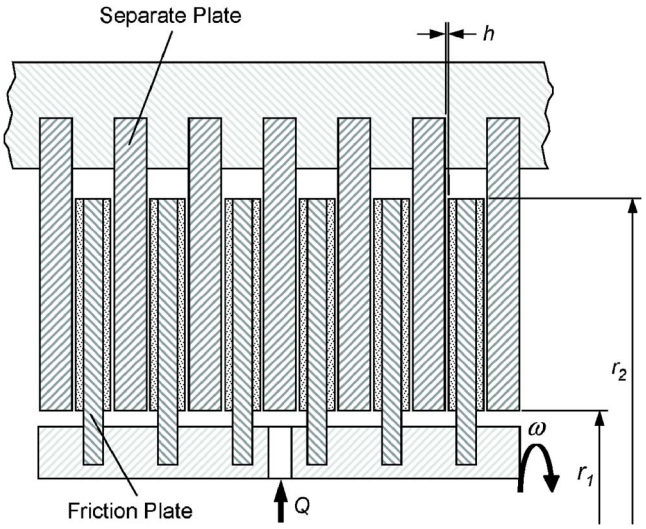

Fig. 1 Schematic of an open clutch pack

$$\mathrm{Ca}_r = \frac{\mu V}{\sigma} \tag{7}$$

The Weber number is the ratio of hydrodynamic force to surface tension force

$$\mathrm{We} = \frac{\rho L V^2}{\sigma} \tag{8}$$

When $\mathrm{Re} \ll 1$, the surface tension effects can be neglected if $\mathrm{Ca} \gg 1$; when $\mathrm{Re} \gg 1$, the surface tension effects can be neglected if $\mathrm{We} \gg 1$. To determine the relative importance of above-mentioned forces, it is crucial to understand that these dimensionless quantities must be utilized in the right direction, i.e., radial, circumferential, or axial. Since the radial direction is of main interest in this study in which the centrifugal force takes effect, the dimensionless quantities have to be evaluated in radial direction as follows:

$$\mathrm{Re}_r = \frac{\rho h V_r}{\mu} \tag{9}$$

$$\mathrm{Ca}_r = \frac{\mu V_r}{\sigma} \tag{10}$$

and

$$\mathrm{We}_r = \frac{\rho h V_r^2}{\sigma} \tag{11}$$

For example, looking at a typical situation below, the numbers do not satisfy either of the above criteria. For a clutch pack of 0.1 mm clearance, 120 mm i.d., 140 mm o.d., 2.5×10^{-6} m^3/s flow rate per facing, $\mathrm{Re}_r = 0.75$, $\mathrm{Ca}_r = 0.014$, $\mathrm{We}_r = 0.010$ at the mean diameter at 93 °C. Therefore, the surface tension effects should not be neglected in this scenario.

In addition, the importance of surface tension depends on the ratio of centrifugal force to surface tension force, i.e., Bond number, which is defined as

$$\mathrm{Bo} = \frac{\rho \omega^2 r (r_2 - r_1) h}{\sigma} \tag{12}$$

The surface tension effects can be neglected if $\mathrm{Bo} \gg 1$. Using the parameters in Eq. (12), at 2000 rpm of rotating speed, $\mathrm{Bo} = O(10^1)$. If the oil has dissolved air or other contamination in it, with the resulted changes in its physical properties, Bo may well drop into the range of $O(10^0)$. In this case, surface tension can no longer be neglected.

The boundary conditions for these equations are

$$\left.\begin{aligned} &V_r(z=0) = V_r(z=h) = 0 \\ &V_\theta(z=0) = r\omega, \quad V_\theta(z=h) = 0 \\ &V_z(z=0) = V_z(z=h) = 0 \end{aligned}\right\} \tag{13}$$

According to Hashimoto et al. [1], integration of Eqs. (4)–(6) along the axial direction yields

$$-\frac{\rho}{r}\int_0^h V_\theta^2\, dz = -\frac{\partial p}{\partial r} h + \tau_{rz}(h) - \tau_{rz}(0) \tag{14}$$

$$0 = \tau_{\theta z}(h) - \tau_{\theta z}(0) \tag{15}$$

$$\frac{\partial}{\partial r}\left(r\int_0^h V_r\, dz\right) + \frac{\partial}{\partial \theta}\left(\int_0^h V_\theta\, dz\right) = 0 \tag{16}$$

For the shear stress terms, we have the following approximation:

$$\tau_{rz}(h) - \tau_{rz}(0) \cong -\frac{\mu}{h G_r} V_{rm} \tag{17}$$

$$\tau_{\theta z}(h) - \tau_{\theta z}(0) \cong -\frac{\mu}{h G_\theta}\left(V_{\theta m} - \frac{r\omega}{2}\right) \tag{18}$$

$$\int_0^h V_\theta^2\, dz \cong h V_{\theta m}^2 + f r^2 \omega^2 h \tag{19}$$

$$V_{rm} = \frac{1}{h}\int_0^h V_r\, dz \tag{20}$$

$$V_{\theta m} = \frac{1}{h}\int_0^h V_\theta\, dz \tag{21}$$

$$f = \begin{cases} 0.885\, \mathrm{Re}_h^{-0.367} & (\mathrm{Re}_h \geqslant 500) \\ 0.09 & (\mathrm{Re}_h < 500) \end{cases} \tag{22}$$

where

$$\mathrm{Re}_h = \frac{\rho \omega r h}{\mu} \tag{23}$$

The turbulence coefficients are related to the local Reynolds number by following expressions:

$$G_r = \tfrac{1}{12}(1 + 0.00069\, \mathrm{Re}_h^{0.88}) \tag{24}$$

$$G_\theta = \tfrac{1}{12}(1 + 0.00069\, \mathrm{Re}_h^{0.95}) \tag{25}$$

$$\frac{\rho}{r} V_{\theta m}^2 + f \rho r \omega^2 = \frac{\partial p}{\partial r} + \frac{\mu}{h^2 G_r} V_{rm} \tag{26}$$

$$V_{\theta m} = \frac{r\omega}{2} \tag{27}$$

$$V_{rm} = -\frac{h^2}{\mu} G_r \frac{\partial p}{\partial r} + \frac{\rho h^2 r \omega^2}{\mu}\left(f + \frac{1}{4}\right) G_r \tag{28}$$

Equation (28) can be rewritten as

$$\frac{\partial p}{\partial r} = -\frac{\mu}{h^2 G_r} V_{rm} + \rho r \omega^2 \left(f + \frac{1}{4}\right) \tag{29}$$

The flow rate through each of the clearances of a clutch is

$$Q = 2\pi r_m h V_{rm} \tag{30}$$

The shape or pattern of the oil film in the clutch depends on the relative significance of centrifugal, viscous, and surface tension

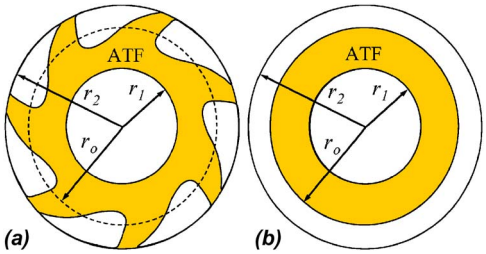

Fig. 2 Schematic of a partial oil film within a clutch

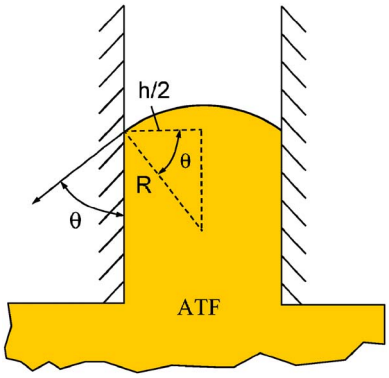

Fig. 3 Schematic of contact angle between the oil film and clutch plate

forces that the fluid is subject to. In the small clearance between the friction and separator plates, the fluid should wet both surfaces due to surface tension. At low rotating speed, the centrifugal force is small and the radial velocity decreases as the fluid approaches the outer radius to satisfy the condition of conservation of mass. Thus, there exists a full oil film between the plates. As rotating speed increases, the fluid starts to lose the "freedom" to slow down as it approaches the outer radius since the centrifugal force becomes dominant that drive the fluid outward. As a result, rivulets of fluid develop between the plates in order to satisfy the conservation of mass, as shown in Fig. 2(*a*). The fraction of wetted area decreases as the fluid moves outward because the fluid is accelerated in the radial direction by the centrifugal force.

To facilitate the inclusion of surface tension in the present analysis, an equivalent radius assumption is introduced. This is the outer radius of a hypothesized film, as shown in Fig. 2(*b*), for which the resultant flow rate and total drag torque equals to that of the original film (Fig. 2(*a*)).

Note in Eq. (30) the flow rate is evaluated at the mean radius r_m located in the oil film where $r_1 \leqslant r_m \leqslant r_o$. Substitution of Eq. (30) into Eq. (29) and integration in radial direction from r_1 to r within the oil yield

$$p(r) - p(r_1) = -\frac{\mu Q}{2\pi r_m h^3 G_r}(r - r_1) + \frac{\rho\omega^2}{2}\left(f + \frac{1}{4}\right)(r^2 - r_1^2) \tag{31}$$

Let r be the outer radius of the oil film r_{o-}, the equation becomes

$$p(r_{o-}) - p(r_1) = -\frac{\mu Q}{2\pi r_m h^3 G_r}(r_o - r_1) + \frac{\rho\omega^2}{2}\left(f + \frac{1}{4}\right)(r_o^2 - r_1^2) \tag{32}$$

Because of the existence of surface tension at the interface between fluid and air, there is a pressure jump across the meniscus, which exists along the interface except in the rivulets where the fluid leaves the clutch. As an intrinsic inference from the above-mentioned equivalent radius assumption, it is further assumed that a meniscus exists along the continuous single interface of the hypothesized film, with the geometrical parameters shown in Fig. 3. It is worth mentioning that this circular interface is not from real-world observation, but an imaginary one that allows the following pressure distribution equations to be formulated. The pressure jump is related to the curvatures of the interface by

$$p(r_{o-}) - p(r_{o+}) = \sigma(k_\theta + k_z) \tag{33}$$

Since k_θ is much smaller than k_z, Eq. (33) can be approximated as

$$p(r_{o-}) - p(r_{o+}) = \sigma k_z = \frac{\sigma}{R} = \frac{2\sigma\cos\theta}{h} \tag{34}$$

Substituting Eq. (34) into Eq. (32) and rearranging, we have

$$p(r_{o+}) - p(r_1) = -\frac{\mu Q}{2\pi r_m h^3 G_r}(r_o - r_1) + \frac{\rho\omega^2}{2}\left(f + \frac{1}{4}\right)(r_o^2 - r_1^2) - \frac{2\sigma\cos\theta}{h} \tag{35}$$

In most of the cases, the feeding pressure is approximately the same as the exiting pressure of the clutch, i.e., $p(r_{o+}) \approx p(r_1)$, Eq. (35) can be used to find the flow rate when r_o is known

$$Q = \frac{\pi r_m h^2 G_r}{\mu(r_o - r_1)}\left[\rho\omega^2 h\left(f + \frac{1}{4}\right)(r_o^2 - r_1^2) - 4\sigma\cos\theta\right] \tag{36}$$

If flow rate is known, then the outer radius r_o of the oil film can be solved from

$$\frac{\rho\omega^2}{2}\left(f + \frac{1}{4}\right)r_o^2 - \frac{\mu Q}{2\pi r_m h^3 G_r}r_o + \frac{\mu Q}{2\pi r_m h^3 G_r}r_1 - \frac{2\sigma\cos\theta}{h} - \frac{\rho\omega^2}{2}\left(f + \frac{1}{4}\right)r_1^2 = 0 \tag{37}$$

Because of the conservation of mass, flow rate Q should be independent of radial position. In real-world engineering practice, the flow rate may be evaluated most conveniently at $r = r_1$. Note that in this case, G_r and f must be evaluated at the same radial position since they could be a function of the radial position.

The shear stress on the rotating plate is [1]

$$\tau_{\theta z}(z = 0) = \frac{\mu\omega r}{h}(1 + 0.0012\,\mathrm{Re}_h^{0.94}) \tag{38}$$

Finally, the drag torque on each of the rotating plate then can be expressed as follows:

$$T = 2\pi\int_{r_1}^{r_o}\frac{\mu\omega r^3}{h}(1 + 0.0012\,\mathrm{Re}_h^{0.94})dr \tag{39}$$

Validation of the Model

In order to validate the model described above, comparisons are made between the model predictions and the available test data [4]. The geometric parameters and test conditions are summarized in Table 1. To better demonstrate the improvements of our model over the existing models, the results from the models proposed by Kato et al. [2] and Kitabayashi et al. [3] are examined as well.

Note that the fluid properties used in the test are unknown and therefore have to be postulated to some extent. The density is assumed to be the same as one type of transmission fluid at the given temperature, and the viscosity is presumed so that the slopes of the torque curves at the low-speed region match each other between the test and model. The surface tension coefficient is obtained by interpolation or extrapolation from the published data

Table 1 Summary of geometric variables and test conditions for various test cases

Case No.	r_1 (mm)	r_2 (mm)	h (mm)	Q/facing (cm^3/s)	T (°C)	ρ (kg/m^3)	μ (Pa s)	σ (N/m)
1	52.6	66.9	0.2	1.07	104	790.8	0.015	0.026
2	52.6	66.9	0.2	3.44	104	790.8	0.015	0.026
3	64.2	73.5	0.1	2.78	80	806.7	0.018	0.028
4	49.8	66.7	0.13	2.54	38	865.0	0.047	0.031

for automatic transmission fluid with foam inhibitor [5]. The contact angle was assumed to be 0 deg, i.e., a convex meniscus.

Shown in Fig. 4 is the outer radius of the oil film predicted by the new model, as a function of clutch speed. In cases 1 and 2, with the clutch speed increasing from 0 rpm, there is a full oil film in the clutch until the speed reaches 2000 rpm, where the outer radius starts to drop sharply. At 3000 rpm, there is roughly only half of the film remaining in the clutch. In case 3, the film outer radius starts to decline at 2500 rpm, and there is less than a quarter of the film remaining at 4000 rpm. Clearly, the speeds at which film radius starts to decline correlate to the peaks in the torque curves in Fig. 6. In other words, the decrease of drag torque after it peaks is due to the shrinking film area. The outer radius predicted by Kato's model is shown in Fig. 5. Although a full oil film exists when clutch speed is low, the film starts to shrink at 500 rpm, 1000 rpm, and 2500 rpm for cases 1–3, respectively. In addition, the oil film shrinks very quickly with speed, and disappears completely within the next 500 rpm of increase in speed.

Figure 6 is the comparison of drag torques predicted by the three models with the test data for case 1. Kitabayashi's model follows the slope of the initial portion of the torque curves in low-speed region to some extent, but with considerable discrepancies. Since the torque increases with speed monotonically in this model, this model can not predict anything in high speed region beyond 2000 rpm with reasonable accuracy. On the other hand, Kato's model predicts that the drag torque begins to decrease with speed right from 500 rpm, which is not accurate at all in terms of the magnitude of the peak and the speed at which the torque peaks. On the contrary, the new model's prediction is in a good agreement with the test result in the range of clutch speed from 500 rpm to 3000 rpm. In particular, both the peak torque and the clutch speed at which the peak occurs are well predicted with an error within 6%. Note that the torque peaks at 2000 rpm, which correlates well with the speed at which the oil film starts to shrink, as shown in Fig. 4.

Figure 7 is the results for case 2. Kitabayashi's model yields an excellent prediction in low-speed range, whereas Kato's model indicates a peak that is not only much smaller than the test result, but also occurs at the much lower speed. The new model shows a peak at 2000 rpm compared to 2500 rpm in test. The prediction follows the test result fairly well, in general. Again, the predicted peaking speed, 2000 rpm, is exactly the same as the onset point of oil film shrinkage shown in Fig. 4.

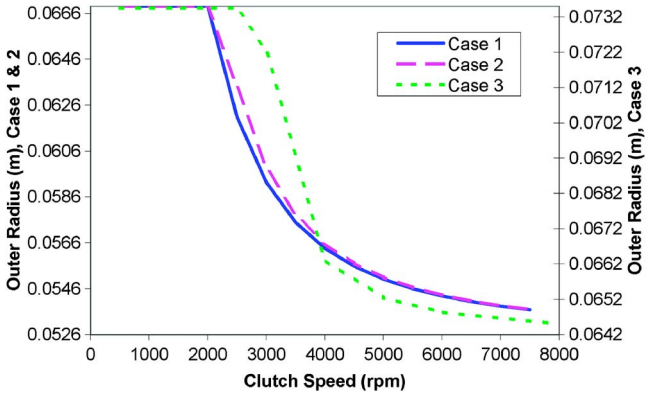

Fig. 4 Oil film outer radius predicted by new model

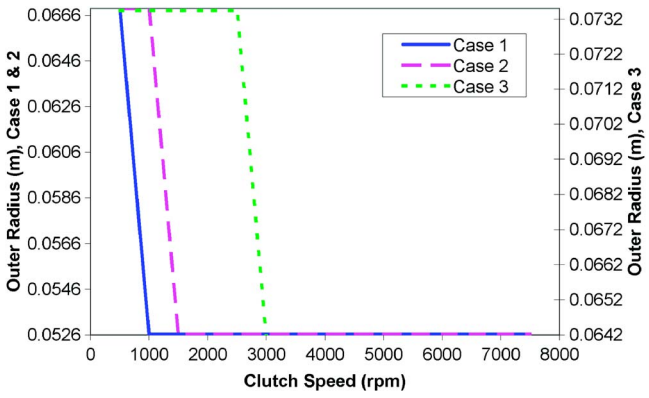

Fig. 5 Oil film outer radius predicted by Kato's model

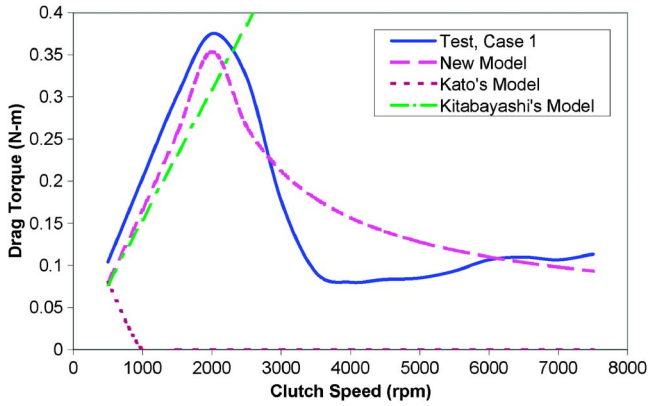

Fig. 6 Comparison of drag torque between model prediction and test for case 1

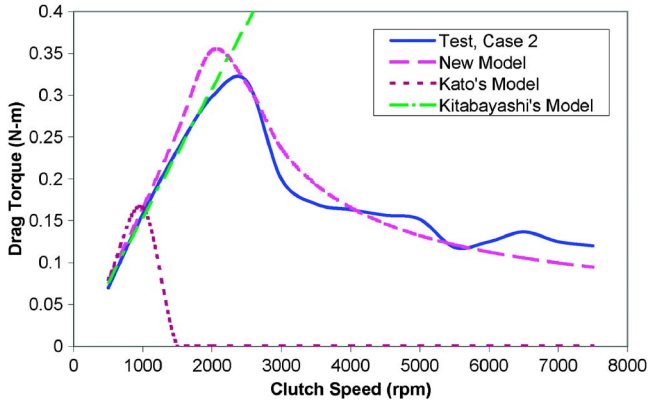

Fig. 7 Comparison of drag torque between model prediction and test for case 2

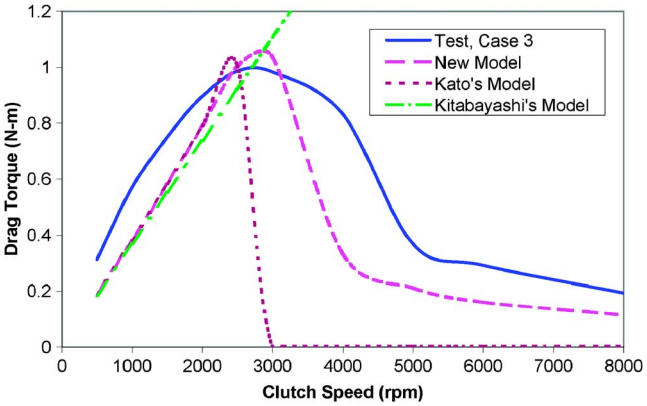

Fig. 8 Comparison of drag torque between model prediction and test for case 3

The results for case 3 are shown in Fig. 8. The prediction of Kitabayashi's model is close to the test result only in terms of slope. Kato's model gives a good prediction near the peak region, but the agreement between the model and test results outside the peak region is very poor. The new model is still the best among the three models in terms of general agreement between the model and the test results.

From the above comparisons made between the new model and Kato's model, it is clear that with surface tension effect accounted, the predicted torque peak shifts toward higher speed. This is simply the most significant difference between these two models. Obviously, the surface tension force acting on the oil film helps retain oil film within the clutch plates as clutch speed increases.

Shown in Fig. 9 is the comparison between the new model prediction and test result for case 4. As can be seen, the difference in the peak drag between model prediction and test is within 10%. Also, both torque curves peak at the same clutch speed, indicating that the mechanism for film diminution with increased clutch speed is well captured in the model.

It must be pointed out that errors remain large in some cases between the new model and the test, typically for those speeds beyond the peak region. Future work is needed to find out the reasons for the discrepancies.

Conclusions

In an open clutch pack, the capillary force can be one to two orders of magnitude larger than the hydrodynamic and viscous forces. As a result, the surface tension effect plays an important role in maintaining the oil film within open clutch packs. This effect was not accounted in any previous clutch models, which is a critical reason for these models' failure in predicting the drag characteristics.

A mathematical model that incorporates the surface tension effects has been formulated. The drag torque predicted by the model correlates well with the test data for non-grooved clutch packs in terms of the peak and the clutch speed at peak. This makes it a valuable tool in the engineering development and design of clutches packs of low parasitic losses.

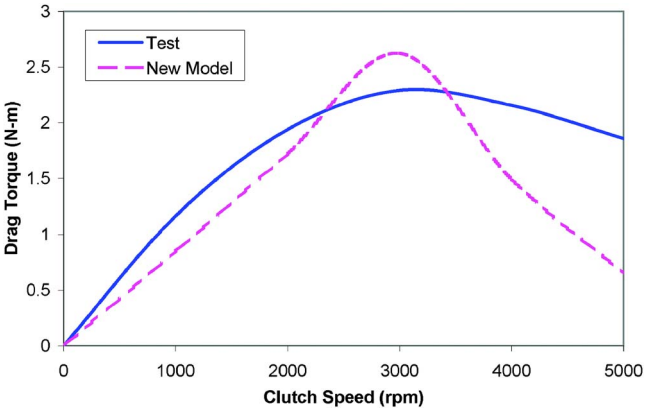

Fig. 9 Comparison of drag torque between model prediction and test for case 4

Nomenclature

Ca = capillary number
f = turbulence coefficient (a function of Reynolds number)
G_r = turbulence coefficient (a function of Reynolds number)
G_θ = turbulence coefficient (a function of Reynolds number)
h = clearance
k = curvature
N = number of frictional surfaces
p = oil film pressure
r = radial coordinate
r_1 = inner radius
r_2 = outer radius
r_o = radius where full oil film breaks due to centrifugal effects
r_m = average (effective) radius
Re = Reynolds number
Re_h = Reynolds number based on clutch clearance $(=\rho\omega rh/\mu)$
O = order of magnitude
Q = flow rate through each clearance of the clutch
Q_s = total flow rate through the clutch
T = torque
V_r = radial velocity component
V = velocity
We = Weber number
z = axial coordinate

Greek Symbols

μ = oil viscosity
ρ = oil density
σ = surface tension coefficient of fluid
θ = angular coordinate
τ = shear stress
ω = angular velocity

Subscripts

m = mean value

References

[1] Hashimoto, H., Wada, S., and Murayama, Y., 1984, "The Performance of a Turbulent-Lubricated Sliding Bearing Subject to Centrifugal Effect," Trans. Jpn. Soc. Mech. Eng., Ser. C **49**(446), pp. 1753–1761.
[2] Kato, Y., Murasugi, T., Hirano, H., and Shibayama, T., 1993, "Fuel Economy Improvement Through Tribological Analysis of the Wet Clutches and Brakes of an Automatic Transmission," SAE Paper No. 938179.
[3] Kitabayashi, H., Li, C., and Hiraki, H., 2003, "Analysis of the Various Factors Affecting Drag Torque in Multiple-Plate Wet Clutches," SAE Paper No. 2003–01–1973.
[4] Fairbank, D., 1996, "Drag Analysis Open Pack Friction Clutch," BorgWarner Technical Report No. 176–05–0029.
[5] Kemp, S., and Linden, J., 1990, "Physical and Chemical Properties of a Typical Automatic Transmission Fluid," SAE Paper No. 902148.

Ramin K. Rahmani[1]
Postdoctoral Fellow
e-mail: rkhrahmani@yahoo.com

Anahita Ayasoufi
Postdoctoral Fellow
e-mail: aayasoufi@yahoo.com

Department of Mechanical Engineering,
The University of Alabama at Birmingham,
Birmingham, AL

Theo G. Keith
Director Research and Technology Directorate
NASA Glenn Research Center,
Cleveland, OH
e-mail: theo.g.keith@grc.nasa.gov

A Numerical Study of the Global Performance of Two Static Mixers

The use of in-line static mixers has been widely advocated for an important variety of applications, such as continuous mixing, heat and mass transfer processes, and chemical reactions. This paper extends previous studies by the authors on industrial static mixers and illustrates how static mixing processes of single-phase viscous liquids can be numerically simulated. Mixing of Newtonian, shear-thinning, and shear-thickening fluids through static mixer, as well as thermal enhancement by static mixer is studied. Using different measuring tools, the global performance and costs of SMX (Sulzer mixer X) and helical static mixers are studied. It is shown that the SMX mixer manifests a higher performance; however, the required energy to maintain the flow across a SMX mixer is significantly higher. [DOI: 10.1115/1.2427082]

Keywords: helical static mixer, SMX static mixer, particles distribution uniformity, residence time distribution, shear-thinning fluids, shear-thickening fluids

Introduction

Mixing is an essential component of nearly all industrial chemical processes, ranging from simple blending to complex multiphase reaction systems for which the reaction rate, yield, and selectivity are highly dependent on the mixing performance. Consequences of improper mixing include nonreproducible processing conditions and lowered product quality, resulting in the need for more elaborate downstream purification processes and increased waste disposal costs. For successful mixing, there must be bulk or convective flow so that stagnant regions do not exist and there must also be regions of intensive or high shear mixing in the flowfield.

Mixing can be achieved in a variety of ways, including mechanical agitation or by static mixers although mechanical agitators are commonly used for batch mixing, static mixers are often preferred for continuous mixing applications. Static mixers offer several advantages. Their particular advantages are inline mixing, low maintenance and operating costs, low space requirements, no moving parts, low power consumption, good mixing at low shear rates (locally high shear rates in agitators can damage sensitive materials), fast product grade changes, simultaneous homogenization of residence time behavior, and self-cleaning.

Generally, a static mixer consists of a number of equal stationary units, placed on the inside of a pipe or channel in order to promote mixing of flowing fluid streams. The mixing elements or segments, as one could imagine, appear to have been cut from a long periodic structure. The purpose of the segments is to redistribute fluid in the directions transverse to the direction of the main flow, i.e., in the radial and tangential directions. A range of designs exists for a wide range of specific applications. The shape of the elements determines the character of the fluid motion and thus determines the effectiveness of the mixer.

Static mixers became established in the process industries in the 1970s; however, the invention of static mixers goes back to the nineteenth century. An English patent in 1874 describes a single element, multilayer mixer used to mix air with a gaseous fuel [1]. Because of a very broad range of applications for static mixers, a variety of segment designs are available. Currently, more than 30 commercial models are available. The shape of the elements determines the character of the fluid motion and thus determines the effectiveness of the mixer. The effectiveness of a static mixer is a function of the specific segment design and the number of elements, as well as the physical properties of the mixing materials and the flow conditions.

Because of the industrial importance of static mixers, many studies have been undertaken in an attempt to characterize their performance. There are several key parameters in the design procedure of a static mixer. Some of the most important ones are the degree of mixing of working fluids, pressure drop across the mixer, and residence time distribution of fluid elements. An ideal static mixer provides a highly mixed material with low pressure drop and similar traveling history for all fluid elements. To choose a static mixer for a given application or in order to design a new static mixer, besides experimentation, it is possible to use powerful computational fluid dynamics (CFD) tools to study the performance of static mixers.

Pressure drop across a static mixer was measured experimentally [2–6], since this information is essential in order to correctly size the pump feeding the static mixer. Mass transfer [7] and also drop size distribution [8] in static mixers have also been studied experimentally. A number of studies have considered heat transfer in different static mixers [9–14].

Helical static mixers (Fig. 1, top), together with the *SMX mixers* (Fig. 1, bottom), are the most common static mixers in the industry. A helical static mixer consists of left- and right-twisting helical elements placed at a right angle to each other. SMX mixer is a multilayer design formed by layers of single plates with opposing orientation. The mixing elements of SMX static mixer consist of crossed bars at a 45 deg angle with the axis of the pipe. Each element is rotated 90 deg with respect to the previous element. The SMX mixer in this study has five plates in each row.

For a given application, besides experimentation, the modern approach to study the performance of static mixers is to use powerful CFD tools. In recent years, significant progress has been made in the characterization of fluid-mechanical mixing using Lagrangian tracking techniques [15–20]. The majority of the previous work on static mixers has focused on model flows that are two-dimensional in space and periodic in time. A smaller set of studies has considered simplified three-dimensional, spatially periodic flows, e.g., [15,16], where a simple, two-dimensional, analytical approximation to the velocity field was developed. A fully three-dimensional simulation can be employed to study the performance of different static mixers in order to select a suitable

[1]Corresponding author.

Contributed by the Fluids Engineering Division of ASME for publication in the JOURNAL OF FLUIDS ENGINEERING. Manuscript received November 21, 2005; final manuscript received August 21, 2006. Assoc. Editor: Paul Durbin. Paper presented at the 2005 ASME International Mechanical Engineering Congress (IMECE2005), Orlando, Florida, USA, November 5–11, 2005.

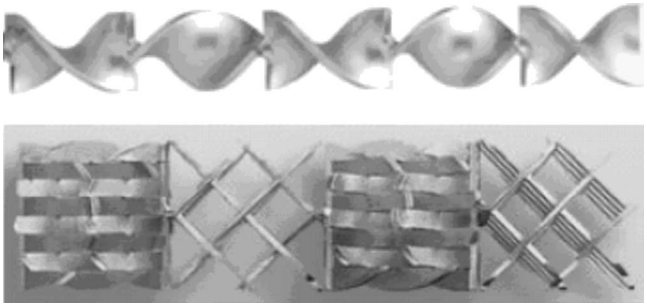

Fig. 1 Top: Helical static mixer, Bottom: SMX mixer

mixer, to improve an existing model, or to design a new one. Rauline et al. studied the performance of six different static mixers (including SMX and helical mixers) using a commercial code (POLY3D) [21]. The fluid was Newtonian and the Reynolds number for all cases was about 5×10^{-4}, using a computational grid with about 19,000 cells [21].

The static mixers studied here are among the most common industrial mixers: the helical static mixer (TAH, Robbinsville, NJ, and Chemineer, Dayton, OH) and the SMX mixer (Sulzer, Winterthur, Switzerland). Both mixers' geometrical parameters are shown in Table 1. In order to compare the mixers properly, the material thickness for both mixers are equal and taken to be 0.1 in. Also, mixers' lengths (and diameters) are chosen to be the same. Although, the ratio of the each segment length to the mixer diameter is ~0.846 for helical mixers manufactured by TAH; and in a standard Kenics mixer (Chemineer), the segment length is 1.5–2.5 times the mixer diameter. It is shown by Hobbs [22] that the ratio of the each segment length to the mixer diameter for a helical static mixer has no impact on the fluid mixing. However, a more compact mixing element can improve the rate of heat transfer in a helical static mixer [10].

In this paper, numerical techniques are applied to quantitatively evaluate the performance of two common static mixers: Helical and SMX. The fluid mixing (considering Newtonian as well as non-Newtonian materials) and heat transfer enhancement by these static mixers are studied and a comparison between their performances is presented.

Analysis

For steady incompressible flow, the mass conservation and momentum equations are given by

$$\frac{\partial u_i}{\partial x_i}=0 \tag{1}$$

$$\rho\frac{\partial(u_iu_j)}{\partial x_j}+\frac{\partial p}{\partial x_i}=\frac{\partial \tau_{ij}}{\partial x_j}+\rho g_i+F_i \tag{2}$$

In the absence of a gravitational body force and any external body force, the two last terms on the right-hand side of Eq. (2) are zero. The stress tensor τ_{ij} in Eq. (2) for incompressible steady flow is given by

$$\tau_{ij}=\mu\left(\frac{\partial u_i}{\partial x_j}+\frac{\partial u_j}{\partial x_i}\right) \tag{3}$$

Table 1 Static mixer dimensions (in inches)

Diameter (d)	1.0
Element length (L)	1.0
Thickness	0.1
Entrance length	2.0
Exit length	2.0

The energy equation for steady incompressible flow is

$$\frac{\partial(\rho u_iE+p)}{\partial x_i}=\frac{\partial}{\partial x_i}\left(K\frac{\partial T}{\partial x_i}+u_j\tau_{ij}\right) \tag{4}$$

The total energy in Eq. (4) is

$$E=h-\frac{p}{\rho}+\frac{u_iu_i}{2} \tag{5}$$

For a pure material with no phase change, the enthalpy is given by

$$h=\int_0^T c_p\,dT \tag{6}$$

For the material used in this study, value of density is assumed 1000 kg/m^3. The specific heat is set at 1000 J/kg K, and the viscosity is set to 0.00127324 kg/m s. Three different values for thermal conductivity are considered: 0.01, 0.1, and 1 W/m K.

For Newtonian fluids, viscosity depends only on temperature and pressure; it is independent of the rate of shear. The flow curve for Newtonian fluids is therefore a straight line of slope μ, and the single constant μ completely characterizes the dynamic viscosity of the fluid. For non-Newtonian fluids, viscosity becomes a function of the strain rate. A large portion of working fluids in industry fall into the time-independent non-Newtonian fluids category. An empirical functional relation known as the *power law* is widely used to characterize fluids of this type. This relation was originally proposed by Oswald [23] and has since been fully described by Reiner [24]. The power-law model for the shear stress uses the following equation for the viscosity:

$$\mu=\kappa e^{T/T_0}\dot{\gamma}^{n-1} \tag{7}$$

Another equation that is used to describe these fluids is called the *Carreau model*. The Carreau model attempts to describe a wide range of fluids by the establishment of a curve fit to piece together functions for both Newtonian and non-Newtonian laws. The Carreau model uses the following equation for the viscosity:

$$\mu=\mu_\infty+(\mu_0-\mu_\infty)[1+(\lambda e^{T/T_0}\dot{\gamma})^2]^{n-1/2} \tag{8}$$

Details about different models for non-Newtonian viscosity can be found in the literature, e.g., [25–27]. The less general (but more commonly used) forms of Eqs. (7) and (8) do not account for the temperature effects on the behavior of non-Newtonian fluids, which, respectively, are $\mu=\kappa\dot{\gamma}^{n-1}$ and $\mu=\mu_\infty+(\mu_0-\mu_\infty)[1+(\lambda\dot{\gamma})^2]^{n-1/2}$. Bird et al. presented an exponential function of time in order to account for this phenomenon [28]. Kumar presented a comprehensive review of the many scattered relationships describing the dependence of viscosity of both Newtonian and non-Newtonian flow regimes on molecular weight, molecular weight distribution, temperature, and chain branching [29].

If index n is set to 1 in Eqs. (7) and (8), these equations reduce to a viscosity relation for a Newtonian fluid. If index n is set to a value of <1, these equations describe the viscosity of a shear-thinning or pseudoplastic, non-Newtonian fluid (the apparent viscosity decreases as the rate of shear increases). If index n is set to a value greater than unity, the equations describe the viscosity of a shear-thickening or dilatant, non-Newtonian fluid (the apparent viscosity for these materials increases with increasing rates of shear). The parameter λ is a constant with units of time, where $1/\lambda$ is the critical shear rate at which viscosity begins to decrease.

Carreau and Kee reviewed more commonly used rheological models [30]. They evaluated the models based on their ability to simultaneously describe most of the rheological functions, such as the non-Newtonian viscosity, the normal stress difference functions, the components of the complex viscosity, stress growth, and relaxation. They reported that the most successful equations appear to be the models obtained from molecular network considerations, such as the Carreau model [30].

Table 2 Mesh quality test results

Maximum volume ratio	1.000014
Maximum face ratio	1.002937
Aspect ratio	1.000001–1.003000
Diagonal ratio	1.000000–1.000001
Edge ratio	1.000000–1.002990
Midangle skewness	<0.000001
Equal-size skewness	<0.000001

In this study, the Metzner-Reed generalized Reynolds number is used for non-Newtonian cases, which was developed originally for flow conditions that are truly laminar and where suspensions are homogeneous. The Metzner-Reed generalized Reynolds number reflects flow behavior in the near-wall region. It refers to the steady-state flow of non-Newtonian liquids in pipes and is based on the nominal value of shear rate at the pipe wall equal to $8U/d$ [31].

Numerical Simulation

Mesh Generation. An unstructured hexagonal mesh was generated to model two-element static mixers inside a pipe, using a code developed by the authors. The geometry was modeled exactly, with no simplifications.

Table 2 shows the results of different mesh quality tests performed on the generated mesh used for the helical static mixer case. Similar results were obtained for the other computational grid used in this study. The generated computational grid is almost a uniform orthogonal grid. Here, maximum volume ratio is the ratio of the volume of the largest cell to the volume of the smallest one. Maximum face ratio is the ratio of the largest face area to the smallest face area. The aspect ratio is the maximum value of the average lengths of the edges in three coordinate directions in a cell to the minimum value of the average lengths of the edges in three coordinate directions in that cell. The diagonal ratio is the ratio of the longest diagonal to the shortest diagonal of a cell. The edge ratio is the ratio of the longest edge to the shortest edge of a cell. The midangle skewness is defined by the cosine of the minimum angle formed between the bisectors of the cell faces and is the maximum amount of the cosines of the three angles computed from the face-bisecting lines of the cell. Finally, the equal-size skewness is a measure of skewness, which is defined as follows:

$$\text{equal-size skewness} = \frac{V_{eq} - V}{V} \tag{9}$$

where V_{eq} is the maximum volume of an equilateral cell the circumscribing radius of which is identical to that of the mesh element. Details about different computational mesh generation algorithms and different mesh quality tests can be found in [32,33].

Flow and Heat Transfer Computation. The solver used in this study is a commercial code (FLUENT). The solver is a segregated, implicit, second-order upwind, finite volume scheme [25] that computes in double precision. Using the segregated approach, the governing equations are solved sequentially. To obtain second-order accuracy, quantities at the cell faces are computed using a multidimensional linear reconstruction approach [34,35]. Pressure-velocity coupling is achieved by using the SIMPLEC (SIMPLE-CONSISTENT) algorithm [36].

Boundary Conditions. No-slip boundary conditions are applied to the solid surface of the static mixer and also at the wall of the pipe. A constant mass flow rate is applied at the inlet and outlet boundaries. (Since the fluid is incompressible, this boundary condition is equivalent to the constant volumetric flow rate.) Different Reynolds numbers for the flow inside the pipe are obtained by varying the mass flow rate at the inlet boundary. For a non-Newtonian fluid, mass flow rate can be related to the generalized Reynolds number using

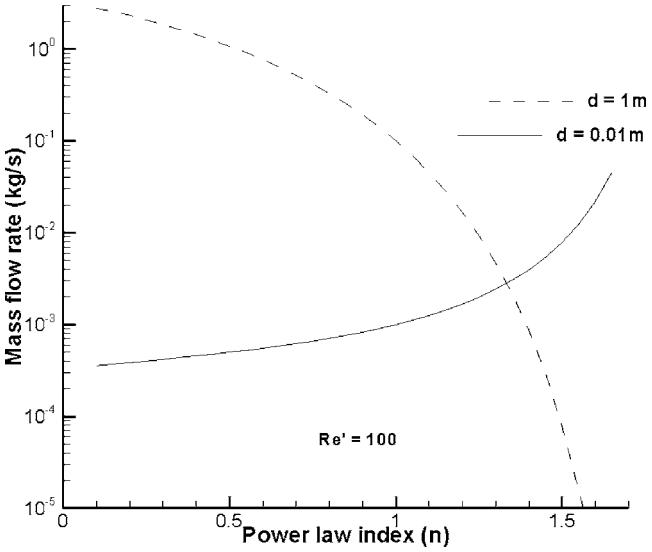

Fig. 2 Mass flow rate calculated based on Metzner-Reed Reynolds number definition

$$\dot{m} = \pi \left[\frac{\kappa \left(\frac{6n+2}{n} \right)^n \mathrm{Re}'}{2^{7-2n} \rho^{n-1} d^{3n-4}} \right] \tag{10}$$

It is mentioned that using large values for the diameter causes the mass flow rate to increase significantly for a given flow Reynolds number, when the power-law index decreases (Fig. 2). This leads to a higher velocity magnitude in the flowfield and the increase of pressure drop of the flow in pipe.

For cases including heat transfer, the fluid temperature at the inlet is set to 300 K. The temperature of the pipe surface is set to 500 K. Two extreme limits for the value of thermal conductivity of a material are zero and infinity; zero thermal conductivity can be modeled by adiabatic conditions and infinite thermal conductivity can be modeled by constant temperature distribution in the material (here, 500 K). These two boundary conditions on the mixer surface model two extreme limits for the mixing element and determine the two borders of the mixer effectiveness.

Numerical Solution Accuracy. The accuracy of the numerical solutions should be analyzed before confidence in the predictive ability of the numerical techniques can be justified. For the present study of mixing under noncreeping flow conditions, there is unfortunately an absence of sufficiently detailed and accurate experimental data to undertake a complete validation of the numerical results. However, the values of pressure drop across a similar mixer, computed by using the same numerical approach, are in good agreement with existing experimental data [37]. As for verification, a detailed mesh convergence study has indicated that the computational mesh employed in the present study is sufficiently refined to provide good numerical resolution. From 941,726 to 1,007,024 computational cells were used to numerically determine the flowfield; the meshing interval size for all cases is the same, the slight difference between the number of cells is because of differences in mixers' geometrical parameters. The predicted pressure drop across mixer shows the most sensitivity to the grid size for the case of Reynolds number of 100, when the working fluid is non-Newtonian ($n=0.60$). For this case, the predicted pressure drop by using a grid with 534,692 cells is ~8.4% less than pressure drop predicted by using a grid with 1,007,024 cells.

A study conducted using different numbers of particles for the mixing analysis has shown that the results are independent of the number of particles when a high number of particles, in this study

about half a million, is employed. The use of an inadequate number of particles to analyze mixing gives the impression that a high level of mixing has been achieved using a smaller number of mixing elements [37]. As the number of particles is increased, the presence of the striations associated with the mixing process becomes more evident.

Key Parameters in the Performance Study of a Mixer

Pressure Drop. The pressure drop across a static mixer has been experimentally measured for Newtonian and non-Newtonian fluids, and for laminar and turbulent flows. The measurements were made because pressure drop is essential in order to correctly size the extruder or pump, feeding the static mixer. Pressure drop across the mixer indicates the energy required to maintain the through flow. It also can be used to determine the static mixer efficiency. Here, the pressure drop is measured based on the difference between the area weighted-averaged pressures in two flow cross sections located at half-segment-length distances from the leading edge of the first mixing element and the trailing edge of the last mixing element. It is common to use a nondimensional pressure drop, *Z*-factor, to characterize static mixers,

$$Z = \frac{\text{Pressure drop in a pipe with static mixer}}{\text{Pressure drop in a pipe without static mixer}} \tag{11}$$

Heywood et al. [38] provided a review containing various functional dependencies of the *Z*-factor on Reynolds number and their theoretical basis.

Particle Tracking. To determine the efficiency of a mixer, it is necessary to establish means by which the fluid mixing can be gaged both qualitatively and quantitatively. In the present study, this was achieved by calculating the trajectories of fluid particles in the flowfield of the mixer. This method avoids the problem of excessive numerical diffusion that is observed if the species continuity equations are solved [39].

For a steady laminar flow, the particle trajectories correspond to streamlines. Therefore, trajectories are tracked by integrating the vector equation of motion, using the numerically computed velocity field as input

$$\frac{dx_i}{dt} = u_i \tag{12}$$

Some care must be taken when integrating the equation that describes particle motion in order to retain a sufficient degree of accuracy. Preliminary tests have indicated that, although lower-order schemes appear to provide acceptable results, they accentuate the problem of lost particles; that is, particles that have certain trajectories cause them to be trapped near a solid wall, where the local velocity is zero, or completely exit the computational domain [39]. For the results presented in this paper, a fourth-order Runge-Kutta integration algorithm with adaptive time-step-size control was employed. In addition, to avoid problems near stagnation points, the numerical integration of the streamline equation was performed using a fixed spatial increment rather than a fixed time step. By this method, the trajectory of each fluid particle released at flowfield inlet can be tracked and the particle locations within different cross sections of the flowfield. The number of lost particles is the most for the case of Re=100 and SMX mixer, which is 9.4% of the particles that entered the flowfield. Figure 3 shows pathline of fluid element through a helical static mixer.

Residence Time Distribution. The residence time distribution (RTD) is used to characterize the uniformity of the history of fluid elements in the static mixer. A similar history for all fluid elements in the flow is a desirable feature in order to provide the uniformity of the product quality. This can be achieved by a narrow distribution of the residence times for chemical reactors. RTD for flows in a static mixer has been studied experimentally [40] and numerically [41–43]. Here, the RTD for flow in a static mixer was calculated by tracking ~55,000 uniformly spaced, zero-mass, zero-volume particles initially located in the top half of the flowfield inlet. For a steady flow, the particle trajectories correspond to streamlines. Therefore, trajectories are tracked by integrating the vector equation of motion, using the numerically computed velocity field as input (Eq. (12)).

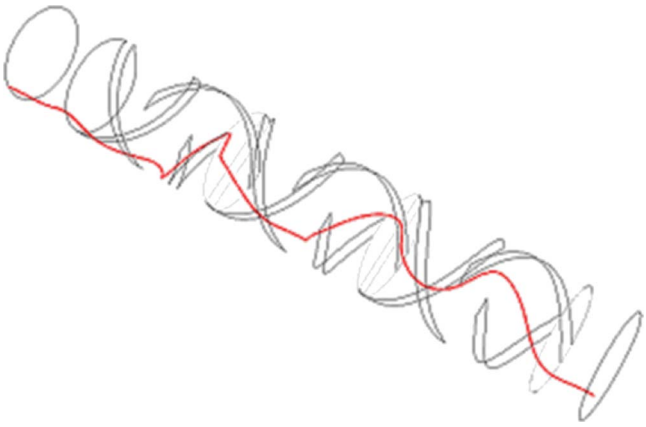

Fig. 3 Path line of one particle through a six-element helical static mixer

The residence time of each particle was measured from the point when the particle passed the cross-sectional plane of the leading edge of the first mixing element to the point when the particle crossed the cross-sectional plane of trailing edge of the last mixing element. The measured residence time is nondimensionalized by the residence time of a fluid particle traveling at the bulk flow velocity in a pipe with no mixer. Given the value of the nondimensionalized residence time (t^*) for all fluid particles that have passed the cross-sectional plane, the fraction of the volumetric flow that has a residence time between t^* and t^*+dt^* can be calculated. This parameter is known as the distribution function, $f(t^*)$.

Particles Distribution Uniformity. A common tool to study the effectiveness of a mixer in of mixing of two fluids is *intensity of segregation* [44]. Dispersive mixing, as well as distributive mixing, can be characterized by the intensity of segregation [45,46]. An alternative tool for measuring the degree of mixing quantitatively is the particles distribution uniformity (PDU) [37]. First, assume that the cross section of the flow is divided into very small plane sectors; also assume the flowfield cross section is divided into equal angles by a large number of symmetry lines. The PDU can be defined as

$$\text{PDU} = \left(1 - \frac{1}{2\left(1 - \frac{1}{N_s}\right)} \sum_{i=1}^{N_s \to \infty} pd_1(i)\right)\left(1 - \frac{1}{N_l} \sum_{i=1}^{N_l \to \infty} pd_2(i)\right) \tag{13}$$

where N_s is the total number of plane sectors that the cross section of the flow is divided into, $N_{(i)}$ is the number of particles placed in the ith sector, N_l is the total number of symmetry lines, $N_{\text{left}}(i)$ is the number of particles on the left side of the ith symmetry line, and the particles on the right side of this line is $N_{\text{right}}(i)$. $pd_1(i)$ is particle distribution function of the first kind ($i=1,\ldots,N_s$), and $pd_2(i)$ is particle distribution function of the second kind ($i=1,\ldots,N_l$) [37]. The computational time needed to determine the value of PDU for a given case, is almost half times the computational time which is needed to calculate the value of intensity of segregation [47]. PDU varies from 0 to 1. For perfect mixing situation, the PDU value is 1.0, otherwise it is <1. A low PDU value indicates poor mixing in the flow cross section.

Table 3 *Z*-factors for two static mixers

	Re	*Z*-factor
Helical	0.1	7.60
	1	7.61
	10	7.82
	100	13.34
SMX	0.1	49.47
	1	49.49
	10	49.99
	100	58.12

Temperature Difference Ratio. Thermal processing by conventional equipment with mechanically moving parts has several shortcomings [48]. To decrease the temperature gradient of fluid elements in a pipe, static mixers can be employed. Effectiveness of static mixers can be estimated using a nondimensional ratio of the temperature difference in fluid at a specific flow cross section in a pipe containing a static mixer to that in an empty pipe of the same diameter. If this ratio >1, the static mixer is not effective; however, this situation does not actually occur in practice. The smaller this ratio is, the more efficient the static mixer becomes. When this ratio is zero at a flow crosssection, it means that in there is no temperature difference in that cross section of the pipe that contains a static mixer. When this ratio is 1, it means that static mixer has no impact on temperature blending of fluid elements in the flow. *Temperature difference ratio* (TDR), in a given flow cross section, is defined as [48]:

$$\mathrm{TDR} = 1 - \frac{(T_{\max} - T_{\min})_{\text{pipe with mixer}}}{(T_{\max} - T_{\min})_{\text{pipe without mixer}}} \tag{14}$$

TDR is between 0 and 1. The higher TDR generally means that the static mixer is more efficient. However, there is one specific situation that the value of TDR is not sufficient enough to determine the mixer efficiency. Consider a case that TDR=1. For such a case, there is no temperature gradient in the fluid inside the pipe that contains a static mixer. It is possible that the temperature gradient of fluid inside an empty pipe of the same diameter is also very small or the temperature gradient might be significant. Therefore, when TDR=1, it cannot provide information regarding the performance of static mixer. In this situation, other parameters rather than TDR should be considered in order to evaluate the performance of mixer.

Heat Flux Ratio. The ratio of heat flux from the solid surface into the fluid in a pipe containing a static mixer to the heat flux in a pipe with no mixer is the heat flux ratio. In practice, helical static mixers, which are used in heat exchangers, are made of conductive materials such as cupper. Therefore, static mixers are able to increase the heat flux significantly. For cases in which the static mixer is made from a nonconductive material, the heat flux ratio can be close to 1 or slightly less than 1, depending on the flow conditions. It is mentioned that the thermal boundary conditions, applied in this study to the mixer surface, simulates a static mixer which is made of a superconductive material.

Results and Discussion

The flow in two different static mixers has been analyzed for a number of different conditions. A residual of $<10^{-9}$ for temperature and residuals of $<10^{-6}$ for all other variables, defined as the L2 norm, were used as the convergence criteria. Reynolds numbers of the flow studied here are 0.1, 1, 10, and 100. Prandtl numbers of the materials studied here are 1.27324, 12.7324, and 127.324. The computational time for the thermofluid part was from $\sim$2.5 h up to $\sim$8.5 h; and the computational time for the trajectory tracking part was from $\sim$3 h up to $\sim$4 h using a 2.01 GHz processor.

Table 3 compares predicted *Z*-factors for helical and SMX mixers for different Reynolds numbers. The *Z*-factor for a SMX mixer is $\sim$6.5 times of the *Z*-factor for a helical mixer when $0.1 \leqslant \mathrm{Re} \leqslant 10$. When Re=100, the *Z*-factor for a SMX mixer is $\sim$4.4 time of the *Z*-factor for a helical mixer. The pressure drop caused by a SMX mixer is significantly higher than the pressure drop across a helical mixer; and consequently, much more energy is needed to maintain the flow across a SMX mixer. For Reynolds numbers up to 10, the *Z*-factor remains almost constant. Similar results have been reported for flow of Newtonian and non-Newtonian fluids across static mixer [49,50]. This can be explained by the fact that the flow pattern (across a static mixer, as well as in a tube) remains the same, when Reynolds number is small (in each given flow cross section, the cross-sectional velocity fields for are almost identical) [37].

The trajectories of 501,740 zero-mass and zero-volume fluid particles injected into the mixer over half of the flow inlet have been calculated. The diameter of this plane is perpendicular to the front edge of the first helical mixing element in the pipe. This is a simplified model for the diametrical feeding of the mixer with two components fluids. Particle trajectories corresponding to only one of the working fluids are calculated. The plots of the positions of fluid particles at flow outlet, for Re=1,10,100, respectively, from top to bottom in Figs. 4 and 5, illustrate the redistribution of the released particles via the combined effects of flow division and reversal, resulting in stretching and folding of observed structures. For Re=0.1, patterns similar to those for Re=1 were observed. The predicted particles distributions for both mixers are in agreement with the published data [19,44].

For a helical static mixer, when Re=0.1 or 1, separated islands are distinguishable after the flow passes the second mixing element and reaches the flowfield outlet. Increasing the Reynolds number breaks these few large islands into several smaller islands. The mixing pattern is different, when Re=100. The secondary flow created by the helical elements is stronger and a large portion of the flow cross section contains curved shape regions of particles. It can be better represented by the cross-sectional velocity vectors. The cross-sectional velocity fields are illustrated in Fig. 6, which show the cross-sectional projection of the velocity vectors at the end of the first and the second elements, respectively, from left to right, and correspond to Re=1 and Re=100, respectively, from top to bottom. To obtain clear images, the length scale of the product of the velocity vector and the Reynolds number in each case is set to a constant. From these plots, it can be seen that the rotation of the fluid in the opposite sense to the helical twist of the mixing element leads to the creation of a whirling structure. For Re=100, contrary to that of Re=1, a secondary vortex is developed. An axially periodic flow, having the same periodicity as the mixer geometry, is observed to be rapidly established. In particular, the primary and secondary flow vortices are seen to contribute to the elongation of the structures and hence to the mixing process.

A SMX mixer leads to a much more uniform distribution of particles in the flow cross section. For Re=0.1 and 1, the islands, observed downstream of the helical mixer, are replaced with several narrow line shape regions by the use of SMX elements. When Re=10, the change in particle redistribution is still minimal. By increasing the Reynolds number to 100, a new pattern is created and a more uniform distribution is achieved. However, the impact of increasing Reynolds number on mixing for a SMX mixer is not as significant as for a helical mixer.

In order to quantitatively measure the mixing capability of these two static mixers, PDU values measured at the flowfield outlet were computed. Table 4 presents the obtained PDU values for two mixers. For all flow Reynolds numbers, the SMX mixer provides a higher PDU value. Although by increasing the Reynolds number, the PDU value increases in most cases, it does not occur in a helical static mixer for Re=10. Helical mixer shows relatively poor performances around Reynolds number of 10. It is in agreement with the published data [20].

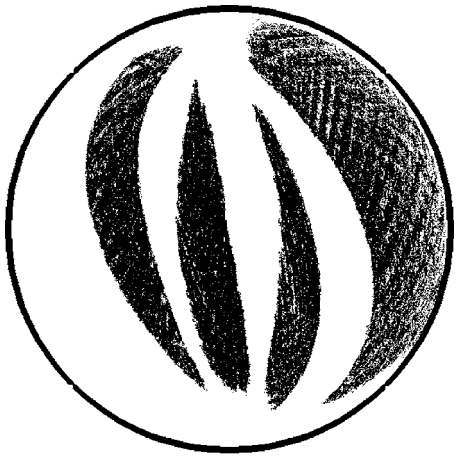

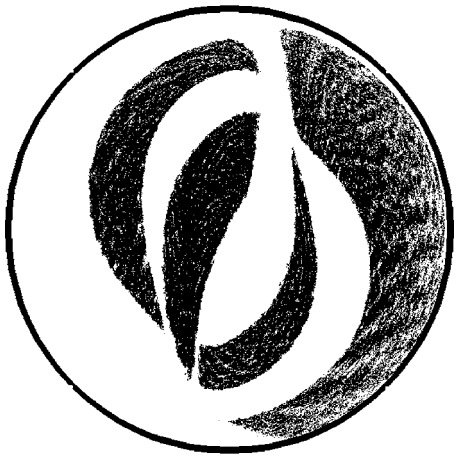

Fig. 4 Particles' locations at outlet Poincaré section (Helical mixer)

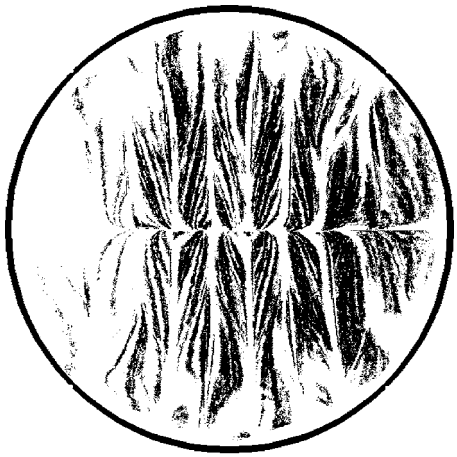

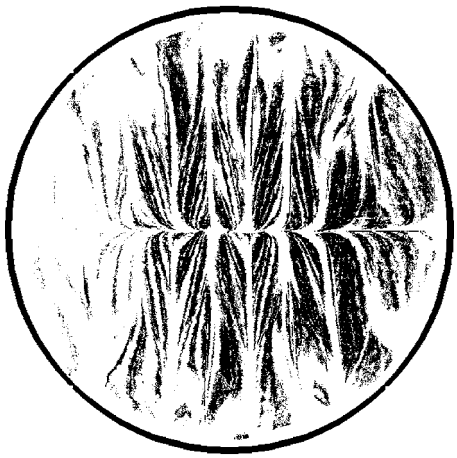

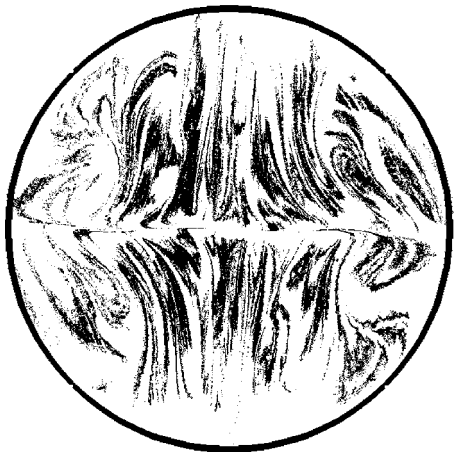

Fig. 5 Particles' locations at outlet Poincaré section (SMX mixer)

The impact of entrance position of the two working fluids relative to the leading edge of the first mixing element of mixer on the mixer performance was studied. Figure 7 (top) shows the positions of fluid particles at the flowfield outlet of the helical mixer for the case of that the particles are initially distributed uniformly in the half of the flow inlet in a way that the diameter of this plane is parallel to the front edge of the first helical mixing element in the pipe. The flow Reynolds number is 0.1. The obtained patterns show lower mixing results for this case; PDU value is decreased ~6%. Figure 7 (bottom) shows the same results obtained for the SMX mixer. The impact of the position of the fluid particles at flowfield inlet is less compared to the case of helical mixer; the PDU decreases ~4% for SMX mixer. Overall, the impact of the position of fluid particles at mixer upstream is not significant.

Rauline et al. reported that, for the creeping flow across a three element mixer, SMX mixer creates a pressure drop 2.54 times of the pressure drop created by a helical mixer and the intensity of segregation (based on the trajectory of 5000 traces first lunched at the center of the inlet section) for SMX mixer is 0.23 times of the intensity of segregation for helical mixer; and they concluded that SMX is the most efficient one among six studied commercial mixers [21].

Residence time distribution for different flow Reynolds numbers and different static mixers are illustrated in Figs. 8 and 9. For

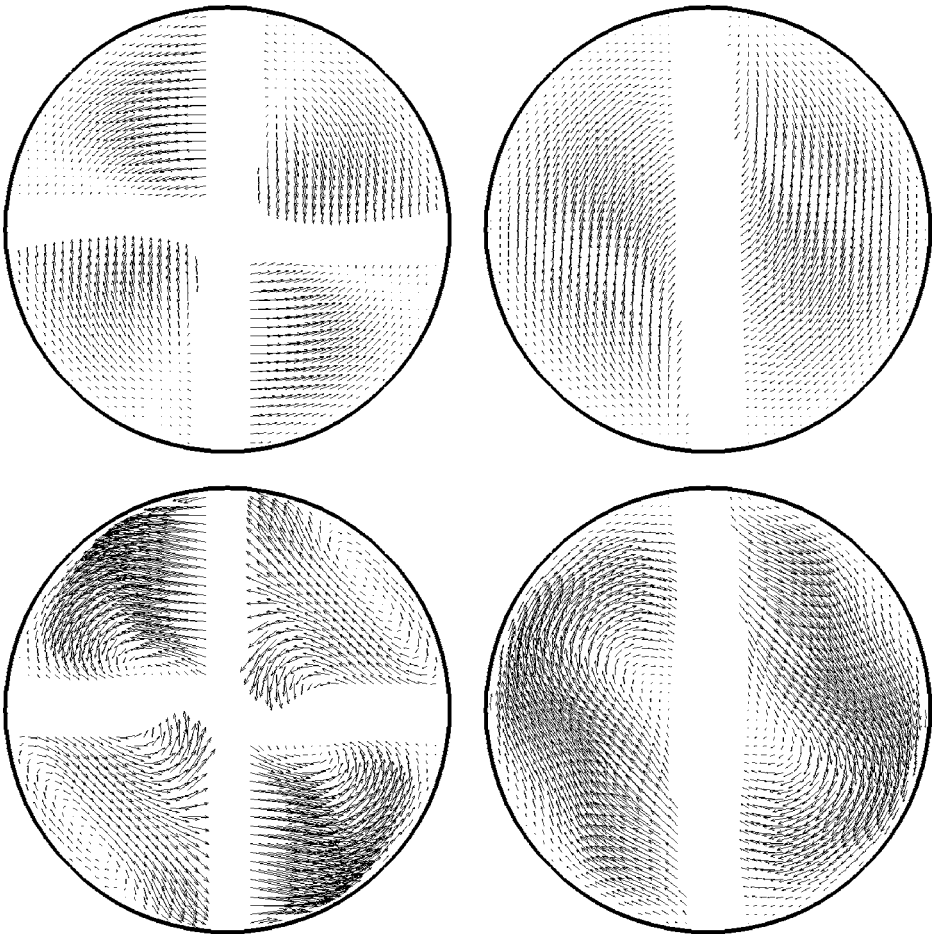

Fig. 6 Velocity field at the first and second helical elements (Top: Re=1, Bottom: Re=100)

the helical mixer, the maximum $t^* > 6$; however, for the SMX mixer $t^* < 3$. For a vast majority of fluid elements $0.3 < t^* < 1.6$ for the helical mixer. For flow across a SMX mixer, $0.5 < t^* < 1.0$. Although, the SMX mixer provides a narrower range of traveling time for fluid elements compare to a helical static mixer, fluid elements across both mixers experience similar history. The standard deviation of $f(t^*)$ for flow in the helical mixer is about 2.5×10^{-2}; and for flow in the SMX mixer, the standard deviation of $f(t^*)$ is about 1.8×10^{-2}.

Thermal performances of SMX and helical static mixers have also been studied. Generally, the heat transfer rate in a static mixer is a function of the physical properties of the working fluid and the solid surface, the flow conditions, and the geometrical parameters of the mixer. In this study, the heat transfer rate for a given geometry can only be related to the flow conditions, thermal conductivity of the working fluid, and the thermal boundary conditions. Values of heat flux ratios for different static mixers and different flow Reynolds numbers are compared in Table 5, when the constant temperature boundary conditions applied to the surface of mixers. It should be mentioned that in this study, only one-third of the tube length was occupied by a static mixer; in a practical heat exchanger, almost the entire tube is filled with mixing elements. Both static mixers show a better performance for a fluid with low thermal conductivity. When thermal conductivity is 0.01 W/m K, the static mixer provides no improvement in the rate heat flux for Re=0.1. The helical (SMX) mixer enhances the heat flux rate ~37% (~64%) when Reynolds number is 1. By increasing the Reynolds number to 10 and 100, the heat flux ratio increases significantly. The SMX mixer delivers heat flux to the flow almost as twice of the heat flux that the helical mixer delivers, when thermal conductivity is 0.01 W/m K and Re=1, 10, or 100. When thermal conductivity is 0.1 W/m K ($\mathrm{Pr} \approx 12.7$), the static mixer provides almost no improvement in the rate heat flux for Re=0.1 and 1. The helical mixer enhances the heat flux rate ~38% (~252%) when Reynolds number is 10 (100); and SMX mixer improves heat flux rate ~63% (~467%) when Re =10(100). By increasing the thermal conductivity of the working fluid to one ($\mathrm{Pr} \approx 1.27$), the impact of static mixer on heat flux rate decreases. For the cases that Re=100, helical mixer improves the heat flux rate by a factor of 1.472 and SMX mixer improves it by a factor of 1.592. The SMX mixer shows a higher ability to enhance heat flux to working fluid compared to the helical mixer. The predicted heat flux ratios, when adiabatic boundary condition is applied to the mixer surface, are shown in Table 6. Again, static mixers show no enhancement in heat transfer rate for low Reynolds numbers. Both mixers manifest a higher performance when Reynolds number and Prandtl number increase. Applying adia-

Table 4 PDU values at flow outlet for two static mixers

	Re	PDU
Helical	0.1	0.240
	1	0.240
	10	0.238
	100	0.297
SMX	0.1	0.361
	1	0.361
	10	0.386
	100	0.409

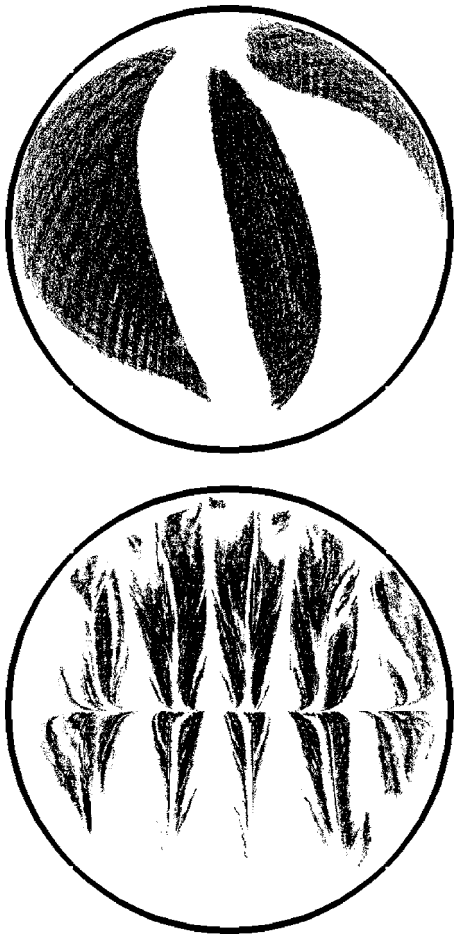

Fig. 7 Particles' locations at outlet (Top: helical mixer, Bottom: SMX mixer)

batic boundary conditions, both mixers show, as it is expected, less heat rate enhancement compared to the results obtained by constant temperature boundary conditions.

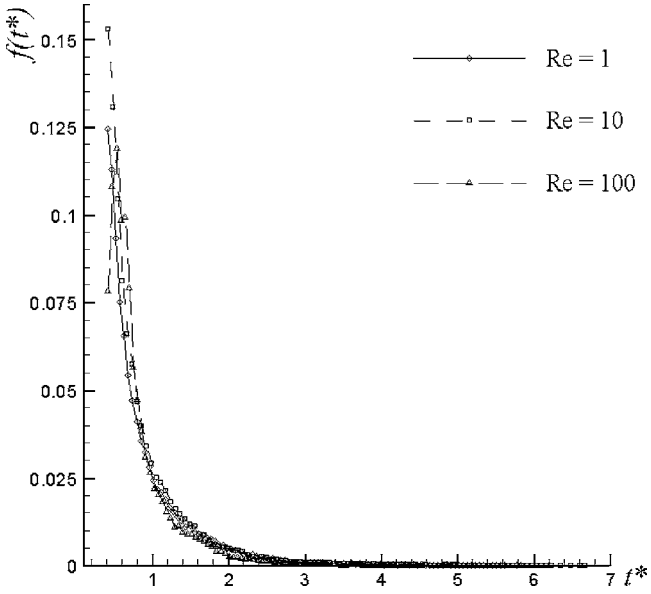

Fig. 8 Distribution function for laminar flow in a two-element helical static mixer ($\Delta t^* = 0.01$)

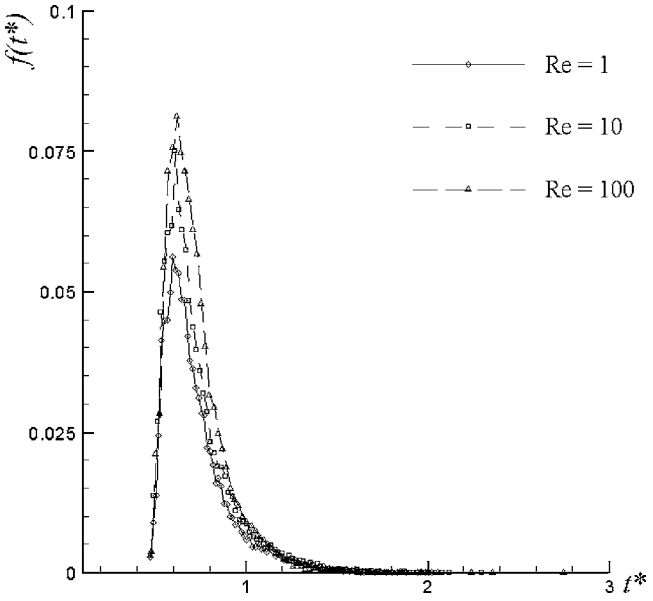

Fig. 9 Distribution function for laminar flow in a two-element SMX static mixer ($\Delta t^* = 0.01$)

The temperature difference ratio is measured for each case at a flow cross-section located at half-segment-length distances from the trailing edge of the last mixing element. Table 7 presents values of TDRs for Re=1, 10, 100 for two types of static mixers, applying the constant temperature boundary conditions. When the flow Reynolds number is 0.1, there is no difference between the temperatures of fluid elements in a tube with no mixer. For a fluid with high thermal conductivity, static mixers show almost no improvement in temperature blending. When the thermal conductivity of the working fluid is 1 W/m K (Pr≈1.27), the difference between fluid element temperatures in a pipe with no mixer, at a flow cross-section located at half-segment-length distances from the trailing edge of the last mixing element, is minimal for Re =0.1, 1, and 10. When Re=100, the difference is ~160.3 K. For such a case, TDR is 0.726 for the helical mixer and it is 0.997 for

Table 5 Heat flux ratios for two static mixers (Constant temperature BC)

	Re	K (W/m K)	Pr	Heat flux ratio
Helical	0.1	0.01	127.32	1.008
	1	0.01	127.32	1.373
	10	0.01	127.32	1.887
	100	0.01	127.32	3.453
	0.1	0.1	12.732	1.011
	1	0.1	12.732	1.008
	10	0.1	12.732	1.380
	100	0.1	12.732	2.524
	0.1	1	1.2732	1.012
	1	1	1.2732	1.011
	10	1	1.2732	1.008
	100	1	1.2732	1.472
SMX	0.1	0.01	127.32	1.001
	1	0.01	127.32	1.635
	10	0.01	127.32	4.617
	100	0.01	127.32	7.144
	0.1	0.1	12.732	1.000
	1	0.1	12.732	1.001
	10	0.1	12.732	1.632
	100	0.1	12.732	4.667
	0.1	1	1.2732	1.000
	1	1	1.2732	1.000
	10	1	1.2732	1.001
	100	1	1.2732	1.592

Table 6 Heat flux ratios for two static mixers (Adiabatic BC)

	Re	K (W/m K)	Pr	Heat flux ratio
Helical	0.1	0.01	127.32	1.008
	100	0.01	127.32	2.217
	0.1	0.1	12.732	1.005
	100	0.1	12.732	1.732
	0.1	1	1.2732	1.006
	100	1	1.2732	1.293
SMX	0.1	0.01	127.32	1.000
	100	0.01	127.32	2.192
	0.1	0.1	12.732	1.000
	100	0.1	12.732	1.821
	0.1	1	1.2732	1.000
	100	1	1.2732	1.218

the SMX mixer. For the case of Re=0.1 and K=0.1 W/m K (Pr $\approx$12.7), all the fluid elements reach to the wall temperature in tube. When Re=1, 10, or 100, static mixer can reduce the difference between fluid element temperatures. SMX mixer provides a higher TDR compared to helical mixer. However, for the case of Re=1, the difference between the highest and the lowest temperatures of fluid elements in a tube with no mixer is only $\sim$2 K. When the fluid thermal conductivity is reduced to 0.01 W/m K, the difference between the highest and the lowest temperatures of fluid elements in a tube with no mixer is $\sim$166 K, for Re=1. For such a case, a static mixer can improve the temperature distribution in flowfield; for helical static TDR=0.556 and for SMX mixer TDR=0.995. However, helical mixer performs poorly when Re=10 or 100.

When K is equal to one, for Re=0.1, 1, and 10, the fluid temperature reaches wall temperature in both mixers and blending affectivities of both mixers are the same. For Reynolds numbers of 100, the TDR=0.726 for the helical mixer and TDR=0.997 for the SMX mixer; SMX mixer shows better performance, when Re=100. When the flow Reynolds number is low and fluid thermal conductivity is high, static mixers do not improve the heat transfer rate or temperature distribution in flowfield.

For Re=100, applying the adiabatic boundary conditions, Table 8 presents values of TDRs measured at a flow cross section located at half-segment-length distances down the trailing edge of the last mixing element. When Re=0.1, TDR is almost one, however, basically there is no temperature gradient in the working fluid in a pipe with no mixer at this cross-section for different values of the fluid thermal conductivity. As can be seen from Table 8, for Re=100, static mixers with adiabatic surfaces do not decrease temperature gradient in the flow when the fluid thermal conductivity is small. By increasing the thermal conductivity of the fluid to one, both mixers are able to decrease the temperature gradient in the flow almost similarly.

Table 7 Temperature difference ratios for two static mixers (Constant temperature BC)

	Re	K (W/m K)	Pr	TDR
Helical	1	0.01	127.32	0.566
	10	0.01	127.32	0.032
	100	0.01	127.32	0.010
	1	0.1	12.732	0.996
	10	0.1	12.732	0.571
	100	0.1	12.732	0.125
SMX	1	0.01	127.32	0.995
	10	0.01	127.32	0.634
	100	0.01	127.32	0.181
	1	0.1	12.732	1.000
	10	0.1	12.732	0.995
	100	0.1	12.732	0.678

Table 8 Temperature difference ratios for two static mixers, Re=100 (Adiabatic BC)

	K (W/m K)	Pr	TDR
Helical	0.01	127.32	0.006
	0.1	12.732	0.062
	1	1.2732	0.413
SMX	0.01	127.32	0.023
	0.1	12.732	0.156
	1	1.2732	0.445

Since most of fluids in industry are non-Newtonian, mainly shear thinning liquids, it is justified to study the performance of mixers under the conditions of shear-thinning liquids as the working fluid. Also, appreciable applications of shear-thickening fluids can be found in the literature; and therefore, the effect of shear-thickening fluids on the mixer's performance is studied as well. The Carreau model is used in this study, in view of the fact that it is superior to power law model [47]. The density (ρ) and zero shear viscosity (μ_0) of non-Newtonian fluids are set to 1000 kg/m^3 and 0.00127324 kg/m s, respectively. The time constant in the Carreau law (λ) is set to unit. μ_∞ is set to zero. The reference temperature and the working temperature are both set to 273.15 K. The only changing parameter, in this work, is the power-law index. Four different values for index n are considered: 0.6, 0.75, 1.2, and 1.25.

Comparison of the pressure drops across static mixers using Newtonian and non-Newtonian fluids shows a significant decrease (increase) in pressure drop for the case of shear-thinning (-thickening) non-Newtonian fluid, as shown in Table 9, when the mass flow rate at inlet is considered the same for Newtonian and Non-Newtonian fluids. The values denoted by ΔP^* represent the pressure drop across static mixer for a non-Newtonian fluid, divided by the pressure drop for a Newtonian fluid. In general, the more deviation from Newtonian fluid for shear-thinning (-thickening) fluid, the lower (higher) value for ΔP^*. However, when mass flow rate is 0.0001 Kg/s, Re=3.937 for the Newtonian fluid, the pressure drop across a helical static mixer does not change significantly. By increasing the flow rate to 0.001 Kg/s (Re=39.37 for the Newtonian fluid), the difference between pressure drop across a static mixer when the working fluid is non-Newtonian and the pressure drop when the fluid is Newtonian is more pronounced.

Comparison of the pressure drops across static mixers when the flow Reynolds number is considered the same for newtonian and non-Newtonian fluids is shown in Table 10. As can be seen from Tables 9 and 10, the pressure drop across helical static mixer is less sensitive to the fluid type compared to the pressure drop across SMX mixer.

Table 9 Pressure drop comparison

	Mass Flow Rate (Kg/s)	n	ΔP^*
Helical	0.0001	0.60	0.952
	0.0001	0.75	0.970
	0.0001	1.20	1.024
	0.0001	1.25	1.031
	0.001	0.60	0.650
	0.001	1.20	1.270
SMX	0.0001	0.60	0.777
	0.0001	0.75	0.854
	0.0001	1.20	1.136
	0.0001	1.25	1.173
	0.001	0.60	0.423
	0.001	1.20	1.642

Table 10 Pressure drop comparison ($Re' = 100$)

	n	ΔP^*
Helical	0.60	0.625
	0.75	0.724
	1.20	1.512
	1.25	1.552
SMX	0.60	0.404
	0.75	0.536
	1.20	1.891
	1.25	2.264

In practice, the flow pressure drop can be affected by other parameters in addition to the power-law index. For example, carboxymethyl cellulose (CMC) solution in water is shear-thinning material. Higher concentration levels of CMC solutions lead to a higher pressure drop of the flow across a static mixer [47]. Although the power-law index decreases by increasing the concentration level of CMC solution, the value of zero shear viscosity increases significantly. This fact can explain the significant increase in the pressure drop.

The plots of the positions of fluid particles at flow outlet are illustrated in Figs. 10–13, respectively for $Re' = 1$ and $n = 0.75$, $Re' = 100$ and $n = 0.75$, $Re' = 1$ and $n = 1.25$, and $Re' = 100$ and $n = 1.25$. Comparison to the obtained results for Newtonian cases shows similarity between the impact of type of the working fluid on the performance of both helical and SMX mixer. For the case of pseudoplastic fluid ($n = 0.75$) and $Re' = 1$, the particles distribution at flow outlet for the helical (SMX) static mixer is similar to particles' locations at outlet for the case of Newtonian fluid when $Re = 10$. For the case of dilatant fluid ($n = 1.75$) and $Re' = 10$, the particles distribution at flow outlet for the helical (SMX) static mixer is similar to particles' locations at outlet for the case of Newtonian fluid when $Re = 1$. Both mixers deliver a more mixed pattern for a given flow Reynolds number when the power-law index (n) is decreased.

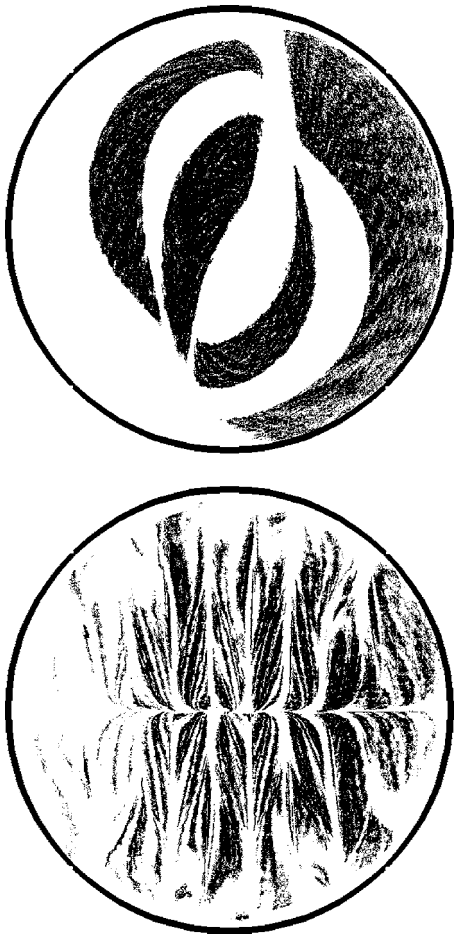

Fig. 10 Particles' locations at outlet, $Re' = 1$, $n = 0.75$ (Top: helical mixer, Bottom: SMX mixer)

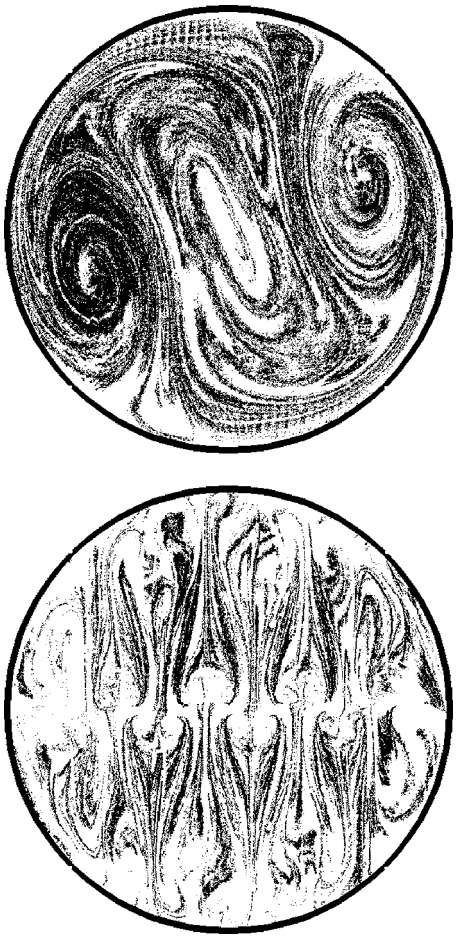

Fig. 11 Particles' locations at outlet, $Re' = 100$, $n = 0.75$ (Top: helical mixer, Bottom: SMX mixer)

Table 11 presents the predicted PDU values for working fluids with different index n, when flow Reynolds number is 100. By increasing the power-law index, the PDU value decreases. For the helical mixer, PDU is about 1.25 (0.818) times of the PDU value for a Newtonian fluid when index n is 0.60 (1.25); and for the SMX mixer, PDU is about 1.49 (0.777) times of the PDU value for a Newtonian fluid when index n is 0.60 (1.25). The SMX mixer is more sensitive to the fluid type compared to the helical mixer.

Conclusions

The performance of two common static mixers for creeping and laminar flows, SMX and helical, using Newtonian and non-Newtonian materials as working fluid, were studied numerically. Both mixers produce similar flow histories for the working fluid. For the range of flow Reynolds number and power-law index studied here, both mixers show higher mixing performance when the Reynolds number is increased or the power-law index is decreased. Pressure drop across mixers increases by increasing the Reynolds number or the power-law index. Both mixers are able to increase the heat flux rate when the Prandtl number is small, and this rates increases as the Reynolds number increases.

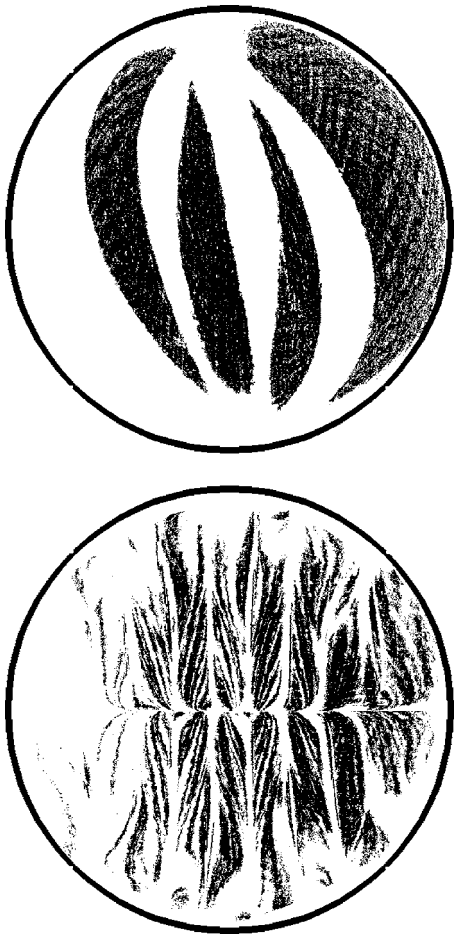

Fig. 12 Particles' locations at outlet, Re′=1, *n*=1.25 (Top: helical mixer, Bottom: SMX mixer)

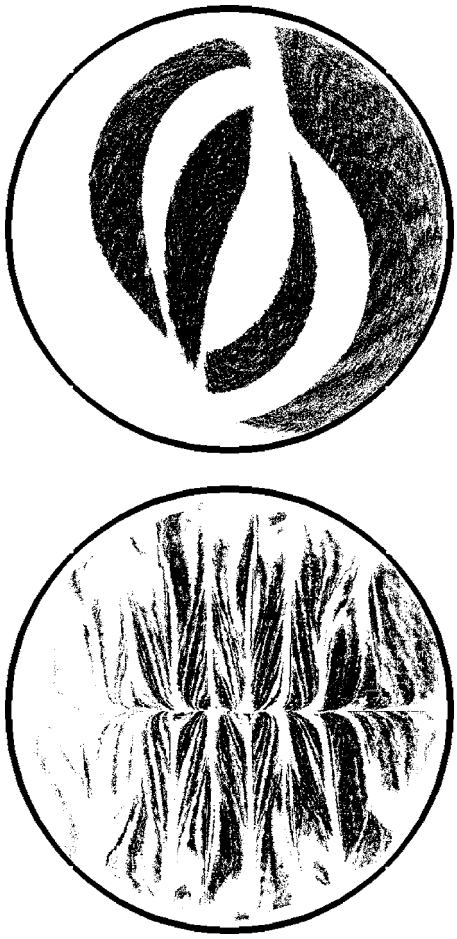

Fig. 13 Particles' locations at outlet, Re′=100, *n*=1.25 (Top: helical mixer, Bottom: SMX mixer)

The SMX mixer manifests a higher performance in fluid mixing, temperature blending, and in heat transfer enhancement compared to the helical mixer. However, the pressure drop created by SMX elements and, consequently, the required energy to maintain the flow in pipe, is significantly higher.

Acknowledgment

This research was partially sponsored by Illinois Tool Works, Inc.

Table 11 PDU values at flow outlet (Reynolds number=100)

	n	PDU
Helical	0.60	0.370
	0.75	0.313
	1.00	0.297
	1.20	0.267
	1.25	0.243
SMX	0.60	0.610
	0.75	0.511
	1.00	0.409
	1.20	0.319
	1.25	0.318

Nomenclature

c_p = specific heat
d = pipe diameter
E = total energy
F_i = external force vector ($i=1,2,3$)
g = acceleration due to gravity
h = enthalpy
K = thermal conductivity
L = mixing element length
n = power-law index
$\dot{m}$ = mass flow rate
p = pressure
Pr = Prandtl number ($=c_p\mu/K$)
Re = Reynolds number ($=\rho Ud/\mu$)
Re′ = Metzner-Reed generalized Reynolds number for non-Newtonian fluid ($=(\rho U^{2-n}d^n)/(\kappa/8)[(6n+2)/n]^n$)
t = time
t^* = nondimensional residence time
T = temperature
T_0 = reference temperature
U = bulk velocity
V = Volume of a computational cell
T_W = wall temperature
u_i = velocity vector ($i=1,2,3$)
x_i = position vector ($i=1,2,3$)
$\dot{\gamma}$ = shear rate
δ_{ij} = Kronecker delta (=1 if $i=j$, =0 if $i\neq j$)
κ = consistency index
λ = time constant in the Carreau law
μ = molecular viscosity

ρ = density
τ_{ij} = stress tensor $(i,j=1,2,3)$

References

[1] Sutherland, W. S., 1874, "Improvement in Apparatus for Preparing Gaseous Fuel," UK Patent No. 1784.
[2] Shah, N. F., and Kale, D. D., 1991, "Pressure Drop for Laminar Flow of Non-Newtonian Fluids in Static Mixers," Chem. Eng. Sci., **46**, pp. 2159–2161.
[3] Chandra, K. G., and Kale, D. D., 1992, "Pressure Drop for Laminar Flow of Viscoelastic Fluids in Static Mixers," Chem. Eng. Sci., **47**, pp. 2097–2100.
[4] Xu, G., Feng, L., Li, Y., and Wang, K., 1997, "Pressure Drop of Pseudo-Plastic Fluids in Static Mixers," Chin. J. Chem. Eng., **5**(1), pp. 93–96.
[5] Pahl, M. H., and Muschlknautz, E., 1982, "Static Mixers and Their Applications," Int. Chem. Eng., **22**, pp. 197–205.
[6] Boss, J., and Czastkiewicz, W., 1982, "Principles of Scale-Up for Laminar Mixing Process of Newtonian Fluids in Fluids in Static Mixer," Int. Chem. Eng., **22**, pp. 362–367.
[7] Morris, W. D., and Misson, P., 1974, "An Experimental Investigation of Mass Transfer and Flow Resistance in the Kenics Static Mixer," I&EC Process Des. Dev., **13**, pp. 270–279.
[8] Middleman, S., 1974, "Drop Size Distributions Produced by Turbulent Pipe Flow of Immiscible Fluids Through a Static Mixer," I&EC Process Des. Dev., **13**, pp. 78–83.
[9] Morris, W. D., and Proctor, R., 1977, "The Effect of Twist Ration on Forced Convection in the Kenics Static Mixer," I&EC Process Des. Dev., **16**, pp. 406–412.
[10] Joshi, P., Nigam, K. D. P., and Nauman, E. B., 1995, "The Kenics Static Mixer: New Data and Proposed Correlations," Chem. Eng. J., **59**, pp. 265–271.
[11] Li, H. Z., Fasol, C., and Choplin, L., 1996, "Hydrodynamics and Heat Transfer of Rheologically Complex Fluids in a Sulzer SMX Static Mixer," Chem. Eng. Sci., **51**(10), pp. 1947–1955.
[12] Qi, Y., Kawaguchi, Y., Christensen, R. N., and Zakin, J. L., 2003, "Enhancing Heat Transfer Ability of Drag Reducing Surfactant Solutions With Static Mixers and Honeycombs," Int. J. Heat Mass Transfer, **46**, pp. 5161–5173.
[13] Lang, E., Drtina, P., Streiff, F., and Fleishli, M., 1995, "Numerical Simulation of the Fluid Flow and the Mixing Process in a Static Mixer," Int. J. Heat Mass Transfer, **38**(12), pp. 2239–2250.
[14] Visser, J. E., Rozendal, P. F., Hoogstraten, H. W., and Beenackers, A. A. C. M., 1999, "Three-Dimensional Numerical Simulation of Flow and Heat Transfer in the Sulzer SMX Static Mixer," Chem. Eng. Sci., **54**, 2491–2500.
[15] Khakhar, D. V., Franjione, J. G., and Ottino, J. M., 1987, "A Case Study of Chaotic Mixing in Deterministic Flows: The Partitioned-Pipe Mixer," Chem. Eng. Sci., **42**, pp. 2909–2926.
[16] Kusch, H. A., and Ottino, J. M., 1992, "Experiments on Mixing in Continuous Chaotic Flows," J. Fluid Mech., **236**, pp. 319–348.
[17] Hobbs, D. M., and Muzzio, F. J., 1998, "Reynolds Number Effects on Laminar Mixing in the Kenics Static Mixer," Chem. Eng. J., **70**, pp. 93–104.
[18] Jones, S. C., Sotiropoulos, F., and Amirtharajah, A., 2002, "Numerical Modeling of Helical Static Mixer for Water Treatment," J. Environ. Eng., **128**, pp. 431–440.
[19] Byrde, O., and Sawley, M. L., 1999, "Optimization of a Kenics Static Mixer for Non-creeping Flow Conditions," Chem. Eng. J., **72**, pp. 163–169.
[20] Byrde, O., and Sawley, M. L., 1999, "Parallel Computation and Analysis of the in a Static Mixer," Comput. Fluids, **28**, pp. 1–18.
[21] Rauline, D., Tanguy, P. A., Le Blevec, J. M., and Bousquet, J., 1998, "Numerical Investigation of the Performance of Several Static Mixers," Can. J. Chem. Eng., **76**(3), pp. 527–534.
[22] Hobbs, D. M., 1998, "Characterization of a Kenics Static Mixer Under Laminar Flow Conditions," Ph.D. thesis, Rutgers, The State University of New Jersey.
[23] Wilkinson, W. L., 1960, *Non-Newtonian Fluids: Fluid Mechanics, Mixing and Heat Transfer*, Pergamon Press, London.
[24] Reiner, M., 1949, *Deformation and Flow*, Lewis, London.
[25] Tanner, R. I., 2000, *Engineering Rheology*, Oxford University Press, London.
[26] Wilkinson, W. L., 1960, *Non-Newtonian Fluids: Fluid Mechanics, Mixing and Heat Transfer*, Pergamon Press, London.
[27] Owens, R. G., and Phillips, T. N., 2002, *Computational Rheology*, Imperial College Press, London.
[28] Bird, R. B., Stewart, W. E., and Lightfoot, E. N., 1960, *Transport Phenomena*, Wiley, New York.
[29] Kumar, N. G., 1980, "Viscosity-Molecular Weight-Temperature-Shear Rate Relationships of Polymer Melts: A Literature Review," J. Polym. Sci., Part A-1, **15**, pp. 255–325.
[30] Carreau, P. J., and Kee, D. D., 1979, "Review of Some Useful Rheological Equations," Can. J. Chem. Eng., **57**(1), pp. 3–15.
[31] Dziubiński, M., and Marcinkowski, A., 2005, "Comments on Reynolds Number Definition for the Discharge of Non-Newtonian Liquids from Tanks," ASME J. Fluids Eng., **127**(5), pp. 1043–1046.
[32] Rahmani, R. K., 1997, "Unstructured Three-Dimensional Delaunay Grid Generation and Solving Three-Dimensional Euler Equations," Master's thesis, Sharif University of Technology, Iran.
[33] Thompson, J. F., Soni, B. K., and Weatherill, N. P., 1999, *Handbook of Grid Generation*, CRC Press, Boca Raton.
[34] Warming, R. F., and Beam, R. M., 1975, "Upwind Second-Order Difference Schemes and Applications in Unsteady Aerodynamic Flows," *Proc. AIAA 2nd Computational Fluid Dynamics Conference*, Hartford, AIAA, Washington, DC, pp. 17–28.
[35] Barth, T. J., and Jespersen, D., 1989, "The Design and Application of Upwind Schemes on Unstructured Meshes," Technical Report No. AIAA-89–0366, AIAA 27th Aerospace Sciences Meeting, Reno.
[36] Vandoormaal, J. P., and Raithby, G. D., 1984, "Enhancements of the SIMPLE Method for Predicting Incompressible Fluid Flows," Numer. Heat Transfer, **7**, pp. 147–163.
[37] Rahmani, R. K., Keith, T. G., and Ayasoufi, A., 2005, "Three-Dimensional Numerical Simulation and Performance Study of an Industrial Helical Static Mixer," ASME J. Fluids Eng., **127**(3), pp. 467–483.
[38] Heywood, N. I., Viney, L. J., and Stewart, I. W., 1984, "Mixing Efficiencies and Energy Requirements of Various Motionless Mixer Designs for Laminar Mixing Applications," Institution of Chemical Engineers Symposium Series No., 89, pp. 147.
[39] Byrde, O., and Sawley, M. L., 1999, "Optimization of a Kenics Static Mixer for Non-Creeping Flow Conditions," Chem. Eng. J., **72**, pp. 163–169.
[40] Tung, T. T., 1976, "Low Reynolds Number Entrance Flows: A Study of a Motionless Mixer," Ph.D. thesis, University of Massachusetts.
[41] Kemblowski, Z., and Pustelnik, P., 1988, "Residence Time Distribution of a Power-Law Fluid in Kenics Static Mixers," Chem. Eng. Sci., **43**(3), pp. 473–478.
[42] Hobbs, D. M., and Muzzio, F. J., 1997, "The Kenics Static Mixer: A Three-Dimensional Chaotic Flow," Chem. Eng. J., **67**, pp. 153–166.
[43] Nauman, E. B., 1991, "On Residence Time and Trajectory Calculations in Motionless Mixers," Chem. Eng. Sci., **47**, pp. 141–148.
[44] Heniche, M., Tanguy, P. A., Reeder, M. F., and Fasano, J. B., 2005, "Numerical Investigation of Blade Shape in Static Mixing," AIChE J., **51**(1), pp. 44–58.
[45] Mickaily-Huber, E. S., Bertrand, F., Tanguy, P., Meyer, T., Renken, A., Rys, F. S., and Wehrli, M., 1996, "Numerical Simulations of Mixing in an SMRX Static Mixer," Chem. Eng. J., **63**, pp. 117–126.
[46] Lawal, A., and Kalyon, D. M., 1995, "Simulation of Intensity of Segregation Distributions Using Three-Dimensional FEM Analysis: Application to Corotating Twin Screw Extrusion Processing," J. Appl. Polym. Sci., **58**, pp. 1501–1507.
[47] Rahmani, R. K., Keith, T. G., and Ayasoufi, A., 2006, "Numerical Simulation and Mixing Study of Pseudo-Plastic Fluids in an Industrial Helical Static Mixer," ASME J. Fluids Eng., **128**(3), pp. 467–480.
[48] Rahmani, R. K., Keith, T. G., and Ayasoufi, A., 2006, "A Numerical Study of the Heat Transfer Rate in a Helical Static Mixer," ASME J. Heat Transfer, **128**(8), pp. 769–783.
[49] Pahl, M. H., and Muschelknautz, E., 1982, "Static Mixers and Their Applications," Int. Chem. Eng., **22**(2), pp. 197–205.
[50] Liu, S., Hrymak, A. N., and Wood, P. E., 2006, "Laminar Mixing of Shear Thinning Fluids in a SMX Static Mixer," Chem. Eng. Sci., **61**, pp. 1753–1759.

Response of Backflow to Flow Rate Fluctuations

Xiangyu Qiao

Hironori Horiguchi
e-mail: horiguti@me.es.osaka-u.ac.jp

Yoshinobu Tsujimoto

Graduate School of Engineering Science,
Osaka University,
Toyonaka, Osaka 560-8531,
Japan

The response of backflow at the inlet of an inducer to the flow rate fluctuation is studied by using three-dimensional numerical calculations based on the k-ϵ turbulence model for the discussion of its effect on cavitation instabilities. It is first shown that the size of the backflow region can be correlated with the angular momentum in the upstream and the phase of the backflow significantly delays behind the quasi-steady response even at a very low frequency. It is then shown that the conservation relation of angular momentum is satisfied with minor effects of the shear stress on the boundary. The supply of the angular momentum by the negative flow is shown to be quasi-steady due to the fact that the pressure difference across the blade causing the backflow is quasi-steady at those frequencies examined. A response function of the angular momentum in the upstream to flow rate fluctuation is derived from the balance of the angular momentum and the results of the numerical calculations. This clearly shows that the backflow responds to the flow rate fluctuation as a first-order lag element. The effects of the backflow cavitation on cavitation instabilities are discussed assuming that the delay of cavity development is much smaller than the delay of the backflow. It was found that the backflow cavitation would destabilize low frequency disturbances due to the effects of the positive mass flow gain factor but stabilize high frequency disturbances due to the effect of the cavitation compliance. [DOI: 10.1115/1.2427081]

Introduction

Cavitation instabilities are one of the most important issues for the development of reliable turbopump inducers for rocket engines. They include various modes such as cavitation surge, rotating cavitation, and their higher order modes. Unlike rotating stall and surge, cavitation instabilities can occur even at the design point, making the problem more serious.

Inducers are designed with a certain incidence angle to ensure that cavitation occurs only on the suction surface of the blades to avoid premature head breakdown caused by the blockage effect of pressure surface cavitation. Due to the incidence, inducers operate with a certain amount of backflow even at the design point. Backflow from the impeller has a swirl velocity of about 20–30% of the impeller tip velocity and a backflow vortex structure is formed at the boundary between the swirling backflow and the straight normal flow [1]. The pressure at the core of a backflow vortex is lower than the ambient pressure due to the centrifugal force on the vortical flow resulting in cavitation if the core pressure becomes lower than the vapor pressure. This is called backflow vortex cavitation. In addition to blade surface and backflow vortex cavitations, tip leakage cavitation occurs for inducers with tip clearance. With these types of cavitation, blade surface, backflow vortex, and tip leakage cavitations, the flow in an inducer presents a very complicated three-dimensional structure [2].

The cause of cavitation instabilities is physically explained as follows. Consider a case when the flow rate is increased. If the flow rate is increased, the incidence angle to a rotor blade is decreased and the volume of the cavitation will be decreased. Then the inlet flow is increased further to fill up the volume once occupied by the cavity. This positive feedback mechanism leads to the positive mass flow gain factor and is responsible for cavitation instabilities [3,4]. Since the size of the backflow becomes smaller when the flow rate is increased, backflow vortex cavitation should also have a destabilizing effect. Thus, if we consider quasi-statically, all three cavitation types, blade surface, tip leakage, and backflow cavitations have a destabilizing effect.

To suppress cavitation instabilities, several methods have been proposed: Increasing the blade leading edge sweep [5,6], increasing the tip clearance [7], and increasing the casing diameter at the inlet [8]. In all of these methods, the size of the inlet backflow is increased. So, contrary to the above quasi-steady considerations, it looks as if the backflow cavitation has a stabilizing effect on the cavitation instabilities.

The present paper focuses on the unsteady response of the backflow to flow rate fluctuations to discuss the contribution of the backflow to cavitation instabilities. Since the flow is very complicated and no reliable method of predicting the backflow vortex cavitation is available at this moment, we apply a noncavitating flow analysis based on the k-ϵ turbulence model. The balance of angular momentum is considered to clarify the mechanism of the backflow response. Discussions on the effects of the backflow vortex cavitation on instabilities are made by assuming that the delay for the development of cavity is negligible as compared with the delay of the backflow response.

Inducer Model and Calculation Method

The impeller used in the present study and its specification is shown in Fig. 1 and Table 1, which is analogous to the liquid oxygen turbopump inducer for the H-II rocket.

A commercial code CFX-TASCflow based on RANS with the k-ϵ model has been used to perform the calculation. The calculations are carried out for a noncavitating condition. The vendor of the CFD code recommends the k-ω shear stress transport (SST) model as a turbulence model. However, the standard k-ϵ turbulence model and wall function option are used in the present study because the backflow region simulated by the standard k-ϵ model is in better agreement with the experiment. The computational domain consists of an inlet pipe, inducer part, and outlet pipe with about 180,000, 240,000, and 50,000 computational cells, respectively, as shown in Fig. 2. The lengths of the inlet and outlet pipes are 10 and 5 times of the inducer radius. Eight grid points in the radial direction are used to describe the flow through the clearance gap between the rotor blade tip and the stationary casing wall. The

Contributed by the Fluids Engineering Division of ASME for publication in the JOURNAL OF FLUIDS ENGINEERING. Manuscript received November 7, 2005; final manuscript received August 31, 2006. Assoc. Editor: Akira Goto.

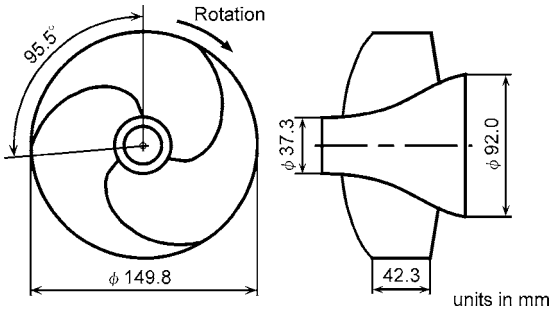

Fig. 1 Inducer geometry

Table 1 Specification of the inducer

Number of blades	3
Tip diameter D_t (m)	0.1498
Inlet tip blade angle (deg)	7.5
Outlet tip blade angle (deg)	9.0
Hub / tip ratio at inlet	0.25
Hub / tip ratio at outlet	0.51
Solidity at tip	1.91
Design flow coefficient ϕ_d	0.078
Tip clearance (m)	0.5×10^{-3}

calculations are made for the flow through all the passages for the purpose of simulating the backflow structure at the inlet. However, the present calculation fails to simulate the vortex structure and only the averaged flow field could be obtained, perhaps caused by the excess damping of the model of simulation. Despite this deficiency, the model can predict the static performance and the backflow length fairly well. Therefore, the RANS code with the k-ϵ turbulence model was applied in the present study.

For steady calculations, the total pressure and the direction of flow are specified at the inlet boundary and the mass flow rate is imposed at the exit. Water at 300 K is used as the working fluid.

For unsteady calculations, the steady flow field is used as the initial condition. A uniform velocity distribution is given as the inlet boundary condition and free flow condition is applied at the exit.

Results and Discussions

Steady Flow Analysis. Before carrying out the unsteady calculation with the flow rate fluctuation, the steady calculation was made with constant flow rates. Figure 3 compares the static pressure performance and axial length of the backflow region obtained by steady calculations and experiments. The location of the upstream edge of the backflow in the experiment was estimated by the movement of the tuft on the casing wall [1]. The static pressure coefficient is based on the inlet wall pressure p_1 at $z/D_t=-1.9$ and the outlet wall pressure p_2 at $z/D_t=0.55$. The results shown in Fig. 3 show that the present calculation predicts the performance and the size of the backflow reasonably, although it fails to simulate the backflow vortex structure.

Response of Backflow to Flow Rate Fluctuations. We consider the flow rate fluctuations expressed by

$$\phi = 0.078 + 0.01\sin(2\pi ft)$$

where 0.078 is the design flow coefficient. Three cases with $f/f_n=0.0625$, 0.125, and 0.25 are examined. These frequencies are typical for the cavitation surge and rotating cavitation [9]. The periods of the flow rate fluctuations correspond to 16, 8, and 4 rotations of the inducer, respectively. The amplitude is about 13% of the design flow coefficient.

Figure 4 shows the instantaneous flow field at a meridional plane for $\phi=0.078$ (Fig. 4(*a*)) at the start of calculation and after one cycle of the flow rate fluctuation with $f/f_n=0.125$ (Fig. 4(*b*)). The meridional plane is located at an angular position $\theta=60$ deg from the leading edge at the tip, in the opposite direction of the impeller rotation. The tangential velocity v_θ is shown by the color level. Although the flow field returns almost to the original, after one cycle of oscillation, calculations are carried out one additional cycle to obtain better periodicity. The instantaneous flow field at the instants (a)–(e) in Fig. 5 are shown in Fig. 6. The region where the flow field is shown in Fig. 6 is the region surrounded with a frame in Fig. 4(*b*). The following observations can be made:

(1) By comparing Figs. 6(*a*) and 6(*e*), we can confirm that reasonable periodicity is obtained;

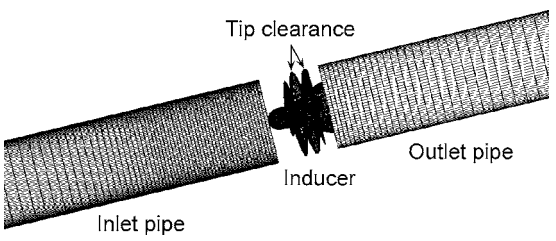

Fig. 2 Computational grid

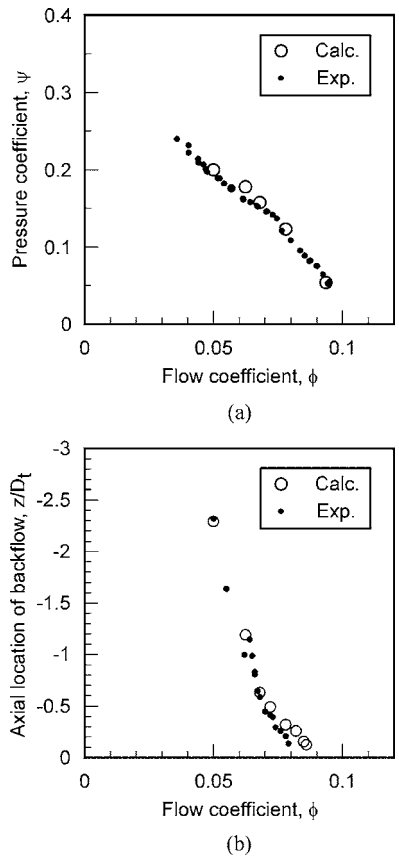

Fig. 3 Comparison of the results by steady calculation and experimental results: (a) Noncavitating performance (uncertainty in $\phi=\pm0.005$ and in $\psi=\pm0.02$ in the experimental results) and (b) location of the upstream edge of the backflow region (Uncertainty in $z/D_t=\pm0.05$ in the experimental results)

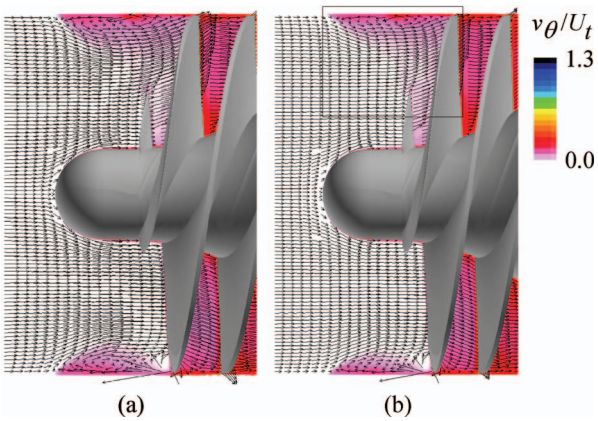

Fig. 4 Flow field at the inlet of the inducer, ϕ=0.078: (*a*) Initial flow field and (*b*) after one cycle of oscillation with f/f_n=0.125

(2) by comparing Figs. 6(*a*) and 6(*c*), we find that the flow field depends not only on the instantaneous flow rate but also on the phase of the disturbance;
(3) by comparing Figs. 6(*b*) and 6(*d*), the length of the backflow at the maximum flow rate ϕ=0.088 is larger than that at the minimum flow rate ϕ=0.068, although the values of the angular momentum in the upstream, *AM*, at ϕ=0.088 and 0.068 are almost the same, as shown in Fig. 7(*b*).

The observations (2) and (3) show that the unsteady effects are important even at a relatively low frequency of f/f_n=0.125.

Figure 8 shows the axial extent of the backflow by plotting the location of the leading edge of the backflow region for the three frequencies. The results of quasi-steady calculations and experiments at each flow coefficient are also plotted. The quasi-steady results agree with each other reasonably and we have a larger backflow region for smaller flow rates.

We can observe the following facts in the results of unsteady calculations:

(1) The amplitude of the backflow oscillations becomes smaller as we increase the frequency;
(2) the phase significantly delays behind the quasi-steady response even with the smaller frequencies examined and the phase delay approaches 90 deg as we increase the frequency.

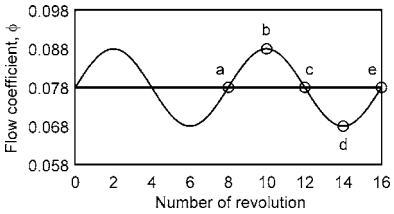

Fig. 5 Inlet flow rate fluctuation with f/f_n=0.125

Balance of the Angular Momentum. In order to clarify the mechanism of the response, we consider the balance of the angular momentum in the upstream of the inducer.

First, we define the angular momentum in the upstream of the inducer

$$AM = \int_V \rho r^2 v_\theta dr d\theta dz/(\rho U_t D_t^4) \tag{1}$$

where *V* represents the whole region upstream of a control surface at the axial location of the blade leading edge at the hub.

The fluctuation of angular momentum is shown in Fig. 7 with its quasi-steady values. If we compare *AM* with the length of the backflow region shown in Fig. 8, we find that *AM* fluctuates in the same phase as the backflow length fluctuation. So, we will use *AM* to represent the size of the backflow region. The amplitude of *AM* significantly decreases and the phase is delayed as we increase the frequency.

Next, the angular momentum transport across the control surface is investigated. The angular momentum supplied by the backflow ($v_z<0$), *AMB*, and the angular momentum removal by the normal flow ($v_z>0$), *AMN*, are defined as

$$AMB = -\int_{v_z<0} \rho r^2 v_\theta v_z dr d\theta/(\rho U_t^2 D_t^3) \tag{2}$$

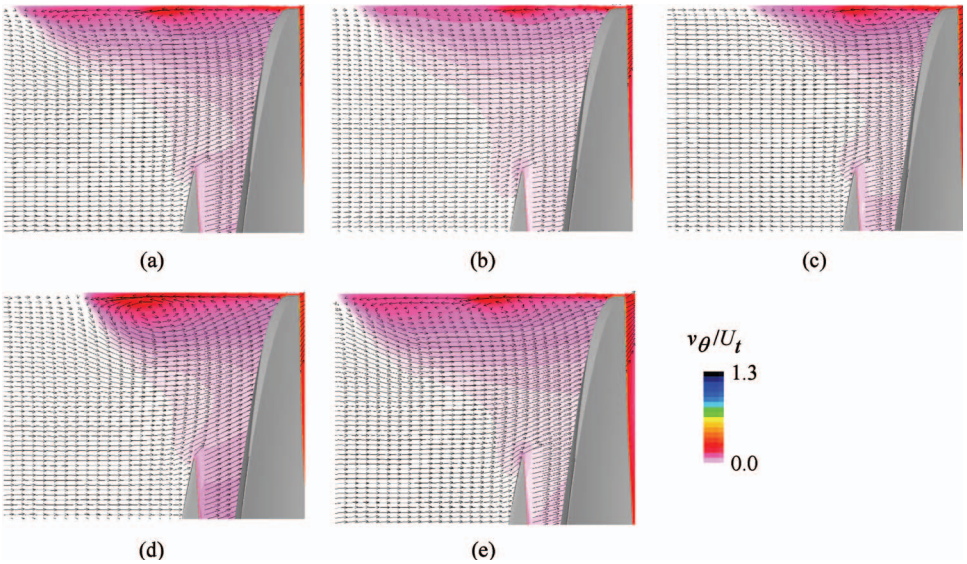

Fig. 6 Backflow region and velocity vector at the instants shown in Fig. 5, with f/f_n=0.125: (*a*) ϕ=0.078 (increasing), (*b*) ϕ=0.088 (maximum), (*c*) ϕ=0.078 (decreasing), (*d*) ϕ=0.068 (minimum), and (*e*) ϕ=0.078 (increasing)

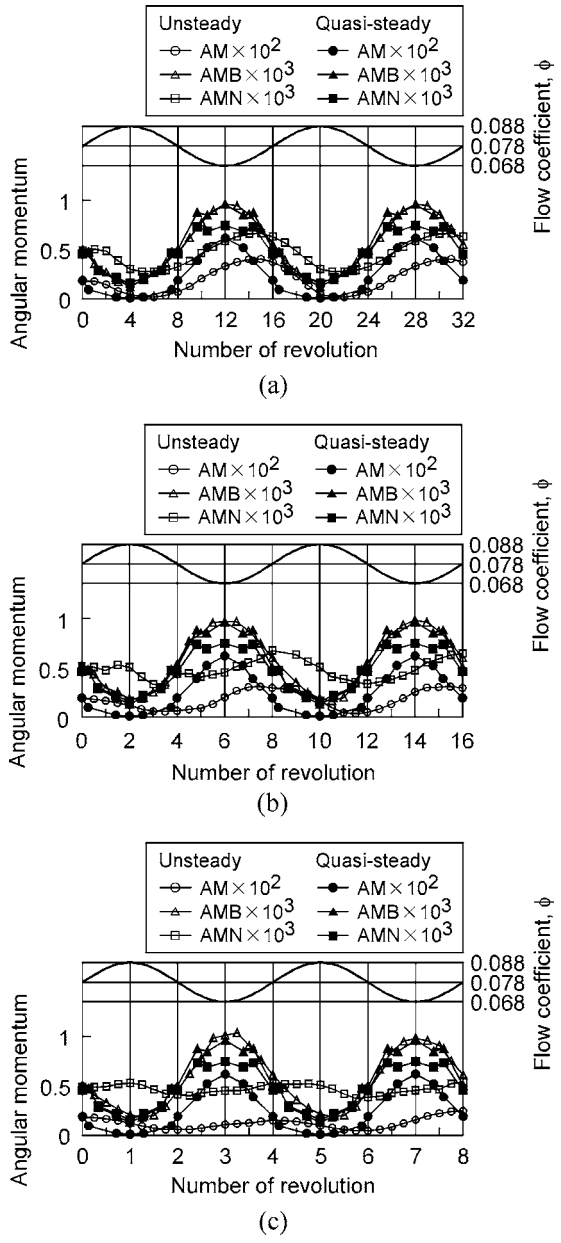

Fig. 7 Angular momentum (*AM*: Angular momentum in the upstream, *AMB*: Angular momentum supply by the backflow, *AMN*: Angular momentum removal by the normal flow): (*a*) $f/f_n=0.0625$, (*b*) $f/f_n=0.125$, and (*c*) $f/f_n=0.25$

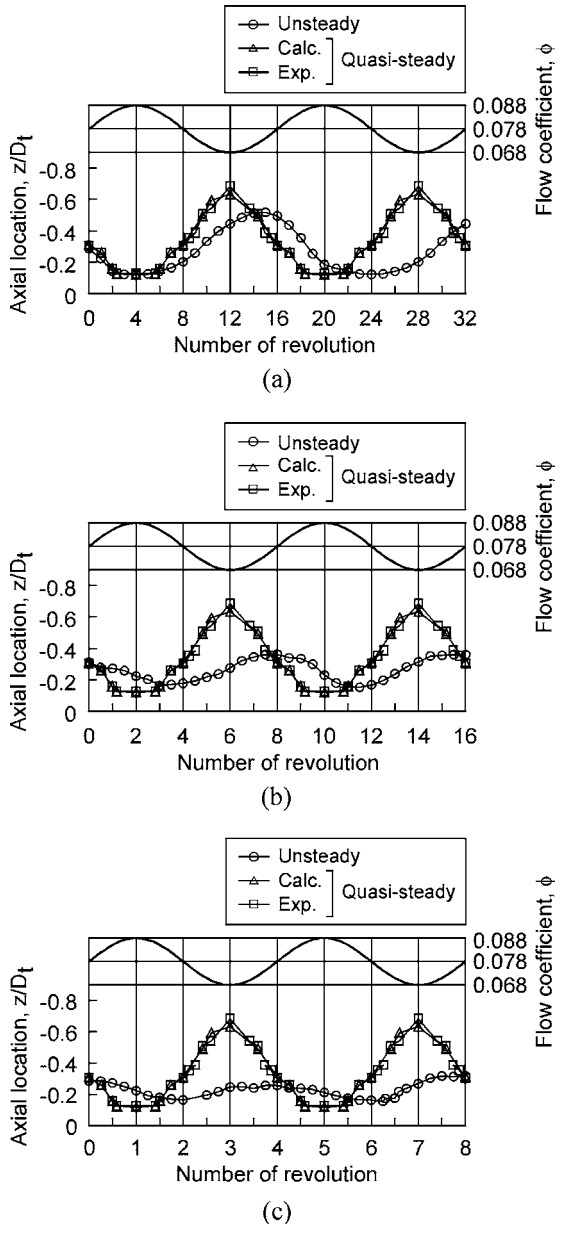

Fig. 8 Location of upstream edge of the backflow region in the flow rate fluctuation (uncertainty in $z/D_t=\pm0.05$ in the experimental results): (*a*) $f/f_n=0.0625$, (*b*) $f/f_n=0.125$, and (*c*) $f/f_n=0.25$

$$AMN=\int_{v_z>0}\rho r^2 v_\theta v_z dr d\theta/(\rho U_t^2 D_t^3) \tag{3}$$

where $v_z<0$ and $v_z>0$ means the integration over the region with $v_z<0$ and $v_z>0$, respectively.

Figure 7 also shows the fluctuations of *AMB* and *AMN* with their quasi-steady values. We observe that:

(1) *AMB* has a phase opposite to the flow rate fluctuation;
(2) *AMB* is almost identical to its quasi-steady value;
(3) under quasi-steady conditions, *AMB* and *AMN* agree with each other except when the flow rate is very small. This suggests that the size of the backflow is determined from the balance of *AMB* and *AMN* for the quasi-steady flow. The unbalance observed at a smaller flow rate should be caused by the skin friction exerted by the pipe wall.
(4) The amplitude of *AMN* becomes smaller and the phase delays as we increase the frequency.

If we neglect the effects of shear stress on the boundary of the control volume, the conservation of angular momentum can be represented by

$$d(AM)/dt^*=AMB-AMN \tag{4}$$

where $t^*=t/(D_t/U_t)$ is a nondimensional time.

Figure 9 examines the dynamic angular momentum balance of Eq. (4). It is observed that $AMB-AMN$, the resultant angular momentum supply, agrees nicely with the time derivative of the angular momentum, $d(AM)/dt^*$.

The results in Figs. 7 and 9 suggest that the size of the backflow is determined by different mechanisms for quasi-steady and unsteady cases. For the quasi-steady case, the size of the backflow is

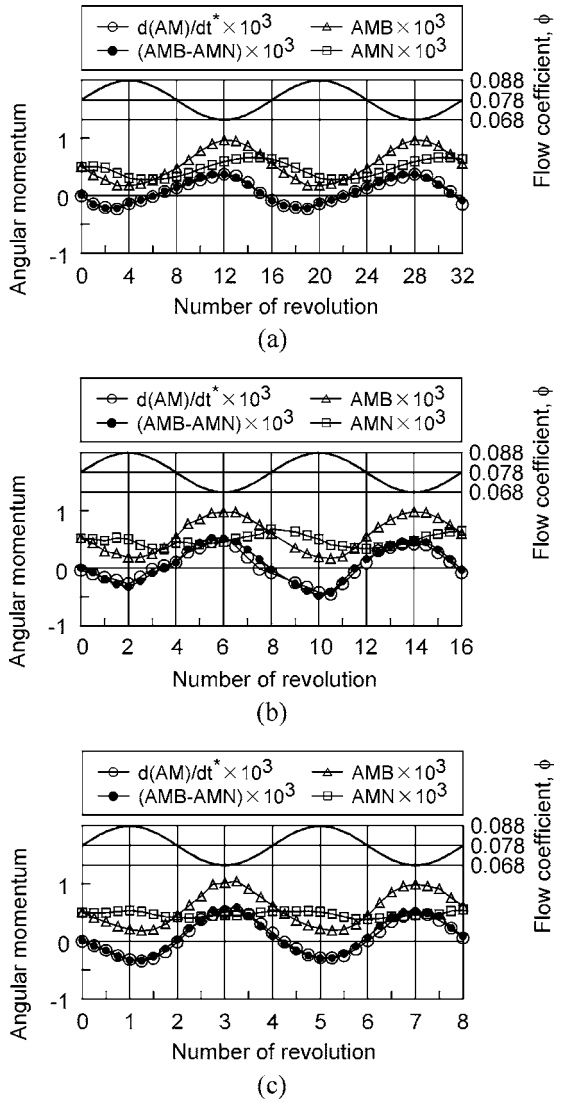

Fig. 9 Angular momentum conservation relation: (*a*) $f/f_n=0.0625$, (*b*) $f/f_n=0.125$, and (*c*) $f/f_n=0.25$

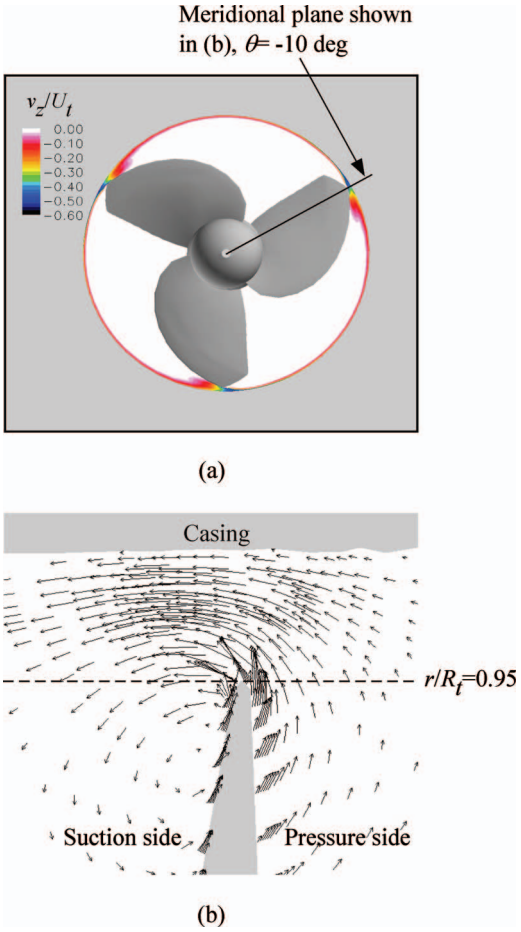

Fig. 10 The region with negative axial flow, $\phi=0.078$: (*a*) Negative axial velocity and (*b*) velocity field in the meridional plane, $\theta=-10$ deg

determined from the balance of the supply of the angular momentum by the backflow, *AMB* and the outflow of the angular momentum on the normal flow, *AMN*. For the cases with a flow rate fluctuation, the difference $(AMB-AMN)$ contributes to the growth of the angular momentum in the upstream, $d(AM)/dt^*$.

Pressure Distribution on the Blade. In Fig. 7, it is shown that the angular momentum supplied by the backflow, *AMB*, depends only on the instantaneous flow rate, with minor effects of unsteadiness. To examine the mechanism of the backflow, Fig. 10(*a*) shows the region with negative axial velocity in the cross section including the leading edge at the tip. The region with negative velocity is limited to the proximity of the casing, and the region ahead of the leading edge near the tip. Figure 10(*b*) shows the velocity field in the meridional plane shown in Fig. 10(*a*). The flow is coming out radially from the pressure side of the leading edge. Similar results are obtained for the cases without tip clearance [10]. These results suggest that the backflow comes mainly from the clearance between the swept part of the leading edge and the casing driven by the centrifugal force and the pressure difference across the blade near the leading edge.

Figure 11 shows the instantaneous pressure distributions near the tip of blade (at $r/R_t=0.99$) for the case with $f/f_n=0.25$ with the quasi-steady pressure distribution. The results are shown for three instants when the flow rate becomes $\phi=0.068$ (minimum), 0.078(mean), and 0.088 (maximum). For $\phi=0.078$, the effects of inertia is canceled out by taking the average of the results in the increasing and decreasing phase of ϕ. It is found that the instantaneous pressure distribution is nearly identical to the quasi-steady distribution.

These two facts that the backflow is driven by the centrifugal force and the pressure difference across the blade, and that the pressure distribution is quasi-steady explain why the angular momentum supplied by backflow, *AMB*, depends only on the instantaneous flow rate, with minor effects of unsteadiness.

Unsteady Pressure Performance. Figure 12 shows the unsteady performance curve for three frequencies along with the quasi-steady performance curve. The unsteady static pressures coefficient ψ is based on the instantaneous wall pressure p_1 and p_2 at $z/D_t=-1.9$ and $z/D_t=0.55$, respectively.

It is found that the unsteady operating points encircle the quasi-steady performance curve in counter-clockwise direction. The difference from the quasi-steady performance is proportional to the frequency, suggesting that the difference is caused by the inertia of the fluid between two pressure taps.

Response Function of Backflow

To examine the phase relationships more quantitatively, the quantities are separated into mean (denoted by an overbar) and fluctuating (denoted by a tilde) components

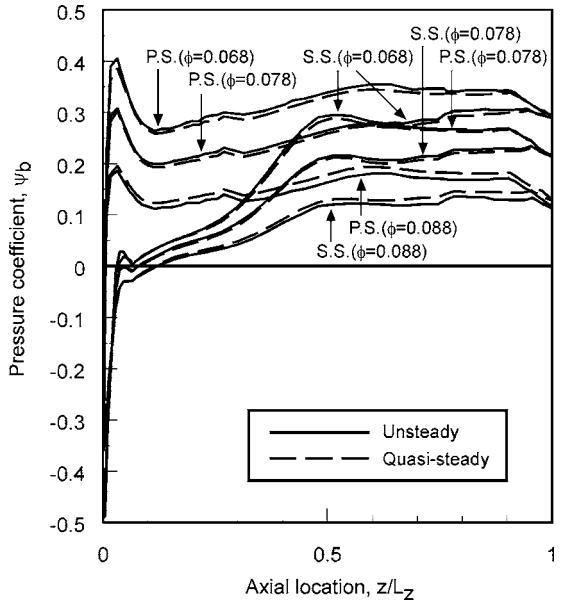

Fig. 11 The instantaneous pressure distribution along the blade for ϕ=0.068, 0.078, and 0.088 at r/R=0.99, with f/f_n =0.25

$$AM = \bar{A} + \tilde{A}e^{j\omega^* t^*} \tag{5}$$

$$AMB = \bar{B} + \tilde{B}e^{j\omega^* t^*} \tag{6}$$

$$AMN = \bar{N} + \tilde{N}e^{j\omega^* t^*} \tag{7}$$

$$\phi = \bar{\phi} + \tilde{\phi}e^{j\omega^* t^*} \tag{8}$$

where $\omega^* = \omega(D_t/U_t) = 2(f/f_n)$ is a nondimensional frequency.

Since the angular momentum supplied by the backflow is increased when the flow rate is decreased, we can express

$$\tilde{B} = -a\tilde{\phi} \tag{9}$$

Further, the angular momentum removal by the normal flow would be larger if the angular momentum in the upstream and the flow rate are larger. So we can assume

$$\tilde{N} = b\tilde{A} + c\tilde{\phi} \tag{10}$$

where a, b, and c are real constants. By putting these expressions into the angular momentum conservation equation (4), we obtain the response function

$$\frac{\tilde{A}}{\tilde{\phi}} = -\frac{a+c}{b+2j(f/f_n)} \tag{11}$$

This clearly shows that the angular momentum responds to the flow rate fluctuation as a first-order lag element. For the case with $f/f_n \to \infty$, the phase of angular momentum in the upstream advances by 90 deg ahead of the flow rate fluctuation and delays by 90 deg behind the quasi-steady backflow fluctuation.

To determine the values of proportionality constants a, b, and c in Eqs. (9) and (10), the numerical results for AM, AMB, AMN are Fourier-analyzed over the second period and the values of $\tilde{A}$, $\tilde{B}$, and $\tilde{N}$ are determined from the first-order components. The value of a is determined from the absolute value of Eq. (9) neglecting the small phase difference between $\tilde{B}$ and $-\tilde{\phi}$. The values of b and c are determined from the real and imaginary parts of Eq. (10). The values of constants determined from the numerical results with f/f_n=0.0625, 0.125, and 0.25 are shown in Table 2.

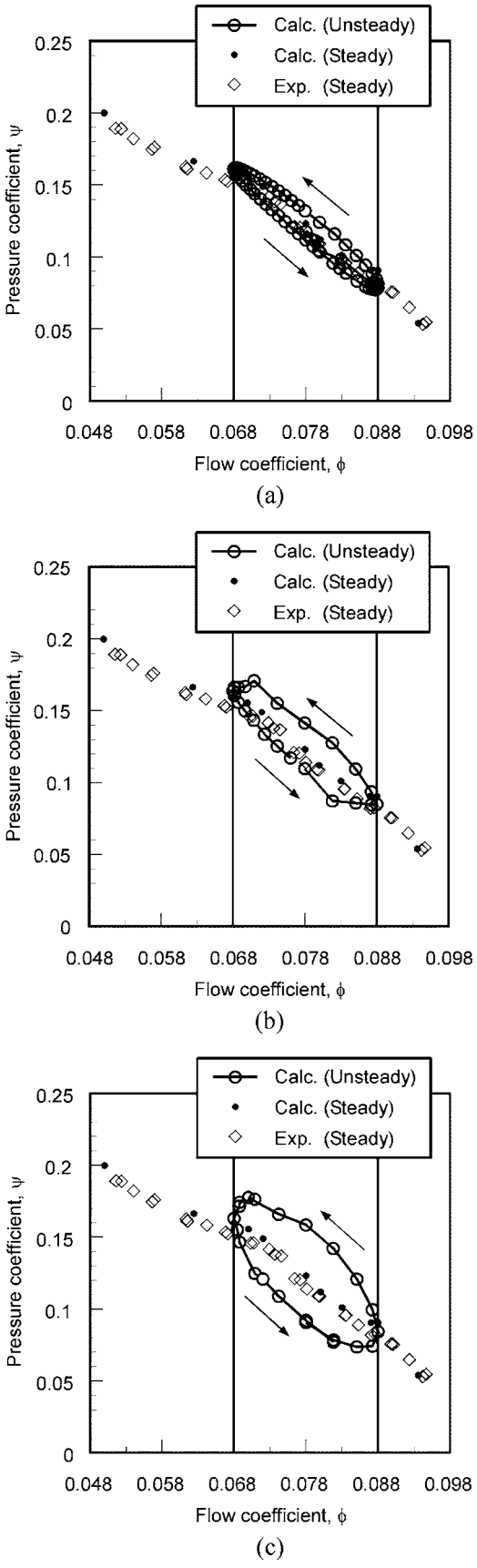

Fig. 12 Unsteady pressure performance of the impeller (uncertainty in ϕ= ±0.005 and in ψ= ±0.02 in the experimental results): (*a*) f/f_n=0.0625, (*b*) f/f_n=0.125, and (*c*) f/f_n=0.25

Table 2 Constants in response function

	a	b	c
f/f_n=0.0625	0.0397	0.0930	0.0095
f/f_n=0.125	0.0411	0.1020	0.0020
f/f_n=0.25	0.0428	0.0783	0.0020
Averaged values	0.0412	0.0911	0.0045

By putting the averaged values of a, b, and c shown in Table 2 into Eq. (11), the complex representation of the response function $\tilde{A}/\tilde{\phi}$ is obtained and shown in Fig. 13. The values of $\tilde{A}/\tilde{\phi}$ of for f/f_n=0, 0.0625, 0.125, and 0.25 determined from the numerical results are also shown in the figure. The data points of the numerical calculations are close to the response function suggesting that the approximations of Eqs. (9) and (10) used for the derivation of the response function (11) is adequate. This response function clearly shows how the magnitude $|\tilde{A}/\tilde{\phi}|$ decreases and the phase delays as we increase the frequency f/f_n. It also shows that the frequency of f/f_n=0.125 is "sufficiently" large to cause the large delay of backflow behind the quasi-steady response.

Comparison With Experiment and Discussion on Stability

The phase lag of backflow has been studied experimentally by Yamamoto [11] in a series of studies on the cavitation surge of a centrifugal pump in which the backflow cavitation plays the critical role. He investigated the response of the backflow to the flow rate fluctuation by measuring the axial velocity fluctuation at the center of the inlet pipe, based on the fact that the main flow velocity is affected by the blockage effect of the backflow. The results are shown in Fig. 14. In this figure, l_m shows the axial distance between the velocity measurement location and the inlet, and D_1 is the inner diameter of the inlet pipe. For the case with l_m/D_1=0.59, the phase delays behind the quasi-steady value (α =−Arg($\tilde{A}/\tilde{\phi}$)=−180 deg) by about −90 deg(α=−Arg($\tilde{A}/\tilde{\phi}$) =−90 deg) as the frequency is increased from 0 to 5 Hz (f/f_n =5/50=0.1). Although this result cannot be compared with the result of the present study quantitatively in which the phase lag of backflow is estimated from the angular momentum, AM, it agrees with the present result qualitatively that the phase delays largely even if the frequency is small. The phase lag is larger than 90 deg higher frequencies in the cases with l_m/D_1=2.29. As mentioned above, the response of backflow is estimated from the fluctuation of the axial velocity in the center of the inlet pipe in the experiment. The larger phase lag at l_m/D_1=2.29 is caused by the time required for the disturbance to reach the measuring point farther from the impeller.

We will discuss the effect of the backflow vortex cavitation assuming that the cavity volume is in phase with the magnitude of the backflow, typically shown by AM. Here, we consider a case of

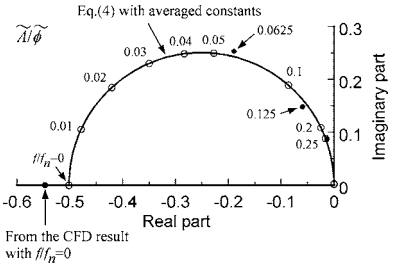

Fig. 13 Response function of the backflow

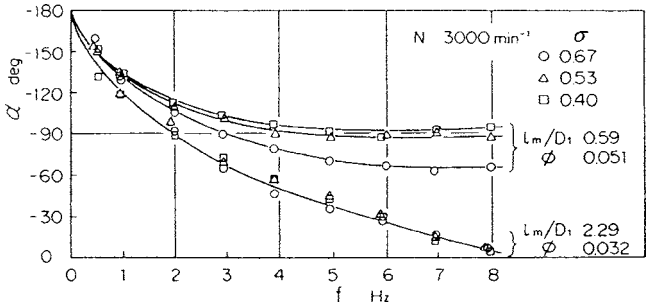

Fig. 14 Phase lag of the backflow [11]

cavity oscillation in a pipe in response to flow rate fluctuation. The velocity fluctuation in the pipe is represented by $u=\bar{U}+\tilde{U}e^{j\omega t}$ and the cavity volume oscillation by $V_c=\bar{v}_c+\tilde{v}_c e^{j(\omega t-\alpha)}$. If we consider that the cavity is located at a distance L from the pipe inlet where the pressure is constant, the pressure fluctuation at the cavity can be represented by $p=-\rho L du/dt$. Then, the displacement work done by the cavity per period can be evaluated by

$$E=\int_{\text{cycle}} pdV_c=\rho\pi L\omega\tilde{U}\tilde{v}_c\cos\alpha \tag{12}$$

This shows that positive work is done by the cavity when $-3\pi/2<\alpha<-\pi/2$ and the cavity fluctuation destabilize the system. With $\alpha=-\pi$, the cavity volume becomes smaller with a higher inlet velocity and this corresponds to the case with a positive mass flow gain factor. With $-\pi/2<\alpha<\pi/2$, E becomes negative and the cavity stabilizes the system. The results in Fig. 14 show that backflow cavitation stabilizes higher frequency oscillations and destabilizes lower frequency oscillations.

By a linear stability analysis it has been shown [4] that the onset condition of the cavitation surge and rotating cavitation can be represented by $M>2(1+\sigma)\phi K$ where M and K are the mass flow gain factor and the cavitation compliance, respectively, and σ is the cavitation number. If we take account of the phase delay $\pi+\alpha$ of the cavity response due to the delay of the backflow development, it can be shown that the onset condition can be represented by

$$M\cos(\alpha+\pi)>2(1+\sigma)\phi K \tag{13}$$

If we neglect the stabilizing effect of cavitation compliance K, the onset condition can be written as $-3\pi/2<\alpha<-\pi/2$. This agrees with the results of the above discussion based on the displacement work E.

Figure 15 shows the resonant frequency f_0 of the system determined by excitation tests and the critical frequency f_{90} at which α becomes $-\pi/2$ [11]. The resonant frequency decreases as the cavitation number σ is decreased and unstable operation is observed in the region of the cavitation number where f_0 would be less than f_{90}. So, in this case of cavitation surge in a centrifugal pump at a low flow rate, the response of the backflow cavitation plays a crucial role.

In the present model, Eq. (11) shows that $\alpha=-\text{Arg}(\tilde{A}/\tilde{\phi})$ never becomes larger than $-\pi/2$ and the backflow cavitation is always destabilizing. However, the result in Fig. 13 shows that α is very close to $-\pi/2$ for frequencies higher than f/f_n=0.1 and the destabilizing effect represented by E should be very small. Since the volume of the backflow cavitation will definitely decrease as the inlet pressure is increased, the backflow cavitation should have a positive cavitation compliance K. As a result of a small destabilization corresponding to a positive mass flow gain factor $M\cos(\pi+\alpha)$ and a certain stabilizing effect of cavitation compli-

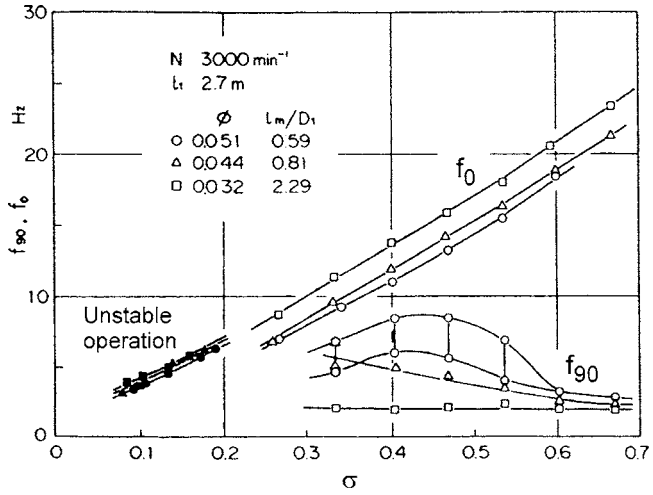

Fig. 15 Resonant frequency f_0 and the critical frequency f_{90} [11]

ance K, the backflow would have a stabilizing effect on the oscillations with higher frequencies. This can be understand from the onset condition of Eq. (13).

The above discussions can be applied for various types of impellers and will be useful for the estimation of the stability of cavitating flow, although the values of parameters a, b, and c will depend on the design.

Conclusions

In order to study the response of backflow to flow rate fluctuations, numerical calculations using a RANS code were made. The results are summarized as follow:

(1) The amplitude of backflow oscillation becomes smaller and the phase delays behind the quasi-steady response as the frequency of the flow rate fluctuation is increased.
(2) The angular momentum supply by backflow, AMB, depends only on the instantaneous flow rate, with minor effects of unsteadiness. This is because the backflow is driven by the pressure difference across the blade and the pressure difference is quasi-steady at least up to the frequency of 25% of the rotational frequency.
(3) The angular momentum removal by normal flow, AMN, can be correlated with instantaneous flow rate and the angular momentum in the upstream, AM.
(4) For the quasi-steady case, the size of the backflow is determined from the balance of the angular momentum supply by the backflow, AMB, and the outflow of the angular momentum on the normal flow, AMN. For the case with flow rate fluctuation, the difference $(AMB-AMN)$ contributes to the growth of the angular momentum in the upstream, $d(AM)/dt^*$.
(5) The unsteady pressure coefficient encircles the quasi-steady performance curve in a counter-clockwise direction due to the effect of inertia of the fluids between the pressure referencing points.
(6) The backflow responds to the flow rate fluctuation as a first-order lag element and the phase delay approaches 90 deg as the frequency is increased.
(7) If we assume that the cavity volume fluctuation is in phase with AM, we can say that the backflow vortex cavitation will destabilize low frequency oscillations and stabilize high frequency oscillations. The critical frequency is about 10% of the rotational frequency.

Nomenclature

a = proportionality constant
A = component of AM, Eq. (5)
AM = normalized angular momentum in the upstream, Eq. (1)
AMB = normalized angular momentum supplied by the backflow, Eq. (2)
AMN = normalized angular momentum removal by the normal flow, Eq. (3)
b = proportionality constant
B = component of AMB, Eq. (6)
c = proportionality constant
D_t = tip diameter of the impeller, m
f = frequency of the flow rate fluctuation, Hz
f_n = rotational frequency, Hz
K = cavitation compliance
L = distance between the cavity and the inlet pipe, m
M = mass flow gain factor
N = component of AMN, Eq. (7)
p = static pressure, Pa
p_1 = static pressure at the inlet, Pa
p_2 = static pressure at the outlet, Pa
r = radius, m
R_t = tip radius of the impeller, m
u = component of velocity U, m/s
U = velocity, m/s
U_t = impeller tip velocity, m/s
v_1 = average axial velocity at the inducer inlet, m/s
v_c = component of cavity volume V_c, m/s
v_z = axial velocity (positive, in the direction of the main flow), m/s
v_θ = absolute tangential velocity (positive, in the direction of the impeller rotation), m/s
V_c = cavity volume, m^3
z = axial coordinate measured from the leading edge at the hub (positive, downstream), m
α = phase angle, deg
ϕ = flow coefficient, v_1/U_t
ϕ = design flow coefficient
θ = angular position around the impeller from the leading edge at the tip in the opposite direction of the impeller rotation, deg
ρ = density of fluid (water), kg/m^3
ψ = static pressure coefficient, $(p_2-p_1)/(\rho U_t^2/2)$
ψ_b = pressure coefficient, $(p-p_1)/(\rho U_t^2/2)$
j = imaginary unit, $j^2=-1$

Superscripts

$\bar{}$ = mean value
$\tilde{}$ = complex amplitude

References

[1] Yokota, K., Kurahara, K., Kataoka, D., Tsujimoto, Y., and Acosta, A., 1999, "A Study of Swirling Backflow and Vortex Structure at the Inlet of an Inducer," JSME Int. J., Ser. B, **42**(3), pp. 451–459.
[2] Tsujimoto, Y., Yoshida, Y., Maekawa, Y., Watanabe, S., and Hashimoto, T., 1997, "Observations of Oscillating Cavitation of an Inducer," ASME J. Fluids Eng., **119**(4), pp. 775–781.
[3] Tsujimoto, Y., Kamijo, K., and Yoshida, Y., 1993, "A Theoretical Analysis of Rotating Cavitation in Inducers," ASME J. Fluids Eng., **115**(1), pp. 135–141.
[4] Tsujimoto, Y., Kamijo, K., and Brennen, C. E., 2001, "Unified Treatment of Cavitation Instabilities of Turbomachines," J. Propul. Power, **17**(3), pp. 636–643.

[5] Acosta, A., Tsujimoto, Y., Yoshida, Y., Azuma, S., and Cooper, P., 2001, "Effects of Leading Edge Sweep on the Cavitating Characteristics of Inducer Pumps," Int. J. Rotating Mach., **7**(6), pp. 397–404.
[6] Yoshida, Y., Tsujimoto, Y., Kataoka, D., Horiguchi, H., and Wahl, F., 2001, "Effects of Alternate Leading Edge Cutback on Unsteady Cavitation in 4-Bladed Inducers," ASME J. Fluids Eng., **123**(4), pp. 762–770.
[7] Fujii, A., Azuma, S., Yoshida, Y., Tsujimoto, Y., Uchiumi, M., and Warashina, S., 2004, "Effects of Inlet Casing Geometry on Unsteady Cavitation in an Inducer," in Japanese, Trans. Jpn. Soc. Mech. Eng., Ser. B, **70**(694), pp. 1459–1466.
[8] Kamijo, K., Yoshida, M., and Tsujimoto, Y., 1993, "Hydraulic and Mechanical Performance of LE-7 LOX Pump Inducer," J. Propul. Power, **9**(6), pp. 819–826.
[9] Brennen, C. E., 1994, *Hydrodynamics of Pumps*, Concepts ETI and Oxford University Press, New York.
[10] Qiao, X., Horiguchi, H., Kato, C., and Tsujimoto, Y., 2001, "Numerical Study of Backflow at the Inlet of Inducers," *Proceedings of the 3rd Int. Symp. on Fluid Machinery and Fluid Engineering*, Beijing, China, A-1, pp. 1–11.
[11] Yamamoto, K., 1992, "Instability in a Cavitating Centrifugal Pump (3rd Report: Mechanism of Low Cycle System Oscillation)," in Japanese, Trans. Jpn. Soc. Mech. Eng., Ser. B, **58**(545), pp. 180–186.

Unsteady Computational Analysis of Vehicle Passing

James Clarke

Antonio Filippone
e-mail: a.filippone@manchester.ac.uk

School of Mechanical, Aerospace & Civil Engineering,
The University of Manchester,
Manchester M60 1QD,
United Kingdom

This paper presents results of the simulation of two vehicles overtaking each other at highways conditions (30 m/s). *The simulation was fully unsteady and tracks the maneuver for several body lengths from downstream to upstream. Different mesh strategies have been investigated and assessed. Structured methods with sliding planes have been found the most feasible. The results shown include the effects of relative speed and lateral separation. The passing maneuver is described in detail, and a number of physical phenomena are identified. In particular, the rapid fluid compression and acceleration at the nose passing situation yields a pulse in the drag of the overtaken vehicle. The high pressure bow wave followed swiftly by the low-pressure wake affects the side force and lateral stability at positions slightly different than the nose passing.*
[DOI: 10.1115/1.2427085]

1 Introduction

The overtaking of one vehicle on highways is a maneuver that takes places at relatively high speeds and short lateral separations. There is a number of passing combinations that include passenger vehicles, trucks, coaches, and vans of various size. This operation often produces a reduction in directional stability. In addition, the use of light materials contributes to a reduction of the average vehicle masses, and increases the sensitivity to aerodynamic inputs. The maneuver may yield severe risks, particularly in adverse weather conditions, such as crosswinds, black ice and surface water, reduced visibility from precipitation, glare etc.

This paper presents a computational simulation developed to better understand the flow physics producing the aerodynamic forces on the vehicles. Similar work was been performed on this subject in the past by Okumura and Kuriyama [1]. However, this was a cursory examination, focusing on a specific case, rather than the effects of varying parameters of lateral separation and relative velocity.

A thorough analysis of the overtaking process has not seemingly been performed. Some recent research on the subject was that by Gilleron and Noger [2], Noger and Szechenyi [3]. Dynamic experimental analysis includes that by Legouis et al. [4], Telionis et al. [5], Yamamoto et al. [6], Tsuei et al. [7,8], and Beauvais [9]. Several studies on static interference have been made, including those by Heffley [10], and Abdel-Azim [11,12]. A mathematical model of the passing process has been proposed by Sanz-Andrés et al. [13,14], based on observations of forces on stationary objects by the roadside. Szechenyi [15] published a book on unsteady vehicle aerodynamics. There are presently various collections on the subject of overall vehicle aerodynamics [16–18], all of which present discussions of the overtaking process to some degree. Due to the higher speeds encountered, considerably more research has been conducted into the passing of trains in the open and in tunnels [19,20].

Noger et al. [21] performed wind tunnel testing of two 1/7 scale Ahmed bodies with a flow velocity of 30 m/s. The effects of lateral separation and relative speeds on both the overtaken and overtaking bodies were studied. The results of these show that the major effects occur while the nose of the overtaking vehicle is aft of the overtaken vehicle's aerodynamic center. In particular, the nose-passing configuration shows a considerable peak in the side force and yawing moment of the overtaken body. The effects are exacerbated by increasing relative velocity and/or decreased lateral separation.

The nose passing configuration occurs when there is still considerable longitudinal separation between the bodies respective aerodynamic centers. Thus, one can assert that the effects on the overtaken body's aerodynamics are predominantly manifested by flow behavior induced at its rear.

The present study focuses on two-dimensional (2D) overtaking as a preliminary means of investigating an appropriate simulation strategy for the complex three-dimensional (3D) flow. Thus, one must make comparisons with the pseudo-2D case of interference between long, slender cylinders of rectangular cross section. A wealth of data are available on interference between square section cylinders. However, this almost always focuses purely on tandem and parallel configurations. Where staggered configurations are investigated the focus is on the downstream body [22,23].

2 Computational Model

The main thrust of this work was to determine a suitable modeling strategy and obtain some preliminary results for discussion and comparison with experimental data. Thus, identification of a viable mesh strategy was the key to this and more complex studies. Simulation of dynamic overtaking places considerable demands on established computational fluid dynamics (CFD) practice, and pushes CFD codes to their limits. Indeed, in selecting a CFD code it is essential to ensure a method of sufficient maturity is available to enable this kind of simulation. The code employed in the present analysis was Fluent V6.2 [24,25]. The computational methods available for this class of problems are now in an advanced stage. Tedzuyar [26] published a detailed account of the computational methods for moving boundaries and interfaces. However, the validation of some of these techniques is a current issue in CFD.

The reference system for the computational model is shown in Fig. 1. In this system overtaking is according to the British convention (passing to the right). The drag and side force coefficients are C_D and C_S, respectively. The pitching moment is called C_{MZ}. The distance between the centers is X, the lateral separation between the centers is Y. The vehicles dimensions in the streamwise and cross-wise direction are L and l, respectively. The drag and side force coefficients are, respectively

$$C_D = D/\zeta, \quad C_S = S/\zeta \tag{1}$$

with the factor ζ defined by $\zeta = \rho U^2 l/2$. For the yawing moment coefficient, C_{MZ}, an additional length is introduced, the stream-

Contributed by the Fluids Engineering Division of ASME for publication in the JOURNAL OF FLUIDS ENGINEERING. Manuscript received March 6, 2006; final manuscript received August 19, 2006. Assoc. Editor: Paul Durbin.

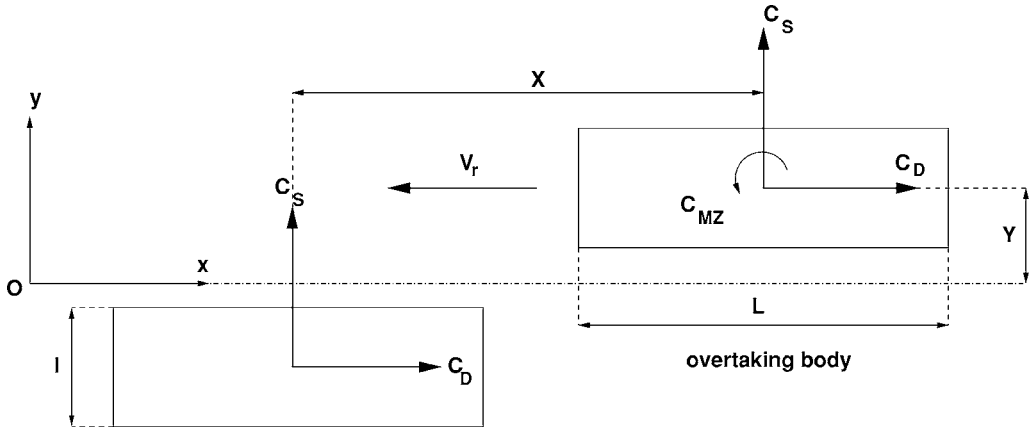

Fig. 1 Reference system for the overtaking maneuver

wise length of the body (in road vehicles the wheel-base is sometimes used). The yawing moment coefficient C_{MZ} is then

$$C_{MZ} = M/(\zeta L) \tag{2}$$

In practice, one is confined by two major constraints. First, in simulating the car passing one must be certain that the influence of the boundary conditions are negligible. Although one can naturally state that the upstream and downstream boundary conditions must be of sufficient distance not to influence the behavior around the bodies of interest this is not normally a problem. The authors' concern was to ensure the lateral boundary conditions were positioned at sufficient distance not to introduce any interference. A sensitivity study showed the minimum distance to be considerable. The mesh converged through static testing, and was relatively insensitive to the cell count.

Second, it is essential that one maintains sufficient mesh refinement to capture the highly energetic vortex shedding behavior from the bodies of interest, while at the same time not permitting the cell count to become so high that individual simulations require excessive processing time. The inherent problem is to maintain adequate mesh refinement in the vicinity of the bodies while permitting a considerably coarser grid at a distance. This ensures that the overall cell count is maintained at a reasonable level, and that simulation times can be minimized. However, the requirement for the overtaking (downstream) body to execute a full pass from a considerable distance downstream to an equivalent upstream position makes the control of the cell size at each time step a taxing affair.

2.1 Unstructured Mesh. An attractive solution is to use a deforming, unstructured mesh with dynamic remeshing which would permit the relative motion of the two bodies. However it was found that the CFD code could not perform this to a satisfactory level. Control of the cell size is accomplished by use of a "size function" that maintains maximum and minimum cell volumes in relation to the distance from the moving bodies.

Figure 2 shows a typical example of this case. The narrow shaded region is the region of the mesh that the overtaking body passes through. This is also the only region subject to remeshing.

However, regardless of which regions are marked for remeshing and which are held static, the software consistently measures cell distance as a ratio of the distance to the nearest boundary. Hence, the authors were unable to produce adequate control of the size function. Contours of size function for this mesh strategy show that the software makes no distinction between regions of the mesh that are deforming and those that are not.

Figure 3 shows the unavoidable consequence of attempting to use size functions to control cell size. Due to the size of the domain the algorithm is unable to maintain a small enough limit and "oversized" cells appear as shown here. The only means of ensuring this does not happen with the deforming mesh is to fill the entire region to be traversed by the overtaking body with very small cells. One can then ignore the size function and specify a very low maximum cell size for remeshing. This ensures that over sized cells will never appear. However, since the region traversed by the overtaking body is so vast, this produces a massive increase in cell count and the simulation time. The y^+ was maintained between 30 and 300. Flow separation and reattachment mean that sometimes these values were exceeded. The cell count was 60,000 at initiation, 38,000 when the bodies were aligned, and 60,000 at the end. Inlets and outlets were at ±14.6 m and lateral boundaries at ±4.69 m.

Thus, it was determined that although an unstructured mesh strategy could work for this type of simulation (and indeed would save a great deal of time in mesh generation), it was not a viable solution. In future it will be necessary to ensure this method, or a similar one, can be made to function appropriately, as we shall require the possibility of enabling more complex overtaking maneuvers, as simulations become increasingly more realistic.

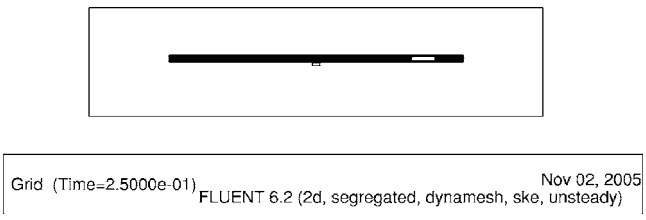

Fig. 2 Deforming region of the mesh

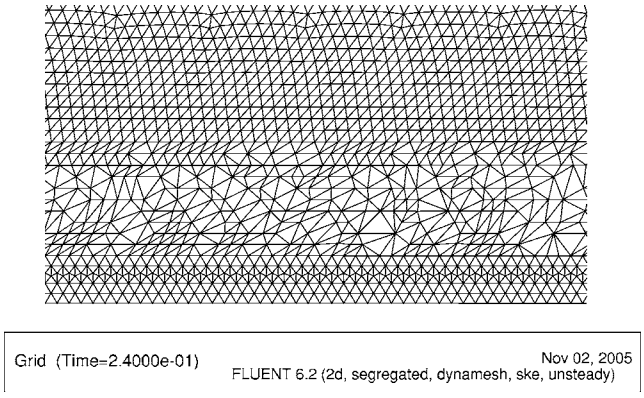

Fig. 3 "Oversized" cells adjacent to overtaking body

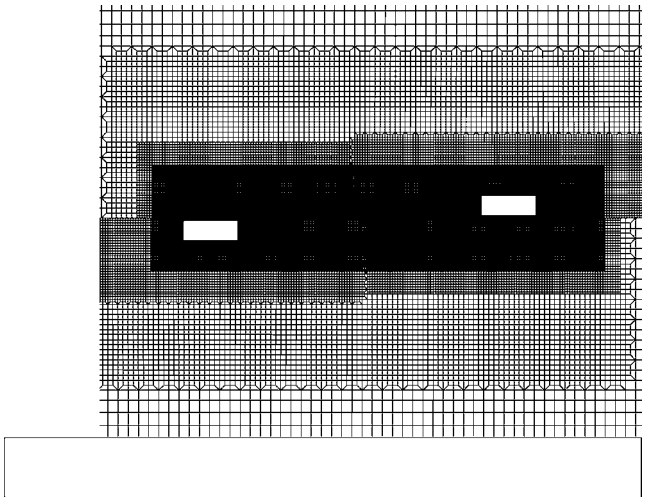

Fig. 4 Final mesh strategy: $x/L=5.5$

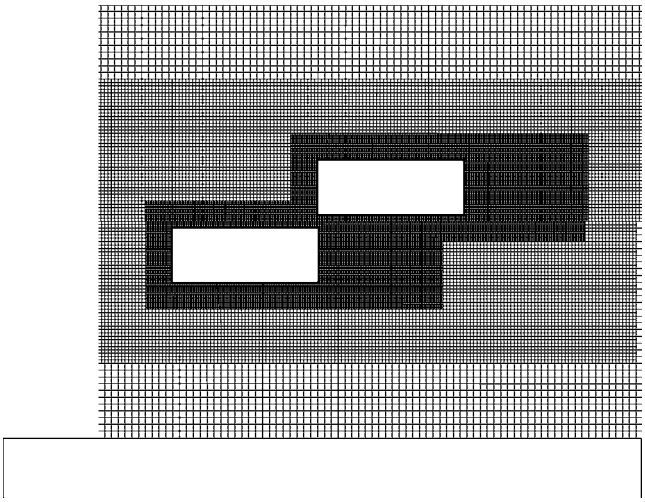

Fig. 6 Grid with $x/L=1$

2.2 Structured Mesh. At present, the only viable alternative is to use a structured grid with sliding interfaces and make heavy use of grid adaption. This means that as the overtaking body approaches, cells can be adapted to provide the necessary refinement to capture the complex flow around the body. Furthermore, as the overtaking body departs, the cells can be recoarsened to reduce the cell count, and hence ensure the solver focuses its computational effort in the regions of interest.

In undertaking to use adaption, one discovers that there is no suitable quantity to refine or coarsen on gradients or curvatures of. Thus, region-based adaption is performed according to the results of mesh convergence studies on the bodies in static, staggered configuration. The final mesh strategy is illustrated in Figs. 4–7.

2.3 Numerical Model. An accurate representation of the real-life case was sought, while maintaining a reasonable time scale for the simulations. Due to the limited experimental research in this field, data for isolated bodies were used to draw comparisons.

The preliminary flow field was obtained by initializing from inlet boundary conditions and then running the case as steady-state in static configuration with SIMPLE pressure–velocity coupling for 1000 iterations. The solver was then switched to unsteady, maintaining the static configuration and running with PISO NITA to a flow time of 2 s to enable the flow to fully develop. The time-step was $dt=2\cdot10^{-4}$ s.

As a variant of the k-ε turbulence model was used, the QUICK scheme was not utilized, so as to avoid any possible overshoots which can lead to negative production [27]. Second-order upwinding was sufficient; neither QUICK nor a third-order scheme was deemed to offer any significant benefit.

2.4 Turbulence Model. For the level of detail desired in this study, the authors have limited themselves to two-equation turbulence models. Three two-equation turbulence models (standard k-ε, RNG k-ε, and k-ω SST) were assessed on their ability to accurately predict the drag coefficient C_D and Strouhal number of the vortex shedding, St, by comparison with experimental results from slender bluff bodies.

Of the available options, the RNG k-ε model fared the best and was thus adopted. The ability of this model to predict the flow phenomena around such bodies is assessed in the discussion below.

Correct selection of a turbulence model is essential in simulation of complex flows such as the present one. The ability to predict flow behavior is critical in ensuring that coefficients of drag and side force, as well as frequency of vortex shedding, are accurately captured. Only two-equation models are capable of achieving this to an appropriate level.

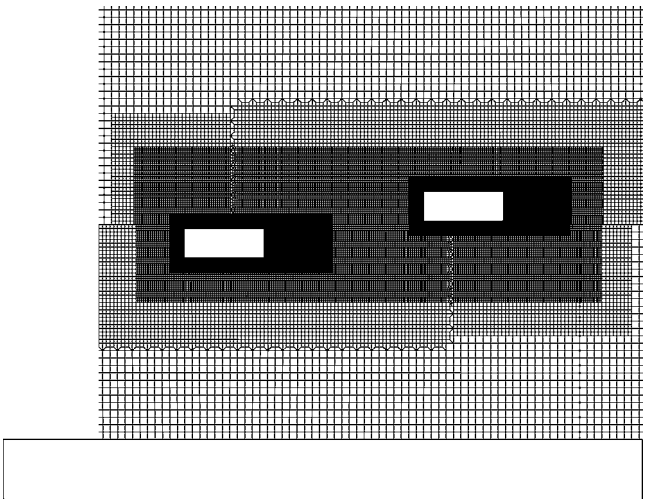

Fig. 5 Grid with $x/L=3$

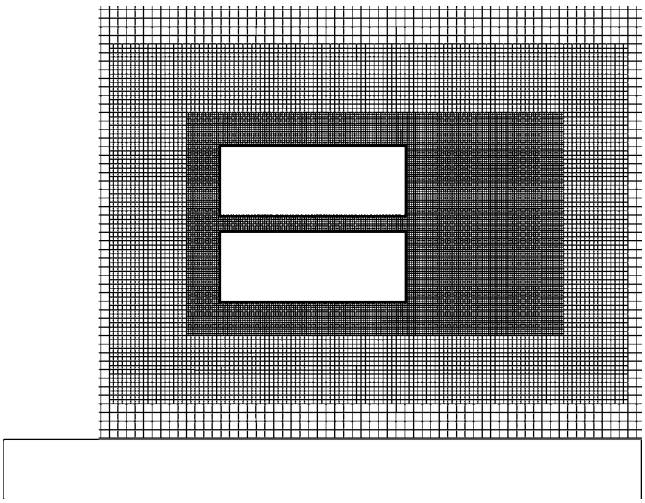

Fig. 7 Grid with $x/L=0$

Table 1 Comparisons of numerical accuracy via dependent variables.

Item	Experiment[29]	Standard k-ε	RNG k-ε	k-ω SST
St	0.16	—	0.168	0.159
C_D	1.3	1.05	1.15	1.23

3 Results

The 2D bodies that have been investigated have cross-sectional aspect ratio of ≈ 2.7. The models lengths were $l=0.2723$ m and $L=0.7308$ m. Thus, experiments on slender bluff bodies with similar aspect ratio are a relatively close approximation. Okajima [28] performed investigations of Strouhal numbers of rectangular cylinders for a relatively low range of Reynolds numbers ($\mathrm{Re}=70$ to 2×10^4). These were limited to cylinders with aspect ratios with integer values from 1 to 4. A Strouhal number of ≈ 0.08 was found for a body with an aspect ratio of 2 and $\mathrm{Re}\simeq 10^4$ and above.

A body with aspect ratio 3 shows widely scattered results in the range $\mathrm{Re}=700-5000$. This is due to a two-mode vortex shedding, as there is a small peak in the lower-frequency range, in addition to the dominant peak. Above $\mathrm{Re}\approx 1220$, two differing signal waves appear.

Norberg [29] and Taylor and Vezza [30] have produced independent reviews of other authors' work and each show a considerable range of results. For example, there is a high dependency on the aspect ratio and the range from 2.5 to 3 is seen to be particularly critical. Results for an aspect ratio of 2.5 show St ≈ 0.07, whereas a step change occurs before an aspect ratio of 3 giving values of St between 0.15 and 0.18. Clearly, this is very close to a critical aspect ratio as shown by the discrete vortex model (DVM) of by Taylor and Vezza. However, the C_D shows less sensitivity and $C_D\approx 1.3$ is apparent. The authors were unable to locate papers detailing the effects on C_S and C_{MZ}.

3.1 Quasi-Steady Analyses. Vortex shedding phenomena from slender bluff bodies is time dependent and unsteady by its nature. However, this behavior is repeatable, and does not alter from one cycle to the next. Thus, the average C_D, RMS value of side force and Strouhal number of the flow are constant and can be considered to be "quasi-steady." Therefore, in the present simulations the term "unsteady" was reserved for the case where dynamic overtaking occurs, as the resulting behavior is not repeatable, and hence cannot be classified in the same way. Experimental results for slender bodies were compared with those from the present simulations as a measure of accuracy.

The perturbed coefficients are relatively large. However, if one considers two rectangular prisms passing at these speeds, it must be recognized that the fluid is forced into an extremely narrow aperture at very high speed. As this is a 2D case, there is nowhere else for the fluid to go. Hence the very high peaks.

Table 1 shows results for the three turbulence models assessed. With the standard k-ε model the overprediction of TKE was highly apparent. This produced an excessive effective viscosity which acted to damp out flow oscillation in the wake of the body. Thus, no vortex shedding was observable, and the model was quickly deemed inadequate. Although the k-ω SST model produces results closer to experiment than the RNG k-ε model, it required a more refined mesh to do so. As the results from the RNG k-ε model are not unreasonable, this is the more attractive model as we are able to perform simulations considerably faster.

3.2 Dynamic Simulations. Dynamic simulations were conducted using the flow field described above as a starting point. In each case, four passes were conducted using different starting points in each case. As the bodies are 2D, the cyclic vortex shedding needed to be taken into consideration. Thus, four starting points were selected where the side force was at a maximum (positive), minimum (negative) and in both cases where it is neutral—crossing the x axis from both the positive and negative sides. The four sets of results were then averaged in each case to provide a coefficient history independent of the point in the vortex shedding cycle at which the overtaking process began.

3.3 Unsteady Analysis. Force and moment coefficient histories for the overtaken body are shown in Figs. 9–14. One can begin by making some general comments on these results. In all cases there is a peak in C_D occurring at the *nose passing* point ($x/L=1$). At the same point a negative peak is seen in both the side force and yawing moment coefficients.

Around $X/L=0.5$, the drag returns to approximately its undisturbed value. Meanwhile a second, smoother, negative peak is seen in the side force. The yawing moment changes sign and reach a positive peak. As the two bodies align ($X/L=0$), oscillations are seen in the C_D. The side force rises rapidly as the yawing moment falls. Between $-0.5>X/L>-1$ the side force shows a positive peak and yawing moment is again at a negative peak. The magnitude of the second negative peak in yawing moment varies in relation to the first as described below. After $X/L\approx -1$, qualitatively similar oscillations are seen in all coefficients. These vary with overtaking speed and/or lateral separation.

3.3.1 Effect of Relative Velocity. Figures 9–11 show the effects of varying the relative velocity of the two bodies. In all cases an increase in relative velocity yields an increase in the peak coefficients. Differences in the points at which secondary peaks occur are evident. It is generally observed that the higher the relative velocity, the later in the passing process the secondary peaks occur. The exception to this is in the case of side force where the secondary negative peak occurs earlier with increasing relative velocity.

3.3.2 Effects of Lateral Separation. Figures 12–14 show the effects of varying lateral separation between the two bodies. There is little variation in the peak C_D and subsequent wave form. The largest separation ($Y/l=0.7$) gives a marginally lower peak. The side force is relatively similar for $Y/l=0.7$ and $Y/l=0.5$; at $Y/l=0.25$ there is a noticeably different wave form with the primary negative peak being considerably sharper than at greater separation; the secondary peak occurs sooner. The third negative peak is markedly lower than at greater separation. The yawing moment coefficient shows the greatest negative peak with the smallest separation. However, the secondary and tertiary peaks are the smallest.

4 Discussion of the Passing Maneuver

The various phases of the passing maneuver are described in detail. A flow visualization for some critical steps is shown in Fig. 8. This case refers to a relative speed $V_r=20$ m/s, and separation $\Delta y/l=0.25$.

4.1 The Approach: $X/L>1$. As the overtaking body approaches, there is an increasingly negative yawing moment on the overtaken body (Fig. 11). This clockwise moment is induced partly by the high pressure region fore of the overtaking body impinging on the aft inner surface of the overtaken body. Moreover, there is an asymmetric flow that is induced over the overtaken body. Hence the flow separation from the overtaken body's leading edge is induced to reattach at the aft inner surface, while shifting the core of the outer recirculating flow to the aft outer surface. The respective increase and decrease in pressure introduces a pressure inequality across the rear of the overtaken body, which acts to turn it in an clockwise manner—pulling its nose into the path of the overtaking body.

4.2 Nose Passing: $X/L=1$. This is the most interesting point in the present study as there is consistently a large increase in the

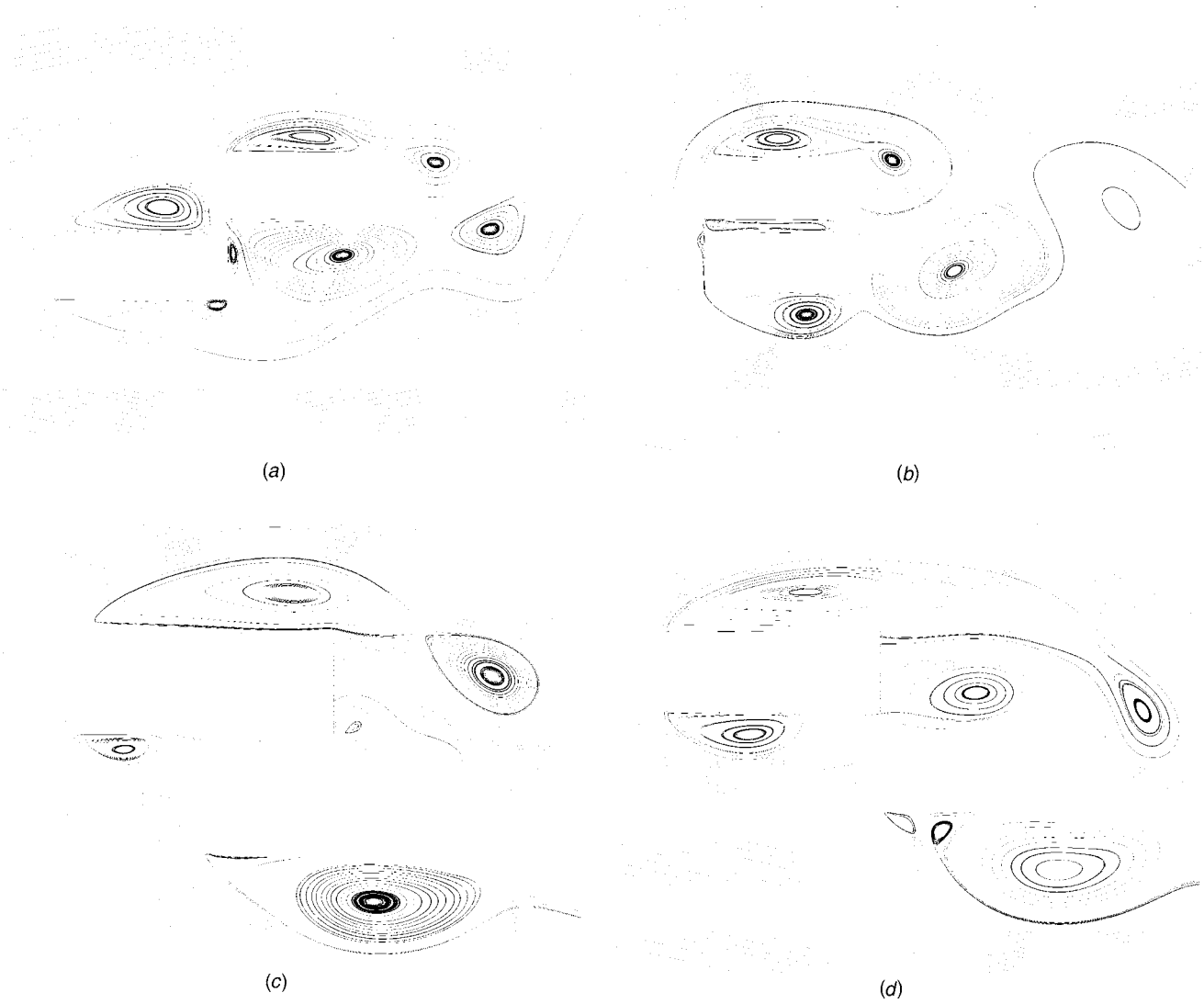

Fig. 8 Particle tracks at four positions. Top vehicle overtakes bottom vehicle from the right; V_r=20 m/s, $\Delta y/l$=0.25.

drag of the overtaken body. The drag rise varies in relation to V_r and $\Delta y/l$. Observation of velocity vectors and contour plots clearly show that the air is squeezed by the rapid advancement of the overtaking body toward the overtaken body. This causes the flow to accelerate rapidly or *squirt* through the narrow gap presented to the flow, causing the maximum flow velocity encountered at any point in the passing to occur. The acceleration causes a pressure drop. However, it also induces flow separation from the inner trailing edge, and the recirculation acts to further reduce the pressure in this zone. Thus, a twofold effect acts to induce a very low pressure aft of the body for a very short time, and the powerful, yet exceptionally brief, drag pulse is found.

In comparing the magnitude of the C_D at this point, it is noted that the effect of the overtaking body's relative velocity cannot be ignored (Fig. 9). Simultaneously, the stagnation of flow at the aft inner surface acts to induce a negative side force and negative (clockwise) yawing moment in all cases. (Note: the negative C_{MZ} is not present in the case of static overtaking.)

Observation of contours of dynamic pressure shows that the pressure loss bound into the acceleration of the fluid, and hence the pressure drop caused by this acceleration. The focus of the pressure drop—the lowest value of static pressure observed—occurs closer to the body than the centreline of the accelerated flow. Therefore the recirculation produces the major contribution to the drag seen.

In the actual road conditions, this would have a greater effect with an overtaking lorry than a car. A car bonnet is lower and allow a larger flow, whereas a lorry restricts more of the flow and creates greater separation.

4.3 Nose to Center: X/L=0.5. As the nose of the overtaking body passes the central region of the overtaken body the drag returns to a more or less normal value. However, the side force remains negative. This finding agrees with experimental results (Note: the sign convention is the reverse of the results of Noger et al. [21]).

The yawing moment shows the most interesting result: it executes a rapid sign change and marked positive peak. This induces an anticlockwise moment on the overtaken body, due to the various points of flow stagnation and separation, and the consequent pressure field. The high pressure trapped at the front of the overtaking body (along with separation at the fore outer surface of the overtaken body) yields the strong, positive yawing moment.

4.4 Parallel Alignment: X/L=0. At the highest V_r, little change is seen from the previous position. However for V_r =15 m/s and below, the yawing moment becomes neutral, as shown in Fig. 11. There is still a high pressure between the bodies,

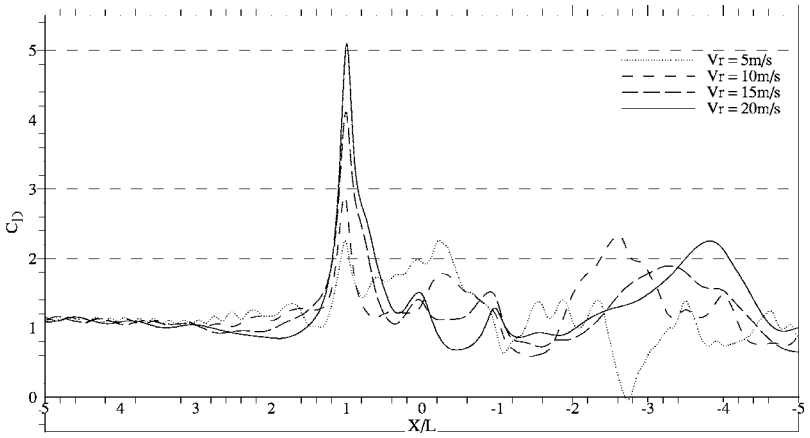

Fig. 9 C_D history of the overtaken body at various relative speeds, lateral spacing $y/l=0.25$

and low pressure at the fore outer surface, due to separation. This means that the outwards directed (negative) side force remains high.

4.5 Tail to Center: $X/L=-0.5$. At the highest V_r, a minor trough in C_D appears. This is unique to the highest velocities, and is an example of the domination of vortex shedding on the 2D case. The overtaking body has shed a vortex from its outer trailing edge into the now mutual wake of the two bodies. This clockwise spinning vortex is drawn inwards, towards the overtaken body and in so doing pulls fluid from the outer wake, throwing this against its trailing edge. Here it stagnates, increasing the pressure and momentarily decreasing the drag on the overtaken body. Note that this occurs irrespective of lateral separation. Yet, it is highly dependent on the relative velocity. Indeed, there is a clear increase in the drag with decreased V_r at this point (Fig. 9). This result is indicative of a timing-related issue.

At this point there is a positive peak in side force. Depending on relative velocity, another sign change for yawing moment and a negative peak occur. The positive side force is yielded from a threefold effect. First, flow between the bodies is now almost exclusively aligned with the free stream and hence accelerates through the gap, causing a drop in pressure (the Bernoulli effect). As the rear of the overtaking body is now around the center of the overtaken body, separation from the overtaking body's inner trailing edge further acts to reduce the pressure seen at the inner surface of the overtaken body. Finally, the action of the aforementioned vortex throwing fluid against the rear of the overtaken body induces an anticlockwise separation at the aft inner surface of the overtaken body. These three factors combine to produce an overriding pressure drop and the positive side force seen. The side force is affected by lateral separation and decreases as $\Delta y/l$ increases. The mechanism appears to be due to the rapid acceleration of flow between the bodies in the case of the smallest separation, which causes a pressure drop and sucks the overtaken body inwards. The diminished acceleration with increasing lateral separation reduces this effect, and hence separation from the fore outer surface becomes increasingly dominant. The effects of relative velocity are less well defined. Figure 10 shows the poor correlation at this point.

4.6 Tail Passing: $X/L=-1$. Drag and side force appear largely disaffected by this particular configuration. The same effects as the previous stage continue. However, the yawing moment shows great susceptibility to the mechanisms occurring at this point, as shown in Fig. 11. The acceleration of flow between the bodies and separation at the inner trailing edge of the overtaking body is now focused between the fore inner surface and the aerodynamic center of the overtaken body. This effect occurs irrespective of V_r (albeit earlier at lower V_r) or $\Delta y/l$, and produces a clockwise moment on the overtaken body.

The reversed flow over the rear of the overtaken body now induces separation at the aft outer edge. The reversed flow also causes the vortex emanating from the overtaking body's inner

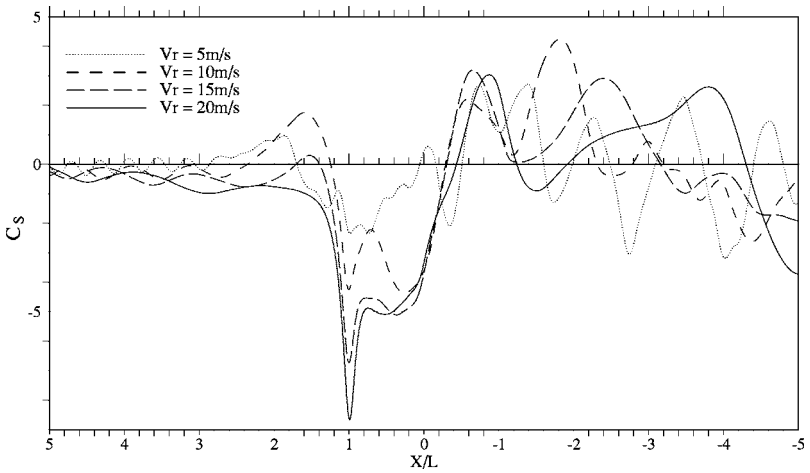

Fig. 10 C_S history of the overtaken body at various relative speeds, lateral spacing $y/l=0.25$

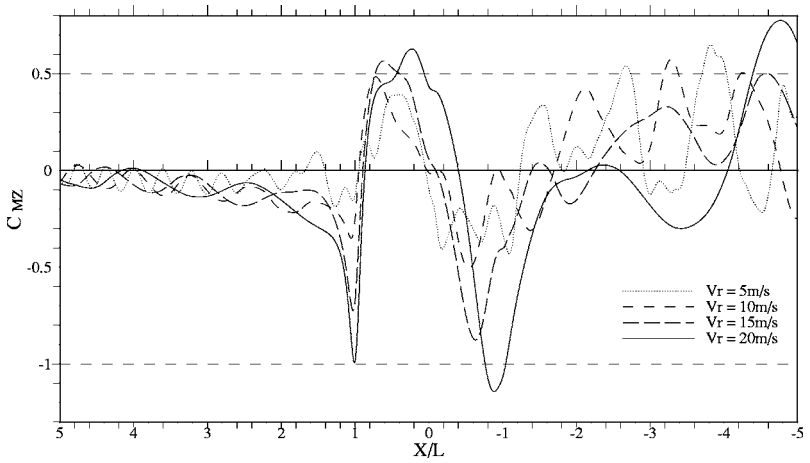

Fig. 11 C_{MZ} history of the overtaken body at various relative speeds, lateral spacing $y/l=0.25$

trailing edge to be pushed forward, and its focus occurs adjacent to the fore inner region of the overtaken body. The vortices work together to increase the clockwise moment. However, due to their dependence on V_r the point at which they contribute most varies, as seen in Fig. 11. Interestingly, increased lateral separation acts to increase the magnitude of the moment, as shown in Fig. 14. The reason is due to increased flow being allowed through the gap, and more energetic separation from the overtaken body's fore inner surface.

4.7 Departure: $X/L=-2$. Finally, the effects of the overtaking body's departure have been observed. The only consistent phenomena identifiable in the present study is that at $V_r=20$ m/s and for $\Delta y/l=0.5$ and 0.7 there is a strong negative peak in side force. As the gap between the bodies opens up, the overtaking body's inner trailing edge vortex loses strength, the outer trailing edge vortex grows rapidly and sheds with great power. This then whips the overtaken body—creating asymmetric flow, inducing stagnation on the inner surface, and exacerbating separation over the outer surface. The resulting pressure differential creates a significant negative side force on this body.

4.8 Coefficient Histories—By Coefficient. By observation of the locations at which peaks, troughs and changes of sign occur, it is found that higher relative velocities show good correlation in terms of their coefficient histories (Fig. 12). It is observed that the higher the relative velocity, the higher the time delay for the yawing moment peak. In the case of side force, the secondary negative peak becomes closer to the first with increasing relative velocity.

Decreasing the lateral separation between 3D vehicles is known to cause an increase in the peaks of side force and drag coefficients [3,15]. In our case it is not apparent, and secondary peaks are actually increased. Due to a fixed lateral separation between bodies, the large-scale flow between the bodies will be reestablished at a very specific moment. This occurs earlier for larger lateral separation and later for smaller separation. The precise moment at which this impetus occurs affects wake stability. If it is directed so as to counteract a pre-existing side force or yawing moment, then the oscillations of these coefficients may well be seen to dampen momentarily. If the impetus acts to coincide with a pre-existing force or moment, it will be seen to enhance this again, albeit momentarily.

The upshot is that consistent decreases or increases in lateral separation cannot be authoritatively determined to produce positive or negative contributions to the body's forces and moments. The details of this aspect of the flow are too specific and require further study. Suffice to say at this stage that during separation. Once the overtaking body has passed, the coefficients of the overtaken body are seen to show little correlation in terms of the lateral separation.

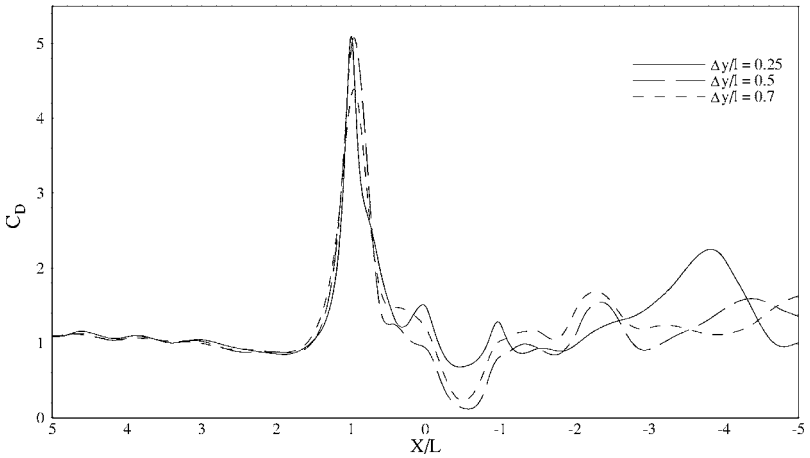

Fig. 12 C_D history of the overtaken body at various lateral spacings, relative speed=20 m/s

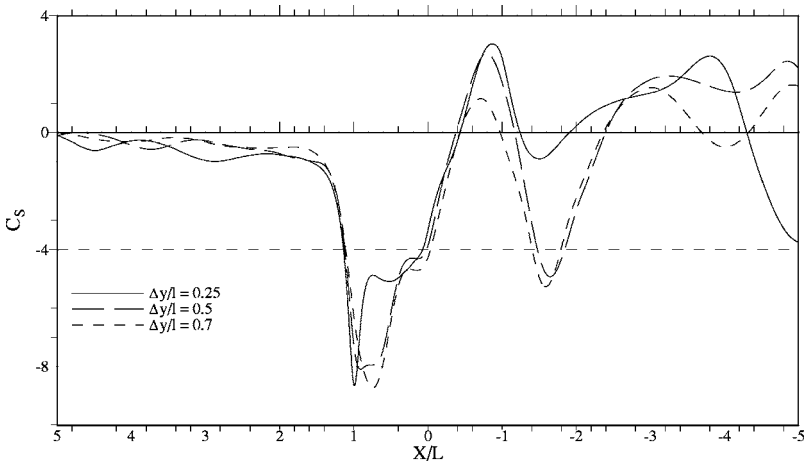

Fig. 13 C_S history of the overtaken body at various lateral spacings, relative speed=20 m/s

4.9 Drag Coefficient of the Overtaken Body. In Fig. 12 there is a peak in the C_D of the overtaken body as the overtaking body reaches the nose passing position. This occurs regardless of overtaking velocity (it is seen in the static, staggered configurations also) or separation (in terms of those tested). Although in the case of overtaking at 10 m/s, there is still a peak at the exact location as all others, but this is superseded by a second, larger peak shortly afterwards for larger separation.

The peak C_D is found to be around 5 for the case of V_r =20 m/s and $\Delta y/l$ of 0.25 and 0.5. Lateral separation of 0.7 returns a lower peak C_D between 4.3 and 4.4. The peak occurs at nose passing where the leading edge of the overtaking body is in line with the trailing edge of body 1, as described earlier.

In 3D an increase in peak drag with decreased lateral separation is noted. These increases are due to the increased velocities experienced as the squeezing effect is enhanced by the narrower gap. Lateral separation is observed to produce similar effects in the case of 2D dynamic overtaking (Fig. 12).

4.10 Side Force Coefficient of the Overtaken Body. In Fig. 13 the side force shows a clear, negative peak at, or immediately after the nose passing situation. This is followed by a secondary negative peak, which is greater than the first at V_r=10 m/s, caused by separation from the fore outer surface being reestablished and inducing low pressure compared to the high pressure between the bodies. Then there is a swift sign reversal as the two bodies leave alignment (after parallel configuration). Increased separation enhances the secondary negative peak, causing it to largely combine with the primary peak. Ultimately, at $\Delta y/l$ =0.7 only one definite peak occurs, with only a minor step in the wave form immediately afterwards.

Decreased relative speed diminishes the primary negative peak. Yet, it has minimal effect on the secondary negative peak down to V_r of 10 m/s. Below this speed, the side force exhibits a very erratic behavior (Fig. 10). The sign reversal occurs at or around X/L=−0.2 at V_r=20 m/s. As V_r decreases and Δy increases it is not possible to assert a reliable point at which the side force changes sign, if at all.

The side force is relatively similar for $\Delta y/l$=0.5 and $\Delta y/l$ =0.7. $\Delta y/l$=0.25 yields a noticeably different wave form with the primary negative peak being considerably sharper than at greater separation and both negative peaks occurring sooner at higher V_r. For V_r=10 m/s there are clear effects on the side force magnitude and timing.

After the overtaking body has passed, the overtaken body exhibits large side force oscillations as the wake of the overtaking body—which is moving faster and thus imparting more energy to the flow—interferes with the flow field. The faster the overtaking body, the lower the periodicity of the side force oscillations on the overtaken body. These oscillations are sometimes found to be of similar magnitude to the case of two bodies in close proximity.

4.11 Yawing Moment Coefficient of the Overtaken Body. In Fig. 14 the yawing moment shows a negative (clockwise) peak at the nose passing point. Then there is a sign reversal, with a strong positive peak occurs. The sign then reverses again, and a negative peak occurs. After this point, wide variations in behavior are seen and no consistent behavior is identifiable, except for V_r =10 m/s where a third negative peak occurs immediately after departure of the overtaking body.

Increased V_r enhances all the effects seen (Fig. 11). Increasing Δy shows an interesting behavior: decreasing the initial negative peak and increasing the magnitude of the subsequent positive and secondary negative peaks at the higher relative velocities (Fig. 14).

The timing of the second negative peak is greatly affected by the relative velocity of the two bodies. Also the timing of certain flow phenomena, such as a sideways whipping motion, or stabilization of asymmetric flow, can reasonably be assumed to be largely affected by the rate at which two bodies pass.

5 Conclusions

Dynamic overtaking between two pseudo-two-dimensional slender bodies exhibits similarities and differences with the case of two 3D bodies. High drag at the nose passing situation does not seem to have been formally identified elsewhere. The "squeeze and squirt" effect and associated flow stagnation and separation yield high drag, high side force and high yawing moment at this point. These increase in magnitude with increasing relative velocity and/or decreasing lateral separation.

The "push–pull" side force seen in 3D tests was seen in the cases presented, although the push was consistently at nose passing, and the pull in our case occurs after the parallel configuration. This result is in stark contrast to the 3D case, where the timings appear highly dependent on the relative velocity. In the present case, clear flow stagnation and separation behavior dominate, and thus the effects are largely independent of V_r or Y/L.

The rapid fluctuation of yawing moment was recreated in the present computations, and agrees well with the 3D case, although direct comparisons could not be done. Thus, the nose and tail passing situations yield similar effects in producing specific flow patterns at the interference of the two corners.

Lateral separation was not a clear determinant of the magni-

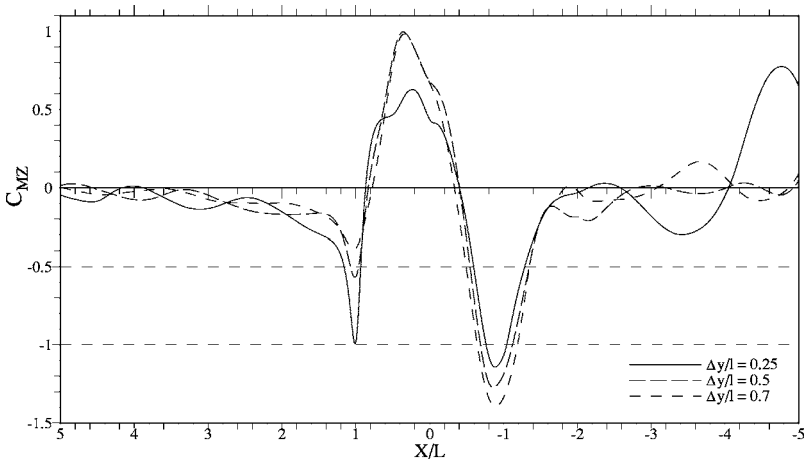

Fig. 14 C_{MZ} history of the overtaken body at various lateral spacings, relative speed=20 m/s

tudes of side forces encountered within the range investigated and shows a greater effect on the timing of peaks and troughs. Forces vary little with lateral separation compared to relative velocity.

Overall, there is good qualitative agreement with 3D experiments, with the exception of side force at parallel configuration being of opposite sign. A number of specific flow characteristics causing these effects have been identified. The authors are confident that further studies and simulations of the 3D case will yield the same stagnation and separation phenomena. Moreover, it was shown that increasing relative velocities and decreasing lateral separations increase the forces and moments a body encounters when overtaken.

The most inconclusive result was the rapid fluctuation of yawing moment which, in the case of a real vehicle, could easily lead to disastrous consequences. This is especially true where contributing factors such as low vehicle mass, high susceptibility to aerodynamic inputs and adverse driving conditions are present.

References

[1] Okumura, K., and Kuriyama, T., 1997 "Transient Aerodynamic Simulation in Crosswind and Passing an Automobile," J. Soc. Auto. Eng., **106**(1), pp. 647–662.

[2] Gilliéron, P., and Noger, C., 2004, "Contribution to the Analysis of Transient Aerodynamic Effects Acting on Vehicles," J. Soc. Auto. Eng., **113**(6), pp. 893–900.

[3] Noger, C., and Széchényi, E., 2004, "Experimental Study of the Transient Aerodynamic Phenomena Generated by Vehicle Overtaking," *Flow Induced Vibration*, de Langre and Axisa, eds., Ecole Polytechnique, Paris.

[4] Legouis, T., Bourassa, Y., and Nguyen, V. D., 1982, "Influence d'un Poids Lourd Equip ou Non de Dispositifs Aerodynamiques sur une Automobile en Manoeuvre de Depassement," J. Wind. Eng. Ind. Aerodyn., **9**, pp. 381–387.

[5] Telionis, D. P., Fahrner, C. J., and Jones, G. S., 1984, "An Experimental Study of Highway Aerodynamic Interferences," J. Wind. Eng. Ind. Aerodyn., **17**, pp. 267–293.

[6] Yamamoto, S. et al., 1997, "Aerodynamic Influence of a Passing Vehicle on the Stability of the Other Vehicles," JSAR Review, **18**, pp. 39–44.

[7] Tsuei, J. L., Savas, O., and Hedrick, J. K., 1999, "Transient Aerodynamic Effects on a Four-Car Platoon During Passing Maneuvers: Data Summary," University of California, Berkeley, Technical Rep. No. UCB-ITS-PRR-99-29.

[8] Tsuei, J. L., Savas, O., and Hedrick, J. K., 2000, "Transient Platoon Aerodynamics During Passing Maneuvers and In-line Oscillations," University of California, Berkeley, Technical Rep. No. UCB-ITS-PRR-2000-26.

[9] Beauvais, F. N., 1969, "Transient Aerodynamic Effects on a Parked Vehicle Caused by a Passing Bus," Proceedings of the Ist Symposium on Road Vehicle Aerodynamics, A. J. Scibor-Rylski, ed., London, November, pp. 10.1–10.22.

[10] Heffley, R. K., 1973, "Aerodynamics of Passenger Vehicles in Close Proximity to Trucks and Buses," J. Soc. Auto. Eng., **82**(2), pp. 901–914.

[11] Abdel Azim, A. F., 1994, "An Experimental Study of the Aerodynamic Interference Between Road Vehicles," SAE World Congress, Detroit, MI. Paper No. 94-0422, February 1994.

[12] Abdel Azim, A. F., and Abdel Gawad, A. F., 2000, "A Flow Visualization Study of the Aerodynamic Interference Between Passenger Cars," SAE World Congress, Detroit, MI. Paper No. 2000-01-0355, March, 2000.

[13] Sanz-Andrés, A. et al., 2004, "Vehicle-Induced Force on Pedestrians," J. Wind. Eng. Ind. Aerodyn., **92**, pp. 185–198.

[14] Sanz-Andrés., A. et al., 2003, "Vehicle-Induced Loads on Traffic Sign Panels," J. Wind. Eng. Ind. Aerodyn., **91**, pp. 925–942.

[15] Széchényi, E., 2004, "The Overtaking Process of Vehicles," *Progress in Vehicle Aerodynamics III—Unsteady Flow Effects*, J. Wiedemann and W.-H. Hucho, eds., Expert-Verlag, Renningen, Germany, pp. 80–88.

[16] Hucho, W. H., 1998, *Aerodynamics of Road Vehicles*, 4th ed., Society Auto. Engineering, Warrendale, PA.

[17] Barnard, R. H., 2001, *Road Vehicle Aerodynamic Design*, 2nd ed., MechAero, St. Albans, Hertfordshire, UK.

[18] Scibor-Rylski, A. J., 1975, *Road Vehicle Aerodynamics*, Pentech Press, London.

[19] Holmes, S., Schroeder, M., and Toma, E., 2000, "High-Speed Passenger and Intercity Train Aerodynamic Computer Modeling," Proceeding of ME2000, The 2000 International Mechanical Engineering Congress & Exposition.

[20] MacNeill, R. A., Holmes, S., and Lee, H. S., 2002, "Measurement of the Aerodynamic Pressures Produced by Passing Trains," Proceedings of the 2002 ASME/IEEE Joint Rail Conference.

[21] Noger, C., Regardin, C., and Széchényi, E., 2005, "Investigation of the Transient Aerodynamic Phenomena Associated with Passing Maneuvers, J. Fluids Struct., **21**, pp. 231–241.

[22] Luo, S. C., and Teng, T. C., 1990, "Aerodynamic Forces on a Square Section Cylinder that is Downstream to an Identical Cylinder," Aeronaut. J., **94**(936), pp. 203–212.

[23] Luo, S. C., Li, L. L., and Shah, D. A., 1999, "Aerodynamic Stability of the Downstream of Two Tandem Square-Section Cylinders," J. Wind. Eng. Ind. Aerodyn., **79**, pp. 79–103.

[24] Fluent Inc. 2005, *FLUENT 6.2 User's Guide*, Fluent Inc., Lebanon, NH.

[25] Fluent 2002, FluentSoftware Training, *Sliding Mesh Modeling*, Fluent Inc., Labanon, NH.

[26] Tedzuyar, T. E., 2001, "Finite Element Methods for Flow Problems With Moving Boundaries and Interfaces," Arch. Comput. Methods Eng., **8**(2), pp. 83–130.

[27] Versteeg, H. K., and Malalasekera, W., 1995, *An Introduction to Computational Fluid Dynamics*, Pearson Prentice Hall, Essex, UK.

[28] Okajima, A., 1982, "Strouhal Numbers of Rectangular Cylinders," J. Fluid Mech., **123**, pp. 379–398.

[29] Norberg, C., 1993, "Flow Around Rectangular Cylinders: Pressure Forces and Wake Frequencies," J. Wind. Eng. Ind. Aerodyn., **49**, pp. 187–196.

[30] Taylor, I., and Vezza, M., 1999, "Prediction of Unsteady Flow Around Square and Rectangular Section Cylinders Using a Discrete Vortex Method," J. Wind. Eng. Ind. Aerodyn., **82**, pp. 247–269.

Shigenori Takada[1]
Grad. Student
Graduate School of Engineering,
Kansai University,
887-2 Yoshino,
Maizuru, Kyoto 625-0003,
Japan
e-mail: elp_110@yahoo.co.jp

Norio Tagawa
Professor
High Technology Research Center (HRC),
Department of Mechanical Engineering,
Kansai University,
3-3-35 Yamate-cho, Suita,
Osaka 564-8680,
Japan
e-mail: tagawa@ipcku.kansai-u.ac.jp

Atsunobu Mori
Professor
Department of Mechanical Engineering,
Kansai University,
3-3-35 Yamate-cho,
Suita, Osaka 564-8680,
Japan
e-mail: moriatsu@ipcku.kansai-u.ac.jp

Yoshiaki Mizoh

Masaru Nakakita

Panasonic Shikoku Electronics Co.,
Ltd., 2131-1,
Minamigata, Toon,
Ehime 791-0395,
Japan

Experimental Study on Flow-Induced Disk Flutter Dynamics by Measuring the Pressure Between Disks

It is important to clarify the characteristics of flow-induced vibrations in hard disk drives in order to achieve an ultrahigh magnetic recording density. In particular, it is necessary to reduce the flow-induced disk vibrations referred to as disk flutter. This paper describes the correlation between the disk vibration amplitude and the pressure fluctuation between a pair of high-speed corotating disks. It also reveals the effects of the arm thickness and arm shape on the disk vibrations and the static pressure between the disks. The disk vibrations were measured using a laser Doppler vibrometer (LDV). The static pressure downstream of the arm between a pair of narrow disks was measured by a method in which a side-hole needle was used as a measurement probe. In addition, the direction of air flow along the trailing edge of the arm was measured using a hot-wire anemometer. The experimental results revealed that the arm inserted between the disks suppresses the disk vibrations. However, the shape and thickness of the arm did not quantitatively affect the disk vibrations. The root-mean-square (RMS) static pressure fluctuation downstream of the arm decreased remarkably, whereas the mean static pressure increased when the arm was inserted between the disks. Furthermore, the circumferential variations in both the RMS and mean static pressures reduced when the arm was inserted. Therefore, it is suggested that the disk vibrations are excited by an increase in the static pressure fluctuation, mean dynamic pressure, and circumferential variation in the static pressure between the disks. Consequently, the disk vibrations can be suppressed by inserting the arm or a spoiler. [DOI: 10.1115/1.2427086]

Keywords: information-processing equipment, hard disk drive, disk flutter, flow-induced vibration, pressure distribution

1 Introduction

The data storage industry has continuously enhanced the capacity and performance of hard disk drives (HDDs) by increasing their track density and disk rotational speed. However, high-density drives have a very narrow track width, and high-speed disk rotation produces a high airflow velocity that causes disk vibrations referred to as disk flutter. This can result in track misregistration (TMR) that leads to a positioning error of the read/write head. Therefore, it is important to clarify the excitation mechanisms of the disk vibrations and develop a technique for designing low-vibration HDDs in order to achieve an ultrahigh magnetic recording density.

Thus far, many numerical simulations and experimental studies on flow-induced disk vibrations in HDDs have been reported. McAlister [1] experimentally demonstrated a significant effect of such disk vibrations on the position error signal. Humphrey et al. [2] showed that the fundamental structure of the unobstructed airflow field between shrouded corotating multiple disks is divided into five regions—rigid body rotation, circulation, Ekman boundary layer, shroud boundary layer, and transition—as shown in Fig. 1. Herrero et al. [3] reported that this air flow field maintained a steady axisymmetric structure at small Reynolds numbers (Re) and small interdisk spacing to disk radius aspect ratios (h); however, it changed to an unsteady nonaxisymmetric structure at large values of Re and h. Moreover, Fukaya et al. [4] indicated that this unsteady nonaxisymmetric flow caused pressure fluctuations on the disk; therefore, the small phase difference between the pressure fluctuations on both sides of the disk excited the eigenmode of its elastic vibrations.

On the other hand, Ono and Maeda [5] proposed squeeze air damping by simply setting a flat surface close to the disk with a clearance of <300 μm and showed a significant effect of damping on the disk vibrations. Imai et al. [6] and Imai [7] also showed that reducing the disk-shroud spacing and the shroud-opening angle could effectively reduce the disk vibrations. Heo et al. [8] reported that the disk flutter could be suppressed by using an extended shroud. Thus far, however, the pressure distribution between the disks has not been measured experimentally. The precise excitation mechanism of the disk vibrations has not yet been elucidated because its behavior is very complicated.

[1]Corresponding author.

Contributed by the Fluids Engineering Division of ASME for publication in the JOURNAL OF FLUIDS ENGINEERING. Manuscript received March 22, 2006; final manuscript received July 26, 2006. Assoc. Editor Phillip M. Ligrani.

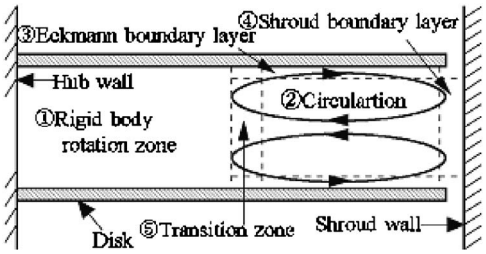

Fig. 1 Schematic of flow field between disks

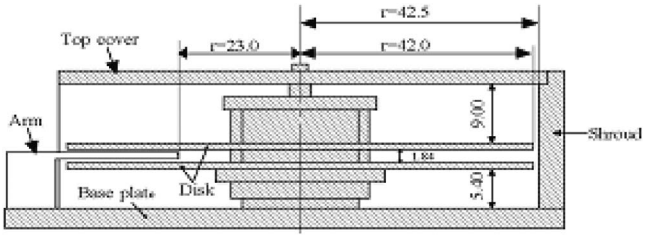

Fig. 3 Sectional view of HDD model

To investigate this mechanism, the authors [9] experimentally studied the interaction between the disk vibrations and the air flow in HDDs and showed that the disk vibration amplitude depends on the fluid density in the HDD. It was concluded that the pressure fluctuation due to an unsteady airflow between the disks must be measured precisely in order to clarify the excitation mechanisms of the disk vibrations. However, this is very difficult because the distance between the disks is too small to measure pressure by the conventional method that employs typical pressure sensors.

Therefore, the purpose of this study is to develop a suitable measurement method for the static pressure between the disks and experimentally investigate the correlation between the flow-induced disk vibrations and the static pressure in order to assist the design of low-vibration HDDs. In particular, we developed a method in which a side-hole needle is used as a probe for measuring the static pressure between the disks. The static pressure in a region downstream of the arm was also measured by this method. We measured the disk vibrations by using a laser Doppler vibrometer (LDV) and studied their correlation with the static pressure between the disks. The effects of the thickness and shape of the arm on the disk vibrations and static pressure were examined experimentally.

2 Experimental

2.1 Experimental Apparatus. Figures 2 and 3 and Table 1 show the schematic diagram, sectional view, and specifications of the HDD model used in the experimental apparatus, respectively. The experimental apparatus comprised a ball-bearing spindle of an actual drive, two corotating disks, and a model arm inserted between the disks. The disks were made of aluminum and their thickness was 1.0 mm. In the operating state, the rotating disks were covered by a top cover and a shroud, as shown in Fig. 3. However, a part of the shroud was opened in order to insert an arm between the disks. The top cover was used to support the spindle at the top in order to reduce its vibrations.

Figure 4 shows the model arm inserted between the disks. Several arms were prepared to investigate the effect of their thickness and shape on the disk vibrations. Three different arms with thicknesses of 1.0 mm, 1.2 mm, and 1.4 mm were tested. Another arm without holes and 1.0 mm in thickness was also examined. The tip thickness of each arm in the swage region was 0.95 mm, and the head-gimbal assembly (HGA) was removed. Hereafter, the conditions that correspond to the use of the arms with thicknesses of 1.0 mm, 1.2 mm, 1.4 mm, 1.0 mm (without holes), and the arm block will be referred to as t10, t12, t14, no-hole, and "without arms," respectively. All experiments were conducted under the condition that each arm was positioned at the inner diameter of the disk and the disk rotational frequency was 10,000 rpm. The disk-to-shroud spacing was maintained constant at 0.5 mm.

Table 2 lists the natural frequencies of the disk calculated by the finite element method (FEM). It is well known that when the disk rotates, the natural frequency divides into two wave modes that correspond to the forward and backward traveling waves; these modes generally depend on the disk rotational frequency [10].

Table 1 Specifications of the experimental setup

Item	Specification
Disk size (mm)	φ 84 (3 in./Al)
Disk number	2
Disk thickness (mm)	1.0
Disk rotational speed (rpm)	10,000
Disk-to-shroud spacing (mm)	0.50
Disk-to-disk spacing (mm)	1.84

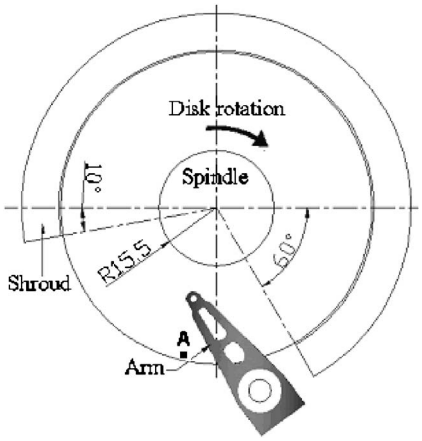

Fig. 2 Schematic of HDD model

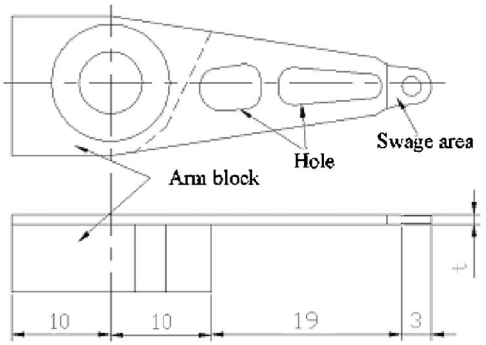

Fig. 4 Schematic of arm inserted between disks

Table 2 Natural frequencies of the disk

n	0	1	2	3
m (Hz)	1042	1004	1157	1914

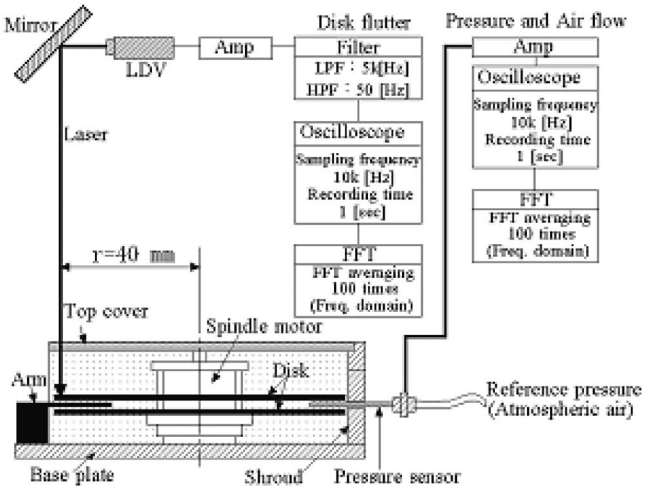

Fig. 5 Schematic of experimental setup for measuring disk vibrations and pressure distribution

2.2 Experimental Procedure. Figure 5 shows the schematic of the experimental setup for measuring the disk vibrations and the static pressure between the disks. These were measured simultaneously to precisely investigate their interrelationship. The following is a detailed description of the measurement methods.

2.3 Disk Vibrations. The transverse vibration of the upper disk at point A, which is 2 mm from the disk rim, was measured by using the LDV. Its output was fed to the digital oscilloscope through the bandpass filter, which was set at 50–5000 Hz, and stored in a computer. The sampling frequency was set at 10,000 Hz after considering the natural frequencies of the disk determined by the FEM.

2.4 Static Pressure Between Disks. A pressure sensor was used to measure the static pressure between the two high-speed corotating disks. The sensor comprised a differential pressure transducer and a side-hole needle as the measurement probe. The specifications of the sensor are listed in Table 3. Figure 6 shows the schematic of the method for measuring the static pressure between the disks. The length of the pressure sensor probe was sufficient for inserting it at the disk inner diameter between the co-rotating disks. The outer and inner diameters of the probe were 1.07 mm and 0.69 mm, respectively. The side-hole diameter was 0.40 mm. When the probe was inserted between the disks, the side

Table 3 Specifications of the pressure sensor

Item	Specification
Sensor type	Differential pressure transducer
Sensitivity (Pa/mV)	1
SNR (dB)	68
Natural frequency (Hz)	6k
Inner diameter of the probe (mm)	0.69
Outer diameter of the probe (mm)	1.07
Side-hole diameter of the probe (mm)	0.40

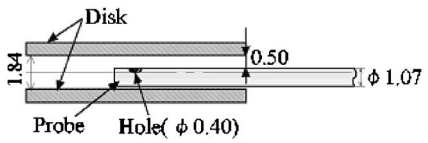

Fig. 6 Schematic of method for measuring static pressure between two disks using pressure sensor

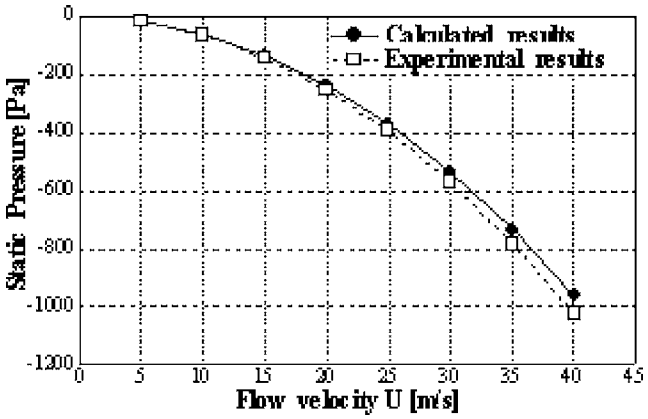

Fig. 7 Static pressure in wind tunnel (calculated versus experimental results)

hole was parallel to the air flow direction. Thus, the method for measuring the static pressure between the disks was similar to the Pitot tube method. In this case, the Helmholtz and organ-pipe resonance frequencies of the probe were ~2635 Hz and ~4605 Hz, respectively. Hence, it was considered that the pressure sensor probe did not resonate with the air flow between the disks. The static pressure was calculated using the Bernoulli equation,

$$P_t = P_s + \frac{\rho U^2}{2} \tag{1}$$

In Eq. (1), P_t is the total pressure; P_s, the static pressure; U, the airflow velocity; and ρ, the air density (1.2 kg/m^3). In this study, P_t was defined as the atmospheric pressure and expediently set to 0 Pa. Therefore, Eq. (1) was modified and used to calculate P_s as follows:

$$P_s = \frac{-\rho U^2}{2} \tag{2}$$

Moreover, U was measured using a hot-wire anemometer. Figure 7 shows the relationship between the calculated and experimental results of the static pressure in the wind tunnel. It is observed that the experimental and calculated results are in agreement. However, the difference between them increases with U. Hence, P_s may not be measured precisely when $U > 40$ m/s. On the other hand, it is considered that $U < 40$ m/s because the circumferential velocity of the disk at its rim exceeds 40 m/s. Therefore, it is confirmed that the static pressure can be measured precisely by using the measurement probe.

However, the static pressure between the disks could not be measured precisely in the HDD model. This was because the airflow between the disks was disturbed by the insertion of an obstacle such as the measurement probe, as reported by Suzuki and Humphrey [11]. On the other hand, Usry et al. [12] indicated that this disturbed airflow between the disks recovered within one revolution of the disk. Therefore, in this study, we decided to measure the static pressure between the disks by inserting the probe downstream of the arm at the points shown in Fig. 8. This method for measuring the airflow velocity between the disks was reported by Watanabe et al. [13]. It was considered that the static pressure could be measured by this method without the influence of the probe on the airflow between the disks.

Figure 9 shows the mean static pressure at the points depicted in Fig. 8. The calculated results were obtained using Eq. (1) and the airflow velocity measured with the hot-wire anemometer. The experimental and calculated results were almost in good agreement. However, the difference between them was large at the inner diameter (Indices 1–5). Therefore, the static pressure at the

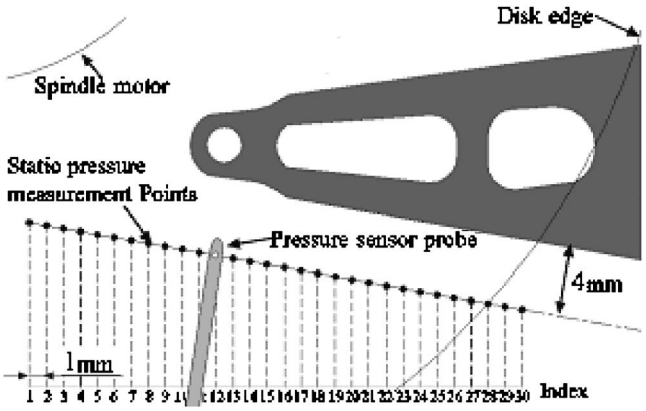

Fig. 8 Schematic of static pressure measurement points downstream of the arm

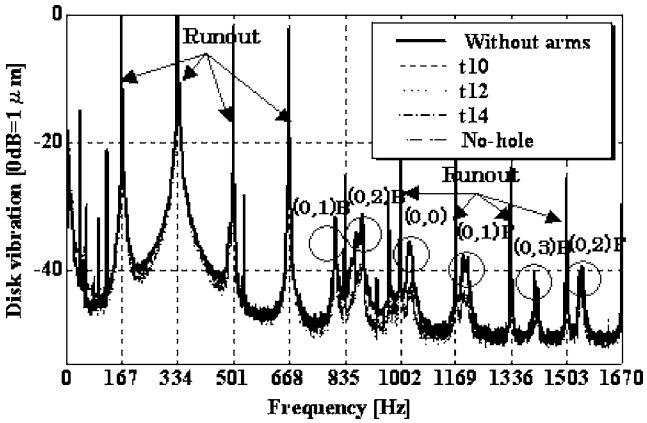

Fig. 10 Experimental results of disk vibration at disk rim

inner diameter may not be measured precisely. Yet, we believe that the static pressure measured by this method provides important information because the pressure at the outer diameter mainly affects the disk vibrations [7]. Hence, it was confirmed that the static pressure from the outer to the middle diameter between the disks could be measured satisfactorily by this method. In this case, the magnitude of fluctuations and the phase of the static pressure in the side-hole part and the transducer may be different because the pressure sensor probe was a long and thin tube. In other words, the change in the magnitude of fluctuations and the phase lag may be caused by the effect of the volume and resistance of the probe. However, we believe that they can be ignored because the purpose of this study is to make a relative comparison of the static pressure between the disks under various conditions. Finally, all the results obtained in this study were reproducible.

3 Results and Discussion

3.1 Disk Vibrations. Figure 10 shows the spectra of the transverse vibration at point A on the upper disk (in Fig. 2) and compares the cases of t10, t12, t14, no-hole, and without arms. The solid curve indicates the case without arms. The other curves correspond to the cases in which the four arms are inserted between the disks. In Fig. 10, (m,n) represents the vibration mode of m nodal circles and n nodal diameters; B and F represent the backward and forward traveling waves, respectively. Several peaks resulting from the runout and vibration modes of the disk are observed. Moreover, the amplitude of each disk vibration mode in the case without arms is the largest. However, it appears that the thickness and shape of the arm do not affect the reduction in the disk vibration amplitude. This is because the difference between the amplitudes of the frequency components of the disk flutter is small. In general, it is considered that disk vibrations increase when the arm is inserted between disks because the disturbed flow induces disk vibrations. However, the present results indicate an opposite tendency. Therefore, in order to clarify this phenomenon, it is necessary to measure the static pressure distribution between the disks with and without the insertion of the arm between them.

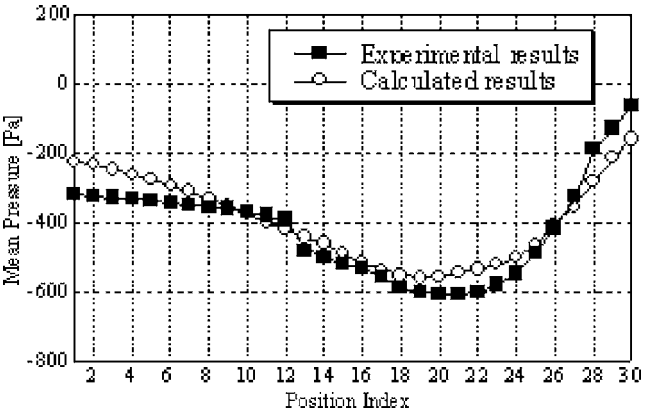

Fig. 9 Static pressure downstream of the arm between disks (calculated versus experimental results)

3.2 Static Pressure Fluctuation Between Disks. Figure 11 compares the radial distributions of the power spectral density (PSD) of the static pressure fluctuation between the disks in the cases of t10, t12, t14, no-hole, and without arms. In each case, several large power spectra are observed; they correspond to a multiple of the disk rotational frequency. Therefore, the static pressure between the disks fluctuates strongly due to disk runout. Large power spectra from the middle to the outer region of the disk (Indices 16–28) and the runout frequency are observed only in the case without an arm. In the high-frequency components of these spectra (encircled with a solid line, Fig. 11(a)), the power spectra corresponding to the (0,1)B mode of the disk vibrations is also confirmed. Furthermore, at indices 13 and 14 (encircled with a dashed line, Fig. 11(a)), large power spectra are produced over a wide frequency range. Therefore, it appears that the airflow field between the disks in the case without arms is extremely complicated because the static pressure fluctuation is very high and its frequency range is very wide. On the other hand, when the arm is inserted between the disks, power spectra similar to those in the case without arms are not observed (although the runout components are observed), and the magnitude of the spectra is generally low. Consequently, it is found that when the arm is inserted between the disks, the static pressure and airflow fluctuations between them are considerably less than those in the case without arms.

We also investigated the static pressure distribution not only near the arm but also downstream of it because it is considered that the static pressure fluctuation at the shroud opening affects the disk vibrations significantly. Figure 12 shows a schematic of the static pressure measurement region downstream of the arm. The method for measuring the static pressure is the same as that in Fig. 6. Figure 13 compares the distributions of the root-mean-square (RMS) static pressure fluctuation between the disks in the cases of t10, t12, t14, no-hole, and without arms. An extremely large fluctuation in the static pressure is observed in the outer region of the disk only in the case without arms. Furthermore, the largest fluctuation in the static pressure occurs near indices 13 and 14 (encircled with a solid line, Fig. 13(a)), where large power spectra are observed over a wide frequency range in Fig. 11(a). On the other hand, when the arm is inserted between the disks, the

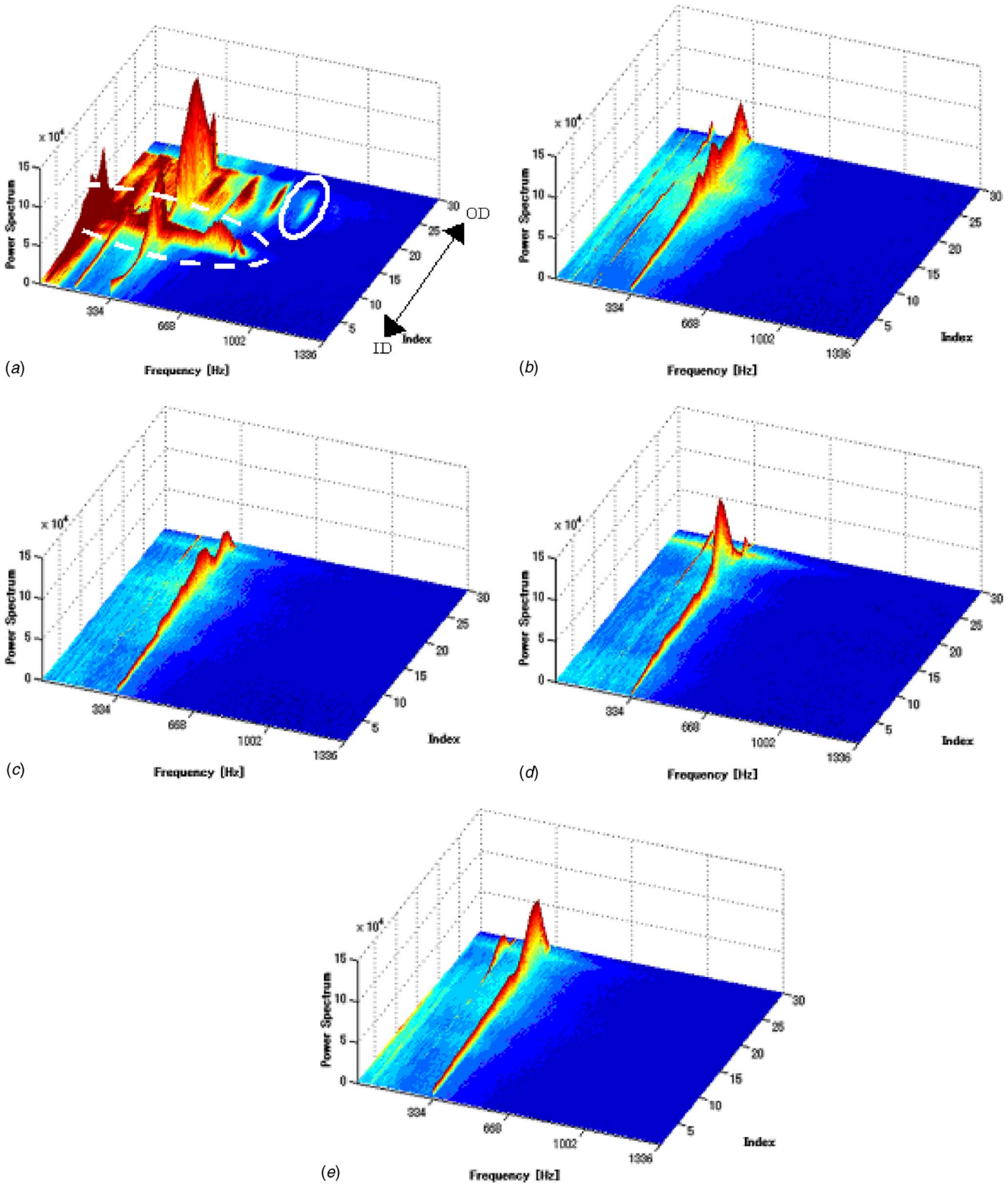

Fig. 11 FFT results of static pressure fluctuation downstream of the arm between disks

RMS static pressure fluctuation is considerably less and its distribution is generally more uniform than that in the case without arms. In addition, its circumferential variation is significantly less than that in the case without arms.

These experimental results indicated that the static pressure fluctuation downstream of the arm was reduced remarkably by inserting the arm between the disks. It was also confirmed that the power spectra corresponding to the (0,1)B mode of the disk vibrations were produced in the PSD without arms. On the other hand, the experimental results of the disk vibration measurement shown in Fig. 10 revealed that the vibrations reduced when the arm was inserted between the disks. Shimizu et al. [14] performed a large eddy simulation (LES) and showed that the pressure fluctuation between the disks was correlated with the disk vibration ampli-

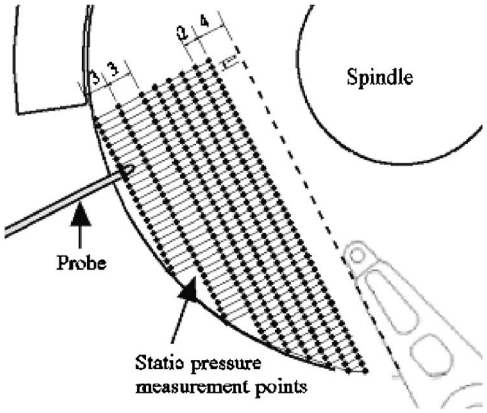

Fig. 12 Schematic of static pressure measurement region downstream of arm

tude. Therefore, it is suggested that this amplitude is strongly correlated with the static pressure fluctuation between the disks and can be suppressed by reducing this fluctuation.

3.3 Mean Static Pressure Between Disks. Figure 14 compares the distributions of the mean static pressure in the measurement region shown in Fig. 12 in the cases of t10 and without arms. The mean static pressure in the case without arms was generally less than that in the case of t10. An extremely low static pressure region (encircled with a solid line, Fig. 14(*a*)) was also observed. On the other hand, when the arm was inserted between the disks, such a region did not appear and the circumferential variation in the mean static pressure was less than that in the case without arms. Therefore, when the arm was inserted between the disks, the mean static pressure downstream of the arm increased with a moderate variation rate. Suzuki and Humphrey [11] showed that disk vibrations could be suppressed by reducing the circumferential variation in the pressure on the disk surface. Therefore, in our experiments, the disk vibrations could be sup-

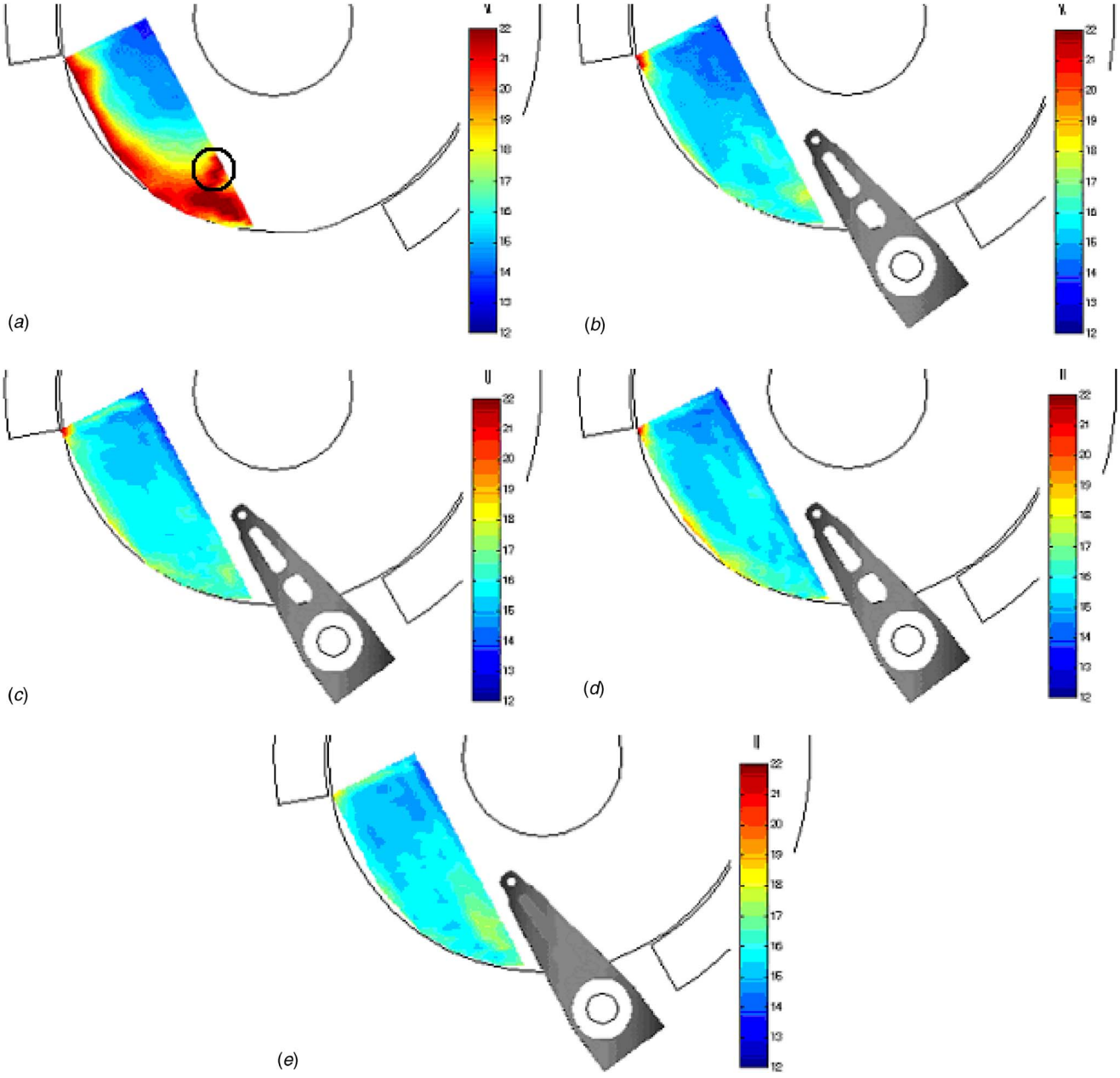

Fig. 13 RMS static pressure fluctuation downstream of the arm

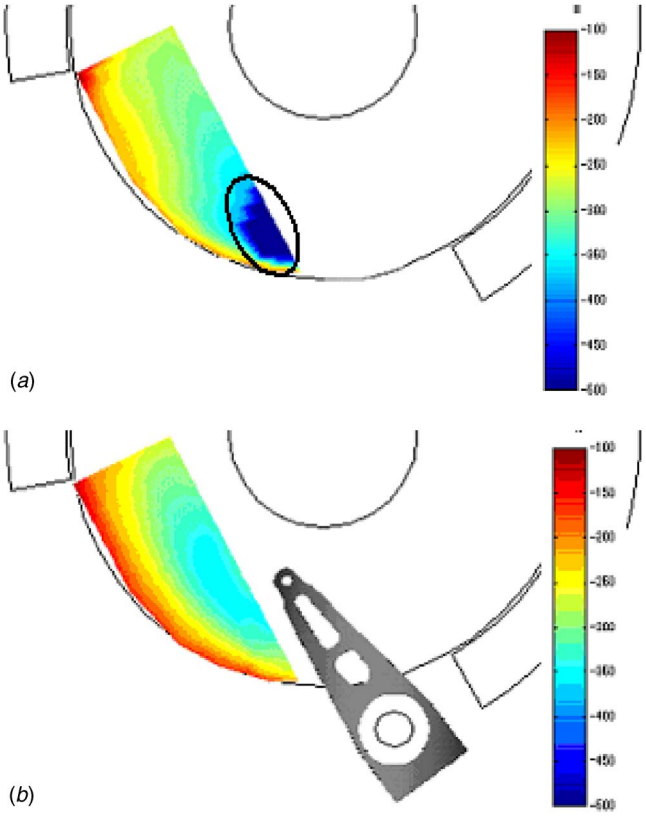

Fig. 14 Mean static pressure distribution downstream region of the arm

pressed by reducing the circumferential variation in the mean static pressure. Furthermore, according to Eq. (1), it is expected that the dynamic pressure between the disks will decrease when the arm is inserted. In a previous study [9], we demonstrated that the disk vibration amplitude is proportional to the dynamic pressure on the disk surface. Therefore, it is proposed that the disk vibration amplitude is reduced by the decrease in the dynamic pressure due to the insertion of the arm between the disks.

Based on these experimental results of the static pressure between the disks, it is suggested that the disk vibrations are excited by an increase in the static pressure fluctuation, mean dynamic pressure, and circumferential variation in the static pressure between the disks. Furthermore, the disk vibration amplitude can be suppressed by inserting the arm or a spoiler that reduces them [15].

3.4 Airflow Direction Downstream of Arm. We measured the airflow direction along the trailing edge of the arm by using the hot-wire anemometer in order to determine the reason for the decrease in the static pressure fluctuation and the mean dynamic pressure when the arm was inserted between the disks. Figure 15 compares the airflow direction downstream of the arm between the disks in the cases of t10 and without arms. It was confirmed that the airflow was partially blocked by the arm and then redirected toward the spindle motor along the leading edge of the arm. This phenomenon was also reported by Humphrey et al. [16]. When the arm was inserted, the inflow and outflow rates appeared to decrease at the shroud opening. Therefore, it was concluded that the inserted arm decreased the static pressure fluctuation, mean dynamic pressure, and circumferential variation in the static pressure by reducing the inflow and outflow rates at the shroud opening. Consequently, the disk vibration amplitude was suppressed in our experiment.

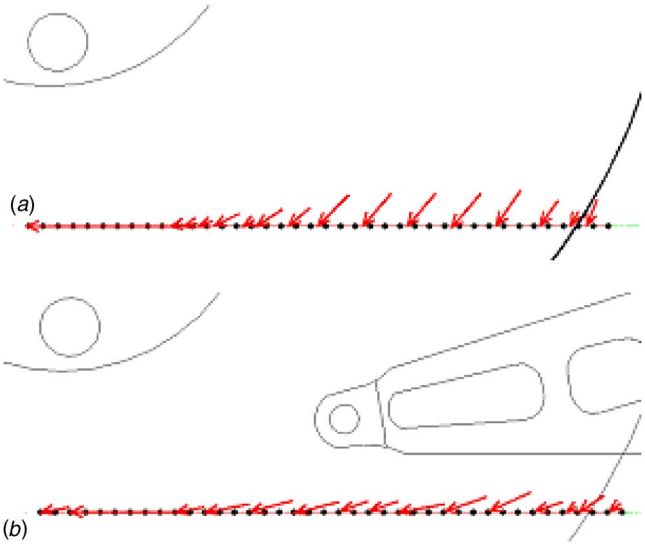

Fig. 15 Airflow direction downstream of the arm between disks

4 Conclusion

In this study, the correlation between the flow-induced disk vibrations and the static pressure between the high-speed corotating disks in the HDD model was investigated experimentally in order to assist the design of low-vibration HDDs. The effects of the arm thickness and arm shape on disk vibrations and the static pressure between the disks were also studied. Three arms (with a hole) of thicknesses 1.0 mm, 1.2 mm, and 1.4 mm were tested. Another arm without a hole and 1.0 mm in thickness was also examined. The disk vibrations were measured using an LDV. The static pressure between the disks was measured by a method developed in this study. Finally, the airflow direction along the trailing edge of the arm was determined using a hot-wire anemometer. The following results were obtained from the experiments:

1. The arm inserted between the disks suppresses disk vibration amplitude. However, the thickness and shape of the arm do not quantitatively affect the disk vibration amplitude.
2. When the arm is inserted between the disks, the static pressure fluctuation downstream of the arm decreases remarkably, while the mean static pressure increases.
3. It is suggested that disk vibrations are excited by an increase in the static pressure fluctuation, mean dynamic pressure, and circumferential variation in the static pressure between the disks. The disk vibrations can be suppressed by inserting the arm or a spoiler that reduces them.

However, in order to successfully design low-vibration HDDs, we believe that the static pressure should be measured in the entire region between the disks.

Acknowledgment

The authors would like to express their gratitude to Prof. David B. Bogy (UC Berkeley) and Toru Watanabe (Fujitsu, Ltd.) for their generous support and cooperation in this study. The present work was supported, in part, by the Kansai University High-Tech Research Center's Project: the development of the innovative nanotechnology for the Tbit class ultrahigh-density information storage systems supporting the ubiquitous society, 2005–2009.

References

[1] McAllister, J. S., 1996, "The Effect of Disk Platter Resonances on Track Misregistration in 3.5 Inch Disk Drives," IEEE Trans. Magn. **32**(3), pp. 1762–1766.

[2] Humphrey, J. A, C., Li, H., and Schuler, C. A., 1991, "Unobstructed and Obstructed Rotating Disk Flows: A Summary Review Relevant to Information Storage Systems," Adv. Inf. Storage Syst. **1**, pp. 79–110.
[3] Herrero, J., Giralt, F., and Humphrey, J. A. C., 1999, "Influence of the Geometry on the Structure of the Flow Between a Pair of Corotating Disks," Phys. Fluids **11**(1), pp. 88–96.
[4] Fukaya, R., Obi, S., Masuda, S., and Tokuyama, M., 2002, "Flow Instability and Elastic Vibration of Shrouded Corotating Disk Systems," Exp. Fluids **33**, pp. 369–373.
[5] Ono, K., and Maeda, E., 2000 "Suppression of Disk Flutter by a Squeeze Air Bearing Plate," J. Inf. Storage Process. Syst. **2**, pp. 33–40.
[6] Imai, S., Tokuyama, M., and Yamaguchi, Y., 1999 "Reduction of Disk Flutter by Decreasing Disk-to-Shroud Spacing," IEEE Trans. Magn. **35**(5), pp. 2301–2303.
[7] Imai, S., 2001, "Fluid Dynamics Mechanism of Disk Flutter by Measuring the Pressure Between Disks," IEEE Trans. Magn. **37**(2), pp. 837–841.
[8] Heo, B., Shen, I. Y., and Riley, J. J., 2000, "Reducing Disk Flutter by Improving Aerodynamic Design of Base Casings," IEEE Trans. Magn. **36**(5), pp. 2222–2224.
[9] Takada, S., Tagawa, N., Mori, A., Mizoh, Y., and Nakakita, M., 2006, "Study on Flow Induced Vibration of Head Disk Assembly Mechanisms With High Speed Rotating Disks (1st Report)," Trans. Jpn. Soc. Mech. Eng., Ser. C in Japanese, **72**, pp. 22–29.
[10] Shen, I. Y., and Ku, C.-P. R., 1995 "On the Vibration Analysis of Multiple Rotating Flexible Disks," Adv. Inf. Storage Syst. **1**, pp. 259–270.
[11] Suzuki, H., and Humphrey, J. A. C., 1997, "Flow Past Large Obstructions Between Corotating Disks in Fixed Cylindrical Enclosures," ASME J. Fluids Eng. **119**, pp. 499–504.
[12] Usry, W. R., Humphrey, J. A. C., and Greif, R., 1993, "Unsteady Flow in the Obstructed Space Between Disks Corotating in a Cylindrical Enclosure," ASME J. Fluids Eng. **115**, pp. 620–626.
[13] Watanabe, T., Gross, H., Bogy, D., and Savas, O., 2002, "Investigation and Characterization of Airflow Effects and Airflow-Induced TMR Past In-line Type Head Stack Assemblies Between co-rotating Disks," *Proceedings of ASME Information Storage and Processing Systems Conference 2002*, Santa Clara, ASME, New York.
[14] Shimizu, H., Tokuyama, M., Imai, S., Nakamura, S., and Sakai, K., 2001, "Study of Aerodynamic Characteristics in Hard Disk Drives by Numerical Simulation," IEEE Trans. Magn. **37**(2), pp. 833–836.
[15] Hirono, Y., Arisaka, T., Nisijima, N., Shimizu, T., Nakamura, S., and Masuda, H., 2004, "Flow-Induced Vibration Reduction in HDD by Using a Spoiler," IEEE Trans. Magn. **40**(4), pp. 3168–3170.
[16] Humphrey, J. A. C., Kazemi, M., and Herrero, J., 2003, "Method for Calculating the Velocity of Air Flowing Past a Pair of Suspensions in a Disk Drive," Microsyst. Technol. **9**, pp. 534–540.